# Characteristics and impact of mesoscale eddies in the eastern tropical North Atlantic

**Dissertation**
zur Erlangung des Doktorgrades
der Mathematisch-Naturwissenschaftlichen Fakultät
der Christian-Albrechts-Universität
zu Kiel

vorgelegt von
Florian Schütte

Kiel 2016

**GEOMAR**
Helmholtz-Zentrum für Ozeanforschung Kiel

Referent: Prof. Dr. Peter Brandt
Korreferent: Prof. Dr. Arne Biastoch
Datum der mündlichen Prüfung: 22.7.2016
Zum Druck genehmigt:
Gez.: Prof. Dr. Wolfgang J. Duschl, Dekan

# Zusammenfassung

In dieser Studie wurden die Eigenschaften mesoskaliger Wirbel im tropischen Nordost Atlantik (12-22°N und 15-26°W) untersucht. Hierfür wurden die mittleren Oberflächensignaturen der Wirbel und Anomalien der Vertikalstrukturen relativ zum umgebenden Wasser aus einer Kombination von mehreren ozeanographischen Messsystemen (Verankerungen, Argo-Floats, Satelliten, Schiffen und Gleitern) erstellt. Berücksichtigt man ausschließlich die Rotationsrichtungen, lassen sich Wirbel in Zyklone und Antizyklone unterteilen. Mithilfe der vertikalen Schichtung kann ein dritter Wirbeltyp unterschieden werden, der sogenannte antizyklonale Modewasser-Wirbel (ACME), welcher auch intra-thermokliner Wirbel genannt wird. Der Kern eines ACME besteht aus einer vergleichsweise homogenen Wassermasse, und wird von nach oben und unten ausgelenkten Dichteflächen eingeschlossen. Somit transportieren ACMEs starke hydrographische Anomalien innerhalb eines relativ schmalen Dichtebereichs. Alle drei Wirbeltypen konnten via Satellitenbeobachtung durch die Kombination der folgenden Parameter identifiziert und klassifiziert werden: Meeresoberflächenauslenkung (SLA), Meeresoberflächentemperatur (SST) und Meeresoberflächensalzgehalt (SSS). Die Oberflächensignaturen von Antizyklonen/Zyklonen weisen erhöhte/reduzierte SLA, SST und SSS auf. Von allen antizyklonal rotierenden Wirbeln zeigten etwa 20% reduzierte SST und SSS auf und konnten somit als ACMEs identifiziert werden. Im gesamten Untersuchungsgebiet wurden 146 ± 4 Wirbel pro Jahr mit einer Lebensdauer von mehr als 7 Tagen gezählt (52% Zyklone, 39% Antizyklone, 9% ACMEs). Alle untersuchten Wirbel waren isoliert und transportierten Wassermassen von der Küste in den offenen Ozean ($\sim$ 2.1 $Sv$; 1 $Sv = 10^6 \ m^3 s^{-1}$). Der vom Wirbeltyp abhängige Wärmefluss (Salzfluss) entsprach -0.46 $TW$ (-23.15 x $10^3 \ kgs^{-1}$) / 0.35 $TW$ (12.9 x $10^3 \ kgs^{-1}$) / -0.49 $TW$ (-29.9 x $10^3 \ kgs^{-1}$) für einen Zyklon / Antizyklon / ACME. Des Weiteren zeichneten sich Zyklone und ACMEs mit einer sehr niedrigen Sauerstoffkonzentration in ihren Wirbelkernen, einer verstärkten Primärproduktion an der Oberfläche (erhöhter Chlorophyll Gehalt) sowie einem, verglichen mit dem Hintergrundfeld, 3-5 mal höheren Sauerstoffverbrauch innerhalb des isolierten Wirbelkerns aus. Trotz der starken Isolation des Kerns, bedingt die erhöhte Primärproduktivität eine vertikale Zufuhr von Nährstoffen in die euphotische Zone. Es wird die Hypothese aufgestellt, dass die Bildung kritischer Schichten und infolgedessen eine intensive vertikale Durchmischung am Wirbelrand auftritt. Hervorgerufen wird diese durch die Wechselwirkung der Rotationsbewegung des Wirbels mit Wellen, die eine Frequenz nahe der Trägheitsfrequenz aufweisen. Dieser Prozess könnte einen Weg beschreiben, der vertikalen Transport von Nährstoffen in die euphotische Zone und die zeitgleiche Existenz eines isolierten Kerns möglich macht. Im Durchschnitt lag die Sauerstoffverbrauchsrate für Zyklone (ACMEs) in den isolierten Kernen bei 0.10 ± 0.12 (0.19 ± 0.08) $\mu mol kg^{-1} d^{-1}$. Bei einer Wirbellebenszeit von bis zu einem Jahr führt das zu den gemessenen hypoxischen, teilweise sogar suboxischen Bedingungen in den Wirbelkernen. Die Analyse zeigt, dass die beobachteten Wirbelkerne, die durch extreme Wassermassenanomalien gekennzeichnet sind, häufiger als zuvor erwartet und sogar nahe dem Äquator (8°N) auftreten. Die Dispersion der niedrigen Sauerstoffkonzentration, entlang von Isopyknen, kann laut regionalen Budgetberechnungen bis zu 6% des Sauerstoffverbrauchs in der oberen Schicht des Nordostatlantiks erklären.

# Abstract

A combination of multiple ocean observing system elements (moorings, Argo floats, satellites, ships, gliders) is used to assess the mesoscale eddy activity in the tropical Atlantic off northwestern Africa (12-22°N and 15-26°W) and to construct mean surface patterns as well as vertical anomalies relative to the surrounding water for the different eddy types. Considering just the rotation direction of the surface flow field, eddies are categorized into cyclonic and anticyclonic eddies. If vertical stratification is considered additionally, a refinement can be made by distinguishing between anticyclonic and anticyclonic modewater eddies (ACMEs, also intra-thermocline eddies). ACMEs are characterized by a subsurface mode of rather homogenous water located between upward and downward displaced isopycnals. Consequently, these eddies may transport large hydrographic anomalies in a relatively narrow density range. Eddies can be identified and classified from space by investigating a combination of three sea surface parameters: Sea level anomaly (SLA), sea surface temperature (SST) and sea surface salinity (SSS). Anticyclones/cyclones are associated with an elevation/depression of SLA and enhanced/reduced SST and SSS in their cores. For both eddy types, SST dominates sea surface density and consequently anticyclones/cyclones are associated to reduced/enhanced surface density. However, 20% of all anticyclonic eddies are associated with reduced SST and SSS instead and are identified as ACMEs. In the area of interest, about $146 \pm 4$ eddies per year with a minimum lifetime of 7 days are identified (52% cyclones, 39% anticyclones, 9% ACMEs). All observed eddies are isolated and serve as transport agents, exporting water from the coast into the open ocean ($\sim 2.1$ $Sv$; 1 $Sv = 10^6$ $m^3 s^{-1}$). The associated eddy type dependent heat (salt) flux is estimated to be -0.46 $TW$ (-23.15 x $10^3$ $kgs^{-1}$) / 0.35 $TW$ (12.9 x $10^3$ $kgs^{-1}$) / -0.49 $TW$ (-29.9 x $10^3$ $kgs^{-1}$) for single cyclone / anticyclone / ACME, respectively. In cyclones and ACMEs low oxygen cores are identified and related to enhanced primary production at the surface (enhanced chlorophyll) and an associated elevated respiration rates (3-5 times higher than the background) within the isolated eddy cores. Despite the isolation of the eddy core, the enhanced primary productivity at the surface requires a vertical supply of nutrients into the euphotic zone. It could be observed that the phase speed of near inertial waves and the speed of the mean eddy flow are of similar magnitude. Therefore, critical layer formation is expected and mixing is likely to occur close to the euphotic zone/mixed layer at the eddy periphery. These processes describe a scenario that supports an upward nutrient flux towards the euphotic zone, but still maintains a highly isolated eddy core, which is seen by the observations. On average the apparent oxygen utilization rate (aOUR) for cyclones (ACMEs) in their isolated cores is $0.10 \pm 0.12$ ($0.19 \pm 0.08$) $\mu mol kg^{-1} d^{-1}$. If the aOUR is continuously active during a typical eddy life time hypoxic or even suboxic conditions in the eddy cores can occur. The analysis of mesoscale eddies in the eastern tropical North Atlantic shows that anomalous environments associated with eddy cores occur more frequently than previously expected and can be observed even in the proximity to the equator (8°N). From regional budget calculations it is shown that an isopycnal dispersion of the low oxygen water after the decay of the eddies can explain up to 6% of the oxygen consumption in the upper northeast Atlantic.

# Contents

# 1 Introduction

The ocean is inherently turbulent on several spatial scales. Some of these turbulent motions are characterized by horizontal shear, grow and develop into linear wave-like patterns and/or nonlinear vortices, whereas the latter are loosely described as eddies. The so-called mesoscale eddies are ubiquitous in the world oceans and an essential part of the oceanic motion on periods greater than the inertial and tidal periods [*Stammer and Wunsch*, 1999; *Chelton et al.*, 2007, 2011b]. Mesoscale eddies have radii of about 10 to 200 $km$ and lifetimes from a few days to one year or even longer [*Chelton et al.*, 2011b]. In contrast to linear waves, coherent mesoscale eddies have the capability to transport physical properties (e.g. heat, salt, mass, momentum) and numerous other biogeochemical tracers over long distances and across frontal boundaries [e.g. *McWilliams*, 1985; *Flierl*, 1981; *Chaigneau et al.*, 2008; *Zhang et al.*, 2014]. Thereby they impact the large-scale water mass distribution, the general circulation and ocean biology [e.g. *Robinson and Leslie*, 1985; *Roemmich and Gilson*, 2001; *Jayne and Marotzke*, 2002; *Biastoch et al.*, 2009; *Nagai et al.*, 2015]. For a while, mesoscale eddies and other random fluctuations were regarded as nuisance, masking the mean flow. Improvements in ocean observing, in particular from satellite missions, but also from high resolution global ocean models revealed that instead they are a prominent feature of the ocean circulation [e.g. *Chelton et al.*, 2007, 2011b; *Capet et al.*, 2008a]. Over the last 20 years mesoscale eddies, and as such the turbulent character of the ocean, have gained much attention. It got obvious that knowledge about the characteristics and impacts of mesoscale eddies will improve our understanding of the whole ocean system covering various research disciplines [e.g. *Lachkar and Gruber*, 2012; *Frenger et al.*, 2013; *Nagai et al.*, 2015]. On the one hand, they physically interact with the mean flow by e.g. energy exchange, dispersing of tracers or play an important role in preconditioning of deep convection and subduction processes [e.g. *Marshall*, 1997; *Qiu et al.*, 2008; *Xu et al.*, 2014]. On the other hand, they influence biogeochemical properties and have an impact on marine life in forming isolated open ocean ecosystems, which could evolve due to vertical transport processes within the eddies [e.g. *McGillicuddy et al.*, 2007; *Mahadevan et al.*, 2008; *Gaube et al.*, 2014b].

The aim of this thesis is to enhance the understanding of the occurrence, characteristics, evolution and impact of mesoscale eddies in the boundary upwelling system of the eastern tropical North Atlantic (ETNA; 4°N to 22°N and from the shelf at the eastern boundary to 38°W) on the basis of observational data. With the aid of satellite data, the general eddy activity is assessed and mean eddy surface signatures are constructed. Due to a combination of satellite data with vertical profiles a mean eddy-type dependent vertical structure, heat, salt and oxygen fluxes are derived. In addition, the physical and biogeochemical co-variability and the associated vertical transport processes within mesoscale eddies are investigated using high-resolution glider surveys.

## 1.1 The eastern tropical North Atlantic

The ETNA region (4°N to 22°N, extending from the eastern boundary shelf offshore to 38°W) includes the area of the unventilated shadow zone [*Luyten et al.*, 1983] as well as one of the world oceans four highly productive eastern boundary upwelling systems (EBUSs) [e.g. *Bakun*, 1990; *Pauly and Christensen*, 1995; *Carr et al.*, 2008; *Messié et al.*, 2009; *Lachkar and Gruber*, 2012, Fig. 1.1]. Within the EBUSs equatorward winds result in offshore Ekman transport driving coastal upwelling and alongshore (under-) currents [e.g. *Bakun and Nelson*, 1991; *Tomczak et al.*, 1994; *Capet et al.*, 2008a]. On the continental shelf upwelling of cold, fresh, nutrient-rich waters with high concentrations in nitrate and organic and inorganic carbon, can create intense fronts over short distances separating coastal from offshore waters, which are warmer, saltier, nutrient-depleted and characterised by low concentrations in nitrate as well as organic and inorganic carbon [e.g. *Wyrtki*, 1962; *Strub et al.*, 1998; *Chavez and Messié*, 2009; *Nagai et al.*, 2015].
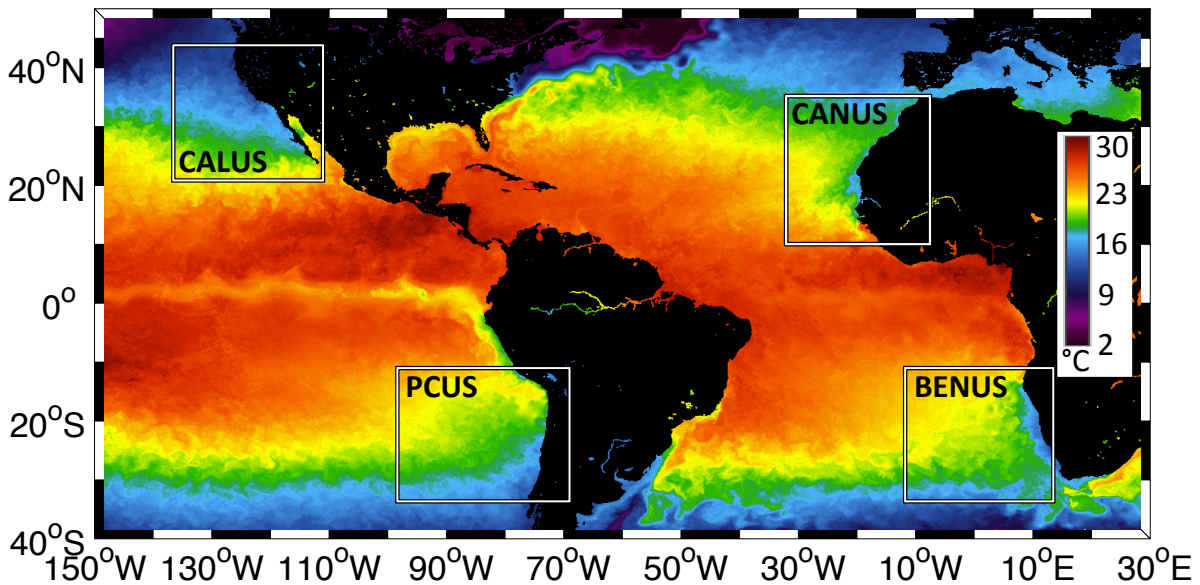


Figure 1.1: Sea surface temperature snapshot (May 4th, 2016) based on satellite measurements (Microwave Infrared Fusion SST from www.remss.com) of the east Pacific and Atlantic Ocean. The boxes highlight the four major eastern boundary upwelling systems (EBUS), namely the Peru-Chile and California upwelling systems (PCUS and CALUS, respectively) in the Pacific Ocean, and the Canary and Benguela upwelling systems (CANUS and BENUS, respectively) in the Atlantic Ocean.

In the EBUSs mesoscale eddies act as a major transport agent between coastal waters and the open ocean [e.g. *Marchesiello et al.*, 2003; *Correa-Ramirez et al.*, 2007; *Chaigneau et al.*, 2008; *Pegliasco et al.*, 2015]. Eddies are generated mostly close to the coast [e.g. *Chelton et al.*, 2011b; *Liang et al.*, 2012], where large horizontal/vertical shears exist in an otherwise quiescent region. The eddies enclose specific coastal water mass properties and, in translating westward, they transport the properties offshore within their core [e.g. *Johnson and McTaggart*, 2010; *Chaigneau et al.*, 2008, 2011; *Nagai et al.*, 2015]. In the open ocean the water mass properties are redistributed once the eddy decays [e.g. *Swart et al.*, 2008]. Regional studies on mesoscale

eddy dynamics and transports in EBUSs are available for the southeastern Pacific Ocean [e.g. *Chaigneau and Pizarro*, 2005; *Chaigneau et al.*, 2008, 2011] and the northeastern Pacific [e.g. *Kurian et al.*, 2011; *Liang et al.*, 2012; *Chang et al.*, 2012], but for the Atlantic Ocean regional eddy studies are rare. *Sangrà et al.* [2009] studied eddies in the northeastern Atlantic but focusing more on the northern Canary Islands and the Mediterranean outflow. The general characteristics of mesoscale eddies in the ETNA as well as their contribution to the dispersal of water mass properties and biogeochemical tracers are undocumented so far. Even less is known about the rich biology and associated strong biogeochemical cycles within eddies and their impact on the open ocean environment. This study will investigate how eddies contribute to the communication of the coastal upwelling region with the open ocean in the ETNA region.

The ETNA region is characterized by a weak, large-scale mean circulation, but pronounced mesoscale eddy variability [*Mittelstaedt*, 1991; *Stammer and Wunsch*, 1999; *Brandt et al.*, 2015]. Strong coastal upwelling between 10°N to 20°N usually occurs in boreal winter and spring, giving rise to a strong phytoplankton bloom near the African coast [e.g. *Messié et al.*, 2009; *Lachkar and Gruber*, 2012]. During the upwelling season the ETNA is governed by substantial variability with intense interweaving of warm offshore waters with cold, upwelled waters as observational evidence indicates (e.g. like in the California current: [*Brink and Cowles*, 1991], or off Peru [*Capet et al.*, 2008b]). In general, in the ETNA region surface heating results in strong stratification of the upper ocean. Beneath the surface waters, a mixture of North Atlantic Central Water (NACW), which is formed in the ventilated part of the subtropical gyre of the North Atlantic, and South Atlantic Central Water (SACW), which is upwelled in coastal and equatorial regions, is typically found. The Cape Verde Frontal Zone (CVFZ) separates these two water masses, with NACW in the northwest and SACW in the southeast of the ETNA region [*Zenk et al.*, 1991]. The upwelling region itself is supplied by waters with South Atlantic origin via a pathway along the North Brazil Current (NBC), the North Equatorial Undercurrent (NEUC) and the Poleward Undercurrent (PUC) [*Glessmer et al.*, 2009; *Peña Izquierdo et al.*, 2015]. The PUC is a highly variable coastal undercurrent induced by the large-scale alongshore pressure gradient set by the southward winds off the African coast [*Barton*, 1989]. It is strongest during the upwelling season with a mean transport estimate of about 1 Sv ($1Sv = 10^6 \ m^3s^{-1}$) [*Tomczak*, 1973; *Mittelstaedt*, 1991; *Schafstall et al.*, 2010]. Simultaneously to the suppression of coastal upwelling south of Cap Blanc at 21°N, a northward surface boundary current called Mauretania Current (MC) is established at the eastern boundary of the ETNA region [*Peña Izquierdo et al.*, 2012, Fig. 1.2a]. The strength of the MC is strongly related to the seasonality of the North Equatorial Counter Current (NECC) being strongest in boreal summer and weaker and more unsteady in boreal winter [*Mittelstaedt*, 1991; *Lázaro et al.*, 2005]. In addition, the ETNA region is characterized by a distinct oxygen minimum zone (OMZ) with a core depth of about 450 m [*Karstensen et al.*, 2008; *Brandt et al.*, 2015]. The OMZ is primarily controlled by sluggish ventilation along the respective isopycnals [*Wyrtki*, 1962; *Luyten et al.*, 1983]. It extends from the eastern boundary into the open ocean and is located within the so-called shadow zone of the ventilated thermocline, bounded by the more energetic circulation of the subtropical gyre in the north and the energetic equatorial current regime in the south [*Luyten et al.*, 1983; *Karstensen et al.*, 2008; *Brandt et al.*,
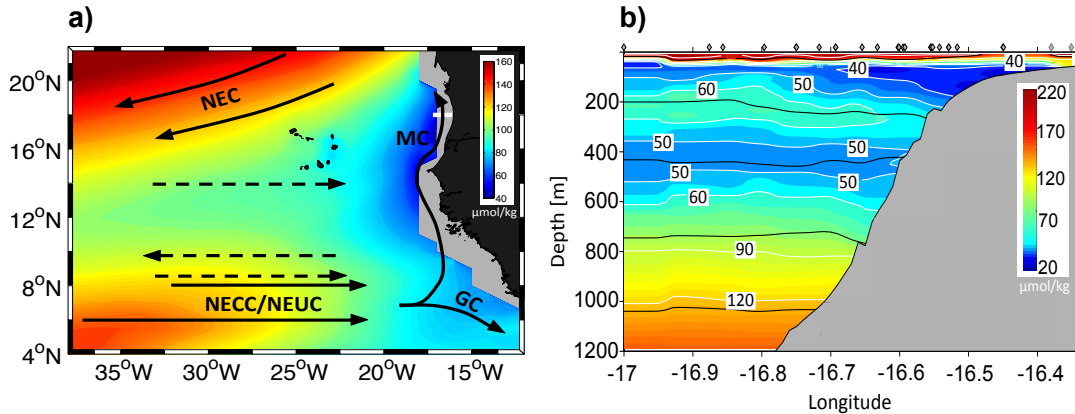
2015, Fig.1.2a].



Figure 1.2: a) Map of the ETNA, where colored contours indicate the oxygen minimum in the upper 200 m (in $\mu molkg^{-1}$) as obtained from the MIMOC climatology [*Schmidtko et al.*, 2013]. Superimposed is a schematic of the surface currents adapted from *Brandt et al.* [2015] (black arrows: North Equatorial Current (NEC), Mauretania Current (MC), North Equatorial Countercurrent (NECC), North Equatorial Undercurrent (NEUC), Guinea Current (GC); black dashed arrows indicate weak zonal current bands observed in the region). The white line marks the shelf section at 18°N off Mauretania shown on the right. b) Shelf section of oxygen in $\mu molkg^{-1}$ along 18°N conducted during the Meteor cruise M107 (June 8-14th, 2014). Black line represent density layer in $kgm^{-3}$.

Besides the deep OMZ with a core at about 450 m depth and created from the gyre scale ventilation, the local ventilation and consumption in the upper layer of the ETNA results in a secondary, shallower oxygen minimum, with a core depth at about 80 m [*Brandt et al.*, 2015; *Karstensen et al.*, 2008, Fig.1.2b]. The shallow oxygen minimum intensifies from the equator towards the north with minimum values between 35-40 $\mu molkg^{-1}$ on the African shelf at about 20°N [*Brandt et al.*, 2015, Fig.1.2]. It is assumed that the shallow OMZ develops due to enhanced biological productivity and an increased respiration associated with sinking particles in the upper water column [*Wyrtki*, 1962; *Karstensen et al.*, 2008; *Brandt et al.*, 2015].

## 1.2 Mesoscale dynamics

Turbulent motions characterize processes over a wide range of scales in the ocean [*Olbers et al.*, 2012]. Mesoscale eddies with diameters of several hundred kilometers compose the upper end of turbulent motions, whereas internal waves with wavelengths on centimeter scale, which can break and stimulate diapycnal mixing taking place on a millimeter scale constitute the lower end of scales of turbulent motions. Traditionally turbulent motions have been classified in three regimes: the two-dimensional geostrophic mesoscale, the internal wave field and the three-dimensional microscale [*Ferrari and Wunsch*, 2009]. In this thesis the characteristics and impacts of geostrophic mesoscale eddies in the described ETNA region are investigated. Mesoscale eddies (the prefix "meso" means "intermediate") describe features with radii of about 10 to 200 $km$ and a lifetime of a few days to one year or even longer [*Chelton et al.*, 2007]. In addition, with sub-

mesoscale processes, a fourth regime expanding the traditional view of the classification will be investigated within the underlying thesis. It is defined as slightly smaller than the mesoscale, with horizontal scales of 100 $m$ to 10 $km$ (or less than the first baroclinic mode Rossby radius of deformation ($R_d$)), vertical scales smaller than the depth of the main pycnocline and a lifetime of one day [*McWilliams and Molemaker*, 2011; *Levy et al.*, 2012]. Submesoscale processes play an important role in the upper layers of the ocean, particularly when ageostrophic motions are relevant [*Thomas*, 2008; *Levy et al.*, 2012]. In order to explain and examine mesoscale and submesoscale processes in the following thesis, it is helpful to define certain metrics of different dynamical regimes.

### 1.2.1 Rossby number, Richardson number and the Rossby radius of deformation

The Richardson ($R_i$) and Rossby ($R_o$) number are non-dimensional numbers, which are used in oceanography to distinguish between dynamical regimes.
$R_o$ is defined as,

$$R_o = U/fL, \tag{1.1}$$

where $f$ is the Coriolis parameter and $U$, $L$ are the characteristic velocity and length scale, which in case of eddies are the maximum circumpolar velocity and eddy radius, respectively. It is a measure to decide whether advection or the Coriolis force dominate within the momentum equation. Large-scale planetary flows have small $R_o$ of up to 0.2, while local rotational effects gain importance with $R_o$ approaching 1. For typical velocity and length scales of mesoscale eddies examined within this thesis, $R_o$ is low or close to 1. Consequently, the horizontal component of the momentum equation reduces to a balance between the pressure gradient force and the Coriolis force, called a geostrophic balance.
$R_o$ can also be expressed as

$$R_o = \xi/f, \tag{1.2}$$

where $\xi = \frac{\partial v}{\partial x} - \frac{\partial u}{\partial y}$ is the vertical component of the relative vorticity, with $u$ and $v$ being zonal and meridional velocity, respectively. Counter-clockwise (clockwise) rotating eddies have positive (negative) relative vorticity and can modify the absolute vorticity, which is $\eta = f + \xi$ [*Kunze*, 1985; *Lee and Niiler*, 1998].
$R_i$ is defined as

$$R_i = N^2/S^2, \tag{1.3}$$

where $N^2 = -\frac{g}{\rho_0}\frac{\partial \rho}{\partial z}$ is the Brunt-Väisälä frequency, with $g$ being the acceleration due to gravity, $\rho_0$ being a reference density, $\rho$ being the locally defined density and $S^2 = (\frac{\partial u}{\partial z})^2 + (\frac{\partial v}{\partial z})^2$ representing vertical shear. Accordingly, $R_i$ describes the ratio between stratification and vertical shear. If $R_i$ is smaller than $\frac{1}{4}$ the flowstructure is more likely to be instable, than stable. The examined mesoscale eddies in this thesis show large $R_i (R_i >> 1)$.
The eddy length scale depends on latitude and ocean stratification and is closely related to the first baroclinic mode Rossby radius of deformation,

$$R_d = c_0/f, \tag{1.4}$$

where $c_0$ is the phase speed of an internal gravity wave of baroclinic mode one and $f$ is the Coriolis parameter. $R_d$ varies with latitude (due to the dependency on $f$, Fig. 1.3) and describes the threshold size of an eddy to be in a geostrophic ($R_o < 1$) or ageostrophic ($R_o > 1$) regime. The ETNA region is characterized by $R_d$ between 40 to 60 $km$ (Fig.1.3).
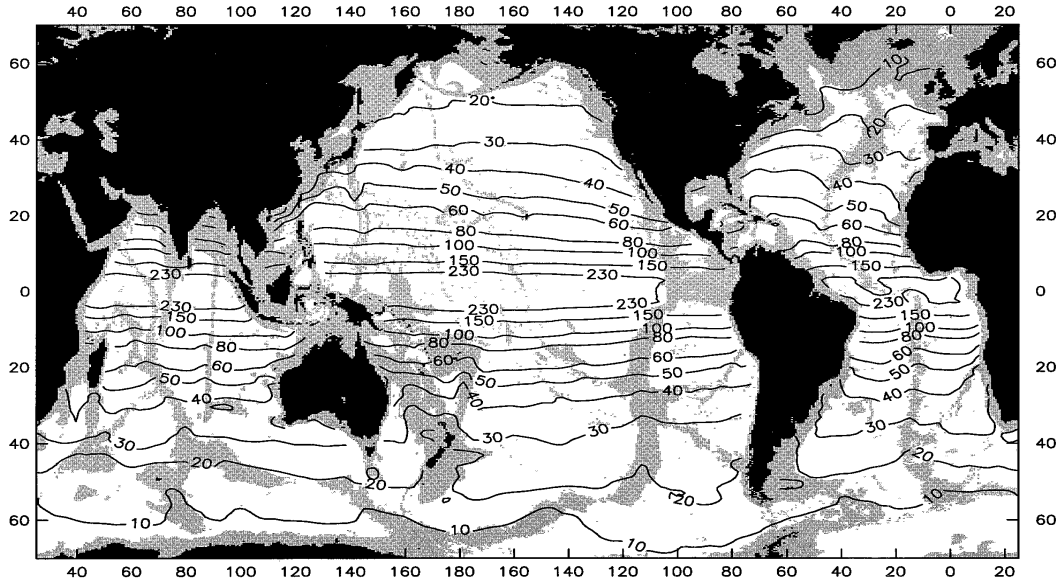


Figure 1.3: Global map of the first baroclinic mode Rossby radius of deformation $R_d$ in kilometer. Water depths shallower than $300\ m$ are shaded [taken from *Chelton et al.*, 1998].

Due to the so-called $\beta$-effect, all reasonably large eddies must propagate in a westward direction. The latitudinal dependency of $f$ results in different Coriolis parameters at the northern and southern edges of the eddies and the pressure gradient force, which is equal at both edges, is not balanced equally. As a compensation, the $\beta$-drift introduces an additional westward velocity which compensates for the imbalanced force.

## 1.2.2 Nonlinearity of eddies

Eddies can be distinguished from linear waves by the nonlinearity parameter $U/c$, where $U$ is the maximum circumpolar velocity and $c$ is the translation speed of the eddy. Features with $U/c > 1$ are considered as nonlinear eddies, whereas features with $U/c < 1$ describe linear waves. Within this study only coherent, nonlinear mesoscale eddies (in the following referred to as eddies) are examined. A nonlinear eddy implies that fluid is trapped within the eddy core and that the exchange between the core and surrounding waters is reduced [e.g. *McWilliams*, 1985; *Flierl*, 1981; *Chelton et al.*, 2011b]. The transport associated with these eddies can be considered as the mean eddy mass flux similar to the Stokes drift. Due to their ability to transport water mass properties in their cores and eventually release them, the isopycnal slopes at the water mass fronts are reduced with time. This mechanism leads to a dispersal of heat, salt, nutrients and other tracers in the ocean and a degradation of fronts due to eddies. This process is particularly important in regions where strong oceanic fronts with steep isopycnal

surfaces develop, for example at the western boundaries, the Antarctic Circumpolar Current (ACC), within the EBUSs or the tropical oceans [e.g. *Roemmich and Gilson*, 2001; *Jayne and Marotzke*, 2002; *Zhang et al.*, 2014; *Biastoch et al.*, 2009; *Pegliasco et al.*, 2015].

### 1.2.3 Overall motivation to study mesoscale eddies

Despite a long history in studies of eddy activity, various aspects regarding processes and impacts of eddies still remain unclear. Studies using climate and ocean-only numerical model simulations show that a poor representation of eddies due to coarse horizontal resolution and/or incorrect parameterisation of the effects of eddies, can lead to major errors in e.g. representing the large scale circulation [e.g. *Oschlies*, 2002; *Fox-Kemper et al.*, 2008; *Delworth et al.*, 2012; *Brüggemann and Eden*, 2014; *Xu et al.*, 2014]. For example, mesoscale eddies contain a considerable amount of the total energy of the oceans [*Ferrari and Wunsch*, 2009]. During their generation, they remove potential energy from the mean flow by barotropic/baroclinic instability transferring it to Eddy Kinetic Energy (EKE) [*Olbers et al.*, 2012]. In the traditional view, an eddy with a length scale larger than $R_d$, will feed kinetic energy into larger scales transferring energy and momentum back into the mean flow according to the theory of geostrophic turbulence [*Charney*, 1971; *Capet et al.*, 2008c]. On the other hand, if an eddy is smaller than the ambient $R_d$, kinetic energy is transferred towards smaller scales until it is lost to heat by dissipation [*Kolmogorov*, 1941]. However, several studies have shown that it is not as simple as that: at the same time EKE can cascade from large eddies towards $R_d$ and simultaneously from smaller eddy scales towards $R_d$ [*Nagai et al.*, 2015; *Brüggemann and Eden*, 2014]. This demonstrates the lack of understanding of the energy flux between the small-scale and geostrophic scales. However, as ocean currents do not accelerate unlimited in time, the total energy input must be balanced by dissipation. The exact role of eddies transferring and dissipating energy is, however, not clear and needs further investigation. One difficulty in the past and still today is the acquisition of a sufficient database to study these short-lived and small-scale phenomena.

## 1.3 Observations of mesoscale eddy activity

### 1.3.1 Past - The last hundred years

#### 1.3.1.1 Eddy observations on a global scale

The first observation of eddies was documented by Columbus Iselin and colleagues in 1930 during repeated cruises between Montauk and Bermuda, which were conducted to obtain Gulf Stream sections [*Cullen*, 2005]. Iselin interpreted some features that appeared to have crossed the Gulf Stream several times as solitary internal waves, but in fact, these rotating currents most likely were eddies. The improvements in ship navigation and the invention of the bathythermographs during World War 2 increased the probability to successfully identify eddies. First intentional measurements of a cyclonic cold core Gulf Stream ring were performed by *Iselin and Fuglister* [1948]. However, it took another twenty years until *Fuglister* [1972] published the first study focusing solely on the dynamics of eddies. This can be considered as the beginning of scientific investigations of eddies and meanders. The first observations of bio/physical interactions and the influence of eddies on marine ecosystems were conducted late in the last century [*The Ring Group*, 1981; *Robinson and Leslie*, 1985]. All of these early observations were limited in data coverage and only provide snapshots of individual eddy events. The breakthrough came along with the launch and progress made in satellite altimetry in the following years. The first studies using global ocean satellite altimetry data (conducted from one satellite) allowed the conclusion of westward propagating mesoscale variability, associated mainly with free, linear Rossby waves [*Le Traon*, 1992; *Chelton and Schlax*, 1996]. Simultaneously, *Chelton and Schlax* [1996] pointed out that the observed westward drift is twice as fast as the predicted drift from the Rossby wave theory [*LeBlond and Mysak*, 1978]. In years to come, theories on Rossby wave propagation were adapted and extended with e.g. bathymetric effects or the vertical shear in background flow, which led to at least some harmonization of observations and theory [*Killworth et al.*, 1997; *Dewar*, 1998; *Szoeke and Chelton*, 1999; *Tailleux and McWilliams*, 2001; *LaCasce and Pedlosky*, 2004]. However, the observed propagation velocity remained faster than predicted by theory. Other observations showing only little evidence of dispersion [*Chelton et al.*, 2003] or small meridional deflections [*Challenor et al.*, 2001] were also not in line with the Rossby wave theory. With increased resolution of the global satellite monitoring in the early 2000s, obtained from merging two simultaneously operating satellite altimeters, it became evident that sea surface height (SSH) variability consists largely of coherent isolated nonlinear mesoscale vortices (eddies) and not linear Rossby waves [*Chelton et al.*, 2007]. These eddies could be separated in cyclones (clockwise surface rotation) and anticyclones (anticlockwise surface rotation). The dominance of eddies explained the observed weak dispersion [*Chelton et al.*, 2003] as the shape of eddies remains rather constant during their propagation. Hence, the energy at every wavenumber propagates at the same speed i.e. non-dispersively [*Chelton et al.*, 2007]. The observed small meridional deflections could be explained by a combined consequence of the $\beta$ effect and self-advection of large nonlinear eddies [*McWilliams and Flierl*, 1979; *Cushman-Roisin et al.*, 1990; *Early et al.*, 2011]. The effect of poleward/equatorward meridional deflection of cyclones/anticyclones could also be verified in subsequent observational studies on regional [*Morrow*

*et al.*, 2004] and global scale [*Chelton et al.*, 2011b].

Due to improved satellite observations and the ability of global ocean models to resolve the mesoscale eddy field in the following years, various studies have identified and tracked eddies based on mapped sea level anomaly (SLA) data using a variety of different automatic eddy identification techniques. Algorithms are based on the Okubo-Weiß parameter [*Isern-Fontanet et al.*, 2003; *Chelton et al.*, 2007], the skewness of the relative velocity [*Niiler et al.*, 2003], criteria based on sea-level contours [*Fang and Morrow*, 2003; *Chaigneau and Pizarro*, 2005; *Chelton et al.*, 2011b; *Faghmous et al.*, 2015], wavelet decomposition [*Lilly et al.*, 2003], geometric criterion [*Nencioli et al.*, 2010; *Souza et al.*, 2011], or the segmentation of SLA patterns [*Wu*, 2014]. In fact, many studies use a combination of different methods. Depending on the chosen method and the individual adjustment of parameters, the number of eddies and their associated properties can vary largely.

However, all of these studies show that eddies are a ubiquitous part of the ocean circulation (e.g. Fig. 1.4ab). In addition, the studies agree on common characteristics of eddy propagation describing a general westward propagation of all eddies due to the $\beta$-effect [*Cushman-Roisin et al.*, 1990]. Exceptions are regions of strong mean eastward currents such as the Kuroshio region [*Isoguchi and Kawamura*, 2003], the ACC region [*Hughes et al.*, 1998; *Fu*, 2009] or the Gulf Stream region [*Brachet et al.*, 2004], where eddies are advected to the east. A global analysis of first eddy detections for long-lived eddies (lifetime > 4 months) shows that eddy generation hot spots are strong western boundary currents, the ACC, as well as defined regions along the eastern boundaries of the ocean basins and near bathymetric gradients [*Chelton et al.*, 2011b, Fig.1.4a]. These eddy hot spots result in a few distinct and observable eddy corridors, which bring some regularity into the chaotic eddy behavior [e.g. *Calil et al.*, 2008; *Sangrà et al.*, 2009]. However, considering all long-lived eddies (lifetime > 4 months) 6% more cyclones than anticyclones are identified globally, whereas anticyclones tend to propagate over larger distances and have a longer lifetime [*Chelton et al.*, 2011b]. This phenomenon could be verified in other observational studies [e.g. *Chaigneau et al.*, 2009] and was theoretically proposed by *Cushman-Roisin et al.* [1990]. The latter study shows that cyclones show a higher tendency for self-destruction and anticyclonic eddies are more robust and merge more freely.

The results of [*Chelton et al.*, 2011b, Fig.1.4] indicate that identification and tracking of eddies from satellite data is difficult in the equatorial band due to fast propagation speeds, weaker nonlinearity and large spatial scales of eddies associated with the large $R_d$ in that region. Here, linear Rossby wave signals a more dominant than coherent mesoscale eddies.

A consistent picture is obtained when comparing the global map of EKE [*Stammer and Wunsch*, 1999] and the global map of the amplitudes of long-lived eddies analyzed by [*Chelton et al.*, 2011b, Fig.1.4c]. It can be shown that eddies have larger amplitudes when they are generated in the vicinity of strong currents like the western boundary currents or along the ACC. The mean eddy radius (Fig.1.4d) and the nonlinearity of the long-lived eddies observed by *Chelton et al.* [2011b] decreases with latitude, similar to the $R_d$. However, at mid to high latitudes the mean eddy radius is much larger than the $R_d$. Consequently, at the mid to high latitudes band the eddy energy is most likely injected into the large-scale flow, following the surface quasi geostrophic
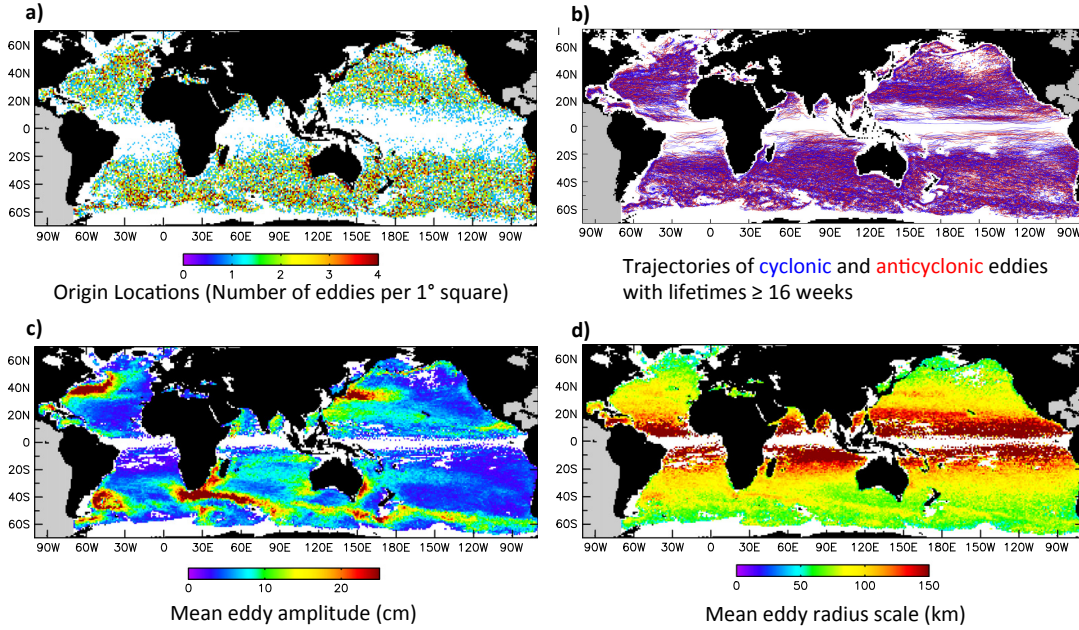
Figure 1.4: Global maps of a) location of the first eddy detection, b) trajectories of all cyclones (blue) and anticyclones (red), c) mean eddy amplitude, d) mean eddy radius of long-lived eddies (lifetime > 4 months). Taken from *Chelton et al.* [2011b]

(SQG) theory. In their model study, *Capet et al.* [2008c] explain the inverse cascade of upper ocean baroclinic energy for larger eddies using SQG theory. *Qiu et al.* [2008] provide the first observational evidence for energy exchange between the mean flow and the eddy field for the region of the Subtropical Countercurrent in the South Pacific.

Nowadays, different satellite monitoring products measuring sea surface salinity (SSS), sea surface temperature (SST), SLA, wind stress, Chlorophyll (Chl) and many other parameters have largely improved in terms of coverage and resolution. Several studies could be performed combining different satellite products, obtaining additional information about the eddy surface signature [e.g. *Chelton et al.*, 2011a; *Frenger et al.*, 2013; *Gaube et al.*, 2014b]. These studies reveal that cyclones (anticyclones) are associated with negative (positive) SLA and SST anomalies [e.g. *Frenger et al.*, 2013; *Gaube et al.*, 2014b]. In addition, cyclones (anticyclones) can be related to enhanced (reduced) Chl concentrations [*Chelton et al.*, 2011a; *Gaube et al.*, 2014a], providing first insights in biological-physical coupling within an eddy. Furthermore, positive/negative SST anomalies associated with eddies result in interactions with the atmosphere in terms of enhanced/reduced wind stress, cloud cover, and rainfall patterns [*Morrow and Le Traon*, 2012; *Frenger et al.*, 2013; *Mahadevan*, 2014; *Villas Bôas et al.*, 2015; *Gaube et al.*, 2014a; *Ma et al.*, 2015].

### 1.3.1.2 Eddy observations in eastern boundary upwelling systems

A particular focus on eddy activity in EBUSs from observations [*Chaigneau et al.*, 2008, 2009; *Rubio et al.*, 2009; *Sangrà et al.*, 2009; *Kurian et al.*, 2011; *Pegliasco et al.*, 2015] as well as numerical simulations [*Capet et al.*, 2008a; *Colas et al.*, 2012; *Nagai et al.*, 2015] reveals that these highly dynamic regions are, at least at the eastern boundary, frequently populated by

eddies. In contrary to the western ocean basins the westward propagation (due to the $\beta$ effect) of the eddies in the EBUSs contribute to a cross-shore transport of the upwelled water properties from the coastal zone towards the open ocean environment [*Chaigneau et al.*, 2011; *Pegliasco et al.*, 2015; *Nagai et al.*, 2015]. In the latter, for example, the primary production is nutrient limited [*Lachkar and Gruber*, 2011] and so the nutrient transport within the eddies extend the area of high productivity offshore [*Correa-Ramirez et al.*, 2007]. This impact was investigated by *Gruber et al.* [2011]; *Lachkar and Gruber* [2012] and *Nagai et al.* [2015], who were able to show that high/low eddy driven transports of nutrient-rich water from the shelf into the open ocean results in lower/higher biological productivity on the shelf itself. In addition it reveals that the cross-shore eddy transport is important for the dispersal of genetic information and biodiversity [*Bucklin*, 1991; *Bucklin et al.*, 2002] and it influences the carbon flux from the atmosphere into the ocean by changing regions where carbon is formed and where it is remineralized [*Turi et al.*, 2014]. Overall, the four EBUSs show very similar eddy statistics (SLA amplitudes of 5-10 $cm$, westward propagation speed of 5-10 $cms^{-1}$ and radii of 50-150 $km$) [e.g. *Morrow et al.*, 2004; *Chaigneau et al.*, 2009; *Pegliasco et al.*, 2015] and only differ in the distribution of eddy generation and eddy frequency/polarity, which indicates different forcing mechanisms [*Chaigneau et al.*, 2009]. Very recent studies, particular focusing on upwelling systems, emphasize that the turbulent transport by submesoscale dynamics likely dominates the lateral transport of properties from the shelf and is involved in the formation of larger eddies [*Nagai et al.*, 2015; *Zhang et al.*, 2016]. It suggests that in future a better knowledge of submesoscale processes is crucial to improve the understanding in large-scale ocean dynamics. Current satellite monitoring reaches its limits resolving submesoscale features including all small-scale processes or filament structures surrounding propagating planetary waves, ocean fronts or mesoscale eddies. New satellite missions improving that point are already in progress of planning and implementing.

### 1.3.2 Present - Improvements and open questions

As described above mainly satellite data was exploited to observe the mesoscale eddy field during the last decades, in particular altimeter data [e.g. *Chelton et al.*, 2007, 2011b; *Chaigneau et al.*, 2008]. However, satellite data is limited to the surface and can be used to characterize the surface eddy structure and activity, while only little is known about what happens beneath the sea surface. Accordingly, it is difficult to explain the vertical structure of eddies, the eddy generation and dissolution, and the coupling of physical and biogeochemical properties within the eddies.

#### 1.3.2.1 Vertical eddy structure

Until relatively recently the only observational information about the vertical eddy structure came from individual eddy crossings during research cruises [e.g. *Zenk et al.*, 1991; *Rossby et al.*, 2011; *Stramma et al.*, 2013]. A few years back a first characterization of the mean vertical eddy structure was obtained using a combination of satellite data (mainly SLA) and a variety of vertical in-situ profiles [from Argo float, shipboard CTD or XBT measurements *Chaigneau et al.*, 2011; *Zhang et al.*, 2013; *Pegliasco et al.*, 2015]: the geostrophic adjustment of the densi-

ty/pressure field and the Coriolis forces relative to the rotation of the eddy (with $R_o < 1$) lead to an upward (downward) bending of isopycnals and an associated cold (warm) eddy core for cyclonic (anticyclonic) rotating eddies [e.g. *Zhang et al.*, 2013]. Although *Zhang et al.* [2013] suggest a universal vertical structure of cyclones and anticyclones, individual eddy crossings described by e.g. *Riser et al.* [1986]; *Lukas and Santiago-Mandujano* [2001]; *Rossby et al.* [2011] indicate that the individual vertical eddy structure can differ strongly among regions and individual eddies. In addition, there are also observations in almost all ocean basins of mode-water type eddies having radii near $R_d$, with elevated isopycnals above the eddy core and depressed isopycnals beneath the eddy core (globally: *Kostianoy and Belkin* [1989]; *McWilliams* [1985] "submesoscale coherent vortices (SCV)"; in the North Atlantic: *Riser et al.* [1986]; *Zenk et al.* [1991] and *Bower et al.* [1995]; *Richardson et al.* [1989]; *Armi and Zenk* [1984] "Meddies"; in the Mediterranean Sea: *Taupier-Letage et al.* [2003] "Leddies"; in the North Sea: *Van Aken et al.* [1987]; in the Baltic Sea *Zhurbas et al.* [2004]; in the Indian Ocean: *Shapiro and Meschanov* [1991] "Reddies"; in the North Pacific: *Lukas and Santiago-Mandujano* [2001]; *Molemaker et al.* [2015] "Cuddies"; in the South Pacific: *Stramma et al.* [2013]; *Colas et al.* [2012]; *Combes et al.* [2015]; *Thomsen et al.* [2016] and *Nof et al.* [2002] "Teddies"; in the Artic *D'Asaro* [1988]; *Oliver et al.* [2008]). For the majority of the observed mode-water type eddies the depressed isopycnals in deeper water mask the elevated isopycnals in the shallow water in terms of geostrophic velocity, resulting in an anticyclonic surface rotation, and a weak positive SLA [*Gaube et al.*, 2014a]. Exceptions are the so-called postconvective "Hetons" in the polar oceans, which are dipoles with surface cyclonic and a weakly stratified subsurface anticyclonic core [*Oliver et al.*, 2008]. However, apart from the polar regions only anticyclonic rotating mode-water eddies are observed. Accordingly, this type of eddy is called in the following anticyclonic mode-water eddy (ACME). Model studies show that they represent a non-negligible part of the eddy field particularly in EBUSs [*Colas et al.*, 2012; *Combes et al.*, 2015; *Nagai et al.*, 2015], but in observational assessments of mesoscale activity they are not represented, because so far detection is only possible based on sub-surface data. More research on this topic is required. However, the vertical eddy structure of all eddy types depends on the generation mechanisms, the background climatological fields traversed by the eddy, the ocean -atmosphere interactions or interactions during the eddy lifetime with other eddies or perturbations [*Pegliasco et al.*, 2015].

### 1.3.2.2 Generation of eddies

On a global scale, the main eddy generation mechanism in the ocean is identified as baroclinic instability of vertically sheared flow, particularly in areas, where the flow has a non-zonal component [*Gill and Clarke*, 1974; *Stammer*, 1997; *Arbic and Flierl*, 2004; *Scott and Wang*, 2005; *Smith*, 2007; *Chelton et al.*, 2011b; *von Storch et al.*, 2012]. The Eady growth rate, which is $\sigma_{eady} = 0.31 f * R_i$, gives a measure of the baroclinicity and the importance of baroclinic instability [*Eady*, 1949; *Olbers et al.*, 2012]. Indeed regions of high EKE are well correlated with regions of high eddy growth rates [*Chelton et al.*, 2007; *Vollmer and Eden*, 2013; *Thomsen et al.*, 2014]. In addition, *Qiu et al.* [2013] show that in dynamically low areas of the North Pacific eddies could be generated by instabilities of wind-forced annual baroclinic Rossby waves. Regarding particu-

larly the EBUSs a variety of different forcing mechanisms for the generation of eddies have been proposed [e.g. *Liang et al.*, 2012]: mainly baroclinic or barotropic instabilities resulting from lateral shear of the near-costal currents [*Chelton et al.*, 2011a, b; *Pantoja et al.*, 2012] triggered by e.g. the passage of poleward propagating coastally trapped waves [*Zamudio et al.*, 2011, 2007], wind perturbations [*Pares-Sierra et al.*, 1993] or interactions with bottom topography [*Kurian et al.*, 2011; *Gula et al.*, 2015]. Several very recent studies also highlight the importance of submesoscale instabilities and the associated upscale transfer of kinetic energy for the generation of mesoscale eddies [*Molemaker et al.*, 2015; *Nagai et al.*, 2015; *Zhang et al.*, 2016]. However, these generation mechanisms (baroclinic, barotropic and submesoscale instability) have no preferred symmetry and cannot explain specifically the generation of ACMEs, which prefer anticyclonic rotation [*McWilliams*, 1985; *Molemaker et al.*, 2015]. The generation of ACMEs is complex and has been subject of scientific interest for several decades already [*McWilliams*, 1985; *D'Asaro*, 1988]. The low stratification of the eddy core cannot be explained by pure adiabatic vortex stretching alone as this mechanism will result in cyclonic vorticity, assuming that $f$ dominates the relative vorticity. Accordingly, the low stratification in the eddy core must be the result of some kind of preconditioning induced by for example upwelling, deep convection [*Oliver et al.*, 2008] or diapycnal mixing near the surface or close to boundaries [*D'Asaro*, 1988] before eddy generation takes place [*McWilliams*, 1985]. *D'Asaro* [1988]; *Molemaker et al.* [2015]; *Thomsen et al.* [2016] highlight the importance of flow separation associated with headlands and sharp topographical variations for the generation of ACMEs. This notion is supported by the fact that low potential vorticity signals are usually observed in the ACMEs [*McWilliams*, 1985; *D'Asaro*, 1988; *Thomas*, 2008; *Molemaker et al.*, 2015; *Thomsen et al.*, 2016]. The low potential vorticity values suggest that the eddy has been generated near the coast as - at least in the tropical latitudes - such low potential vorticity values are rarely observed in the open ocean. Furthermore, the above-mentioned studies argue that the ACMEs' core waters originate to a large extent from the bottom boundary layer at the continental slopes [*D'Asaro*, 1988; *Molemaker et al.*, 2015; *Thomsen et al.*, 2016].

### 1.3.2.3 Dissolution of eddies

Along with the vertical eddy structure and generation processes of eddies, the dynamics of dissolution processes are of equal interest, because of their consequences for the release of tracer anomalies transported by the eddies. Does an eddy release its core properties to the surrounding waters on isopycnal surfaces or along with strong mixing in a more diapycnal way? Compared to the vertical eddy structure and the eddies' generation mechanisms, the understanding of eddy dissolution is relatively poor [*Zhang et al.*, 2016]. Different mechanisms for eddy dissolution have been proposed including damping by ocean bottom drag [*Sen et al.*, 2008; *Arbic et al.*, 2009], surface wind stress [*Duhaut and Straub*, 2006; *Hughes and Wilson*, 2008], turbulent atmospheric heat fluxes [*Ma et al.*, 2016], radiation of near inertial waves (NIWs) [*Williams et al.*, 2008; *Alford et al.*, 2013], generation of lee-waves over small-scale bottom topography [*Marshall and Garabato*, 2008; *Nikurashin and Ferrari*, 2010; *Nikurashin et al.*, 2013] and a scattering into high-wavenumber vertical modes along the ocean's western boundaries [*Zhai et al.*, 2010]. Another

way to dissolutioon is, as for the generation, the occurrence of submesoscale motions transferring energy from the mesoscale towards smaller length scales [*Capet et al.*, 2008c; *Molemaker et al.*, 2010; *Brüggemann and Eden*, 2014]. A very recent study by *Zhang et al.* [2016] confirms that the generation of submesoscale motions with the associated downscaling of energy, plays a dominant role for the dissolution of the eddies. They observed enhanced vertical mixing during the dissolution of an anticyclone in the South China Sea, and suggest that it is primarily caused by breaking of strong internal tides and/or the breaking of NIWs radiating from the eddy itself [*Zhang et al.*, 2016]. All of the above-mentioned candidates for eddy dissolution may play a role, but the quantification of their relative contributions in different oceanic regions is still pending.

### 1.3.2.4 Physical and biogeochemical coupling in mesoscale eddies

Due to the high efficiency of phytoplankton to strip nutrients out of the surface layers (euphotic zone) to stoke their growth, primary productivity is limited by the vertical flux of nutrients from the subsurface layers (aphotic zone), where nutrients are remineralized from sinking organic material back to their inorganic form. Primary productivity in the nutrient-depleted surface can be influenced by eddies due to horizontal or vertical nutrient supply [*Gaube et al.*, 2014a]. The horizontal eddy supply of nutrients can be split in two mechanisms: eddy stirring, occurring at the periphery of the eddy [*Gaube et al.*, 2014a; *Chelton et al.*, 2011a] and eddy transport of phytoplankton or nutrients, which are trapped in the eddy interior [*Gaube et al.*, 2014a, b]. The vertical eddy supply of nutrients can also be split in two mechanisms: Shoaling of isopycnal surfaces during the intensification or decay of an eddy [*Falkowski et al.*, 1991; *McGillicuddy et al.*, 1998; *Siegel et al.*, 1999, 2008, 2011], and Ekman pumping due to interactions of the overlying wind field with the eddy currents [*Dewar and Flierl*, 1987] and SST anomalies [*Chelton et al.*, 2004; *ONeill et al.*, 2010; *Gaube et al.*, 2014a], resulting in upwelling and downwelling in the cores of the eddies. However, the magnitudes of the effect of the different mechanisms are still not clear and under debate [e.g. *Oschlies*, 2001; *Flierl and McGillicuddy*, 2002; *Williams et al.*, 2003; *Mahadevan et al.*, 2008; *Gaube et al.*, 2014a]. Eddy-induced nutrient supply remains a pathway that is being discussed to close the nutrient budget over wide regions of the ocean, the latter of which remains a major open question of marine biogeochemistry [e.g. *Williams and Follows*, 2011]. Modeling studies [*Lévy et al.*, 2012] and recent observational studies [*Brannigan et al.*, 2015; *Omand et al.*, 2015] may deliver the missing key in highlighting the point that submesoscale instabilities within or at the periphery of the eddies are responsible for vertical nutrient flux. In addition, it has been shown that anticyclonic eddies (both "normal" anticyclones and ACMEs) can trap NIWs, which leads to vertical transport of tracers [*Kunze*, 1985; *Gregg et al.*, 1986; *Lee and Niiler*, 1998; *Koszalka et al.*, 2010; *Alford et al.*, 2016]. In more detail, a so-called critical layer or critical level is reached, if the phase speed of the NIW matches the velocity of the mean current. It permits a transfer of energy between the basic current and the wave. Depending on the vertical distribution of N the NIW can generate an amplification of the wave energy and eventually part of that energy may be dissipated by intense vertical mixing [e.g. *Kunze*, 1985; *Joyce et al.*, 2013]. Contrary to the traditional view of upwelling/downwelling in the eddy center, these submesoscale processes are mainly located at the periphery of eddies,

where vertical flow associated with ageostrophic motion becomes important [*Mahadevan et al.*, 2008; *Brannigan et al.*, 2015; *Zhang et al.*, 2016].

Regardless of the exact mechanism for vertical tracer transport, individual eddies have been observed to be highly productive and the transport of properties into the mixed layer - either inside or at the periphery of eddies - is trapped in the eddy where it can be utilized efficiently. In most regions cyclones and ACMEs seem to be more capable than "normal" anticyclones to upwell nutrient-enriched deep waters and thereby increasing primary productivity [*Falkowski et al.*, 1991; *Martin and Richards*, 2001; *McGillicuddy et al.*, 2007; *Löscher et al.*, 2015; *Hauss et al.*, 2016; *Fiedler et al.*, 2016]. Consequently, the biogeochemical responses in the eddy cores and the enhanced primary production at the eddy surface can be very anomalous compared to oligotrophic background conditions [*Baird et al.*, 2011; *Stramma et al.*, 2013; *Mahadevan*, 2014; *Fiedler et al.*, 2016; *Hauss et al.*, 2016; *Löscher et al.*, 2015]. A case study of a recently observed ACME in the ETNA region reveals that underneath the productive surface layer, enhanced sinking of organic matter occurs [*Fischer et al.*, 2016], which could be associated with an increased respiration [*Fiedler et al.*, 2016]. A drawdown of oxygen in the eddy core was observed. The low oxygen conditions subsequently impacted microbial processes and community composition [*Löscher et al.*, 2015] as well as the behavior of sensitive metazoans [*Hauss et al.*, 2016]. The eddy core was found to be highly isolated, as such it is surprising that the isolated core could exist in parallel to the vertical flux, which was needed for the enhanced primary production in the surface layers. Submesoscale processes at the periphery of the eddy might have caused those vertical fluxes while maintaining the isolation of the core at the same time.

Eddies influence the productivity of the pelagic ecosystem from phytoplankton over zooplankton distribution, feeding and growth of fish eggs and larvae [*Bakun and Weeks*, 2006] to the abundance of pelagic predators [*Logerwell and Smith*, 2001; *Seki et al.*, 2002] or even seabirds [*Spear et al.*, 2001; *Yen et al.*, 2006]. The key point is the physical-biological coupling, which is strongly linked to the vertical velocities of submesoscale physics, stimulating primary production (upward nutrient flux) in particular under oligotrophic conditions [*Falkowski et al.*, 1991; *Levy et al.*, 2001; *McGillicuddy et al.*, 2007]. The detailed understanding of the physical and biogeochemical processes and their linkages in eddies is still scarce [*Levy et al.*, 2012]. One reason for this scarcity is the lack of sufficient long-term high-resolution data around and inside of eddies.

## 1.4 Approach and data strategy of this thesis

In order to investigate the generation, development and general occurrence of eddies in the ETNA region different satellite product data sets spanning up to 20 years (SLA, SSS, SST and Chl) are used in this thesis. By collocating eddies, which are identified in the SLA data, with all available vertical profiles (from Argo float, shipboard CTD, mooring and glider measurements) the vertical eddy structure and type-dependent eddy transports are assessed. Furthermore, in order to study individual eddies in more detail a dedicated multi-platform, interdisciplinary field study was conducted in the ETNA. For this purpose, an "eddy detection system" for productive eddies running in near real time was established using Argo float data and various satellite

observations (SLA, SST, Chl). In spring 2014 the detection system indicated the existence of a suitable eddy candidate northeast of the Cabo Verde Islands. Two glider-based surveys were immediately launched, followed by two ship surveys a few weeks later and a third glider survey a month later. The high-resolution multidisciplinary data from the glider and the ship surveys provide an unprecedented view on the complex hydrographic property distribution and velocity field within and around the eddy over a timespan of three months. The data were used in this thesis to analyse small-scale processes within and around the eddy.

## 1.5 Scientific key questions

This study presents four published/submitted papers in the following paragraphs, which include a comprehensive description of eddy characteristics in general, their vertical structure, their impact regarding heat, salt and oxygen transport and a description of the physical and biogeochemical coupling within the eddies in the EBUS of the ETNA region. Apart from the general necessity to further understand the mesoscale eddy field, four scientific key questions are phrased that motivated this study:

1. **What are the characteristics of eddies generated in the ETNA region?**

2. **What is the mean vertical structure of the different eddy types in the ETNA region?**

3. **What is the impact of eddies on heat, salt, and oxygen distributions in the ETNA region?**

4. **How do biogeochemical extreme environments develop within eddies in the ETNA region?**

5. **Which processes drive vertical exchange in an isolated eddy?**

# 2 Open ocean dead zones in the tropical North Atlantic Ocean

Now follows a study, which reports for the first time about the existence of low oxygen eddies in the ETNA. A concept that resamples the formation of dead zones known for limnic system and coastal system applies to the low oxygen eddies, also called dead zone eddies. The combination of multiple ocean observing system elements (mooring, floats, satellites, ships) allows to reconstruct the generation of the dead zone eddies and to connect the formation to enhanced respiration within mesoscale ocean eddies. The dead zones present specific threats to the ecosystem, such as the interruption of the diurnal migration of zooplankters.

The manuscript is published. The candidates contribution to this publication is as follows:

The Author contributed to the manuscript in identifying eddy locations and trajectories. In addition he determine the relative position of Argo float and mooring data within the eddy (all satellite based tasks) and produced figure 1 of the manuscript. Based on the trajectory analysis the author contributed to analyze the eddy evolution, which includes identifying and analyzing additional data along the trajectory. He contributed with the interpretation and discussion of the results.

**Biogeosciences**

Open Access

# Open ocean dead zones in the tropical North Atlantic Ocean

**J. Karstensen**[1], **B. Fiedler**[1], **F. Schütte**[1], **P. Brandt**[1], **A. Körtzinger**[1], **G. Fischer**[2], **R. Zantopp**[1], **J. Hahn**[1], **M. Visbeck**[1], **and D. Wallace**[3]

[1]GEOMAR Helmholtz Centre for Ocean Research Kiel, Kiel, Germany
[2]Faculty of Geosciences and MARUM, University of Bremen, Bremen, Germany
[3]Halifax Marine Research Institute (HMRI), Halifax, Canada

*Correspondence to:* J. Karstensen (jkarstensen@geomar.de)

**Abstract.** Here we present first observations, from instrumentation installed on moorings and a float, of unexpectedly low ( $< 2\,\mu\mathrm{mol\,kg}^{-1}$ ) oxygen environments in the open waters of the tropical North Atlantic, a region where oxygen concentration does normally not fall much below $40\,\mu\mathrm{mol\,kg}^{-1}$. The low-oxygen zones are created at shallow depth, just below the mixed layer, in the euphotic zone of cyclonic eddies and anticyclonic-modewater eddies. Both types of eddies are prone to high surface productivity. Net respiration rates for the eddies are found to be 3 to 5 times higher when compared with surrounding waters. Oxygen is lowest in the centre of the eddies, in a depth range where the swirl velocity, defining the transition between eddy and surroundings, has its maximum. It is assumed that the strong velocity at the outer rim of the eddies hampers the transport of properties across the eddies boundary and as such isolates their cores. This is supported by a remarkably stable hydrographic structure of the eddies core over periods of several months. The eddies propagate westward, at about 4 to $5\,\mathrm{km\,day}^{-1}$, from their generation region off the West African coast into the open ocean. High productivity and accompanying respiration, paired with sluggish exchange across the eddy boundary, create the "dead zone" inside the eddies, so far only reported for coastal areas or lakes. We observe a direct impact of the open ocean dead zones on the marine ecosystem as such that the diurnal vertical migration of zooplankton is suppressed inside the eddies.

## 1 Introduction

The concentration of dissolved oxygen (DO) in seawater is of critical importance to almost all marine life and oceanic biogeochemical cycling (Wilding, 1939; Diaz and Rosenberg, 2008; Vaquer-Sunyer and Duarte, 2008; Wright et al., 2012; Kalvelage et al., 2011). Local DO concentrations are the result of a delicate balance between oxygen supply and consumption, and eventually regions of extremely low DO content are created: at the microscale at particle boundaries (Alldredge and Cohen, 1987), at the mesoscale as coastal dead zones (Diaz and Rosenberg, 2008) or at the large scale as eastern boundary oxygen minimum zones (OMZs) (Luyten et al., 1983; Karstensen et al., 2008; Brandt et al., 2015). Quantifying and fully understanding processes that control the DO supply and consumption balance, and any possible alterations over time, remain challenges in current research.

Critical DO concentration thresholds which lead to major reorganizations of the marine ecosystems have been identified (Vaquer-Sunyer and Duarte, 2008; Wright et al., 2012; Kalvelage et al., 2011). For higher trophic levels, such as those of fish, the impact of a certain DO level on metabolism, and as such fitness, is species-dependent (Wilding, 1939). Nevertheless, for DO below $20\,\mu\mathrm{mol\,kg}^{-1}$ ("severe hypoxia"), mass mortality of fish has been reported (Diaz and Rosenberg, 2008). At severe hypoxia DO levels, microbes begin to convert nitrite and ammonium to nitrogen gas, thus removing fixed nitrogen from the water, which in turn limits primary productivity (Wright et al., 2012; Kalvelage et al., 2011). A next distinct DO threshold is for concentrations below about $5\,\mu\mathrm{mol\,kg}^{-1}$, where microbes begin to utilize nitrate (and other nitrogen species) as terminal
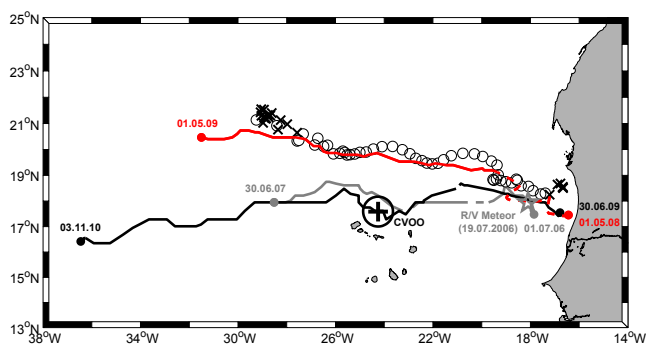
**Figure 1.** Overview map of the eastern tropical North Atlantic oxygen minimum zone. The tracks of the two anticyclonic-modewater eddies (CVOO2007, grey line; CVOO2010, black line) observed at CVOO (plus sign; $17°35.39'$ N, $24°15.12'$ W) as well as the track of the cyclonic eddy (Argo2008, red line), surveyed with an Argo float are shown. The position (dots) and dates (label) of the first and last identification of the three eddies are given. The RV *METEOR* survey of the CVOO2007 (grey star) is labelled accordingly. For reference, the average footprint (circle at CVOO) is given. Positions of the Argo float profiles surveyed inside (white circles) as well as outside the cyclonic eddy radius (crosses) are shown.

electron acceptors in anaerobic respiration ("denitrification") (Wright et al., 2012; Kalvelage et al., 2011). Finally, when DO reach concentrations around $1\,\mu\text{mol\,kg}^{-1}$ ("anoxia"), only specifically adapted microbes can exist (Wright et al., 2012).

The pelagic zones of the eastern tropical North Atlantic OMZ are considered to be "hypoxic", with minimal DO of marginally below $40\,\mu\text{mol\,kg}^{-1}$ (Stramma et al., 2009; Karstensen et al., 2008). As such it is assumed that the DO levels pose some limitation in biodiversity on the regional ecosystem, primarily through avoidance and possibly increased mortality (Vaquer-Sunyer and Duarte, 2008). The region is thus very much in contrast to the major OMZs in the eastern North and South Pacific Ocean and the northern Indian Ocean, where DO concentrations pass all DO thresholds outlined above, and as such specifically adapted ecosystems must exist.

Here the discovery of extremely low DO in mesoscale eddies in the eastern tropical North Atlantic is documented. The DO values fall in the range of severe hypoxia and even anoxia. They extend over horizontal scales of about 100 km and vertical scales of about 100 m.

## 2 Data and methods

### 2.1 Moored sensors

One set of DO time series we discuss below was acquired at the Cape Verde Ocean Observatory (CVOO) mooring. CVOO is located in the eastern tropical North Atlantic, about 100 km northeast of the São Vicente ($17°35'$ N, $24°15'$ W),

Cabo Verde, and approximately 800 km from the Mauritanian coast (Fig. 1). Since 2006 the observatory has been equipped with oxygen sensors: first only one sensor was installed at about 140 m depth, but since the beginning of 2008 at least two sensors have been installed, one of which measuring at depths shallower than 60 m.

The oxygen measurements at the CVOO mooring were done with AADI Aanderaa oxygen optode (type 3830) sensors. For the first two deployments (period from July 2006 to October 2009) we followed the recommendation of the manufacturer and performed a calibration against zero oxygen concentration, by submerging the optodes in a sodium sulfite solution, and against saturated waters. For the following periods a more advanced technique was used, based on a number of calibration points at different temperatures and oxygen concentrations (Hahn et al., 2014). In brief, one set of calibration values was obtained from a comparison of oxygen data from an optode attached to a CTD rosette and the accompanying CTD oxygen sensor (Sea-Bird Electronics 43 Clark electrode) calibrated itself using the Winkler titration method. This comparison was done by keeping the CTD over several minutes at a certain depth where a weak vertical oxygen gradient was seen. This procedure was done before and after the deployment of the respective optodes. In this way we obtained > 15 independent calibration points for each optode. In addition, a lab calibration at zero oxygen was done. All calibration points were used to derive a final calibration equation for one deployment of one certain optode. The chemically forced (and thus more precise) zero oxygen calibration was weighted 3 times higher than the CTD/oxygen cast reference values. The difference between calibration point observations and calibrated optode suggests an overall RMSE of $3\,\mu\text{mol\,kg}^{-1}$. Comparison of the chemically forced zero oxygen phase data and the phase readings at low-oxygen concentrations suggests a higher accuracy at low DO concentrations of about $1\,\mu\text{mol\,kg}^{-1}$. Pressure and salinity variability was corrected according to the AADI manual.

### 2.2 Argo float data

A profiling float was launched in the tropical North Atlantic region to document the seasonal variability in upper layer DO and particle load. By accident it was entrained into the low-oxygen eddy. The float was a PROVOR profiling Argo float (WMO 6900632; Martec Inc., France) equipped with a standard CTD (SBE 41CP), an oxygen optode (AADI Aanderaa optode 3830) and a transmissometer (CRV5, WETLabs). The float was programmed to conduct a vertical profile every 5th day between 400 dbar (nominal drift depth) and the surface with a vertical resolution of 5 dbar throughout the profile. The DO concentrations obtained from the float were corrected for salinity effects (using the float CTD salinity) and a pressure correction was applied to the data (Tengberg et al., 2006), increasing the oxygen linearly by 4 % per 100 bar.

Moreover, we had one in situ calibration CTD calibration cast available, recorded a few hours after deployment of the float. The CTD oxygen sensor (Sea-Bird Electronics 43 Clark electrode) was again calibrated using the Winkler titration method. This procedure resulted in a post-offset correction of float-based DO measurements. The transmissometer data were not further calibrated and are reported here in units of $m^{-1}$ (beam attenuation coefficient) based on the factory calibration. The sensor data are presumably impacted by bio-fouling within the optical path, and this was accounted for by subtracting the minimum deep water beam attenuation value from each profile.

### 2.3 Satellite data and eddy tracking

The delayed time reference product of merged sea-level anomaly (SLA) data (version 2010) provided by AVISO (Archiving, Validation, and Interpretation of Satellite Oceanographic) was used for tracking of the three eddies under discussion. The SSALTO/DUACS project constructs a merged satellite product projected on a $1/3°$ horizontal resolution Mercator grid every 7 days (e.g. Pascual et al., 2006, and references therein).

Initially we tracked the three eddies under discussion visually by inspecting individual SLA maps. This was possible as we knew the exact time and location of the appearance of low-DO eddies from the in situ observations (mooring, float). By looking up subsequent SLA maps, the displacement of an identified SLA that was associated with the three eddies was charted and eddy tracks were constructed for the period before and after the in situ observation (Fig. 1).

However, in addition we used an automatic detecting and tracking algorithm, based on the Okubo–Weiß method (Okubo, 1970). The method is robust and widely used to detect mesoscale eddies in satellite data as well as numerical model output (Chelton et al., 2007; Sangrà et al., 2009; Souza et al., 2011). In brief, the method is based on quantifying the contribution of relative vorticity on the strain tensor, and an eddy is defined as a region of negative $W$ (vorticity dominates over strain) surrounded by a region of positive $W$ (strain dominates over vorticity). A threshold $W_0$ has to be chosen, and we used $W_0 = -2 \times 10^{-12}\,\mathrm{s}^{-2}$ for our eddy detection limit. Tracking was done by following the centre of individual $W_0$ areas in SLA maps from 1 (maximum 10 km) to 3 weeks (maximum distance 60 km). The automatic detection reproduced well the tracking that was obtained using the visual inspection method.
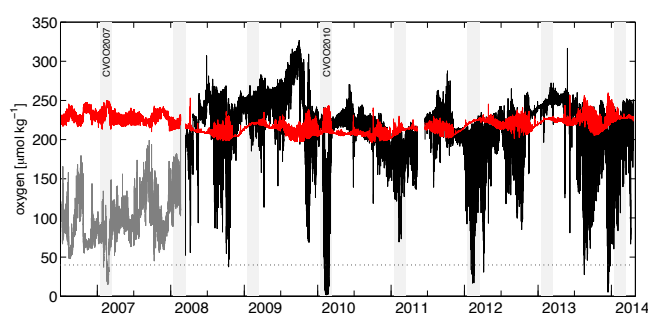


**Figure 2.** Time series of DO from the CVOO site at 40 to 60 m depth (black line) and at 140 m (grey line) during the beginning of the time series. The passage of the two anticyclonic-modewater eddies in February 2007 (CVOO2007) and February 2010 (CVOO2010) is labelled accordingly. The theoretical oxygen surface saturation (red line) is shown, as well as the $40\,\mu\mathrm{mol\,kg}^{-1}$ threshold reported in the literature. The period from 15 January to 15 March for each year is indicated by grey-shaded area.

## 3 Results and discussion

### 3.1 Open ocean low-oxygen events from moored observation

Anomalously low DO, in reference to the expected lower limit for the tropical North Atlantic of about $40\,\mu\mathrm{mol\,kg}^{-1}$ (Stramma et al., 2009), was first identified in the DO time series available from the CVOO mooring (Fig. 2). At the CVOO mooring the typical DO concentrations in the upper 60 m are close to the oxygen saturation value ($> 200\,\mu\mathrm{mol\,kg}^{-1}$; Garcia and Gordon, 1992), with variability of about $50\,\mu\mathrm{mol\,kg}^{-1}$ over periods of a few days or so. However, exceptionally low DO events were observed during boreal winters of 2007, 2010, 2011 and 2012. In the following we concentrate on the two most extreme low-DO events in 2007 and 2010.

The most intense low-DO event was recorded in February 2010 (CVOO2010, Fig. 3a) at the mooring site and persisted over a period of about 1 month. During that period, DO concentrations at shallow depth (42 m) were $< 2\,\mu\mathrm{mol\,kg}^{-1}$ and thus close to the DO threshold for anoxia. A second sensor, installed deeper, at a nominal 170 m, also showed a drastic DO decrease from the typical $100\,\mu\mathrm{mol\,kg}^{-1}$ to less than $30\,\mu\mathrm{mol\,kg}^{-1}$ during the event. Inspecting the hydrography and currents, recorded with multiple other moored instruments, we observed that the low-DO event was accompanied by the appearance of a lens of cold and less saline water (Fig. 3c, d) and a strong and reversing meridional flow (Fig. 3b). The flow reversal (from a northward flow to a southward flow) indicates the passage of an anticyclonic eddy across the mooring.

Further inspection of the temporal evolution of isopycnals (surfaces of constant water density) during the eddy passage
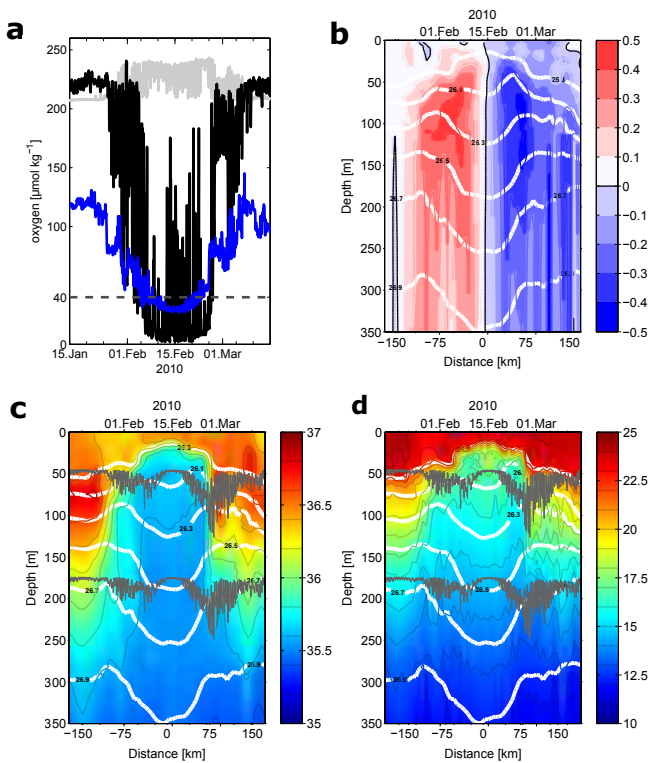
Figure 3. (a) Time series of DO from the two sensors available at nominal 42 m (black line) and 170 m depth (blue line). For reference, the oxygen surface saturation (grey line) and the $40\,\mu\text{mol}\,\text{kg}^{-1}$ threshold (black broken line) are shown. Corresponding time series of (b) meridional flow ($\text{m}\,\text{s}^{-1}$), (c) salinity (in PSS-78), and (d) potential temperature (°C) in the upper 350 m as observed during the CVOO2010 passage are shown. The black line in (b) indicates zero meridional velocity, and the grey lines in (c) and (d) indicate the varying depth of the oxygen sensors shown in (a) during instalment. Selected potential density anomaly surfaces are shown as white contours in (b), (c) and (d) for reference, and the time series data were converted into distance assuming an eddy translation speed of $5\,\text{km}\,\text{day}^{-1}$.

indicated that a special type of anticyclonic eddy, a so-called anticyclonic-modewater or intrathermocline eddy (Kostianoy and Belkin, 1989; McGillicuddy et al., 2007), crossed the mooring. Anticyclonic-modewater eddies can be identified from downward/upward-bent isopycnals towards the eddy centre below/above a subsurface swirl velocity maximum. The transition between upward- and downward-bent isopycnals forms a lens (or mode) of a specific water mass which can be at all water depths. Prominent examples of intrathermocline eddies are so-called "meddies", which propagate at depths between 500 and 1500 m and have been formed from instabilities of the Mediterranean outflow after entering the North Atlantic through the Strait of Gibraltar (Armi and Zenk, 1984). In our observations the mode is at much shallower depth, centred at about 70 m, and had a height of about 50 m or so. It contained the most extreme low DO concen-
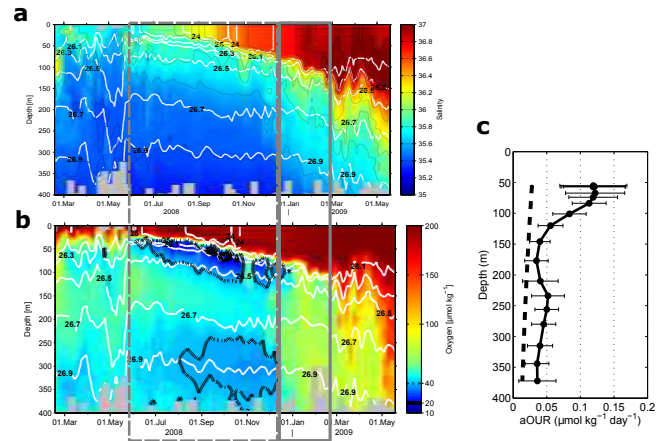


Figure 4. Time series of (a) salinity and (b) oxygen from profiling float data. The two grey boxes indicate the period when the float was trapped in the cyclonic eddy; these represent the isolated period (dashed box, left) and the non-isolated period (solid box, right). Potential density anomaly contours are shown as contour lines. (c) Vertical profile of the aOUR derived from successive dives during the period when the eddy was isolated. The thick broken line shows the background aOUR (Karstensen et al., 2008).

trations. Below this mode, the eddy had a structure of a typical anticyclone and reached deeper than 1400 m (not shown). Along with the passage of the CVOO2010 eddy, the surface mixed layer shoaled from a thickness of about 50–60 m before (and after) the eddy passage to less than 20 m during the eddy passage.

Another extreme event in the DO record from the CVOO mooring time series (Fig. 2) is seen in February 2007 (CVOO2007), almost exactly 3 years before the 2010 event. Again the low-DO event was accompanied by a flow reversal and hydrographic anomalies as seen during CVOO2010; as such it was associated with the passage of an anticyclonic-modewater eddy. At that time only a single oxygen sensor was installed at the CVOO mooring at 120 m depth (nominal), and the lowest DO concentrations were about $15\,\mu\text{mol}\,\text{kg}^{-1}$, indicating severe hypoxia ($20\,\mu\text{mol}\,\text{kg}^{-1}$) conditions at the given depth.

### 3.2 Open ocean low-oxygen events from Argo float data

One further severe hypoxia event was detected within a cyclonic eddy that was surveyed with an Argo type float (Fig. 4a and b). The float was operating from mid-February 2008 until the end of May 2009. Launched in the Mauritanian upwelling region, the float remained in the coastal area until the end of May 2008, when it began to move in a west-northwest direction into open waters (Fig. 1). Overlayed on the west-northwest movement, the float trajectory revealed "loops", which indicate rotational movement of a drifter, and the direction of rotation indicated a movement in a cyclonic eddy.

With the westward propagation, into the open ocean waters, a decrease in DO at all depth levels below the mixed layer is observed. The decrease in DO lasted until mid-December 2008, and lowest DO concentrations (about $14\,\mu\mathrm{mol\,kg^{-1}}$) were always found close to the mixed-layer base, which, however, successively deepened. After December 2008 the DO rather abruptly increased again (Fig. 4b), accompanied by drastic changes in temperature (not shown here) and salinity (Fig. 4a). However, from the eddy trajectory analysis presented below, it turned out that the float was still inside the eddy at the time of the abruptly changing interior structure.

### 3.3 Propagation of oxygen anomalies

The in situ data (CVOO2007, Argo2008, CVOO2010) provided us time periods and positions of low-DO events. Therefore it was simple to identify associated mesoscale eddies in SLA maps. The SLA maps revealed what was already seen from the hydrography – the two eddies observed at CVOO were anticyclonic eddies (the modewater character cannot be identified from the SLA data), and the Argo float surveyed a cyclonic eddy. Considering the along-path characteristics from concurrent SLA maps, all three eddies had roughly similar diameters (about 130 km) and propagated westward, with a speed of about $4.5\,\mathrm{km\,day^{-1}}$. As such they can be categorized as "typical" for this latitude range (Chelton et al., 2011b; Chaigneau et al., 2009). All three eddies had a similar region of origin at about 18° N, 16.5° W. The cyclone was formed in May 2008 (the float entered the eddy core about 1 month later), and the two anticyclonic-modewater eddies in July 2006 and 2009, respectively.

The SLA across the eddy radius was rather weak, with an amplitude of only $1.5\,(\pm1.5)\,\mathrm{cm}$ (negative for the cyclone, positive for the anticyclones). Such a SLA translates into maximum geostrophic surface currents of about $0.05$–$0.10\,\mathrm{m\,s^{-1}}$, which is slow when compared with global eddy characteristics (Chelton et al., 2011b; Risien and Chelton, 2008). However, this is not too much of a surprise, as we knew, at least for the CVOO2007 and CVOO2010 eddies, from the in situ velocity data that the maximum velocity was at the subsurface, at about 70 m depth, and velocity rapidly decreased towards the surface (Fig. 3b). Thus the maximum in SLA-derived surface geostrophic flow is only 10–20 % of the interior maximal swirl velocity directly observed with an acoustic Doppler current profiler (ADCP). We also used the density field derived from moored sensors and calculated a geostrophic velocity under the assumption that there is a layer with no motion at 1400 m. This approach resampled the velocity structure fairly well and in particular the subsurface swirl velocity maximum at about 70 m depth.
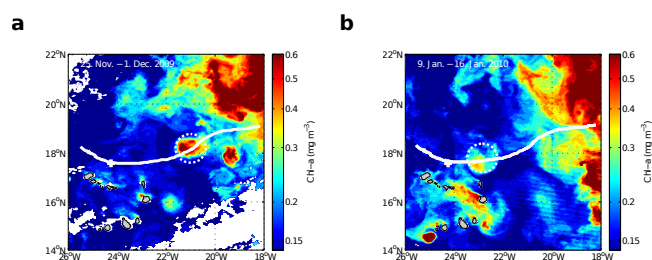
**Figure 5.** Surface chlorophyll concentration of the CVOO2010 anticyclone at two life stages approximately 2 months (**a**) and 1 month (**b**) before the centre of the anticyclone crossed the CVOO mooring. The SLA-derived track of the anticyclone centre (see Fig. 1) and the approximate diameter (130 km) are shown for reference. The white plus sign marks the CVOO position.

### 3.4 Respiration in isolated eddies

Various physical and biogeochemical processes have been identified as possible drivers of the ecosystem responses in mesoscale eddies. In particular, intense phytoplankton blooms have been reported for cyclonic and anticyclonic-modewater eddies (Mahadevan et al., 2008; McGillicuddy et al., 2007; Chelton et al., 2011a; Gaube et al., 2014). Phytoplankton blooms are likely important for creating a low-DO zone, because subsequent sinking of detritus is accompanied by oxygen consumption. Satellite-derived surface chlorophyll images would help to at least identify strong near-surface bloom events in the three eddies, but cloud-free periods are rare in the region. However, the few available images with sufficient coverage (Fig. 5) show high chlorophyll fluorescence signals related to the eddies and suggest phytoplankton blooms to occur.

From the difference in DO concentrations between concurrent Argo float profiles we were able to estimate a depth-dependent respiration rate (Fig. 4c) or apparent oxygen utilization rate (aOUR) profile. Only profiles where DO decreased (May to mid-December 2008) were considered. In order to take the successive deepening of isopycnals over time into account (e.g. Fig. 4a, contours), the aOUR was calculated in density classes and subsequently projected back to depth, using the mean vertical density profile.

The aOUR is highest, more than $0.15\,\mu\mathrm{mol\,kg^{-1}\,day^{-1}}$, just below the mixed layer and levels out to about $0.05\,\mu\mathrm{mol\,kg^{-1}\,day^{-1}}$ between 120 m and the maximum depth the float surveyed (400 m). The rates are 3 to 5 times higher than typical rates for the thermocline (Jenkins, 1982; Karstensen et al., 2008). Moreover, the rates must be seen as a lower bound of the real respiration inside of the eddy, as we assume no supply of DO by vertical mixing or from outside the eddy. Nevertheless, remarkable constant hydrography of the eddy core over time (Fig. 4b for temperature) suggests that lateral exchange across the eddy rim with surrounding waters is small. A connection between sinking particles and

oxygen respiration is also seen in the transmissometer data (not shown). The transmissometer signal is at maximum just at the base of the mixed layer, while minimal DO is observed about 5 m below that particle maximum, indicating that the net oxygen respiration is related to sinking particles.

For the anticyclonic-modewater eddies a net DO respiration can only be derived for the CVOO2007 eddy and for one depth only. This is because the eddy was surveyed only twice during its lifetime: once by RV *METEOR* off Mauritania (Fig. 6), and 7 months later from the moored sensors at the CVOO mooring. Between these two surveys the DO concentrations at the 120 m depth (only depth with DO instrument at CVOO2007) changed by more than $50 \mu$mol kg$^{-1}$, which translate into an aOUR of $0.25 \mu$mol kg$^{-1}$ day$^{-1}$. This is an even higher aOUR when compared with the aOUR profile derived from the cyclonic eddy at a corresponding depth, which might be related to a higher productivity (and subsequently oxygen drawdown through sinking particles) reported for anticyclonic-modewater eddies in the past (McGillicuddy et al., 2007). Moreover, comparison of the ship data from July 2006 and the mooring data from February 2007 (CVOO2007) reveals that the core of the eddy remained rather unchanged in temperature and salinity over a period of 7 months (Fig. 6), as well as after propagating more than 650 km westward.

A key process in the context of productivity is the vertical transport of nutrients into the euphotic zone. Different processes, operating on the sub-mesoscale, have been identified as being responsible for intense vertical velocities within eddies. However, the exact details are a topic that has been under debate for more than a decade (see Klein and Lapeyre, 2009; Lévy et al., 2012; Gaube et al., 2014; Pascual et al., 2015, for further references). Also, the trapping of surface waters by eddies should play a role (d'Ovidio et al., 2013). The data at hand do not allow for conclusions to be made on nutrient pathways within eddies, nor can we estimate productivity. However, a bulk estimate for the vertical velocity across the eddies can be done, making use of an approach based on wind stress variations generated by wind/surface current shear (Martin and Richards, 2001; McGillicuddy et al., 2007; Pascual et al., 2015). In brief, on one side of the eddy, where the wind blows against the eddy rotation, the wind stress is elevated while the contrary happens on the opposite side. The resulting wind stress curl drives an Ekman flux divergence, which in turn is compensated for by an upwelling in the case of anticyclonic surface eddy rotation (McGillicuddy et al., 2007). Using typical wind (10 m s$^{-1}$) and current speed (0.5 m s$^{-1}$) across an eddy with a diameter of 130 km (as observed for the CVOO2010 and CVOO2007 eddy), we estimate an upwelling of about 9 m month$^{-1}$, corresponding to 65 m over the 7 months – the time it takes the eddies to propagate from the formation region, off West Africa, to the CVOO site. However, controversy exists regarding the validity of this concept (Mahadevan et al., 2008; Eden and Dietze, 2009).
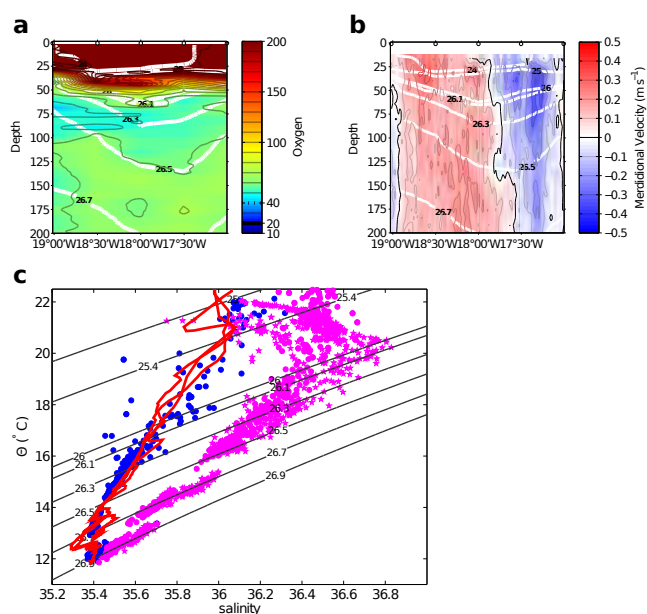


**Figure 6.** Vertical distribution of **(a)** oxygen ($\mu$mol kg$^{-1}$) and **(b)** meridional velocity (m s$^{-1}$) surveyed with RV *METEOR* (cruise M68/3) on the 18 July 2006, at 18° N and from 17 to 19° W (see Fig. 1 for position). **(c)** Hydrographic characteristics of the eddy core as observed with RV *METEOR* (red lines) and as observed 7 months later during the CVOO2007 passage (blue dots). For reference typical background conditions at CVOO are shown (magenta dots and stars).

Besides productivity, and the related sinking of detritus, the "isolation" of the eddy core from surrounding waters will also contribute to an increased net respiration. A clear indication of minimal exchange was seen in the constancy of the hydrographic structure of the eddy core, comparing properties of the eddy during the RV *METEOR* survey and from CVOO2007 (Fig. 6), as well as during the Argo2008 eddy survey. However, further support comes from dynamical considerations. A proxy for the coherence of an eddy, which also indicates the isolation of the eddy core, is the ratio ($\alpha$) of swirl velocity to translation speed (e.g. Chelton et al., 2011b; Chaigneau et al., 2009). For the anticyclonic-modewater eddies (CVOO2007, CVOO2010) we have direct velocity observations, and just below the mixed-layer base they show a maximum $\alpha > 9$ and a clear indication of the coherence of this part of these anticyclonic-modewater eddies.

For the Argo2008 survey of the cyclonic eddy, no direct swirl velocity observation exists, and as such $\alpha$ cannot be calculated. However, we used float profiles recorded before and after the float entered (May/June 2008) and left (March/April 2009) the eddy, and observed a fundamental change in the velocity shear profile – from a rotation with nearly constant velocity from just below the mixed layer (30 m) to 400 m depth (maximum observation depth) at the beginning of the survey to a profile with a distinct peak in

swirl velocity at about 110 m depth at the end of the float survey. Such a change in the flow structure indicates that the maximum $\alpha$ moved to deeper levels. We can only speculate that this vertical movement of maximum $\alpha$ and associated local decrease in $\alpha$ allowed surrounding waters to enter the eddy core and ended the isolation (Fig. 4).

## 4 Conclusions

Dead zones are observed in the open tropical North Atlantic at shallow depth, just below the mixed layer. The dead zones are generated in either cyclonic or anticyclonic-modewater eddies. Tracking of the eddies reveals them to be generated off the northwestern African coast. They propagate westward, with a speed of about 4.5 km day$^{-1}$ into the open ocean. We find, from direct observations of respiration within one cyclonic eddy, a 3- to 5-fold elevated aOUR profile when compared with the typical rates reported for the thermocline waters. High respiration rates were also found in anticyclonic-modewater eddies, but from measurements at one single depth only. From the few observations available, it seems that anticyclonic-modewater eddies may create more intense dead zones (DO close to zero) when compared with those in cyclonic eddies. This is possibly related to higher productivity in connection with the eddy–wind interaction or other mechanisms (Martin and Richards, 2001; McGillicuddy et al., 2007; Chelton et al., 2011a; Gaube et al., 2014). Moreover, the mixed-layer depth in anticyclonic-modewater eddies is very shallow, only a few tens of metres; as such nutrients from below will be lifted far up into the euphotic zone.

There is clearly a local impact of dead zone eddies on the ecosystem. During the passage of the anticyclonic-modewater eddies at the CVOO, we observed, in the target strength data from moored ADCPs, that acoustic backscatterers, such as zooplankters, stopped their diurnal migration cycle (Fig. 7). Such absence of vertical migration is indicative of zooplankters in the major OMZ regions (Ayon et al., 2008). While in the open ocean mobile organisms may escape from the dead zone, other organisms, such as the wide range of prokaryotes, may need to adapt to the environment in order to survive. In that sense the dead zone eddies can be seen as gigantic natural laboratories where an extreme environment is created in a relatively short period of time (a few months). These features may open new ways in investigating the adaptation techniques of organisms to survive low-DO environments.

In principle, open ocean dead zones in cyclonic and anticyclonic-modewater eddies could be created in all oceanic regions. Sufficient productivity, and particle sinking and remineralization, as well as non-linearity (and thus isolation) of the eddies, must be ensured for long enough periods of time. One other important control parameter is presumably the initial DO concentration. At the West African
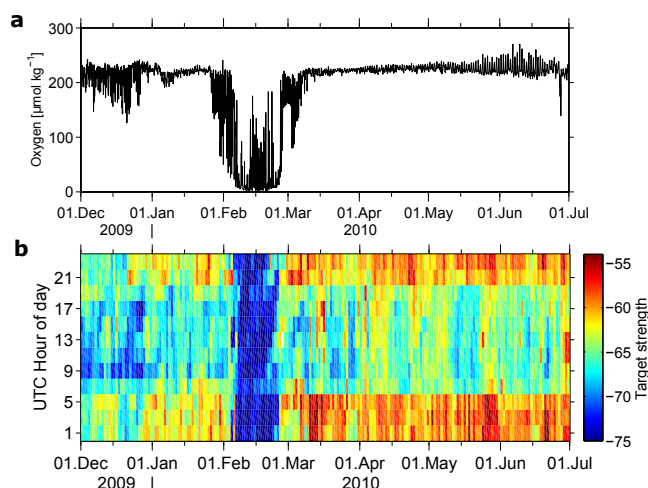


**Figure 7.** Time series of **(a)** oxygen at nominal 42 m depth and **(b)** relative target strength between 65 and 70 m depth against hours of the day (in dB). Target strength was calculated from the 300 kHz acoustic Doppler current profiler data at CVOO. Minimal target strength during all hours of the day is seen during the passage of the low-DO anticyclonic-modewater eddy between 8 and 25 February 2010.

coast, where we report here the eddies are created, DO concentrations are around 40 to 70 $\mu$mol kg$^{-1}$ in the depth level that will later be occupied by low-DO waters. However, in the Pacific or the Indian Ocean, coastal DO concentrations are lower and extremes in other biogeochemical parameters may be generated. Here, anomalous nitrogen isotope compositions (Altabet et al., 2012) or anomalous phytoplankton distributions (Morales et al., 2012) have been reported to exist in anticyclonic-modewater eddies in the past.

In order to detect dead zone eddies from space, via SLA data, concurrent in situ observations of the vertical structure of the water column are required. A combination of Argo float data and SLA data is a promising technique that has been already applied regionally (southeastern Pacific; Chaigneau et al., 2009) and globally (Zhang et al., 2013) but without a focus on detecting anticyclonic-modewater eddies or water mass anomalies in general. We did a preliminary analysis for the North Atlantic OMZ region, using SLA data and Argo float data, that revealed about 10% of the anticyclones are anticyclonic-modewater eddies (Florian Schütte, personal communication). However, information about the oxygen distribution would still be required to quantify the impact of the dead zone eddies on the large-scale oxygen budget.

Eddies were observed less than 100 km north of the Cabo Verde islands; thus a possible interaction of a dead zone eddy with an island must be considered. Given the shallow depth of a few tens of metres where lowest DO concentrations are found, a sudden flooding of a coastal areas with low-DO waters may occur. A dramatic impact on the local ecosys-

24

tems and sudden fish or crustacean death may be the consequence. In retrospect, such eddy–island interactions may explain events that have been reported in the past (O. Melicio, personal communication, National Fisheries Institute INDP, Mindelo, São Vicente, Cabo Verde).

One may wonder why dead zone eddies have not been discovered before. Besides possible undersampling issues for the tropical eastern North Atlantic in the past, it is likely that such low DO concentrations were disregarded as "outliers" in the data sets. In fact, we first interpreted the low DO at CVOO2007 as an outlier related to an instrumental error, and only the more recent events recorded with the double-sensor package at CVOO2010, combined with sophisticated optode calibration procedures, gave us confidence that our observations were real.

# References

Alldredge, A. L. and Cohen, Y.: Can microscale chemical patches persist in the sea?, Microelectrode study of marine snow, fecal pellets, Science, 235, 689–691, 1987.

Altabet, M. A., Ryabenko, E., Stramma, L., Wallace, D. W. R., Frank, M., Grasse, P., and Lavik, G.: An eddy-stimulated hotspot for fixed nitrogen-loss from the Peru oxygen minimum zone, Biogeosciences, 9, 4897–4908, doi:10.5194/bg-9-4897-2012, 2012.

Armi, L. and Zenk, W.: Large Lenses of Highly Saline Mediterranean Water, J. Phys. Oceanogr., 14, 1560–1576, 1984.

Ayon, P., Criales-Hernandez, M. I., Schwamborn, R., and Hirche, H.-J.: Zooplankton research off Peru: a review, Prog. Oceanog., 79, 238–255, 2008.

Brandt, P., Bange, H. W., Banyte, D., Dengler, M., Didwischus, S.-H., Fischer, T., Greatbatch, R. J., Hahn, J., Kanzow, T., Karstensen, J., Körtzinger, A., Krahmann, G., Schmidtko, S., Stramma, L., Tanhua, T., and Visbeck, M.: On the role of circulation and mixing in the ventilation of oxygen minimum zones with a focus on the eastern tropical North Atlantic, Biogeosciences, 12, 489–512, doi:10.5194/bg-12-489-2015, 2015.

Chaigneau, A., Eldin, G., and Dewitte, B.: Eddy activity in the four major upwelling systems from satellite altimetry (1992–2007), Prog. Oceanogr., 83, 117–123, 2009.

Chaigneau, A., Le Texier, M., Eldin, G., Grados, C., and Pizarro, O.: Vertical structure of mesoscale eddies in the eastern South Pacific Ocean: a composite analysis from altimetry and Argo profiling floats, J. Geophys. Res., 116, C11025, doi:10.1029/2011JC007134, 2011.

Chelton, D., Schlax, M., Samelson, R., and de Szoeke, R. A.: Global observations of large oceanic eddies, Geophys. Res. Lett., 34, L15606, doi:10.1029/2007GL030812, 2007.

Chelton, D. B., Gaube, P., Schlax, M. G., Early, J. J., and Samelson, R. M.: The Influence of Nonlinear Mesoscale Eddies on Near-Surface Oceanic Chlorophyll, Science, 334, 328–332, 2011a.

Chelton, D. B., Schlax, M. G., and Samelson, R. M.: Global observations of nonlinear mesoscale eddies, Prog. Oceanogr., 91, 167–216, 2011b.

Diaz, R. J. and Rosenberg, R.: Spreading dead zones and consequences for marine ecosystems, Science, 321, 926–929, 2008.

d'Ovidio, F., Monte, S. D., Penna, A. D., and Guinet, C. C. C.: Ecological implications of eddy retention in the open ocean: a Lagrangian approach, J. Phys. A, 46, 254023, doi:10.1088/1751-8113/46/25/254023, 2013.

Eden, C. and Dietze, H.: Effects of mesoscale eddy/wind interactions on biological new production and eddy kinetic energy, J. Geophys. Res., 114, C05023, doi:10.1029/2008JC005129, 2009.

Garcia, H. and Gordon, L.: Oxygen solubility in seawater: Better fitting equations, Limnol. Oceanogr., 37, 1307–1312, 1992.

Gaube, P., McGillicuddy, D. J., Chelton, D. B., Behrenfeld, M. J., and Strutton, P. G.: Regional variations in the influence of mesoscale eddies on near-surface chlorophyll, Geophys. Res., 119, 8195–8220, 2014.

Hahn, J., Brandt, P., Greatbatch, R., Krahmann, G., and Körtzinger, A.: Oxygen variance and meridional oxygen supply in the Tropical North East Atlantic oxygen minimum zone, Clim. Dynam., 43, 2999–3024, 2014.

Jenkins, W. J.: Oxygen utilization rates in North Atlantic subtropical gyre and primary production in oligotrophic systems, Nature, 300, 246–248, 1982.

Kalvelage, T., Jensen, M. M., Contreras, S., Revsbech, N. P., Lam, P., Günter, M., LaRoche, J., Lavik, G., and Kuypers, M. M. M.: Oxygen sensitivity of anammox and coupled N-cycle processes in oxygen minimum zones, PLoS ONE, 6, e29299, doi:10.1371/journal.pone.0029299, 2011.

Karstensen, J., Stramma, L., and Visbeck, M.: Oxygen minimum zones in the eastern tropical Atlantic and Pacific oceans, Prog. Oceanogr., 77, 331–350, 2008.

Klein, P. and Lapeyre, G.: The oceanic vertical pump induced by mesoscale and submesoscale turbulence, Ann. Rev. Mar. Sci., 1, 351–375, 2009.

Kostianoy, A. and Belkin, I.: A survey of observations on intrathermocline eddies in the world ocean, in: Mesoscale/Synoptic Coherent Structures in Geophysical Turbulence, edited by: Nihoul, J. and Jamart, B., vol. 50, Elsevier, New York, 821–841, 1989.

Lévy, M., Ferrari, R., Franks, P. J. S., Martin, A. P., and Rivière, P.: Bringing physics to life at the submesoscale, Geophys. Res. Lett., 39, L14602, doi:10.1029/2012GL052756, 2012.

Luyten, J., Pedlosky, J., and Stommel, H.: The ventilated thermocline, J. Phys. Oceanogr., 13, 292–309, 1983.

Mahadevan, A., Thomas, L. N., and Tandon, A.: Comment on "Eddy/wind interactions stimulate extraordinary mid-ocean plankton blooms", Science, 320, p. 448, doi:10.1126/science.1152111, 2008.

Martin, A. and Richards, K.: Mechanisms for vertical nutrient transport within a North Atlantic mesoscale eddy, Deep-Sea Res., 48, 757–773, 2001.

McGillicuddy, D. J., Anderson, L. A., Bates, N. R., Bibby, T., Buesseler, K. O., Carlson, C. A., Davis, C. S., Ewart, C., Falkowski, P. G., Goldthwait, S. A., Hansell, D. A., Jenkins, W. J., Johnson, R., Kosnyrev, V. K., Ledwell, J. R., Li, Q. P., Siegel, D. A., and Steinberg, D. K.: Eddy/wind interactions stimulate extraordinary mid-ocean plankton blooms, Science, 316, 1021–1026, 2007.

Morales, C. E., Hormazabal, S., Correa-Ramirez, M., Pizarro, O., Silva, N., Fernandez, C., Anabalon, V., and Torreblanca, M. L.: Mesoscale variability and nutrient–phytoplankton distributions off central-southern Chile during the upwelling season: The influence of mesoscale eddies, Prog. Oceanog., 104, 17–29, 2012.

Okubo, A.: Horizontal dispersion of floatable particles in the vicinity of velocity singularity such as convergences, Deep-Sea Res., 17, 445–454, 1970.

Pascual, A., Faugere, Y., Larnicol, G., and Le Traon, P.-Y.: Improved description of the ocean mesoscale variability by combining four satellite altimeters, Geophys. Res. Lett., 33, L02611, doi:10.1029/2005GL024633, 2006.

Pascual, A., Ruiz, S., Buongiorno Nardelli, B., Guinehut, S., Iudicone, D., and Tintore, J.: Net primary production in the Gulf Stream sustained by quasi-geostrophic vertical exchanges, Geophys. Res. Lett., 42, 441–449, 2015.

Risien, C. M. and Chelton, D. B.: A Global Climatology of Surface Wind and Wind Stress Fields from Eight Years of QuikSCAT Scatterometer Data, J. Phys. Oceanogr., 38, 2379–2413, 2008.

Sangrà, P., Pascual, A., Rodríguez-Santana, Á., Machín, F., Mason, E., McWilliams, J. C., Pelegrí, J. L., Dong, C., Rubio, A., Arístegui, J., Marrero-Díaz, Á., Hernández-Guerra, A., Martínez-Marrero, A., and Auladell, M.: The Canary Eddy Corridor: A major pathway for long-lived eddies in the subtropical North Atlantic, Deep-Sea Res. Pt. I, 56, 2100–2114, 2009.

Souza, J. M. A. C., de Boyer Montegut, C., and Le Traon, P.-Y.: Comparison between three implementations of automatic identification algorithms for the quantification and characterization of mesoscale eddies in the South Atlantic Ocean, 7, 317–334, 2011.

Stramma, L., Visbeck, M., Brandt, P., Tanhua, T., and Wallace, D.: Deoxygenation in the oxygen minimum zone of the eastern tropical North Atlantic, Geophys. Res. Let., 36, 9248276, doi:10.1029/2009GL039593, 2009.

Tengberg, A., Hovdenes, J., Andersson, H., Brocandel, O., Diaz, R., Herbert, D., Arnerich, T., Huber, C., Kortzinger, A., Khripounoff, A., Rey, F., Rönning, C., Schimanski, J., Sommer, S., and Stangelmayer, A.: Evaluation of a lifetime-based optode to measure oxygen in aquatic systems, Limnol. Oceanogr., 4, 7–17, 2006.

Vaquer-Sunyer, R. and Duarte, C. M.: Thresholds of hypoxia for marine biodiversity, P. Natl. Acad. Sci. USA, 105, 15452–15457, 2008.

Wilding, J.: The oxygen threshold for three species of fish, Ecology, 20, 253–263, 1939.

Wright, J. J., Konwar, K. M., and Hallam, S. J.: Microbial ecology of expanding oxygen minimum zones, Nature Rev. Microbiol., 10, 381–394, 2012.

Zhang, Z., Zhang, Y., Wang, W., and Huang, R. X.: Universal structure of mesoscale eddies in the ocean, Geophys. Res. Lett., 40, 3677–3681, 2013.

26

# 3 Occurrence and characteristics of mesoscale eddies in the tropical northeastern Atlantic Ocean

Now follows a study, which examines the general characteristics of mesoscale eddies in the tropical northeast Atlantic. It reveals, that the eddies serve as transport agents, exporting water from the coast, into the open ocean. In most studies, eddies are categorized with respect to their rotation: cyclonic and anticyclonic. However, through a combination of in-situ with satellite data it was deduced that, in the ETNA, ACMEs could be identified from SLA (rotation), SST (cold), and SSS (fresh). ACMEs are relevant because of the way they transport and disperse anomalies.

The manuscript is published. The candidates contribution to this publication is as follows:

The Author did the analysis and produced all the figures. He designed and authored the study from the first draft to the final version.

Ocean Science

# Occurrence and characteristics of mesoscale eddies in the tropical northeastern Atlantic Ocean

**Florian Schütte[1], Peter Brandt[1,2], and Johannes Karstensen[1]**

[1]GEOMAR Helmholtz Centre for Ocean Research Kiel, Kiel, Germany
[2]Christian-Albrechts-Universität zu Kiel, Kiel, Germany

*Correspondence to:* Florian Schütte (fschuette@geomar.de)

**Abstract.** Coherent mesoscale features (referred to here as eddies) in the tropical northeastern Atlantic Ocean (between 12–22° N and 15–26° W) are examined and characterized. The eddies' surface signatures are investigated using 19 years of satellite-derived sea level anomaly (SLA) data. Two automated detection methods are applied, the geometrical method based on closed streamlines around eddy cores, and the Okubo–Weiß method based on the relation between vorticity and strain. Both methods give similar results. Mean eddy surface signatures of SLA, sea surface temperature (SST) and sea surface salinity (SSS) anomalies are obtained from composites of all snapshots around identified eddy cores. Anticyclones/cyclones are identified by an elevation/depression of SLA and enhanced/reduced SST and SSS in their cores. However, about 20 % of all anticyclonically rotating eddies show reduced SST and reduced SSS instead. These kind of eddies are classified as anticyclonic mode-water eddies (ACMEs). About $146 \pm 4$ eddies per year with a minimum lifetime of 7 days are identified (52 % cyclones, 39 % anticyclones, 9 % ACMEs) with rather similar mean radii of about $56 \pm 12$ km. Based on concurrent in situ temperature and salinity profiles (from Argo float, shipboard, and mooring data) taken inside of eddies, distinct mean vertical structures of the three eddy types are determined. Most eddies are generated preferentially in boreal summer and along the West African coast at three distinct coastal headland regions and carry South Atlantic Central Water supplied by the northward flow within the Mauretanian coastal current system. Westward eddy propagation (on average about $3.00 \pm 2.15$ km d$^{-1}$) is confined to distinct zonal corridors with a small meridional deflection dependent on the eddy type (anticyclones – equatorward, cyclones – pole-ward, ACMEs – no deflection). Heat and salt fluxes out of the coastal region and across the Cape Verde Frontal Zone, which separates the shadow zone from the ventilated subtropical gyre, are calculated.

## 1 Introduction

The generation of eddies in coastal upwelling regions is strongly related to the eastern boundary circulation and its seasonal variations. Within the tropical Atlantic Ocean off northwestern Africa (TANWA; 12 to 22° N and 26 to 15° W), the large-scale surface circulation responds to the seasonal variability of the trade winds and the north–south migration of the Intertropical Convergence Zone (ITCZ) (e.g., Stramma and Isemer, 1988; Siedler et al., 1992; Stramma and Schott, 1999). The seasonal wind pattern results in a strong seasonality of the flow field along the northwestern African coast and in coastal upwelling of different intensity. The coastal upwelling in the TANWA is mainly supplied by water masses of South Atlantic origin (Jones and Folkard, 1970; Hughes and Burton, 1974; Wooster et al., 1976; Mittelstaedt, 1991; Ould-Dedah et al., 1999; Pastor et al., 2008; Glessmer et al., 2009; Peña-Izquierdo et al., 2015), which are relatively cold and fresh compared to the North Atlantic waters further offshore. The water mass transition region coincides with the eastern boundary shadow zone, where diffusive transport pathways dominate (Luyten et al., 1983) with weak zonal current bands superimposed (Brandt et al., 2015). The oceanic circulation in the TANWA is most of the time weak and the velocity field is dominated by cyclonic and anticyclonic eddies. However, global as well as regional satellite-based studies of eddy

distribution and characterization (Chelton et al., 2007, 2011; Chaigneau et al., 2009) found high eddy activity in terms of eddy generation in the TANWA, but only rare occurrence of long-lived eddies (> 112 days referred to Chelton et al., 2007, > 35 days, referred to Chaigneau et al., 2009). Karstensen et al. (2015) studied individual energetic eddy events based on a combination of in situ and satellite-based sea level anomaly (SLA) data, and reported eddy life times of more than 200 days in the TANWA region. These individual eddies carried water mass characteristics typical for the shelf region up to 900 km off the African coast. One possible generation area for such eddies is the Cap-Vert headland at about 14.7° N near the Senegalese coast (Karstensen et al., 2015). Analyzing surface drifter data and high-resolution satellite data, Alpers et al. (2013) described the evolution of an energetic sub-mesoscale eddy at the Cap-Vert headland that was presumably generated by flow separation of a wind-forced coastal jet. Earlier studies reported on the importance of eddy transport in the TANWA region (e.g., Hagen, 1985; Barton, 1987; Zenk et al., 1991). However, characteristics of the eddy field in the TANWA region such as seasonality in eddy generation, eddy lifetime, vertical structure, or frequency of occurrence are so far undocumented.

More comprehensive information on eddy dynamics was gained for the Pacific Ocean eastern boundary upwelling systems. The eddy generation in the northeastern Pacific Ocean, off California and Mexico including the California Current System, was studied with high-resolution models applied to reproduce observed characteristics of the eddy field (Liang et al., 2012; Chang et al., 2012). These studies not only highlight hotspots of eddy generation associated with local wind fluctuations (e.g., over the Gulf of Tehuantepec and Papagayo), but also suggest an important role of low-frequency wind and boundary forcing. For the southeastern Pacific Ocean, off Peru and Chile, including the Peru–Chile Current System, Chaigneau et al. (2008, 2011) analyzed the seasonal to interannual variability of eddy occurrence as well as the mean vertical structure of eddies based on Argo floats.

A schematic of the current system of the TANWA in boreal spring and in boreal autumn is presented in Fig. 1. In the north of the TANWA the Canary Current (CC) transports cold water southwards along the African shelf. It detaches from the coast around Cap Blanc (more specifically at about 20° N during spring and 25° N during autumn) and joins the North Equatorial Current (NEC) (Mittelstaedt, 1983, 1991). The dominant feature south of the TANWA is the eastward flowing North Equatorial Countercurrent (NECC) extending over a latitudinal range from 3° N to about 10° N. It has a pronounced seasonal cycle with maximum strength in boreal summer and autumn, when the ITCZ reaches its northernmost position. During that period the NECC is a continuous zonal flow across the entire tropical Atlantic (e.g., Garzoli and Katz, 1983; Richardson and Reverdin, 1987; Stramma and Siedler, 1988; Polonsky and Artamonov, 1997). When approaching the African coast, the current is partly de-

flected to the north feeding a sluggish northward flow along the coast. This current is referred to as Mauretania Current (MC) and reaches latitudes up to 20° N (Mittelstaedt, 1991). The strength of the MC is strongly related to the seasonally varying NECC with a time lag of 1 month (Lázaro et al., 2005). During boreal winter and spring when the NECC is pushed to the Equator and becomes unstable, the MC becomes weak and unsteady and only reaches latitudes south of Cap-Vert (Mittelstaedt, 1991; Lázaro et al., 2005). During this period the wind induced coastal upwelling is at its maximum. Simultaneously, the large-scale pressure gradient set by the southward winds induces an along-slope subsurface current, known as Poleward Undercurrent (PUC) (Barton, 1989). During boreal summer the MC re-establishes contemporaneously to the suppression of coastal upwelling south of Cap Blanc at 21° N (Peña-Izquierdo et al., 2012).

The eastern boundary upwelling is supplied by waters of South Atlantic origin through a pathway consisting of the North Brazil Current (NBC), the North Equatorial Undercurrent (NEUC) and the PUC. Hence, the purest South Atlantic Central Water (SACW) within the TANWA is found close to the coast (Fig. 2), while further offshore a transition towards the more saline and warmer North Atlantic Central Water (NACW) is observed. The boundary between the regimes is associated with the Cape Verde Frontal Zone (CVFZ; Fig. 2), characterized by a sharp horizontal salinity gradient of 0.9 per 10 km (Zenk et al., 1991). In this study, salinities are reported dimensionless, defined by the UNESCO Practical Salinity Scale of 1978 (PSS-78). The efficiency of mesoscale eddies to transport cold and less saline SACW from their generation regions near the coast into the open ocean where NACW dominates is one topic investigated in this paper. In particular, the characteristics of these eddies (size, structure, frequency) and their potential role in the transport of heat and salt will be examined in more detail.

The paper is organized as follows: in Sect. 2, the different data types (satellite derived and in situ) will be introduced as well as the techniques to automatically detect and track eddies from satellite data and to derive their vertical structure. In Sect. 3 the eddy characteristics (origin, pathways, surface signature) and statistics (frequency) are discussed and the temporal and spatial variability of eddy generation and eddy pathways are examined. The mean horizontal and vertical eddy structures are derived and, in combination with the eddy statistics, used to estimate the transport of volume, heat, and salt from the shelf region into the open ocean. Finally our results are summarized in Sect. 4.
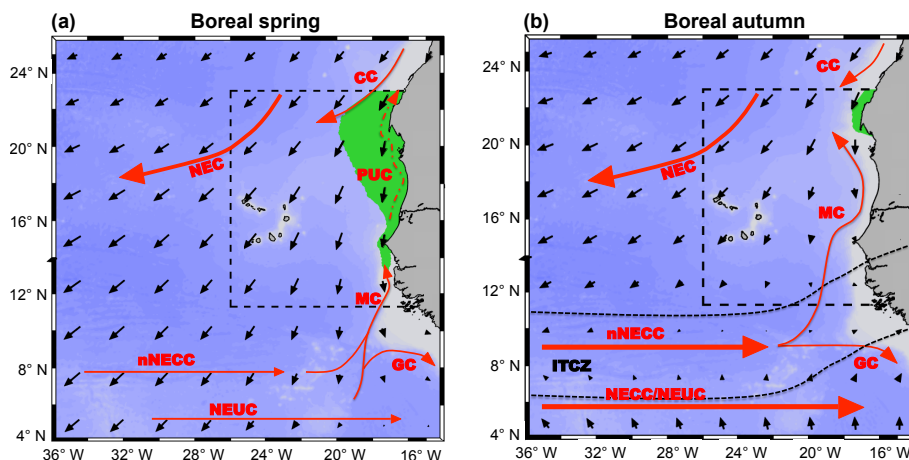
**Figure 1.** Schematic of the current system of the eastern tropical North Atlantic (red arrows; North Equatorial Current (NEC), Canary Current (CC), Poleward Undercurrent (PUC), Mauretania Current (MC), North Equatorial Countercurrent (NECC), Guinea Current (GC), North Equatorial Undercurrent (NEUC)) **(a)** in boreal spring and **(b)** in boreal autumn. Black arrows are mean wind vectors, green areas indicate seasonal mean SST < 21 °C. Blue colors represent topography and the dashed box indicates the TANWA area. The mean position of the Intertropical Convergence Zone (ITCZ) in autumn is indicated as the region bounded by the two black dashed lines in **(b)**.
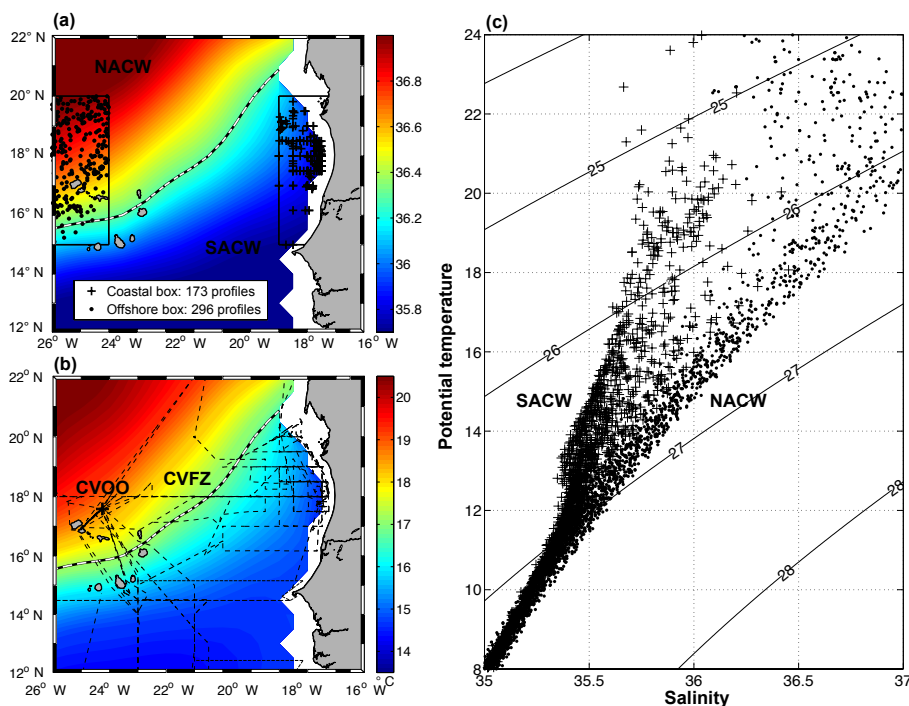


**Figure 2.** Mean salinity **(a)** and potential temperature **(b)** at 100 m depth in the TANWA from the monthly, isopycnal/mixed-layer ocean (MIMOC) climatology (Schmidtko et al., 2013) and $\theta/S$ diagram **(c)**. The thick black/white line in **(a)** and **(b)** indicates the CVFZ. In **(a)** crosses and dots represent all available profiles (from Argo floats and ships) in the marked coastal and offshore boxes, respectively. In **(c)**, the thin dashed line mark cruise tracks of 20 research cruises to the TANWA taking profiles used in the present study. The black cross in **(b)** indicates the position of the Cape Verde Ocean Observatory (CVOO) mooring. In **(c)** data from the coastal and offshore boxes are marked by crosses and dots, respectively; superimposed are isolines of potential density.

## 2 Data and methods

### 2.1 Satellite data

#### 2.1.1 SLA, SST, and SSS

The delayed-time reference data set "all-sat-merged" of SLA (Version 2014), which is used in the study, is produced by Ssalto/Duacs and distributed by AVISO (Archiving, Validation, and Interpretation of Satellite Oceanographic), with support from CNES (http://www.aviso.altimetry.fr/duac/). The data are a multi-mission product, mapped on a $1/4° \times 1/4°$ Cartesian grid and has a daily temporal resolution. The anomalies are computed with respect to a 20-year mean. Data for the period January 1995 to December 2013 are considered here. Geostrophic velocity anomalies derived from the SLA provided by AVISO for the same timespan are also used in this study. Given the interpolation technique applied to the along track SLA data Gaussian shaped eddies with a radius $> \sim 45$ km can be detected; eddies of smaller diameter may be detected but their energy is damped (Fu and Ferrari, 2008).

For sea surface temperature (SST) the data set "Microwave Optimally interpolated Sea Surface Temperature" from Remote Sensing Systems (www.remss.com) is used. It is derived from satellite microwave radiometers, which have the capability to measure through clouds. It has a 25 km resolution and contains the SST measurements from all operational radiometers for a given day. All SST values are corrected using a diurnal model to create a foundation SST that represents a 12:00 LT temperature (www.remss.com). Daily data from the outset (1 January 1998 to 31 December 2013) are used here and mapped similar to the SLA data on a $1/4° \times 1/4°$ Cartesian grid.

Our study also includes sea surface salinity (SSS) data. We make use of the LOCEAN_v2013 SSS product available from 1 January 2010 until the end of our analysis period (31 December 2013). The data are distributed by the Ocean Salinity Expertise Center (CECOS) of the Centre National d'Etudes Spatiales (CNES) – Institut Français de Recherche pour l'Exploitation de la Mer (IFREMER) Centre Aval de Traitemenent des Donnees SMOS (CATDS), at IFREMER, Plouzane (France). The data are created using the weight averaging method described in Yin et al. (2012) and the flag sorting described in Boutin et al. (2013). Finally the data are mapped on a $1/4° \times 1/4°$ Cartesian grid and consist of 10-day composites.

#### 2.1.2 Eddy identification and tracking from satellite data

In order to detect eddy-like structures, two different methods are applied to the SLA data. The first method, the Okubo–Weiß method (OW method; Okubo, 1970; Weiss, 1991), has been frequently used to detect eddies using satellite data as well as the output from numerical studies (e.g., Isern-Fontanet et al., 2006; Chelton et al., 2007; Sangrà et al., 2009). The basic assumption behind the OW method is that regions, where the relative vorticity dominates over the strain, i.e., where rotation dominates over deformation, characterize an eddy. In order to separate strong eddies from the weak background flow field a threshold needs to be identified. For this study the threshold is set to $W_0 = -0.2 \times \sigma$, where $\sigma$ is the spatial standard derivation of the Okubo–Weiß parameter $W = s_n^2 + s_s^2 - \omega^2$. Here, $s_n = \frac{\partial u}{\partial x} - \frac{\partial v}{\partial y}$ is the normal strain, $s_s = \frac{\partial v}{\partial x} + \frac{\partial u}{\partial y}$ is the shear strain and $\omega = \frac{\partial v}{\partial x} - \frac{\partial u}{\partial y}$ is the relative vorticity. A similar definition of the threshold was used in other eddy studies applying the OW method (e.g., Chelton et al., 2007). The maximum (minimum) SLA marks the eddy center.

The second method for eddy detection is based on a geometric approach (in the following GEO method) analyzing the streamlines of the SLA-derived geostrophic flow. An eddy edge is defined as the streamline with the strongest swirl velocity around a center of minimum geostrophic velocity (Nencioli et al., 2010). For the detection of an eddy, the algorithm requires two parameters $a$ and $b$ to be defined. The first parameter, $a$, is a search radius in grid points. Inside the search radius, the velocity reversal across the eddy center is identified ($v$ component on an east–west section, $u$ component on a north–south section). The second parameter, $b$, is used to identify the point of minimum velocity within a region that extends up to $b$ grid points (for a more detailed description of the method see Nencioli et al., 2010). After a few sensitivity tests in comparison with the results of the OW method and following the instructions of Nencioli et al. (2010), we set $a = 3$ and $b = 2$. Optimal results were obtained when we linearly interpolated the AVISO velocity fields onto a $1/6° \times 1/6°$ grid before we applied the algorithm (for more information see also Liu et al., 2012). If an eddy is detected, then an eddy center is identified in analogy to the OW method as the maximum (anticyclone) or the minimum (cyclone) of SLA within the identified eddy structure.

When applying the two different eddy detection methods to the SLA data from the TANWA region, we used the same eddy detection thresholds for both methods; i.e., a feature only counts as an eddy, if its radius is larger than 45 km and it is detectable for a period of more than 7 days. Note, as the identified eddy areas are rarely circular we used the circle-equivalent of the area of the detected features to estimate the radius. For eddy tracking both eddy detection methods use the same tracking algorithm. An eddy trajectory was calculated if an eddy with the same polarity was found in at least 7 consecutive SLA maps (corresponding to 1 week) within a search radius of up to 50 km. Due to, e.g., errors in SLA mappings (insufficient altimetric coverage) an eddy could vanish and re-emerge after a while. Therefore we searched in 14 consecutive SLA maps (corresponding to 2 weeks) in a search radius of up to 100 km after an eddy disappearance, if

eddies with the same polarity re-emerges. If more than one eddy with the same polarity emerge within the search radius, we defined the following similarity parameter to discriminate between these eddies:

$$X = \sqrt{\left(\frac{\text{distance}}{100}\right)^2 + \left(\frac{\Delta\,\text{radius}}{\text{radius}_0}\right)^2 + \left(\frac{\Delta\,\text{vorticity}}{\text{vorticity}_0}\right)^2 + \left(\frac{\Delta\,\text{EKE}}{\text{EKE}_0}\right)^2}, \quad (1)$$

which include four terms based on the distance between the disappeared and newly emerged eddies and the difference of their radii, mean vorticity, and mean eddy kinetic energy (EKE). $\text{Radius}_0$, $\text{vorticity}_0$, and $\text{EKE}_0$ are the mean radius, vorticity and EKE of all identified eddies in TANWA. The newly emerged eddy with the smallest $x$ is selected to be the same eddy. To give an idea of the uncertainty related to the detection technique, both methods are applied to the data. Every step is computed separately with both methods and the results are compared.

### 2.1.3 Eddy classification and associated mean spatial surface pattern

From the geostrophic velocity data, anticyclones (cyclones) can be identified due to their negative (positive) vorticity. In the SLA data anticyclones (cyclones) are associated with a surface elevation (depression). The maximum (minimum) SLA marks the eddy center. In general, anticyclones (cyclones) carry enhanced (reduced) SST and enhanced (reduced) SSS in their cores, respectively. However, we found that 20 % of all detected anticyclones had cold anomalies in their cores and a reduced SSS. This kind of eddies is classified as an anticyclonic mode-water eddy (ACME) or intrathermocline eddy (Kostianoy and Belkin, 1989) as will later be confirmed when considering the in situ observations (see below). Given that ACMEs show distinct characteristics, which are contrasting to anticyclones (see below), we distinguish in the following three types of eddies: anticyclones, cyclones, and ACMEs.

Composites of satellite-derived SST and SSS anomalies with an extent of 300 km × 300 km around the eddy centers yield the mean spatial eddy surface pattern of temperature and salinity for the respective eddy type. The information whether an eddy is cold/warm or fresh/saline in the core is obtained by subtracting the average value over the edge of the box from the average value over the eddy center and its closest neighboring grid points. To exclude large-scale variations in the different data sets, the SST and SSS fields are low-pass filtered with cutoff wavelength of 15° longitude and 5° latitude. Thereafter the filtered data sets are subtracted from the original data sets thus preserving the mesoscale variability. The composite plots are based only on eddies with a radius between 45 and 70 km and an absolute SLA difference between the eddy center and the mean along the edge of the 300 km × 300 km box used for the composites greater than 2 cm.

## 2.2 In situ data

### 2.2.1 Argo floats

A set of irregular distributed vertical CTD (conductivity–temperature–depth) profiles was obtained from the autonomous profiling floats of the Argo program. The freely available data were downloaded from the Global Data Assembly Centre in Brest, France (www.argodatamgt.org) and encompasses the period from July 2002 to December 2013. Here only pressure ($P$), temperature ($T$), and salinity ($S$) data flagged with Argo quality category 1 are used. The given uncertainties are $\pm 2.4$ dbar for pressure, $\pm 0.002\,°C$ for temperature, and $\pm 0.01$ for uncorrected salinities. In most cases the salinity errors are further reduced by the delayed-mode correction. For this analysis an additional quality control is applied in order to eliminate spurious profiles and to ensure good data quality in the upper layers. In the following, we give the criteria applied to the Argo float profiles and in brackets the percentage, to which the criteria were fulfilled. Selected profiles must (i) include data between 0 and 10 m depth (98.2 %), (ii) have at least 4 data points in the upper 200 m (98.8 %), (iii) reach down to 1000 m depths (95 %), with (iv) continuous and consistent temperature, salinity, and pressure data (78 %). This procedure reduced the number of profiles by around 30 % to 2022 Argo float profiles for the TANWA.

### 2.2.2 Shipboard measurements

In situ CTD profile data collected during 20 ship expeditions to the TANWA within the framework of different programs are used (Fig. 2b; see Table 1 for further details). In total 579 profiles were available taken within the TANWA during the period March 2005 to June 2013. Data sampling and quality control followed the standards set by Global Ocean Ship-Based Hydrographic Investigations Program (GO-SHIP) (Hood et al., 2010). However, we assume a more conservative accuracy of our shipboard data of about twice the GO-SHIP standard, which is $\pm 0.002\,°C$ and $\pm 0.004$ for temperature and salinity, respectively.

### 2.2.3 CVOO mooring

The third set of in situ data stems from the Cape Verde Ocean Observatory (CVOO) mooring. The CVOO mooring is a deep-sea mooring deployed at a depth of about 3600 m, 60 km northeast of the Cabo Verdean island of São Vicente (Fig. 2b). The nominal mooring position is 17°36′ N, 24°15′ W. The mooring was first deployed in June 2006 and has been redeployed in March 2008, October 2009, May 2011, and October 2012. Temperature and salinity measurements in the upper 400 m have been typically recorded at depth of 30, 50, 70, 100, 120, 200, 300, and 400 m using MicroCAT instruments. Data calibration is done against ship-

**Table 1.** Data from the following research cruises were used.

| Cruise | Ship | Time | Region | No. of profiles |
|---|---|---|---|---|
| Pos 320 | *Poseidon* | Mar–Apr 2005 | TANWA East | 38 |
| M 68/2 | *Meteor* | Jul 2006 | 23° W Section | 10 |
| M 68/3 | *Meteor* | Jul–Aug 2006 | 18° N Section | 81 |
| Pos 347 | *Poseidon* | Jan–Feb 2007 | TANWA East | 125 |
| Pos 348 | *Poseidon* | Feb 2007 | TANWA East | 32 |
| Ata 3 | *L'Atalante* | Feb 2008 | TANWA East | 58 |
| Ata 4 | *L'Atalante* | Mar 2008 | 23° W Section | 6 |
| MSM 8 | *Maria S. Merian* | May 2008 | South TANWA | 3 |
| MSM 10 | *Maria S. Merian* | Dec 2008 | South TANWA | 5 |
| Pos 399 | *Poseidon* | May–Jul 2009 | TANWA East | 21 |
| M 80/1 | *Meteor* | Nov 2009 | 23° W Section | 9 |
| M 80/2 | *Meteor* | Dec 2009 | South TANWA | 8 |
| M 81/1 | *Meteor* | May 2010 | Central TANWA | 12 |
| M 83/1 | *Meteor* | Dec 2010 | 14.5° N Section | 27 |
| MSM 18/2 | *Maria S. Merian* | May 2011 | 23° W Section | 6 |
| MSM 18/3 | *Maria S. Merian* | Jun 2011 | South TANWA | 6 |
| MSM 22 | *Maria S. Merian* | Nov 2012 | 18° N Section | 76 |
| MSM 23 | *Maria S. Merian* | Nov 2012 | 14.5° N Section | 13 |
| M 96 | *Meteor* | May 2013 | 14.5° N Section | 14 |
| M 97 | *Meteor* | Jun 2013 | 14.5° N Section | 7 |
| | | | | $\sum$ 557 |

board CTD data during the service cruises. The uncertainties are $\pm 0.002\,°\mathrm{C}$ for temperature and $\pm 0.01$ for salinity.

The eddy detection method identifies 22 eddies passing the CVOO mooring. For these eddy events, the original time series with a temporal resolution of 15 or 20 min were low-pass filtered with a cutoff period of 24 h and consecutively subsampled to 1-day values in order to reduce instrument noise and to match the resolution of the SLA maps. In total 429 profiles could be obtained. $T/S$ (temperature/salinity) anomaly profiles were derived as the difference of profiles inside and outside of the eddies. The outside profiles were taken shortly before the eddy passage.

### 2.3 Determining the vertical structure of eddies detected in SLA data

In order to investigate the vertical structure of eddies identified in SLA data, a combination of all available in situ data sets was used. We had a total of 3030 CTD profiles available for the time period 2002 to 2013, with about 67 % Argo float profiles, 19 % shipboard CTD profiles, and 14 % mooring-based profiles (Fig. 3). All profiles were vertically interpolated or re-gridded to 1 m vertical resolution in the depth range 5 to 1000 m. Missing data points within the first few meters of the water column were filled by constant extrapolation. For each profile, we determined the mixed layer depth (MLD) as the depth where the in situ temperature decreased by 0.2 °C relative to 10m depth (de Boyer Montégut et al., 2004).
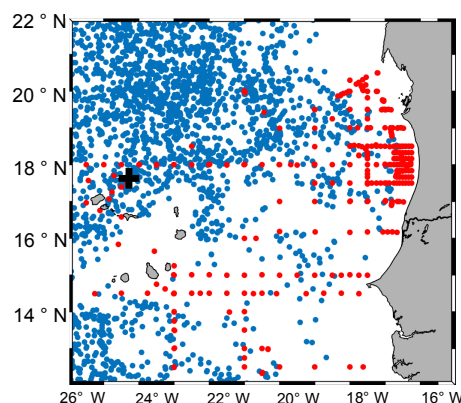


**Figure 3.** Locations of available temperature and salinity profiles obtained in the TANWA between 1995 and 2013. Red dots mark shipboard CTD stations, blue dots locations of Argo float profiles, and the black cross the location of the CVOO mooring.

By co-location, in space and time, of eddies, which are identified in the SLA data using a combination of the OW and the GEO method (an eddy has to be identified by both algorithms), with the combined in situ data set, the vertical structures of anticyclones and ACMEs (positive SLA) and cyclones (negative SLA) were assessed (Fig. 4). The classification results in 675 profiles taken in anticyclones/ACMEs, 499 profiles taken in cyclones, and 1856 profiles taken outside of detected eddies. Excluding the mooring-based pro-
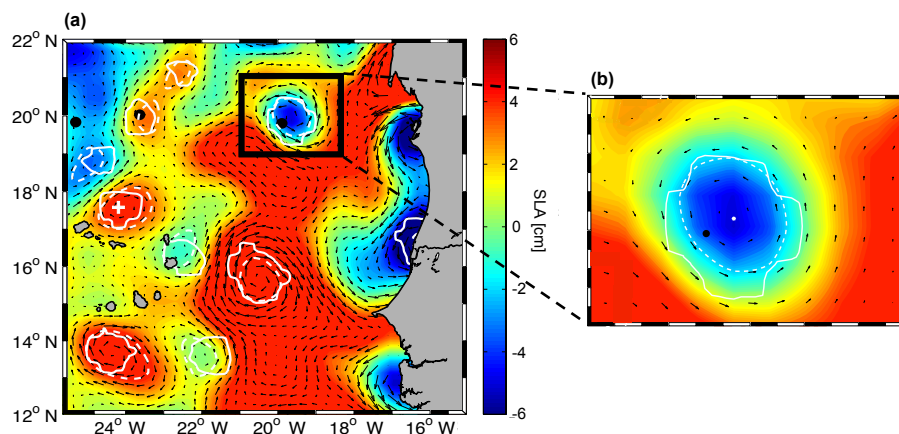
**Figure 4.** Snapshot of the SLA for 22 December 2010, with the results of the eddy-detection methods: OW method (solid white line) and the GEO method (dashed white line) with geostrophic velocities superimposed (black arrows). The black dots mark Argo float profiles, the white cross in **(a)** indicates the CVOO mooring. In **(b)** a zoom of a selected region with a cyclonic eddy is shown.

files, from which we only extracted eddy events, around $\sim 29\%$ of all profiles (Argo float and shipboard CTD profiles) were taken coincidentally inside of an eddy. This proportion is in the range of earlier results derived by Chaigneau et al. (2011), who estimated that $\sim 23\%$ of their Argo float profiles in the eastern upwelling regions of the Pacific Ocean are conducted in eddies and Pegliasco et al. (2015), who found 38% of all their Argo float profiles in the eastern upwelling areas conducted in eddies. We could also confirm with the result of Pegliasco et al. (2015) that the majority of all Argo float profile in eddies are conducted in long-lived anticyclones/ACMEs.

However, we are interested in the anomalous water mass characteristic inside the eddy compared to the surrounding water. Anomaly profiles of potential temperature, $\theta$, salinity, $S$, and potential density, $\sigma_\theta$, were derived as the difference of the profiles inside and reference profiles outside of an eddy. Profiles outside of eddies are required to be taken within a maximum distance of 120 km from the eddy center and at maximum $\pm 25$ days apart from the time the profile inside of the eddy was taken (Fig. 4). For 176 profiles out of the 1174 profiles inside of eddies, no reference profile could be found fulfilling these criteria. In total 587 anomaly profiles for anticyclones/ACMEs and 411 anomaly profiles for cyclones were derived. As mentioned before it was useful to further separate anticyclonically rotating eddies into two types: conventional anticyclones with downward bending isopycnals (and isotherms) throughout and ACMEs with upward bending isopycnals in the upper 50 to 100 m depth and downward bending isopycnals below. As a consequence, the MLD inside the ACMEs is shallower compared to background values, while it can be several tens of meters deeper in conventional anticyclones. We used the MLD difference to proof the separation into conventional anticyclones and ACMEs from the satellite-based surface signatures, described above. In all

cases, where the MLD inside of an anticyclonically rotating eddy was at least 10 m shallower than the MLD outside the eddy, the eddy was associated with a negative SST anomaly. Hence, the eddy-type separation through satellite-based surface signatures appears to be accurate. The separation identified 95 out of 587 profiles in anticyclonically rotating eddies as being taken in ACMEs (Fig. 5). Averaging all anomaly profiles for anticyclones, cyclones, and ACMEs yields mean anomaly profiles for potential temperature, $\overline{\theta'}$, salinity, $\overline{S'}$, and potential density, $\overline{\sigma_\theta'}$, for the three different eddy types. Profiles of available heat and salt anomalies available heat anomalies (AHA [J m$^{-1}$]) and available salt anomalies (ASA [kg m$^{-1}$]) per meter on the vertical were then derived as

$$\text{AHA} = \pi r^2 \rho C_p \overline{\theta'}, \tag{2}$$

$$\text{ASA} = 0.001 \times \pi r^2 \rho \overline{S'}, \tag{3}$$

where $\rho$ is density (in kg m$^{-3}$), $C_p$ is specific heat capacity (4186.8 J kg$^{-1}$ K$^{-1}$), and $r$ is the mean radius. The factor 0.001 in Eq. (2) is an approximation to convert PSS-78 salinity to salinity fractions (kg of salt per kg of seawater). These calculations are partly adapted from Chaigneau et al. (2011), where AHA and ASA are computed for eddies in the eastern Pacific. Integrating AHA and ASA per meter over the depth range 0 to 350 m, the AHA$_\text{total}$ (in J) and ASA$_\text{total}$ (in kg) was obtained. The lower boundary of integration was chosen as below; 350 m no significant temperature and salinity anomalies could be identified for the composite eddies of the three eddy types.

Eddies that pinch off from the eastern boundary are expected to carry waters with SACW signature westward into areas where waters with NACW signature prevail. To quantify the amount of SACW carried by these eddies, we follow a method developed by Johns et al. (2003) used to quantify the amount of water of Southern Hemisphere origin carried by North Brazil Current rings. Accordingly the high-
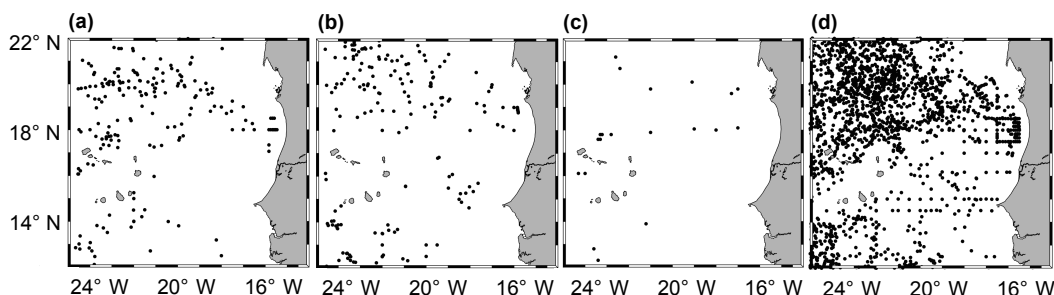
**Figure 5.** Location of all profiles taken in **(a)** cyclones, **(b)** anticyclones, **(c)** ACMEs, and **(d)** outside of an eddy.

est/lowest 10 % of the salinity values on potential density surfaces were averaged to define the mean NACW/SACW characteristics in the region as function of potential density. The obtained characteristics were used to determine the percentage of SACW contained in any profile taken inside and outside of eddies. Anomaly profiles of SACW percentage as function of potential density were then calculated as the difference of the profiles inside and outside of eddies and were eventually transformed back into depth space using a mean density profile.

To illustrate mean anomalies in potential temperature, salinity, potential density, and SACW percentage for each eddy type as a function of depth and radial distance, the available profiles were sorted with respect to a normalized distance, which is defined as the actual distance of the profile from the eddy center divided by the radius of the eddy. The profiles were grouped and averaged onto a grid of 0.1 between 0 and 1 of the normalized radial distance. Finally, the field was mirrored at zero distance and a running mean over three consecutive horizontal grid points was applied.

### 2.4 Determining the heat, salt, and volume transport

The three-dimensional structures of composite cyclones, anticyclones, and ACMEs produced out of the combination of altimetry data and all available profiles were used to estimate the relative eddy contribution to fluxes of heat, salt, and volume in the TANWA. Here we chose to define enclosed areas with area I representing the extended boundary current region, area II the transition zone, and area III the subtropical gyre region. By multiplying the heat transport of the composite eddies with the number of eddies dissolving during a year in a given area (corresponding to an flux divergence) a mean heat release (in $\text{W m}^{-2}$) and a mean salt release (in $\text{kg m}^{-2}$) were calculated. The mean heat release can be compared to the net atmospheric heat flux in the area here derived from the NOCS Surface Flux Dataset (Berry and Kent, 2011).

Using the volume of a composite eddy (defined by the mean radius and the depth range 0 to 350 m) and the mean SACW percentage within the eddy, the total volume transport of SACW of cyclones, anticyclones, and ACMEs was calculated.
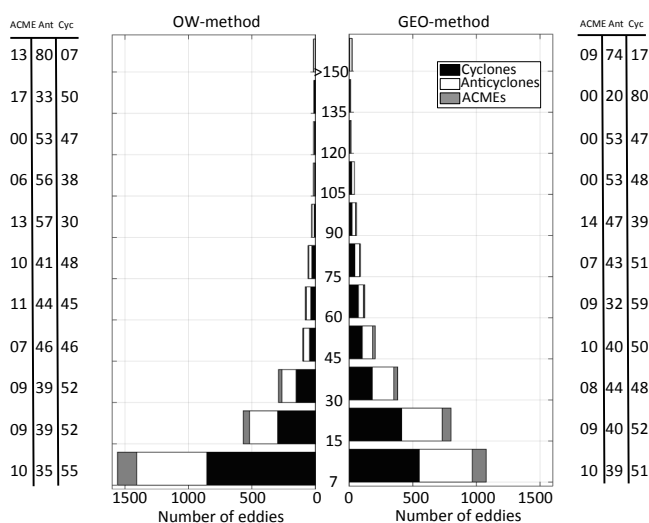


**Figure 6.** Number of eddies against lifetime in days from the OW method (left) and GEO method (right). Percentage of ACMEs, anticyclones (Ant), and cyclones (Cyc) is given in the tables on the right and left.

## 3 Results and discussion

### 3.1 Eddy statistics from SLA data

The two eddy tracking methods applied to the SLA data detected $\sim 2800$ eddies over the 19 years of analyzed data (Table 2, Fig. 6) with slightly more cyclones than anticyclones/ACMEs (6 % more in the OW method, 2 % more in the GEO method). Note, that the given number of eddies must be seen as a lower limit due to the coarse resolution of the satellite products. All of the detected eddies are nonlinear by the metric $U/c$, where $U$ is the maximum circumpolar geostrophic surface velocity and c is the translation speed of the eddy. A value of $U/c > 1$ implies that fluid is trapped within the eddy interior (Chelton et al., 2011) and exchange with the surrounding waters is reduced. Many of the eddies are even highly nonlinear, with 60 % having $U/c > 5$ and 4 % having $U/c > 10$.

36

**Table 2.** Mean properties of anticyclones, cyclones, and ACMEs in the region of 12–22° N, 16–26° W (TANWA) and their standard deviation given in brackets, detected from the OW method and the GEO method (detectable longer than 1 week and with a radius > 45 km). Coastal area is defined as an ∼ 250 km wide corridor near the coast (see Fig. 7).

| Property (based on SLA data between 95–2013) | OW method | | | GEO method | | |
|---|---|---|---|---|---|---|
| Detected eddies | 2741 (144 yr$^{-1}$) | | | 2816 (148 yr$^{-1}$) | | |
| | Anticyclones | Cyclones | ACMEs* | Anticyclones | Cyclones | ACMEs* |
| | 1041 (38 %) | 1443 (53 %) | 257 (9 %) | 1137 (40 %) | 1422 (51 %) | 257 (9 %) |
| Detected eddies in coastal area | 186 (10 yr$^{-1}$) | 241 (13 yr$^{-1}$) | 43 (2 yr$^{-1}$) | 178 (9 yr$^{-1}$) | 199 (10 yr$^{-1}$) | 45 (3 yr$^{-1}$) |
| Average lifetime (days) | 30 (±31) max 282 | 24 (±22) max 176 | 26 (±28) max 197 | 32 (±32) max 277 | 27 (±29) max 180 | 26 (±28) max 175 |
| Average radius (km) | 53 (±5) | 51 (±5) | 52 (±5) | 60 (±20) | 62 (±22) | 59 (±20) |
| Average westward propagation (km d$^{-1}$) | 2.8 (±2.4) | 2.7 (±2.4) | 2.8 (±2.5) | 3.3 (±1.8) | 3.1 (±1.9) | 3.3 (±1.9) |

* Note, that the properties of ACMEs are based on fewer years of SLA data (1998–2013), due to the unavailable SST data.

Considering only the period after 1998, i.e., when our SST data set becomes available, a satellite data-based separation between anticyclones (positive SST anomalies) and ACMEs (negative SST anomalies) is possible. We found that about 20 % of the anticyclonically rotating eddies are ACMEs. However, the number of ACMEs might be underestimated, because ACMEs are associated with a weak SLA signature and therefore more difficult to detect with the SLA-based algorithms. Also the nonlinearity of ACMEs is underestimated by using geostrophic surface velocity as they have a subsurface velocity maximum.

Although the GEO method in general detects slightly more eddies than the OW method (in total 75 eddies more, which is 2.7 % more than the OW method) the situation is different near the coastal area where the OW method detects 30 eddies per year but the GEO method only 22 eddies per year. This results from the strong meandering of the boundary current, where meanders are sometimes interpreted as eddies by the OW method due to the high relative vorticity. In contrast, the GEO method uses closed streamlines and therefore does not detect meanders as eddies, which makes this method more suitable for eddy detection in coastal areas. The average eddy radius in the TANWA is found to be 56 ± 12 km (given here as mean and standard derivation) with the GEO method resulting not only in around 10 km larger radii but also with a 4 times higher standard deviation when compared with the OW method. The difference in the standard deviation of the eddy radius derived from GEO and the OW method is partly due to the identification of relatively few very large eddies using the GEO method. In general, the OW method appears to be the more reliable tool for identifying the eddy surface area and the corresponding radius in the TANWA.

Both algorithms show that on average the anticyclones and ACMEs are larger and have a longer lifetime than the cyclones. The average westward propagation speed is 3.00 ± 2.5 km d$^{-1}$ for all eddy types, which is on the order of the first baroclinic mode Rossby wave phase speed at that latitude range (Chelton et al., 1998). The average tracking period (or lifetime) of an eddy in the TANWA is 28 days with a high standard deviation of 28 days. The longest consecutive tracking period for a single eddy (found similar in both algorithms) was around 280 days for an anticyclone, 180 days for a cyclone and 200 days for an ACME. However, most of the eddies were detectable for a period of 7 to 30 days. The number of eddies decreases rapidly with increasing tracking period (Fig. 6). Note that the OW method detects 450 eddies with a lifetime between 7 and 14 days, which is more than the GEO method. However, for longer lifetimes the GEO method detects more eddies than the OW method. As the tracking procedure in both algorithms is the same, the GEO method seems to be more reliable in identifying and following eddy-like structures from one time step to another. The percentage of tracked anticyclones/ACMEs and cyclones is close to 50 % for short tracking periods. For longer lifetimes anticyclonic eddies tend to dominate, this is also reflected in the slightly shorter mean lifetimes of cyclones compared to anticyclones. The dominance of long-lived anticyclones is also shown in the observational studies of Chaigneau et al. (2009), Chelton et al. (2011), and theoretically suggested by Cushman-Roisin and Tang (1990). The latter authors showed that in an eddying environment anticyclonic eddies are generally more robust and merge more freely than cyclones producing long-lived eddies, while cyclones show a higher tendency to self-destruction.

Note, that tracking of eddies in the TANWA is prone to errors in particular regarding the information about the eddies' lifetime. Some eddies disappear in single SLA maps, which is at least partly due to the separation of the satellite ground tracks (Chaigneau et al., 2008). In order to avoid loosing an eddy, we search 2 weeks after its assumed disappearance within a defined radius for an eddy with the same polarity (see Sect. 2.1.2). The fact that purest SACW, which in the TANWA occurs in the eastern boundary region, is found regularly in eddy cores at the CVOO mooring ($\sim 850$ km offshore) (Karstensen et al., 2015) shows that long-lived eddies must exist in the TANWA. Hence, the eddy tracking algorithms underestimate the eddy lifetime and accordingly overestimate the number of newly generated eddies.

This challenge for the eddy tracking algorithms in the TANWA is probably the reason why Chelton et al. (2011) and Chaigneau et al. (2009) could not detect many long-lived eddies in this area. Their definition of long-lived eddies requires eddies to be trackable for longer than 112 days (Chelton et al., 2011) or 35 days (Chaigneau et al., 2009). With the adaption of the method for the TANWA with the 2 weeks search radius as described above, eddy tracking has improved; however, some eddies might still be lost. In addition, the mean eddy lifetime of eddies in TANWA is underestimated due to the restriction of eddy trajectories at the northern, southern, and western boundaries.

## 3.2 Generation areas and pathways

To identify hot spots of eddy generation, the locations of the first detection of each eddy is counted in $1° \times 1°$ boxes (Fig. 7). The OW method and the GEO method do not show a significantly different pattern, except near the coast, where the local maximum in the number of newly detected eddies is shifted slightly offshore for the GEO method compared to the OW method. However, the distribution shows that most eddies are generated in the coastal area along the shelf. Within this region the headlands of the coast seem to play an important role as about nine newly detected eddies per year are found around Cap-Vert (Senegal), about four eddies per year off Saint-Louis (Senegal) and about five eddies per year off Cap Timris (Mauretania). At these spots the algorithms detect more than 70 % of the newly detected eddies (18 out of 25) per year in the coastal area. Another location of high eddy generation is southeast of the Cabo Verde islands, especially south of the northwesternmost island Santo Antão with about two newly detected eddies per year and southwest of Fogo with about five newly detected eddies per year.

To identify the preferred eddy propagation pathways, the locations of eddy centers, which were tracked for longer than 1 month (35 days), were counted in $1/6° \times 1/6°$ boxes over all time steps. The spatial distribution of eddy activity indeed shows some structures and eddies tend to move along distinct corridors westward, away from the coast into the open ocean (Fig. 8) as also shown for the Canary Island region
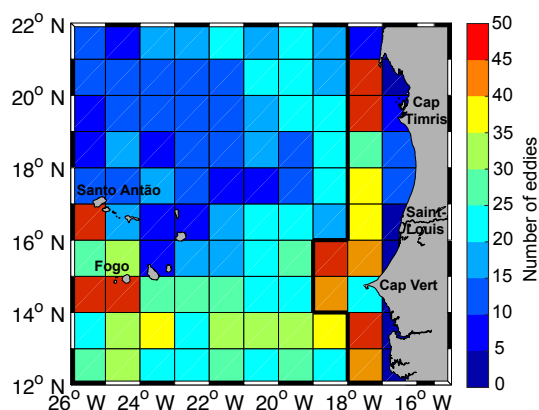


**Figure 7.** Number of eddies generated in $1° \times 1°$ boxes (colors) between 1995 and 2013 based on the results of the OW method. Marked are the headlands Cap Timris (Mauretania), Saint-Louis (Senegal), Cap-Vert (Senegal), and the islands Santo Antão (Cabo Verde) and Fogo (Cabo Verde), which can be associated with high eddy generation. The thick solid black line along 18° W/19° W separates the coastal region from the offshore region.

(Sangrà et al., 2009). The propagation pathways can be separately investigated for the different eddy types: most of the anticyclones are generated along the coast south of Cap Timris, off Saint-Louis, and north off Cap-Vert. They propagate either north of 18° N from their generation areas westward into the open ocean or south of 18° N with a southward deflection offshore. Their mean westward propagation speed is $3.05 \pm 2.15$ km d$^{-1}$. Other generation hotspots for anticyclones are around the Cabo Verde islands south of Santo Antão and south of Fogo. For cyclones the generation areas are more concentrated than for anticyclones. North of Cap Timris and off Cap-Vert are the main hotspots near the coast. On their way westwards cyclones tend to have a northward deflection in their pathways. The hotspot for cyclone generation around the Cabo Verde islands is west of Fogo. Cyclones have a mean westward propagation speed of $2.9 \pm 2.15$ km d$^{-1}$. Although not significantly different, the larger westward propagation speed of anticyclones compared to cyclones does agree with theoretical considerations regarding the westward eddy drift on a beta plane (Cushman-Roisin et al., 1990).

The main generation areas for ACMEs near the coast are north of Cap Timris and off Saint-Louis around 18° N. ACMEs generated north of Cap Timris tend to have a slightly southward deflection on their way westwards into the open ocean, whereas the eddies generated off Saint-Louis show no meridional deflection and propagate along $\sim 18°$ N into the open ocean. Their mean westward propagation speed is $3.05 \pm 2.1$ km d$^{-1}$. The main generation area of ACMEs near Cabo Verde islands is located south of the northwesternmost island Santo Antão.
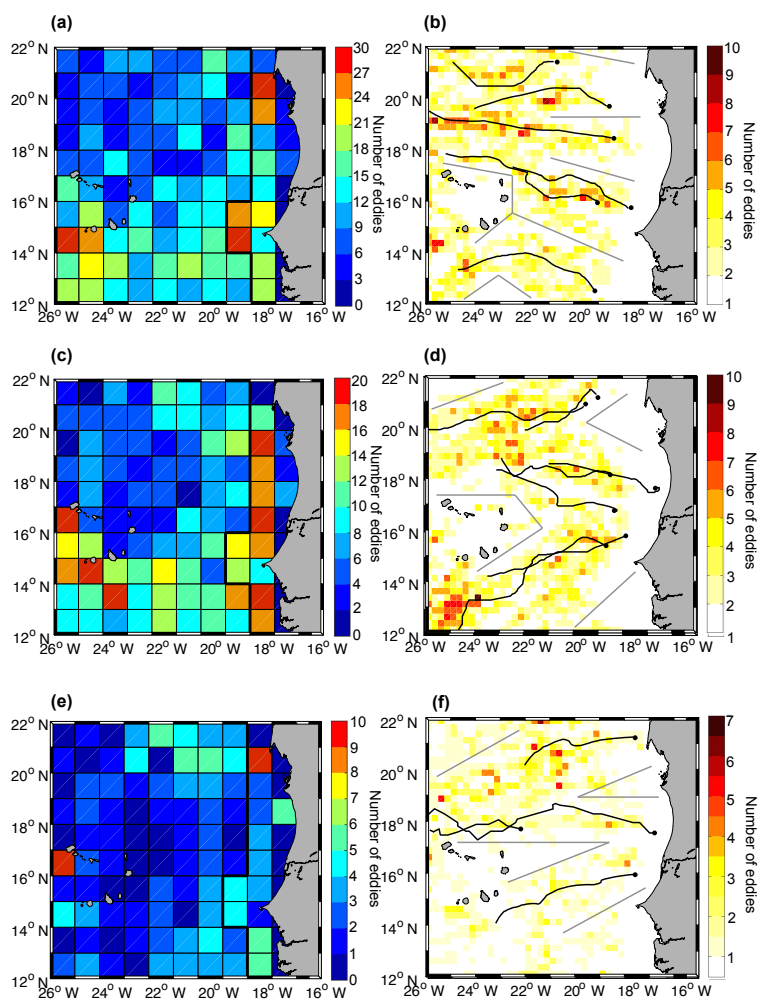
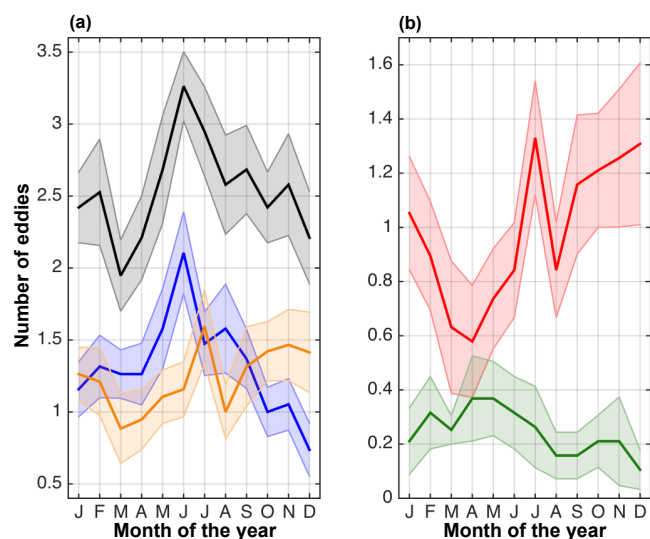**Figure 8.** Number of eddies generated in $1° \times 1°$ boxes **(a, c, e)** and number of long-lived eddies detected in $1/6° \times 1/6°$ boxes based on the results of the OW method **(b, d, f)** for cyclones **(a, b)**, anticyclones **(c, d)**, and ACMEs **(e, f)**. In **(b)**, **(d)**, and **(f)** only eddies with a lifetime larger than 35 days are counted. In **(b)**, **(d)**, and **(f)** main eddy propagation corridors are indicated by straight gray lines; black lines show trajectories of long-lived eddies with a lifetime larger than 150 days. The thick solid black line along $18°$ W/$19°$ W in **(a)**, **(c)**, and **(e)** separates the coastal region from the offshore region.

## 3.3 Seasonal variability of eddy generation

While the two eddy detection methods differ mostly in the number of identified eddies close to the coast, the season of peak eddy generation is very stable for both methods. A pronounced seasonality with a maximum of newly formed eddies during boreal summer (June/July) is obtained from both methods (Fig. 9). During April to June newly generated eddies are mostly cyclonic, while during October to December newly generated eddies are mostly anticyclonic (anticyclones plus ACMEs). These seasonal differences indicate different eddy generation mechanisms at play in the TANWA during the different seasons. Different mechanisms for the generation of eddies in eastern boundary upwelling regions have been proposed (e.g., Liang et al., 2012). Barotropic and baroclinic instabilities of the near-coastal currents (Pantoja et

al., 2012) triggered by, e.g., the passage of poleward propagating coastal trapped waves (Zamudio et al., 2001, 2007), wind perturbations (Pares-Sierra et al., 1993), or interactions of the large-scale circulation with the bottom topography (Kurian et al., 2011) are the main processes identified for the eddy generation in eastern boundary upwelling regions. In the TANWA, the period of maximum eddy generation (June/July) is characterized by a strong near-surface boundary current, the MC (Lázaro et al., 2005) suggesting dynamic instabilities of the boundary current as an important generation mechanism. However, there is a difference in peak generation of cyclones and anticyclones. While the maximum generation of cyclones occurs in June during the acceleration phase of the MC, the seasonality of anticyclone generation is not as distinct with weaker maxima in July and at the end of the year. The generation of ACMEs has the main

**Figure 9.** Seasonal cycle of the number of eddies generated in the costal region per year based on the results of the OW method as shown in Figs. 7 and 8. In **(a)** the seasonal cycle of all eddies is marked by the black line, of cyclones by the blue line and of all anticyclonic eddies by the orange line. In **(b)** the seasonal cycle of anticyclonic eddies is separated into anticyclones (red line) and ACMEs (green line). The shaded areas around the lines represent the standard error.

peak in April to May, which is at the end of the upwelling season. During that period the PUC is likely getting unstable and vanishes later on (Barton, 1989).

The seasonal peak in eddy occurrence appears to propagate westwards into the open ocean. To illustrate this, annual harmonics are fitted to the number of eddies detected per month in $2° \times 2°$ boxes (Fig. 10). Note, that the phase of a box is only shown when the amplitude is larger than 2.5 eddies per box. After the main generation of cyclones in the coastal area in June, the eddies enter the open ocean in late boreal autumn, passing the Cabo Verde islands and the ventilated gyre regime north of the CVFZ in boreal winter/spring. As mentioned before anticyclones are generated 1 to a few months later at the coast (July and October, November). They dominantly reach the open ocean in boreal winter and spring and accordingly pass the Cabo Verde islands and the ventilated gyre regime north of the CVFZ in late boreal spring and summer. Note, that the relatively clear signal of the annual harmonic of eddy detections (Fig. 10) also suggests that eddies with lifetime > 9 months are more frequent in the TANWA than indicated by the statistical output of the algorithms.

## 3.4 Mean eddy structure

### 3.4.1 Surface anomalies related to eddies

For the three types of eddies, composite were constructed from daily SLA, SST, and SSS anomaly fields. An area of $300 \, \text{km} \times 300 \, \text{km}$ around every identified eddy center (center is the maximum value of SLA) was considered (Fig. 11). Overall we had about 40 000 snapshots of eddies between 1993 and 2013 available to calculate the mean SLA and SST anomalies. To derive mean SSS anomalies, only about 10 000 snapshots were merged because of the shorter time period of the SSS satellite data record (2010–2013).

For anticyclones, we found a positive SLA (maximum value in the eddy core is 6.9 cm (3.02; 11.01 cm), given here as mean and the upper and lower limits of the 68 % quartile range), a positive SST anomaly (maximum value in the eddy core 0.13 °C (0.03; 0.24 °C)) and a positive SSS anomaly (maximum value in the eddy core is 0.20 (−0.04; 0.52)). For cyclones, we found a negative SLA (minimum value in core −5.5 cm (−1.57; −7.37 cm)), a negative SST anomaly (minimum value in the core is −0.15 °C (−0.04; −0.30 °C)), and a negative SSS anomaly (minimum value in the core is −0.16 (0.08; −0.48)). However, for the ACMEs (about 20 % of the anticyclones) we found a negative SST anomaly (minimum value in the core is −0.15 °C (−0.04; −0.31 °C)) was observed. The vertical structure of these anticyclones as obtained from temperature and salinity profiles revealed the characteristic pattern of ACMEs with a very shallow mode in the upper 100 m or so. ACMEs also have a negative SSS anomaly (minimum value in the core is −0.13 (0.10; −0.33)). For all eddy types, SST dominates sea surface density.

Compared to SLA and SST measurements, the satellite-based observations of SSS are afflicted with high uncertainties and large measuring gaps. However, in the composite it is possible to detect eddy-type dependent anomalies, even if they are not as clear and circular as the SLA and SST anomalies. The zonally stretched structures in the composites of SSS anomalies may also result from the coarser temporal resolution of SSS data (i.e., 10 days) resulting in a smearing of the eddy signal in the direction of propagation. Note, that the composites of SSS anomalies showed only coherent eddy structures when selecting energetic eddies (i.e., with a radius between 45 and 70 km and an absolute SLA anomaly > 2 cm). The composites of SLA and SST anomalies are much less affected by the restriction with regard to the eddy amplitude.

In summary, the absolute SST and SSS anomalies of all three eddy types are of similar magnitude. The magnitude of absolute SLA of anticyclones and cyclones is also somehow similar, while ACMEs have a weaker SLA signature (which makes them more difficult to be detected and tracked by satellite altimetry). The maximum surface circumpolar velocity is $0.18 \pm 0.12$ in cyclones, $0.17 \pm 0.12$ in anticy-
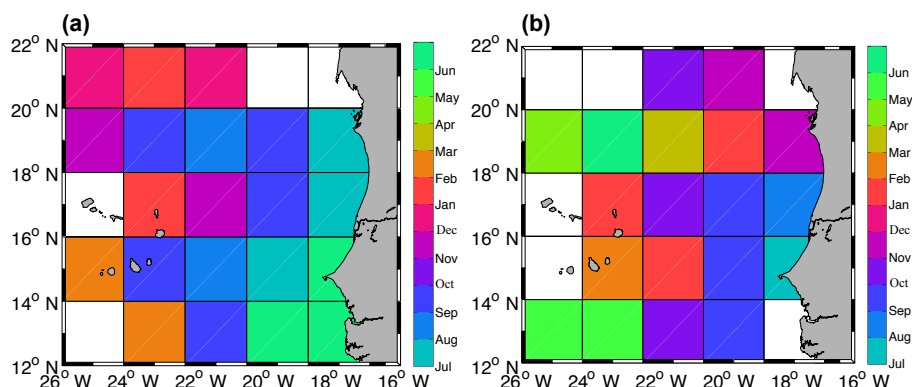
**Figure 10.** Phase of the annual harmonic of the number of detected eddies in $2° \times 2°$ boxes based on the results of the OW method for (a) cyclones and (b) anticyclones. Phases are only shown for boxes with an amplitude larger than 2.5 eddies. Phase is given in month of the year with maximum eddy number.
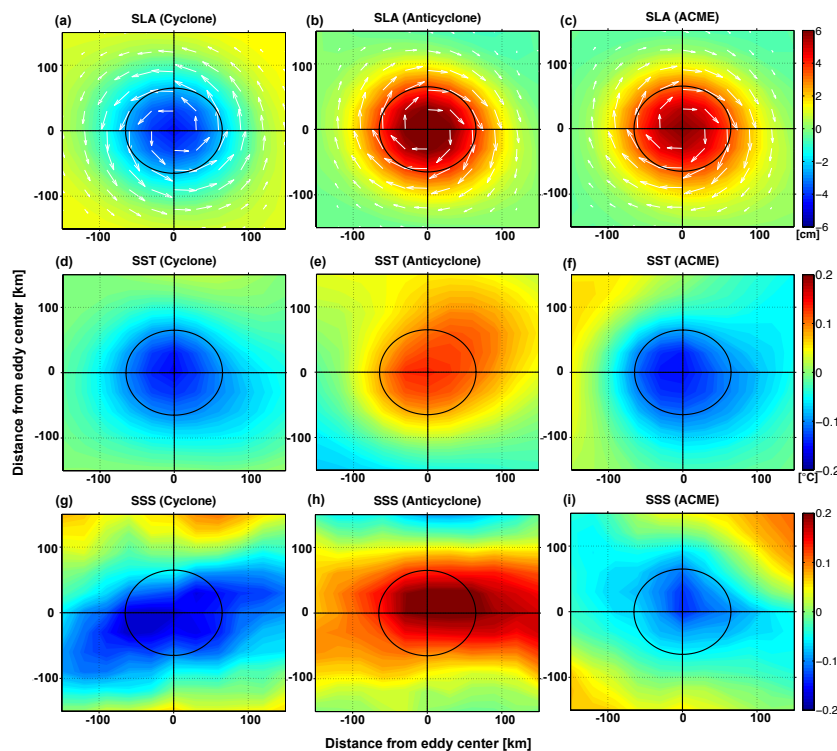


**Figure 11.** SLA, SST, and SSS anomalies of the composite cyclone, anticyclone, and ACME in the TANWA based on the results of the OW method. SLA (color) and the associated geostrophic velocity (white arrows) are shown for each eddy type in (a), (b), and (c); SST anomaly in (d), (e), and (f); and SSS anomaly in (g), (h), and (i). The circles mark the mean eddy radius.

clones, and $0.16 \pm 0.10\,\mathrm{m\,s^{-1}}$ in ACMEs. Overall, cyclones are slightly smaller, rotate faster, and therefore have a shorter lifetime than the other eddy types.

### 3.4.2 Vertical structure of eddies

Profiles from Argo floats, shipboard CTD, and moorings were used to derive a mean vertical eddy structure. Here, we calculated anomaly profiles of potential temperature, salinity

and potential density derived from profiles inside and outside of eddies. The mean vertical structure and the anomalies presented here (Fig. 12) are based on 492 profiles in anticyclones, 411 profiles in cyclones, but only 95 profiles in ACMEs. Consequently, the statistics for ACMEs are weakest and the mean vertical structure must be interpreted with care. Cyclones, anticyclones, and ACMEs are characterized by a different shallowing/deepening of isopycnal surfaces. Anticyclones carry a warm and saline water anomaly, whereas
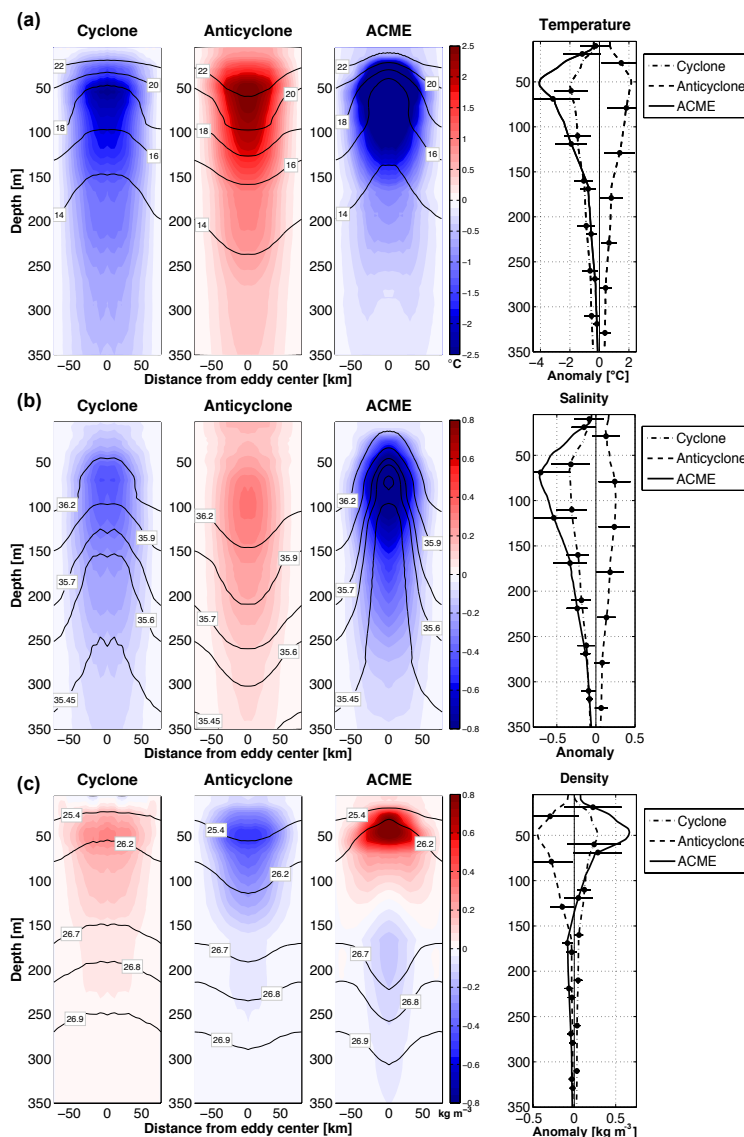
**Figure 12.** Vertical structure of the composite cyclone, anticyclone, and ACME in the TANWA as presented as sections through the eddy center (left three columns) and mean anomaly profiles (right column). In **(a)** potential temperature anomaly, in **(b)** salinity anomaly, and in **(c)** potential density anomaly as calculated by using the nearest profile outside of the eddy is shown. Black contour lines in the left three columns mark isolines of temperature **(c)**, salinity **(b)**, and potential density **(c)**. In the right column, solid lines represent the composite ACME, dashed lines the anticyclone, and dashed-dotted lines the cyclone; the error bars at selected depths represent the standard deviation calculated from the individual anomaly profiles.

cyclones and ACMEs host cold and less saline water in their cores. The effect of temperature anomalies on density anomalies dominates over the effect of salinity anomalies, which results in a positive density anomaly associated with cyclones (shoaling of isopycnals) and a negative density anomaly associated with anticyclones (deepening of isopycnals). This is illustrated by the elevation (deepening) of 25 m (36 m) of the density surface of $26.2\,\mathrm{kg\,m^{-3}}$ in the core of the cyclone (anticyclone) compared to the surroundings. Due to the specific vertical structure of ACMEs, characterized by a strengthening of the anticyclonic rotation with depth

in its upper part and a weakening of the anticyclonic rotation in its lower part, the ACMEs have a positive density anomaly in about the upper 100 m (shoaling of isopycnals) and a negative density anomaly below down to about 350 m (deepening of isopycnals). The mode water in the core of the ACMEs is only weakly stratified. This is illustrated by the elevation of 48 m of the density surface of $26.2\,\mathrm{kg\,m^{-3}}$ slightly above the core and the deepening of 52 m of the density surface of $26.7\,\mathrm{kg\,m^{-3}}$ below the core compared to the surroundings. From the mean vertical eddy profiles, we diagnose a maximum temperature anomaly underneath the mean

mixed layer depth, which is at a depth of about 50 m. It is $-2.42 \pm 1.23\,°C$ at 55 m for cyclones and $+1.88 \pm 1.37\,°C$ at 54 m for anticyclones. The maximum salinity anomaly is $-0.34 \pm 0.25$ at 70 m depth for cyclones and $+0.25 \pm 0.2$ at 100 m for anticyclones and as such located below the maximum temperature anomaly. The respective maximum density anomalies are, as expected, close to the location of the maximum temperature anomaly, and are $0.28 \pm 0.42\,kg\,m^{-3}$ at 48 m for cyclones and $0.44 \pm kg\,m^{-3}$ at 50 m for anticyclones. The mean ACME structure is characterized by a much stronger temperature anomaly of $-4.0 \pm 2.2\,°C$ at 51 m depth and salinity anomaly of $0.72 \pm 0.38$ at 74 m depth in comparison to cyclones and anticyclones. Note, that the cold and fresh SACW in the ACME core does not produce a positive temperature anomaly when it reaches deeper levels due to the downward bending of isopycnal surfaces below the eddy core. The ACME density anomaly has a maximum of $0.66 \pm 0.35\,kg\,m^{-3}$ at about 47 m and a minimum of $-0.08 \pm 0.06\,kg\,m^{-3}$ at about 168 m, which reflects the shoaling and deepening of isopycnals towards the eddy center above and below its core. Note, that below the eddy core ($> 150$ m depth) horizontal density anomalies are dominated by salinity with temperature playing a minor role. For all eddy types, cyclones, anticyclones, and ACMEs, temperature, salinity, and density anomalies reach down to about 300–350 m depths with a maximum beneath the mixed layer or slightly deeper.

Chaigneau et al. (2011) observed mean maximum anomalies of $\pm 0.7\,°C$ in temperature and $\pm 0.06$ in salinity based on Argo float measurements in eddy cores within the southeastern Pacific. For the TANWA the mean maximum anomalies of about $\pm 2\,°C$ in temperature and $\pm 0.3$ in salinity are more than twice as high. The presence of different water masses, cold and fresh SACW prevailing in the coastal region and warmer and saltier NACW further offshore, results in the large temperature and salinity anomalies in eddy cores in the TANWA compared to the southeastern Pacific. Furthermore the reference used for calculating an anomaly can create large differences. Chaigneau et al. (2011) computed the anomalies of Argo float profiles relative to interpolated climatological profiles taken from Commonwealth Scientific and Industrial Research Organization (CSIRO) Atlas of Regional Seas (CARS). Here, we tested five different references to calculate anomalies and found significantly different anomalies, even with reversed sign (Table 3). The differences in the mean anomalies depend on the reference profiles that are used. Besides the "next profile outside", we used different climatologies as reference. However, differences in temperature and salinity between the different climatologies are of similar magnitude as the derived mean anomalies of the different eddy types (Table 1). When using the "next profile outside" as reference, we obtained larger mean anomalies, which could suggest that the "next profile outside" is systematically biased by nearby eddies of reversed polarity (which are possibly not well identified by the eddy detect-

**Table 3.** Temperature and salinity anomalies of cyclones and anticyclones vertically averaged in the upper 350 m. Anomaly profiles are calculated relative to different reference data sets: (1) the nearest in situ profile in time and space, (2) the CSIRO CARS2009a v1.1 climatology, (3) the monthly WOA09 climatology, (4) the monthly MIMOC v2.2 climatology, and (5) the monthly Levitus94 climatology (salt values are not included in monthly database).

| | Cyclones | | Anticyclones | |
| --- | --- | --- | --- | --- |
| | Temp (°C) | Salt | Temp (°C) | Salt |
| (1) Next profile outside | $-1.22$ | $-0.26$ | $0.87$ | $0.13$ |
| (2) CSIRO | $-0.21$ | $-0.08$ | $0.94$ | $0.06$ |
| (3) WOA | $-0.32$ | $-0.10$ | $0.85$ | $0.05$ |
| (4) MIMOC | $-0.56$ | $-0.32$ | $0.60$ | $-0.17$ |
| (5) Levitus | $-0.16$ | | $0.97$ | |

ing methods). However, in particular in regions with strong gradients/fronts (e.g., CVFZ, coastal upwelling) with strong seasonality and variability, the "next profile outside" should deliver the most realistic background condition surrounding an eddy and thus should be preferably used to calculate water mass anomalies transported by eddies.

Here, we want to note that the uppermost data point (at 5 m) of the mean temperature and salinity anomaly profiles of the three types of eddies from the selected in situ data (Fig. 12) agree well with the surface anomalies based on satellite data composites (Fig. 11) and amounts to maximum values of $-0.15\,°C$ (in situ: $-0.15\,°C$) for cyclones, $0.13\,°C$ (in situ: $0.25\,°C$) for anticyclones, and $-0.15\,°C$ (in situ: $-0.20\,°C$) for ACMEs; corresponding salinity anomalies are $-0.16$ (in situ: $-0.10$) for cyclones, $0.2$ (in situ: $0.13$) for anticyclones, and $-0.13$ (in situ: $-0.11$) for ACMEs.

## 3.5 Contribution of eddies to zonal transport of properties

### 3.5.1 Thermohaline content and associated transport of eddies

For all cyclones/anticyclones/ACMEs a mean eddy volume of $2.860 \times 10^{12}\,m^3/3.089 \times 10^{12}\,m^3/2.973 \times 10^{12}\,m^3$ is derived, considering their mean radii (51 km/53 km/52 km) and a mean depth of 350 m for all three eddy types. Distributed over a period of 1 year this leads to a westward volume flux associated with a single eddy of about 0.1 Sv.

The mean three-dimensional structure of temperature and salinity anomalies associated with cyclones, anticyclones, and ACMEs (Fig. 12) was used to estimate profiles of AHA and ASA per meter (Fig. 13). The maximum AHA per meter is located at depths comparable to the maximum temperature anomaly and at about 55 m for all eddy types. The maximum ASA per meter is located deeper at about 80 m depth ($\sim 70$ m depth for cyclones, $\sim 80$ m for ACMEs, and

43
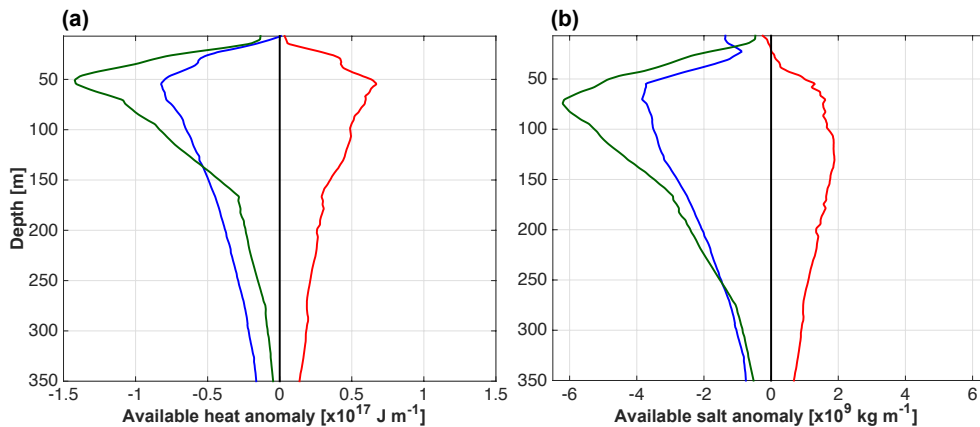
**Figure 13.** Mean profiles of available **(a)** heat and **(b)** salt anomaly per meter of the composite cyclone (blue line), anticyclone (red line), and ACME (green line).

**Table 4.** Total available heat anomaly ($AHA_{total}$) and total available salt anomaly ($ASA_{total}$) of the composite cyclones, anticyclones, and ACMEs as well as contribution of a single eddy to the annual heat and salt transport and its mean volume.

|  | Cyclones | Anticyclones | ACMEs |
|---|---|---|---|
| $AHA_{total}$ ($\times 10^{18}$ J) | $-14.5$ | $11.0$ | $-15.4$ |
| $ASA_{total}$ ($\times 10^{10}$ kg) | $-73.0$ | $40.7$ | $-94.2$ |
| Heat transport ($\times 10^{11}$ W) | $-4.6$ | $3.5$ | $-4.9$ |
| Salt transport ($\times 10^3$ kg s$^{-1}$) | $-23.2$ | $12.9$ | $-29.9$ |
| Volume ($\times 10^{10}$ m$^3$) | $286.0$ | $308.9$ | $297.3$ |

$\sim 110$ m for anticyclones). The $AHA_{total}$ ($ASA_{total}$), derived by integrating the profiles of AHA (ASA) per meter from the surface to 350 m, is $-14.5 \times 10^{18}$ J ($-73.0 \times 10^{10}$ kg) for cyclones, $11.0 \times 10^{18}$ J ($40.7 \times 10^{10}$ kg) for anticyclones, and $-15.4 \times 10^{18}$ J ($-94.2 \times 10^{10}$ kg) for ACMEs (see also Table 4).

Comparing our results to the southeastern Pacific (cyclones: $AHA_{total} = -5.5 \times 10^{18}$ J, $ASA_{total} = -9.8 \times 10^{10}$ kg; anticyclones: $AHA_{total} = 8.7 \times 10^{18}$ J, $ASA_{total} = 23.8 \times 10^{10}$ kg) (Chaigneau et al., 2011), we found an overall smaller volume of the eddies in the TANWA, but derived larger heat and salt anomalies. On the one hand, this could be explained by the fact that we averaged over a smaller area. However, regional differences should also exist, e.g., related to the boundary current hydrographic structure or the mean rotation speed (hence bending of isopycnals). For ACMEs in the southeastern Pacific there is only one recent estimate

by Stramma et al. (2013) for comparison, who estimated the $AHA_{total}$ and $ASA_{total}$ of a well-observed ACME to be $17.7 \times 10^{18}$ J and $36.5 \times 10^{10}$ kg, respectively. The heat and salt anomalies are on the same order as that found for the mean ACME in the TANWA but with reversed sign, which is remarkable. The ACME observed in the southeastern Pacific transports, in contrast to the composite ACMEs in the TANWA, warm and saline waters in its core offshore. One possible explanation is the different water mass characteristics in the source (coastal) region of the ACMEs in the southeastern Pacific compared to the TANWA.

Evenly distributed over a period of 1 year the heat (salt) transport associated with one single eddy is $-4.6 \times 10^{11}$ W ($-23.2 \times 10^3$ kg s$^{-1}$) for cyclones, $3.5 \times 10^{11}$ W ($12.9 \times 10^3$ kg s$^{-1}$) for anticyclones, and $-4.9 \times 10^{11}$ W ($-29.9 \times 10^3$ kg s$^{-1}$) for ACMEs. As expected from the lower $AHA_{total}$ ($ASA_{total}$) that has been derived for eddies in the southeastern Pacific (Chaigneau et al., 2011), the heat (salt) transport due to eddies in the TANWA is comparably large (see also Table 4).

In order to estimate the large-scale impact of the heat and salt transport by these eddies in the TANWA, we define three characteristic areas (see Fig. 14): the extended boundary current region (area I), the transition zone (area II), and the subtropical gyre region (area III). Based on the results from the GEO method, 21 eddies are formed each year in the extended boundary current region of the TANWA. While about five eddies dissipate quickly and only influence the near-coastal regions, about 16 eddies per year leave the extended boundary current region and propagate into the transition zone of the TANWA (Fig. 14a). Based on the mean temperature and salinity anomalies derived above, it equates to a heat (salt) transport of $-35.9 \times 10^{11}$ W ($-180.6 \times 10^3$ kg s$^{-1}$) by cyclones, $23.0 \times 10^{11}$ W ($85.3 \times 10^3$ kg s$^{-1}$) by anticyclones, and $-8.8 \times 10^{11}$ W ($-53.8 \times 10^3$ kg s$^{-1}$) by ACMEs. With regard to the number of eddies that dissolve in the different areas per year an equivalent surface heat flux (ESHF) is

44
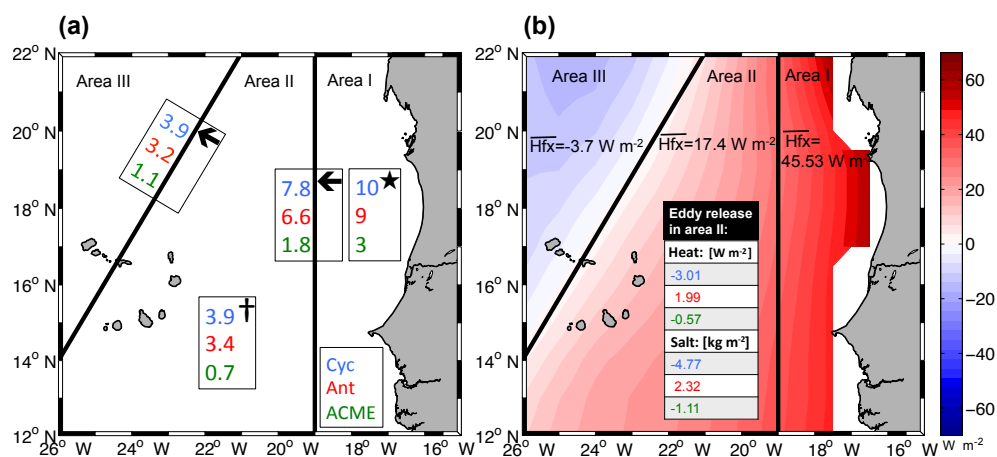
**Figure 14. (a)** Map of the TANWA divided into three areas (area I: the extended boundary current region, area II: the transition zone, and area III: the subtropical gyre region). Numbers inside of the boxes are the numbers of eddies (blue: cyclones, red: anticyclones, green: ACMEs), which are generated (star) and cease (cross) in an area or propagate from one area into another (arrow). **(b)** Annual mean net heat flux from NOC Surface Flux Dataset (colors) with three areas marked. Black numbers are the area-averaged net heat fluxes ($\overline{Hfx}$) in the corresponding areas. The table includes the eddy-type dependent (blue: cyclones, red: anticyclones, green: ACMEs) heat and salt release in area II.

computed and compared with the annual mean net surface heat flux for the respective regions as taken from the NOC Surface Flux Dataset (Berry and Kent, 2011) (Fig. 14b).

The anomalies in heat and salt associated with the three different types of eddies partly counteract each other. Anomalies in cyclones and ACMEs are negative, indicating heat and salt deficiencies in their core, while anomalies in anticyclones represent a surplus of heat and salt with respect to the background conditions. The cyclonic eddies provide an ESHF in area II of about $-3.0\,\mathrm{W\,m^{-2}}$, anticyclones of about $+2.0\,\mathrm{W\,m^{-2}}$, and ACMEs of about $-0.6\,\mathrm{W\,m^{-2}}$, which results in a net ESHF associated with all eddies of about $-1.6\,\mathrm{W\,m^{-2}}$. This heat flux due to eddies represents about 10 % of the net surface heat flux in the transition zone of the TANWA that is about $+17.4\,\mathrm{W\,m^{-2}}$.

In the open ocean of the TANWA, cyclones and ACMEs contribute to a cooling and freshening of the upper ocean and anticyclones to a warming and salinity increase. As such, the mesoscale eddy field and its seasonal to interannual variability can have an impact on the regional heat and salt budgets of the TANWA. However, because our calculations only account for long-lived eddies with a radius larger than 45 km, the calculated absolute eddy fluxes represent a lower limit that might increase when accounting also for short-lived, non-coherent eddies and/or sub-mesoscale variability.

### 3.5.2 Zonal eddy-dependent westward transport of SACW

Many of the eddies that originate in the eastern boundary region carry water of South Atlantic origin westward. In order to quantify the SACW signature in the eddies, a water mass analysis was performed. For all isopycnals SACW (labeled

100 %) and NACW (labeled 0 %) temperature and salinity pairs were defined using extremes of all observational data (see Fig. 2). Then the percentages of SACW concentrations contained inside the eddy cores were estimated. However, because the background field also transitions along the eddy trajectories towards stronger NACW characteristic, we estimated the SACW content of the eddies relative to the surrounding waters. Figure 15 shows the average vertical structure of the trapped SACW anomaly relative to the background for each eddy type. The different eddy types have a different potential in trapping SACW in their cores. Cyclones contain on average 16 % (maximum core value: 35 %) more SACW than the surrounding water and ACMEs even 21 % (maximum core value: 60 %). This implies a negative heat and salt anomaly along isopycnal layers inside of cyclones and ACMEs. Furthermore, it shows the prominent capability of ACMEs to trap and isolate anomalous water inside their cores. In contrast, the SACW anomaly in anticyclones is weak and negative (on average $-4$ %; minimum core value $-10$ %), implying that anticyclones contain on average a positive heat and salt anomaly along isopycnal layers. As such, anticyclones counteract the westward transport of SACW associated with the propagation of cyclones and ACMEs. Anticyclones instead transport small amounts of NACW westward.

To estimate an absolute transport of SACW from the eddy generation area at the eastern boundary into the open ocean, the mean percentages of SACW contained inside the different eddy types can be used. The highest percentage of SACW ($> 80$ %) is found in the extended boundary current region (area I). Northwestward towards the open ocean, the SACW percentage decreases (area II $\sim 57$ %, area III $< 23$ %; Fig. 16b). Hence, when the eddies are generated in the ex-
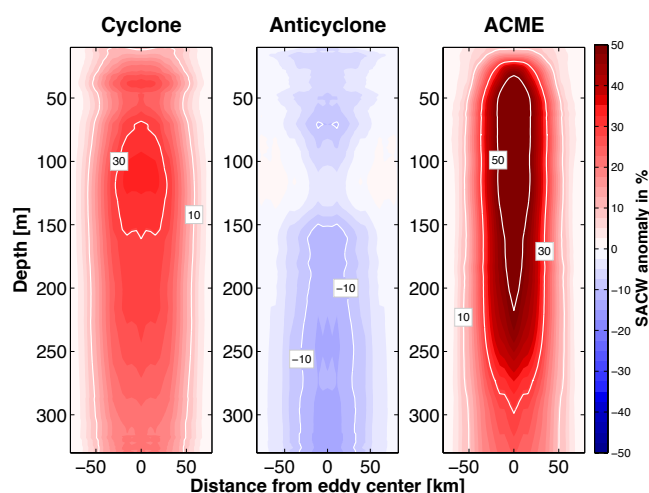
**Figure 15.** Vertical sections of SACW anomaly through the center of the composite cyclone (left), anticyclone (middle), and ACME (right) in the TANWA.

tended boundary current region (in area I) they trap waters with SACW signature in their cores and transport it westward into the open ocean (area II and area III), where waters with NACW signature prevail. These anomalous properties with respect to the surrounding waters can be visualized in a salinity versus sigma-theta diagram (Fig. 16a). ACMEs exhibit the strongest SACW signature, indicating again that ACMEs have the best capability to trap water. The percentage of SACW in the different eddy types within the three separated areas are shown in the white circles in Fig. 16b. Again the strong capability of ACMEs to transport SACW is obvious. In area II (background $\sim 57\%$ SACW) ACMEs still exhibit 82 % SACW and in area III (background $< 23\%$ SACW) it is 78 % SACW, indicating that ACMEs are only weakly affected by lateral and vertical mixing. Cyclones contain 69 % SACW in area II and 52 % SACW in area III and as such lose SACW signature from their cores much faster. Anticyclones with 59 % SACW in area II and 29 % SACW seem to have almost the same SACW signature as the background. This indicates that either they are not well isolated, and their cores are already replaced with the surrounding water, or that they are transporting low SACW signatures in their cores from the beginning.

Using the number of eddies passing the boundaries of the areas and the "excess" percentage of SACW in their cores (relative to the background), an "eddy-type dependent" absolute transport of SACW out of the boundary current was derived (Fig. 16b). We obtained an absolute transport of 2.07 Sv of SACW out of the boundary current near the coast into the extended boundary current region (area I) of which about 0.81 Sv of SACW reached the transition zone (area II). Further to the west, about 0.36 Sv of SACW reached the subtropical gyre region west of the Cabo Verde islands (area III). Considering the volume of the upper 350 m of the transition

zone (area II; $2 \times 10^5$ km$^3$) the eddy transport will replenish the SACW part in about 2.5 years. Note, that these calculations represent conservative assumptions about the SACW transport since the contribution of short-lived, non-coherent, and smaller-scale eddies to the SACW transport is not included. For example, the highly energetic cyclone generated at the headland of Cap-Vert discussed in detail by Alpers et al. (2013), which has a radius of 10 to 20 km and a Rossby number larger than 1, is not detected by the eddy detection algorithms used in this paper due to its small scale, but certainly contributed to the westward transport of near-coastal water masses.

## 4 Summary and conclusion

Within this study we analyzed satellite-based remotely sensed data, including SLA, SST, SSS, as well as in situ temperature and salinity profiles, taken from Argo floats, ships, and moorings, in order to examine the eddy characteristics and dynamics in the TANWA. Eddies were identified based on their manifestation in SLA data using two different eddy detection algorithms, the OW method and the GEO method. Both detection algorithms produced rather similar results except for the open ocean/coastal transition zone, where the OW methods seem to overestimate the amount of eddies due to high vorticity values associated with the meandering boundary current.

We found that anticyclones (cyclones) are associated with enhanced (reduced) SLA, enhanced (reduced) SST and enhanced (reduced) SSS in their eddy cores. However, 20 % of all eddies with enhanced SLA showed reduced SST and reduced SSS and we were able to classify these eddies as anticyclonic mode-water eddies (ACMEs). Of the average $146 \pm 4$ eddies detected per year in the TANWA over 19 years of SLA data, the ratio of cyclonic and anticyclonic eddies is nearly equal (52 % cyclones, 39 % anticyclones, 9 % ACMEs), with a similar radius of $56 \pm 12$ km for all three eddy types.

In agreement with earlier findings (Chaigneau et al., 2009), we found eddies being generated mainly near the coast and here at some topographic "hot spots". For the TANWA these hot spots are associated with the headlands of Cap-Vert (Senegal) and Cap Timris (Mauretania). We could also confirm the existence of a seasonality in the eddy generation (Chaigneau et al., 2009; Kurczyn et al., 2012) and found cyclones form preferably during April to June, while anticyclones and ACMEs are mostly generated from October to December. After their generation, eddies of all three types propagate westward with a speed, $c$, of about $3.00 \pm 2.15$ km d$^{-1}$, which is in general agreement with the first baroclinic mode Rossby wave phase speed at that latitude range (Chelton et al., 1998). We found that anticyclones/cyclones follow distinct corridors with a meridional deflection towards the Equator/pole. This is in agreement
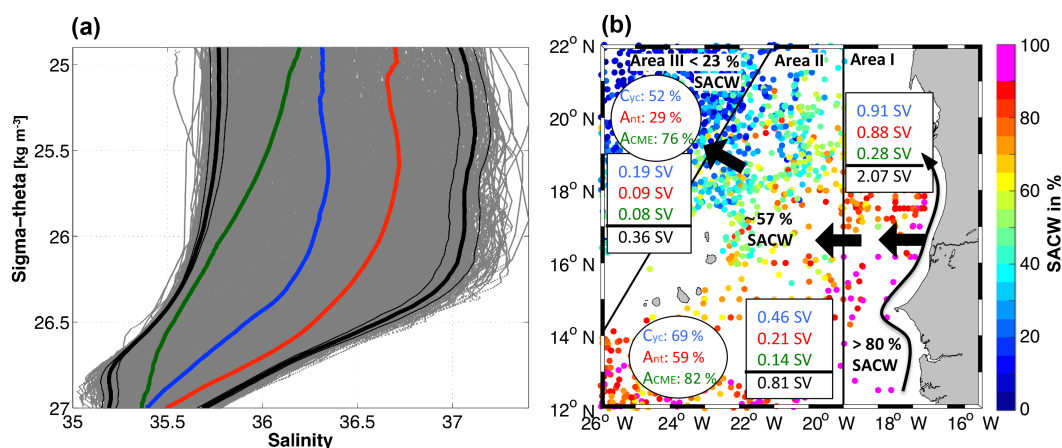
**Figure 16. (a)** $S$-$\sigma_\theta$ diagram with thick and thin black lines indicating mean and standard deviation, respectively, of characteristic SACW and NACW properties derived from the ensemble of profiles taken in the TANWA (gray lines). Mean eddy-dependent water mass properties are given for cyclones (blue line), anticyclones (red line), and ACMEs (green line). **(b)** Percentage of SACW in the upper 350 m as shown for all available profiles (color) and as mean numbers for the three regions: the extended boundary current region (area I), the transition zone (area II), and the subtropical gyre region (area III) that are separated by black straight lines. Numbers in the white circles are the mean percentage of SACW of the composite cyclones (blue), anticyclones (red), and ACMEs (green) in the corresponding areas. The eddy transport of SACW from the boundary current into area I, from area I into area II, and from area II into area III is marked by thick black arrows with transport numbers in Sv given in the white boxes for composite cyclones (blue), anticyclones (red), ACMEs (green), and total transport (black).

with the theoretical and observational findings of the deflection from the $\beta$-drift of anticyclones and cyclones (Chelton et al., 2011). In contrast, ACMEs do not show a significant meridional deflection.

We suspect that the eddy generation is related to instabilities of the eastern boundary current. Eddy generation resulting from interactions of coastal currents with headlands is a well-known process and has been extensively investigated (e.g., Røed, 1980; Klinger, 1994a, b; Pichevin and Nof, 1996; Crawford et al., 2002; Zamudio et al., 2007). Most likely the generation is driven by flow separation at the headlands of the West African coast, triggered by seasonality in the wind forcing. For the northeastern Pacific it has been shown that coastal trapped waves have an impact on the stability of coastal currents and hence eddy generation (Zamudio et al., 2001, 2006, 2007). Such eddy generation mechanisms may explain the high eddy generation in the TANWA found during phases of strongest boundary current velocities. However, the detailed investigation of the generation mechanisms of eddies in the TANWA requires realistic high-resolution modeling and is beyond the scope of the present study.

The maximum swirl velocity of the eddies, $U$, as obtained from the surface geostrophic velocity is about $14.7 \pm 9.5\,\mathrm{km\,d^{-1}}$ indicating a high nonlinearity of the observed eddies, i.e., $U/c > 1$. Due to this nonlinearity the exchange between eddy core and surrounding water is limited and hence they are able to trap water masses and transport them over large distances. In the TANWA the eddies act as transport agents for SACW that is present in the eastern boundary upwelling region toward, and across the CVFZ into the subtropical gyre region, where NACW dominates.

In order to estimate the water mass anomalies transported by the different eddy types, their vertical water mass structures were estimated. Cyclones (anticyclones) are associated with maximum temperature/salinity anomalies of about $-2.42 \pm 1.23\,^{\circ}\mathrm{C}/-0.34 \pm 0.25$ ($1.88 \pm 1.37\,^{\circ}\mathrm{C}/0.25 \pm 0.2$), respectively, most intense just beneath the mixed layer in the depth range 55 to 100 m. With respect to water mass anomalies the ACMEs stand out because their maximum absolute anomaly is more than twice as large (temperature anomalies of $-4 \pm 2.2\,^{\circ}\mathrm{C}$ and salinity anomalies of $+0.72 \pm 0.38$) compared to the corresponding anomalies of cyclones or normal anticyclones. Moreover, their mixed layer depth is found at much shallower depth of 40 to 70 m. Given the fundamentally different anomalies that are associated with the two types of eddies with anticyclonic surface flow (normal anticyclones and ACMEs), a separate treatment of these eddy types seems to be mandatory when discussing eddy transports. This has not been done routinely in the past (e.g., Chaigneau et al., 2009; Zhang et al., 2014) primarily because SLA data alone do not provide the necessary information. Here, we were able to distinguish ACMEs from normal anticyclones by using SSS and SST data in parallel.

The magnitude of the obtained anomalies varies according to the reference data set (background data) being used. We tested nearby in situ data collected outside of eddies as well as different climatological fields (Table 3) as, e.g., in Chaigneau et al. (2009). Using the inferred temperature and salinity anomalies, we were able to calculate the associated heat (salt) transports for the different eddy types. They amount to $-4.6 \times 10^{11}\,\mathrm{W}$ ($-23.15 \times 10^{3}\,\mathrm{kg\,s^{-1}}$) for cyclones, $3.5 \times 10^{11}\,\mathrm{W}$ ($12.9 \times 10^{3}\,\mathrm{kg\,s^{-1}}$) for anticyclones,

and $-4.9 \times 10^{11}$ W ($-29.9 \times 10^3$ kg s$^{-1}$) for ACMEs. Out of the 21 eddies formed each year in the TANWA along the eastern boundary, five dissipate in a band of about 250 km width near the coast and about 16 propagate into the open ocean adding up to an annual eddy net heat (salt) transport of about $50 \times 10^{11}$ W ($-150 \times 10^3$ kg s$^{-1}$). Converting the divergence of the heat transport in the transition zone (area II) into an equivalent surface heat flux we found a cooling of the ocean of $-1.6$ W m$^{-2}$ due to eddy heat transport, which as such balances about 10 % of the net surface heat flux of 17.4 W m$^{-2}$ as obtained from the NOC Surface Flux Dataset (Berry and Kent, 2011).

The TANWA is a crossroad for water masses, with NACW prevailing in the northwest within the ventilated subtropical gyre and SACW in the eastern boundary upwelling region. In order to estimate the dispersal of SACW due to eddies within the TANWA, we analyzed the SACW content in the three different eddy types using the in situ profile data. We found that cyclones contain on average about 16 % more SACW than the surrounding water, ACMEs 21 %, and normal anticyclones do not carry any SACW anomaly. Some ACMEs efficiently isolate their eddy cores from the surrounding waters reaching maximum SACW anomalies of more than 60 %, which indicates a high nonlinearity and coherence of these eddies (Karstensen et al., 2015).

Considering the total tracer transport of the eddies along isopycnals (spiciness), the negative heat and salt anomaly within cyclones and ACMEs results in a mean water mass transport of 2.07 Sv of SACW out of the boundary current region, of which about 0.36 Sv of SACW reach the subtropical gyre region northwest of the Cabo Verde islands. Hence, the SACW transport due to eddies would renew the SACW part of the transition zone located between the extended eastern boundary region and the subtropical gyre region (assuming a layer thickness of 350 m) in about 2.5 years.

This study gives a first insight into the types and characteristics of eddies within the TANWA as well as in the fluxes of heat and salt associated with their westward propagation. Remaining open questions regard the importance of short-lived eddies for the transport of heat and salt (which could not be evaluated due to the resolution of the available data sets), as well as the individual processes responsible for eddy generation. The distinction of anticyclonic rotating eddies into ACMEs and "normal anticyclones" seems to be mandatory for future eddy studies as these two eddy types strongly differ in their efficiency to carry water mass anomalies. Moreover, the biogeochemical responses in ACMEs have been found to be very distinct from normal anticyclones and a sufficient representation of both types of anticyclones in coupled physical-biogeochemical models may be crucial for a realistic simulation of eastern boundary upwelling systems.

**Data availability**

The used satellite data SLA, SST and SSS can be downloaded at http://www.aviso.altimetry.fr/en/data/products/sea-surface-height-products/global/msla-h.html, http://www.remss.com/measurements/sea-surface-temperature/oisst-description and http://catds.ifremer.fr/Products/Available-products-from-CEC-OS/Locean-v2013, respectively. The NOCS Surface Flux is accessible at http://noc.ac.uk/science-technology/earth-ocean-system/atmosphere-ocean/noc-surface-flux-dataset. The Argo float data is freely available at http://www.argodatamgt.org/Access-to-data/Argo-data-selection, the exact same dataset used in the paper is downloaded in January 2015 and available at http://dx.doi.org/10.13155/29825. The assembled shipboard measurements (20 research cruises) and the part of the CVOO mooring data used in this paper are available at https://doi.pangaea.de/10.1594/PANGAEA.860251.

## References

Alpers, W., Brandt, P., Lazar, A., Dagorne, D., Sow, B., Faye, S., Hansen, M. W., Rubino, A., Poulain, P.-M., and Brehmer, P.: A small-scale oceanic eddy off the coast of West Africa studied by multi-sensor satellite and surface drifter data, Remote Sens. Environ., 129, 132–143, 2013.

ARGO: Argo float data, http://www.argodatamgt.org/Access-to-data/Argo-data-selection, 2015.

AVISO: MSLA – H: Maps of Sea Level Anomalies: Height, http://www.aviso.altimetry.fr/en/data/products/sea-surface-height-products/global/msla-h.html, 2015.

Barton, E.: Meanders, eddies and intrusions in the thermohaline front off Northwest Africa, Oceanol. Acta, 10, 267–283, 1987.

Barton, E. D.: The Poleward Undercurrent on the Eastern Boundary of the Subtropical North Atlantic, in: Poleward Flows Along Eastern Ocean Boundaries, edited by: Neshyba, S. J., Mooers, C. N. K., Smith, R. L., and Barber, R. T., Coastal and Estuarine Studies, Springer New York, 82–95, 1989.

Berry, D. I. and Kent, E. C.: Air–Sea fluxes from ICOADS: the construction of a new gridded dataset with uncertainty estimates, Int. J. Climatol., 31, 987–1001, 2011.

Boutin, J., Martin, N., Reverdin, G., Yin, X., and Gaillard, F.: Sea surface freshening inferred from SMOS and ARGO salinity: impact of rain, Ocean Sci., 9, 183–192, doi:10.5194/os-9-183-2013, 2013.

Brandt, P., Bange, H. W., Banyte, D., Dengler, M., Didwischus, S.-H., Fischer, T., Greatbatch, R. J., Hahn, J., Kanzow, T., Karstensen, J., Körtzinger, A., Krahmann, G., Schmidtko, S., Stramma, L., Tanhua, T., and Visbeck, M.: On the role of circulation and mixing in the ventilation of oxygen minimum zones with a focus on the eastern tropical North Atlantic, Biogeosciences, 12, 489–512, doi:10.5194/bg-12-489-2015, 2015.

Carval, T., Keeley, R., Takatsuki, Y., Yoshida, T., Schmid, C., Goldsmith, R., Wong, A., Thresher, A., Tran, A., Loch, S., and Mccreadie, R.: Argo user's manual V3.2, doi:10.13155/29825, 2015.

CATDS: French ground segment for the SMOS Level 3 and 4 data, http://catds.ifremer.fr/Products/Available-products-from-CEC-OS/Locean-v2013, 2015.

Chaigneau, A., Gizolme, A., and Grados, C.: Mesoscale eddies off Peru in altimeter records: Identification algorithms and eddy spatio-temporal patterns, Prog. Oceanogr., 79, 106–119, 2008.

Chaigneau, A., Eldin, G., and Dewitte, B.: Eddy activity in the four major upwelling systems from satellite altimetry (1992–2007), Prog. Oceanogr., 83, 117–123, 2009.

Chaigneau, A., Le Texier, M., Eldin, G., Grados, C., and Pizarro, O.: Vertical structure of mesoscale eddies in the eastern South Pacific Ocean: A composite analysis from altimetry and Argo profiling floats, J. Geophys. Res.-Ocean., 116, C11025, doi:10.1029/2011JC007134, 2011.

Chang, C.-H., Xie, S.-P., Schneider, N., Qiu, B., Small, J., Zhuang, W., Taguchi, B., Sasaki, H., and Lin, X.: East Pacific ocean eddies and their relationship to subseasonal variability in Central American wind jets, J. Geophys. Res.-Ocean., 117, C10001, doi:10.1029/2011JC007315, 2012.

Chelton, D. B., deSzoeke, R. A., Schlax, M. G., El Naggar, K., and Siwertz, N.: Geographical Variability of the First Baroclinic Rossby Radius of Deformation, J. Phys. Oceanogr., 28, 433–460, 1998.

Chelton, D. B., Schlax, M. G., Samelson, R. M., and de Szoeke, R. A.: Global observations of large oceanic eddies, Geophys. Res. Lett., 34, L15606, doi:10.1029/2007GL030812, 2007.

Chelton, D. B., Schlax, M. G., and Samelson, R. M.: Global observations of nonlinear mesoscale eddies, Prog. Oceanogr., 91, 167–216, 2011.

Crawford, W., Cherniawsky, J., Foreman, M., and Gower, J.: Formation of the Haida – 1998 oceanic eddy, J. Geophys. Res.-Ocean., 107, 6-1–6-11, 2002.

Cushman Roisin, B. and Tang, B.: Geostrophic Turbulence and Emergence of Eddies beyond the Radius of Deformation, J. Phys. Oceanogr., 20, 97–113, 1990

Cushman-Roisin, B., Tang, B., and Chassignet, E. P.: Westward Motion of Mesoscale Eddies, J. Phys. Oceanogr., 20, 758–768, 1990.

de Boyer Montégut, C., Madec, G., Fischer, A. S., Lazar, A., and Iudicone, D.: Mixed layer depth over the global ocean: An examination of profile data and a profile-based climatology, J. Geophys. Res.-Ocean., 109, C12003, doi:10.1029/2004JC002378, 2004.

Fu, L.-L. and Ferrari, R.: Observing Oceanic Submesoscale Processes From Space, Eos, T. Am. Geophys. Union, 89, 488–488, 2008.

Garzoli, S. L. and Katz, E. J.: The Forced Annual Reversal of the Atlantic North Equatorial Countercurrent, J. Phys. Oceanogr., 13, 2082–2090, 1983.

Glessmer, M. S., Eden, C., and Oschlies, A.: Contribution of oxygen minimum zone waters to the coastal upwelling off Mauritania, Prog. Oceanogr., 83, 143–150, 2009.

Hagen, E.: A meandering intermediate front North-West off Cape Verde islands, 1985, Oceanogr. Trop., 20, 71–83, 1985.

Hood, E. M. C., Sabine, L., and Sloyan, B. M.: The GO-SHIP repeat hydrography manual: A collection of expert reports and guidelines, IOCCP Rep. 14, 2010.

Hughes, P. and Barton, E. D.: Stratification and water mass structure in the upwelling area off Northwest Africa in April/May 1969, Deep-Sea Res., 21, 6111–628, 1974

Isern-Fontanet, J., García-Ladona, E., and Font, J.: Vortices of the Mediterranean Sea: An Altimetric Perspective, J. Phys. Oceanogr., 36, 87–103, 2006.

Johns, W. E., Zantopp, R. J., and Goni, G. J.: Cross-gyre transport by North Brazil Current rings, Elsev. Oceanogr. Serie., 68, 411–441, 2003.

Jones, P. G. W. and Folkard, A. R.: Chemical oceanographical observations off the coast of North-West Africa, with special reference to the process of upwelling, Rapports et proc's verbaux du Conseil International pour l'Exploration de la Mer, 159, 38–60, 1970

Karstensen, J., Fiedler, B., Schütte, F., Brandt, P., Körtzinger, A., Fischer, G., Zantopp, R., Hahn, J., Visbeck, M., and Wallace, D.: Open ocean dead zones in the tropical North Atlantic Ocean, Biogeosciences, 12, 2597–2605, doi:10.5194/bg-12-2597-2015, 2015.

Klinger, B. A.: Baroclinic eddy generation at a sharp corner in a rotating system, J. Geophys. Res.-Ocean., 99, 12515–12531, 1994a.

Klinger, B. A.: Inviscid Current Separation from Rounded Capes, J. Phys. Oceanogr., 24, 1805–1811, 1994b.

Kostianoy, A. G. and Belkin, I. M.: A Survey of Observations on Emtrathermocline Eddies in the World Ocean, in: Elsev.

Oceanogr. Serie., edited by: Nihoul, J. C. J. and Jamart, B. M., Elsevier, 1989.

Kurczyn, J., Beier, E., Lavín, M., and Chaigneau, A.: Mesoscale eddies in the northeastern Pacific tropical – subbtropical transition zone: Statistical characterization from satellite altimetry, J. Geophys. Res.-Ocean., 117, C10021, doi:10.1029/2012JC007970, 2012.

Kurian, J., Colas, F., Capet, X., McWilliams, J. C., and Chelton, D. B.: Eddy properties in the California current system, J. Geophys. Res.-Ocean., 116, C08027, doi:10.1029/2010JC006895, 2011.

Lázaro, C., Fernandes, M. J., Santos, A. M. P., and Oliveira, P.: Seasonal and interannual variability of surface circulation in the Cape Verde region from 8 years of merged T/P and ERS-2 altimeter data, Remote Sens. Environ., 98, 45–62, 2005.

Liang, J.-H., McWilliams, J. C., Kurian, J., Colas, F., Wang, P., and Uchiyama, Y.: Mesoscale variability in the northeastern tropical Pacific: Forcing mechanisms and eddy properties, J. Geophys. Res.-Ocean., 117, C07003, doi:10.1029/2012JC008008, 2012.

Liu, Y., Dong, C., Guan, Y., Chen, D., McWilliams, J., and Nencioli, F.: Eddy analysis in the subtropical zonal band of the North Pacific Ocean, Deep-Sea Res. Pt. I, 68, 54–67, 2012.

Luyten, J. R., Pedlosky, J., and Stommel, H.: The ventilated thermocline, J. Phys. Oceanogr., 13, 292–309, 1983.

Mittelstaedt, E.: The upwelling area off Northwest Africa – a description of phenomena related to coastal upwelling, Prog. Oceanogr., 12, 307–331, 1983.

Mittelstaedt, E.: The ocean boundary along the Northwest African Coast – circulation and oceanographic properties at the sea-surface, Prog. Oceanogr., 26, 307–355, 1991.

Nencioli, F., Dong, C., Dickey, T., Washburn, L., and McWilliams, J. C.: A Vector Geometry–Based Eddy Detection Algorithm and Its Application to a High-Resolution Numerical Model Product and High-Frequency Radar Surface Velocities in the Southern California Bight, J. Atmos. Ocean. Tech., 27, 564–579, 2010.

NOC: NOC Surface Flux Dataset, http://noc.ac.uk/ science-technology/earth-ocean-system/atmosphere-ocean/ noc-surface-flux-dataset, 2015.

Okubo, A.: Horizontal dispersion of floatable particles in the vicinity of velocity singularities such as convergences, Deep-Sea Res. Oceanogr., 17, 445–454, 1970.

Ould-Dedah, S., Wiseman Jr, W. J., and Shaw, R. F.: Spatial and temporal trends of sea surface temperature in the northwest African region, Oceanol. Acta, 22, 265–279, 1999.

PANGEA: Occurrence and characteristics of mesoscale eddies in the tropical northeast Atlantic Ocean, doi:10.1594/PANGAEA.860251, 2013.

Pantoja, D., Marinone, S., Parés-Sierra, A., and Gómez-Valdivia, F.: Numerical modeling of seasonal and mesoscale hydrography and circulation in the Mexican Central Pacific Modelación numérica de la hidrografía y circulación estacional y de mesoescala en el Pacífico central mexicano, Cienc. Mar., 38, 363–379, 2012.

Pares-Sierra, A., White, W. B., and Tai, C. K.: Wind-driven Coastal Generation of Annual Mesoscale Eddy Activity in the California Current, J. Phys. Oceanogr., 23, 1110–1121, 1993.

Pastor, M. V., Pelegrí, J. L., Hernández-Guerra, A., Font, J., Salat, J., and Emelianov, M.: Water and nutrient fluxes off Northwest Africa, Cont. Shelf Res., 28, 915–936, 2008.

Pegliasco, C., Chaigneau, A., and Morrow, R.: Main eddy vertical structures observed in the four major Eastern Boundary Upwelling Systems, J. Geophys. Res., 120, 6008–6033, 2015

Peña-Izquierdo, J., Pelegrí, J. L., Pastor, M. V., Castellanos, P., Emelianov, M., Gasser, M., Salvador, J., and Vázquez-Domínguez, E.: The continental slope current system between Cape Verde and the Canary Islands, Sci. Mar., 76, 65–78, 2012.

Peña-Izquierdo, J., van Sebille, E., Pelegrí, J. L., Sprintall, J., Mason, E., Llanillo, P. J., and Machín, F.: Water mass pathways to the North Atlantic oxygen minimum zone, J. Geophys. Res.-Ocean., 120, 3350–3372, 2015.

Pichevin, T. and Nof, D.: The eddy cannon, Deep-Sea Res. Pt. I, 43, 1475–1507, 1996.

Polonsky, A. and Artamonov, Y.: North equatorial countercurrent in the tropical Atlantic: Multi-jet structure and seasonal variability, Deutsche Hydrographische Zeitschrift, 49, 477–495, 1997.

REMSS: Microwave OI SST Product Description, http: //www.remss.com/measurements/sea-surface-temperature/ oisst-description, 2015.

Richardson, P. L. and Reverdin, G.: Seasonal cycle of velocity in the Atlantic North Equatorial Countercurrent as measured by surface drifters, current meters, and ship drifts, J. Geophys. Res.-Ocean., 92, 3691–3708, 1987.

Røed, L. P.: Curvature effects on hydraulically driven inertial boundary currents, J. Fluid Mech., 96, 395–412, 1980.

Sangrà, P., Pascual, A., Rodríguez-Santana, Á., Machín, F., Mason, E., McWilliams, J. C., Pelegrí, J. L., Dong, C., Rubio, A., Arístegui, J., Marrero-Díaz, Á., Hernández-Guerra, A., Martínez-Marrero, A., and Auladell, M.: The Canary Eddy Corridor: A major pathway for long-lived eddies in the subtropical North Atlantic, Deep-Sea Res. Pt. I, 56, 2100–2114, 2009.

Schmidtko, S., Johnson, G. C., and Lyman, J. M.: MIMOC: A global monthly isopycnal upper-ocean climatology with mixed layers, J. Geophys. Res.-Ocean., 118, 1658–1672, 2013.

Siedler, G., Zangenberg, N., Onken, R., and Morlière, A.: Seasonal changes in the tropical Atlantic circulation: Observation and simulation of the Guinea Dome, J. Geophys. Res.-Ocean., 97, 703–715, 1992.

Stramma, L. and Isemer, H.-J.: Seasonal variability of meridional temperature fluxes in the eastern North Atlantic Ocean, J. Mar. Res., 46, 281–299, 1988.

Stramma, L. and Siedler, G.: Seasonal changes in the North Atlantic subtropical gyre, J. Geophys. Res.-Ocean., 93, 8111–8118, 1988.

Stramma, L. and Schott, F.: The mean flow field of the tropical Atlantic Ocean, Deep-Sea Res. Pt. II, 46, 279–303, 1999.

Stramma, L., Bange, H. W., Czeschel, R., Lorenzo, A., and Frank, M.: On the role of mesoscale eddies for the biological productivity and biogeochemistry in the eastern tropical Pacific Ocean off Peru, Biogeosciences, 10, 7293–7306, doi:10.5194/bg-10-7293-2013, 2013.

Wooster, W. S., Bakun, A., and McLain, D. R.: Seasonal upwelling cycle along the eastern boundary of the North Atlantic, J. Mar. Res., 34, 131–141, 1976

Weiss, J.: The dynamics of enstrophy transfer in two-dimensional hydrodynamics, Physica D, 48, 273–294, 1991.

Yin, X., Boutin, J., and Spurgeon, P.: First assessment of SMOS data over open ocean: Part I – Pacific Ocean, IEEE T. Geosci. Remote, 50, 1648–1661, 2012.

50

Zamudio, L., Leonardi, A. P., Meyers, S. D., and O'Brien, J. J.: ENSO and eddies on the southwest coast of Mexico, Geophys. Res. Lett., 28, 13–16, 2001.

Zamudio, L., Hurlburt, H. E., Metzger, E. J., Morey, S. L., O'Brien, J. J., Tilburg, C., and Zavala-Hidalgo, J.: Interannual variability of Tehuantepec eddies, J. Geophys. Res.-Ocean., 111, C05001, doi:10.1029/2005JC003182, 2006.

Zamudio, L., Hurlburt, H. E., Metzger, E. J., and Tilburg, C. E.: Tropical wave – induced oceanic eddies at Cabo Corrientes and the María Islands, Mexico, J. Geophys. Res.-Ocean., 112, C05048, doi:10.1029/2006JC004018, 2007.

Zenk, W., Klein, B., and Schroder, M.: Cape Verde Frontal Zone, Deep-Sea Res. Pt. A, 38, Supplement 1, S505–S530, 1991.

Zhang, Z., Wang, W., and Qiu, B.: Oceanic mass transport by mesoscale eddies, Science, 345, 322–324, 2014.

51

_

# 4 Characterization of dead-zone eddies in the tropical Northeast Atlantic Ocean

In order to show that low oxygen eddies occur more frequent than expected the study of chapter 3 is refined and expanded with a special focus on the impact of ACMEs and cyclones on oxygen cycling and budgets in the ETNA region. It could be shown that on average 14 cyclonic eddies and 2 ACMEs each year, with large oxygen anomalies beneath the mixed layer, are propagating from the upwelling region into the unventilated shadow zone and dissipate here. From budget calculations it is shown that the dispersion of the low oxygen mode after decay of the eddies can explain up to 6% of the oxygen consumption in the upper tropical Northeast Atlantic. Furthermore, a surprisingly high number of low oxygen eddies are found even close to the equator (8°N).

Citation: **Schütte, F., J. Karstensen, G. Krahmann, H. Hauss, B. Fiedler, P. Brandt, M. Visbeck and A. Körtzinger: Characterization of "dead-zone eddies" in the Northeast Atlantic Ocean, 2016, Biogeosciences Discussions, doi: 10.5194/bg-2016-33.**

The manuscript is published in Biogeosciences Discussions (unreviewed publication) and was reviewed for Biogeosciences with minor revisions. The candidates contribution to this manuscript is as follows:

The Author did the analysis and produced all the figures. He designed and authored the study from the first draft to the final version.

Biogeosciences

Discussions

Open Access

EGU

# Characterization of "dead-zone" eddies in the tropical Northeast Atlantic Ocean

**Florian Schütte [1], Johannes Karstensen [1], Gerd Krahmann [1], Helena Hauss [1], Björn Fiedler [1],**

**Peter Brandt [1,2], Martin Visbeck [1,2] and Arne Körtzinger [1,2]**

[1] GEOMAR Helmholtz Centre for Ocean Research Kiel, Germany

[2] Christian Albrechts University Kiel, Germany

*Correspondence to*: F. Schütte (fschuette@geomar.de)

**Abstract**

Localized open-ocean low–oxygen dead-zones in the tropical Northeast Atlantic are recently discovered ocean features that can develop in dynamically isolated water masses within cyclonic eddies (CE) and anticyclonic modewater eddies (ACME). Analysis of a comprehensive oxygen dataset obtained from gliders, moorings, research vessels and Argo floats revealed that eddies with low oxygen concentrations at 50-150 m depths can be found in surprisingly high numbers and in a large area (from about 4°N to 22°N, from the shelf at the eastern boundary to 38°W). Minimum oxygen concentrations of about 9 µmol kg$^{-1}$ in CEs and severely suboxic concentrations (< 1 µmol kg$^{-1}$) in ACMEs were observed. In total, 173 profiles with oxygen concentrations below the minimum background concentration of 40 µmol kg$^{-1}$ could be associated with 27 independent "dead-zone" eddies (10 CEs; 17 ACMEs) over a period of 10 years. The eddies' oxygen minimum is located in the eddy core beneath the mixed layer at a mean depth of 80 m. Compared to the surrounding waters, the mean oxygen anomaly between 50 and 150 m depth for CEs (ACMEs) is -38 (-79) µmol kg$^{-1}$. The low oxygen concentration right beneath the mixed layer has been attributed to the combination of high productivity in the eddies' surface waters and the isolation of their cores with respect to lateral oxygen supply. Indeed, eddies of both types feature a cold sea surface temperature anomaly and enhanced chlorophyll concentrations in their center. The locally increased consumption within these eddies represents an essential part of the total consumption in the open tropical Northeast Atlantic Ocean and might be partly responsible for the formation of the shallow oxygen minimum zone. Eddies south of 12°N carry weak hydrographic anomalies in their cores and seem to be generated in the open ocean away from the boundary. North of 12°N, eddies of both types carry anomalously low salinity water of South Atlantic Central Water origin from the eastern boundary upwelling region into the open ocean. Water mass properties and satellite eddy tracking both point to an eddy generation near the eastern boundary.

1

Biogeosciences

Discussions

Open Access

EGU

## 1. Introduction

The Eastern Tropical North Atlantic off northwest Africa (ETNA: 4°N to 22°N and from the shelf at the eastern boundary to 38°W, Fig. 1) is one of the biologically most productive areas of the global ocean (Chavez and Messié, 2009; Lachkar and Gruber, 2012). In particular, the eastern boundary current system close to the Northwest African coast is a region where northeasterly trade winds force coastal upwelling of cold, nutrient rich waters, resulting in high productivity (Messié et al., 2009). The ETNA region is characterized by a weak large-scale circulation (Brandt et al., 2015), but pronounced mesoscale variability (here referred to as eddies) acting as a major transport process between coastal waters and the open ocean (Schütte et al., 2015; Thomsen et al., 2015). In the ETNA, open ocean eddies with particularly high South Atlantic Central Water (SACW) fractions in their cores have been found offshore, where typically North Atlantic Central Water (NACW) dominates (Karstensen et al., 2015; Pastor et al., 2008). Due to low lateral mixing, SACW from the generation regions near the coast is trapped in the eddies' cores and transported offshore over long distances (Schütte et al., 2015). The impact of the eddy transport on the coastal productivity was investigated by Lachkar and Gruber (2012), who were able to show that high (low) eddy driven transports of nutrient-rich water from the shelf into the open ocean results in lower (higher) biological production on the shelf. Besides acting as export agents for coastal waters, coherent eddies in the ETNA have been reported to establish and maintain a sealed ecosystem (Fiedler et al., 2016; Hauss et al., 2015; Karstensen et al., 2015; Löscher et al., 2015). Coherent/isolated mesoscale eddies can exist over periods of several months or even years (Chelton et al., 2011). Enhanced vertical fluxes of nutrients and the dynamical isolation of the eddy interior from surrounding waters create very distinct biogeochemical conditions within these eddies, that can be very different from the surrounding water masses (Fiedler et al., 2016). Hypoxic to suboxic conditions have been observed in cyclonic eddies (CEs) and anticyclonic modewater eddies (ACMEs) caused by a combination of eddy dynamics and biogeochemical cycling within the eddies (Karstensen et al., 2015). The appearance of the low oxygen concentrations at shallow depth (about 50 to 100 m, just beneath the mixed layer) has been attributed to the combination of high productivity in the surface waters of the eddy, enhanced respiration of sinking organic material at subsurface depth and the isolation of the eddy core from the surrounding conditions. As such, these eddies resemble an environment similar to the "dead-zone" formation in coastal areas and lakes and therefore have been termed "dead-zone" eddies (Karstensen et al., 2015).

The ventilation and consumption processes of thermocline waters in the ETNA result in two separate oxygen minima (Fig. 1b): a shallow one with a core depth of about 80 m and a deep one at a core depth of about 450 m (Brandt et al., 2015; Karstensen et al., 2008). The deep minimum is the core of the OMZ and is primarily created by sluggish ventilation of the respective isopycnals (Luyten et al., 1983; Wyrtki, 1962). It extends from the eastern boundary into the open ocean and is located in the so-called shadow zone, with the more energetic circulation of the subtropical gyre in the north and the equatorial region in the south (Karstensen et al., 2008; Luyten et al., 1983). The shallow oxygen minimum intensifies from the equator towards the north with minimal values near the coast at about 20°N (Brandt et al., 2015) (Fig. 1a). It is assumed that the shallow OMZ originates from enhanced biological productivity and an increased respiration associated with sinking particles in the water column (Brandt et al., 2015; Karstensen et al., 2008; Wyrtki, 1962). In this paper we draw a connection between the enhanced consumption and associated low-oxygen concentration in "dead-zone" eddies and the formation of the regional observed shallow oxygen minimum zone. To assess the influence of "dead-zone" eddies on the oxygen budget of the upper water column, a sub-region between the ventilation pathways of the subtropical gyre and the zonal current bands of the equatorial Atlantic was chosen. This region includes the most pronounced

2

1    shallow oxygen minimum and is in the following referred to as shallow oxygen minimum zone (SOMZ, Fig. 1a).

2    The probability of "dead-zone" eddy occurrence per year is more or less evenly distributed in the ETNA (Fig.
3    1a). Particularly in the SOMZ there seems to be neither a distinctly high nor an explicitly low "dead-zone" eddy
4    occurrence. However, due to the absence of other ventilation pathways, the influence of "dead-zone" eddies on
5    the shallow oxygen minimum budget may be elevated and a closer examination worth the effort. The eddies in
6    this study were identified in 19 years of sea level anomaly (SLA) and sea surface temperature (SST) data based
7    on methods published by Schütte et al. (2015). After their formation near the eastern boundary, Rossby wave
8    dynamics and the basin scale circulation force eddies in the SOMZ to generally propagate westwards. The
9    dynamically protected eddy cores transport temperature, salinity, nutrient, carbon and oxygen conditions of their
10    formation region far offshore. At about 100 m depth, biogeochemical processes further increase the nutrient and
11    oxygen anomalies with respect to the surrounding waters. In order to further investigate the physical,
12    biogeochemical and ecological structure of dead-zone eddies, an interdisciplinary field study was carried out in
13    the ETNA, north of Cape Verde, using dedicated ship, mooring and glider surveys supported by satellite and
14    Argo float data. The analysis of the field study data revealed surprising anomalies in eddy meta-genomics
15    (Löscher et al., 2015), zooplankton (Hauss et al., 2015), carbon chemistry (Fiedler et al., 2016) and nitrogen
16    cycling (Karstensen et al. 2016). Furthermore, analyses of particle flux time series, using sediment trap data from
17    the Cape Verde Ocean Observatory (CVOO), were able to confirm the impact of highly productive dead-zone
18    eddies on deep local export fluxes (Fischer et al., 2015).

19    In this paper, we determine the average characteristics of "dead-zone" eddies in ETNA, addressing their
20    hydrographic features as well as occurrence, distribution, generation and frequency. Based on oxygen anomalies
21    and eddy coverage we estimate their contribution to the oxygen budget of the SOMZ. The paper is organized as
22    follows. Section 2 addresses the different in-situ measurements, satellite products and methods we use. Our
23    results are presented in section 3, discussed in section 4 and summarized in section 5.
24

25    **2. Data and methods**

26    **2.1 In-situ data acquisition**
27    For our study we employ a quality-controlled database combining shipboard measurements, mooring data and
28    Argo float profiles as well as autonomous glider data in ETNA. For details on the structure and processing of the
29    database, see Schütte et al. (2015). For this study we extended the database in several ways. The region was
30    expanded to now cover the region from 0° to 22° N and 13° W to 38° W (see Fig. 2). We then included data
31    from five recent ship expeditions (RV Islandia ISL_00314, RV Meteor M105, M107, M116, M119), which
32    sampled extensively within the survey region. Data from the two most recent deployment periods of the Cape
33    Verde Ocean Observatory (CVOO) mooring from October 2012 to September 2015 as well as Argo float data
34    for the years 2014 and 2015 were also included. Furthermore, oxygen measurements of all data sources were
35    collected and integrated into the database. As last modification of the database we included data from four
36    autonomous gliders that were deployed in the region and sampled two ACMEs and one CE. Glider IFM11
37    (deployment ID: ifm11_depl01) was deployed March 13, 2010. It covered the edge of an ACME on March 20
38    and recorded data in the upper 500 m. Glider IFM05 (deployment ID: ifm05_depl08) was deployed June 13,
39    2013. It crossed a CE on July 26 and recorded data down to 1000 m depth. IFM12 (deployment ID:

3

Biogeosciences
Discussions

Open Access

EGU

1    ifm12_depl02) was deployed January 10, 2014 north of the Cape Verde island São Vicente and surveyed

2    temperature, salinity and oxygen to 500 m depth. IFM13 (deployment ID: ifm13_depl01) was deployed on

3    March 18, 2014 surveying temperature, salinity and oxygen to 700 m depth. IFM12 and IFM13 were able to

4    sample three complete sections through an ACME. All glider data were internally recorded as a time series along

5    the flight path, while for the analysis the data was interpolated onto a regular pressure grid of 1 dbar resolution

6    (see also Thomsen et al., 2015). Gliders collect a large number of relatively closely spaced slanted profiles. To

7    reduce the number of dependent measurements, we limited the number of glider profiles to one every 12 hours.

8    The processing and quality control procedures for temperature and salinity data from shipboard measurements,

9    mooring data and Argo floats has already been described by Schütte et al. (2015). The processing of the gliders'

10   temperature and salinity measurements is described in Thomsen et al. (2015). Oxygen measurements of the

11   shipboard surveys were collected with Seabird SBE 43 dissolved oxygen sensors attached to Seabird SBE 9plus

12   or SBE 19 conductivity-temperature-depth (CTD) systems. Sampling and calibration followed the procedures

13   detailed in the GO-SHIP manuals (Hood et al., 2010). The resulting accuracies were $\leq$1.5 $\mu$mol kg$^{-1}$. Within the

14   CVOO moorings, a number of dissolved oxygen sensors (Aanderaa optodes type 3830) were used. The optodes

15   were calibrated at dedicated CTD casts and in the laboratory with water featuring 0% air saturation before

16   deployment and after recovery following the procedures described by Hahn et al. (2014). We estimate their

17   accuracies at <3 $\mu$mol kg$^{-1}$. A number of the Argo floats were equipped with oxygen sensors. As a full

18   calibration of these is usually not available, the measured data based on the factory calibration was included into

19   the database after a strict visual control removing suspicious profiles. The different manufacturers of Argo float

20   oxygen sensors specify their accuracy at least better than 8 $\mu$mol kg$^{-1}$ or 5%, whichever is larger. Note that early

21   optodes can be significantly outside of this accuracy range, showing offsets of 15-20 $\mu$mol kg$^{-1}$, in some cases

22   even higher. All four autonomous gliders were equipped with Aanderaa optodes which were calibrated on

23   dedicated CTD casts following the procedures of Hahn et al. (2014). As gliders move through the water column

24   the oxygen measurements are not as stable as those from moored optodes analyzed by Hahn et al. (2014). We

25   thus estimate their accuracy to about 3 $\mu$mol kg$^{-1}$.

26

27   As final result the assembled in-situ database of the ETNA contains 15059 independent profiles (Fig. 2). All

28   profiles include temperature, salinity and pressure measurements while some 38.5% include oxygen

29   measurements. The total number is composed of 13% shipboard, 22.5% CVOO mooring, 63% Argo float and

30   1.5% glider profiles. To determine the characteristics of different eddy types from the assembled profiles, we

31   separated them into anticyclones, CEs, ACMEs and the "surrounding area" not associated with eddy-like

32   structures following the approach of Schütte et al. (2015).

33

34   **2.2 Satellite data**

35   We detected and tracked eddies following the procedures described in Schütte et al. (2015). In brief we used the

36   delayed-time reference dataset of Sea Level Anomaly (SLA; version 2014). The data is produced by

37   Ssalto/Duacs and distributed by AVISO (Archiving, Validation, and Interpretation of Satellite Oceanographic),

38   with support from CNES [http://www.aviso.altimetry.fr/duac/]. We used the multi-mission product, which is

39   mapped on a 1/4° x 1/4° Cartesian grid and has a temporal resolution of one day. The anomalies were computed

40   with respect to a twenty-year mean. Data of the SLA and of the geostrophic velocities, derived from the SLA

41   and also provided from AVISO, for the period January 1998 to December 2014 were chosen.

4

1   For Sea Surface Temperature (SST) the dataset "Microwave Infrared Fusion Sea Surface Temperature" from

2   Remote Sensing Systems (www.remss.com) is used. It is a combination of all operational microwave (MW)

3   radiometer SST measurements (TMI, AMSR-E, AMSR2, WindSat) and infrared (IR) SST measurements (Terra

4   MODIS, Aqua MODIS). The dataset thus combines the advantages of the MW data (through-cloud capabilities)

5   with the IR data (high spatial resolution). The SST values are corrected using a diurnal model to create a

6   foundation SST that represents a 12-noon temperature (www.remss.com). Daily data with 9 km resolution from

7   January 2002 to December 2014 is considered.

8   For sea surface chlorophyll data (Chl) we use the MODIS/Aqua Level 3 data available at

9   http://oceancolor.gsfc.nasa.gov provided from the NASA. The data is measured via IR and is therefore cloud

10  cover dependent. Daily data mapped on a 4 km grid from January 2006 to December 2014 is selected.

11

12  **2.3 "Dead-zone" eddy detection and surface composites**

13  In order to verify whether low oxygen concentrations (<40 $\mu$mol kg$^{-1}$) at shallow depth (above 200 m) are

14  associated with eddies we applied a two step procedure: First, all available oxygen measurements of the

15  combined in-situ datasets are used to identify low oxygen values. Next, the satellite data based eddy detection

16  results (Schütte et al., 2015) were matched in space and time with the location of anomalously low oxygen

17  profiles. In this survey the locations of 173 of the 180 low oxygen profiles coincide with surface signatures of

18  mesoscale eddies. Schütte et al. (2015) showed that ACMEs can be distinguished from normal anticyclonic

19  eddies by considering the SST anomaly (cold in case of ACMEs) and SSS anomaly (fresh in case of ACMEs) in

20  parallel to the respective SLA anomaly. The satellite based estimates of SLA and SST used in this study are

21  obtained by subtracting low-pass filtered (cutoff wavelength of 15° longitude and 5° latitude) values from the

22  original data to exclude large-scale variations and preserve only the mesoscale variability (see Schütte et al. 2015

23  for more detail). All eddy-like structures with low oxygen profiles are visually tracked in the filtered SLA

24  (sometimes SST data) back- and forward in time in order to obtain eddy propagation trajectories. The surface

25  composites of satellite-derived SLA, SST and Chl data consist of 150 km x 150 km snapshots around the

26  obtained eddy centers. For construction of the composites the filtered SLA and SST is used as well.

27

28  **2.4 Reconstruction of oxygen concentrations in "dead-zone" eddy cores**

29  About 30 % of the profiles from the combined in-situ dataset conducted in CEs or ACMEs do not have oxygen

30  measurements available. However, we are only interested in oxygen measurements in isolated CE or ACME

31  cores. These isolated eddy cores carry anomalously low salinity SACW of coastal origin in their cores, while the

32  surrounding waters are characterized by an admixture of more saline NACW (Schütte et al., 2015). The fresh

33  cores indicate a generation site near the coast and strong isolation due to reduced lateral mixing with the more

34  saline surrounding waters during their westward migration into the open ocean. Due to this strong isolation and

35  an intensified biogeochemical cycling within the eddies, the oxygen content in the eddy cores decreases rapidly

36  (Karstensen et al., 2015). The salinity-$\sigma_0$ diagram (Fig. 3a) based on the profiles with oxygen measurements

37  indicates that low saline waters in the eddy cores are related to low oxygen concentrations (considering here only

38  eddies which are located in the open ocean, west of 19°W). To compensate for missing oxygen measurements a

39  salinity-oxygen relation in combination with isolation time and associated oxygen consumption within the eddy

40  cores was derived. To assess the consumption within the eddies, an average oxygen utilization rate per day based

41  on the available oxygen measurements is derived for both eddy types. In detail, the distance of the eddy to the

5

Biogeosciences

Discussions

Open Access

EGU

1   eastern boundary and the associated propagation time is derived We assume a mean westward eddy propagation

2   of 3 km d$^{-1}$ (Schütte et al., 2015). Further we assume a typical oxygen profile at the eastern boundary (mean of

3   all profiles east of 18°W) as initial oxygen condition in the eddy core (see Fig. 3b). The mean eddy consumption

4   rate is now the difference from the initial oxygen condition and the actual oxygen concentration in the eddy core

5   divided by the propagation time. If an eddy without oxygen measurements and SACW water mass characteristics

6   (less saline and colder water than the surrounding water) is identified we assume a strong isolation of the eddy.

7   Using the consumption rates of isolated CEs and ACMEs and the associated propagation time a reconstructed

8   oxygen value within the eddy could be derived. Using this method, oxygen values could be constructed for all

9   profiles within CEs or ACMEs, even if only salinity and temperature measurements are available. To validate

10  the method we reconstruct oxygen profiles for the eddies with available oxygen measurements and compared

11  them (Fig. 3b). An average uncertainty of ±12 (16) μmol kg$^{-1}$ is associated with the reconstructed oxygen values

12  (Fig. 3c) of CEs (ACMEs). This uncertainty is even higher in the core region of the eddies. Depending on the

13  status of isolation of the eddy lateral mixing could take place, which is assumed to be zero in our method.

14  However, this approach enables us to enlarge the oxygen dataset by 30%. In this paper the reconstructed oxygen

15  values are only used for the derivation of the mean vertical oxygen anomaly.

16

17  **2.5 Mean vertical oxygen anomaly of "dead-zone" eddies and their impact on the SOMZ**

18  To illustrate mean oxygen anomalies for CEs and ACMEs as a function of depth and radial distance, all oxygen

19  profiles (observed and reconstructed) were sorted with respect to a normalized distance, which is defined as the

20  actual distance of the profile from the eddy center divided by the radius of the eddy (the shape and thus the

21  radius of the eddy are gained from the last closed contour of the geostrophic surface velocity). The oxygen

22  profiles were grouped and averaged onto a grid of 0.1 increments between 0 and 1 of the normalized radial

23  distance. Finally a running mean over three consecutive horizontal grid points was applied. A mean oxygen

24  anomaly for the CEs and the ACMEs was constructed by the comparison with the oxygen concentrations in the

25  surrounding waters. To illustrate the influence of the reconstructed oxygen values, the mean vertical oxygen

26  anomaly is also constructed based only on original measured oxygen values, both anomalies are shown for

27  comparison.

28

29  An oxygen deficit profile due to "dead-zone" eddies in the SOMZ is derived by building an oxygen anomaly of

30  each eddy type on density surfaces ($O_2'$). The derived anomalies are multiplied by the mean number of eddies

31  dissipating in the SOMZ per year ($n$) and weighted by the area of the eddy compared to the total area of the

32  SOMZ ($A_{SOMZ}$ = triangle in Fig. 1a). Differences in the mean isopycnal layer thickness of each eddy type and

33  the SOMZ are considered by multiplying the result with the ratio of the mean Brunt-Väisälä frequency (N$^2$)

34  outside and inside the eddy, resulting in an apparent oxygen utilization rate per year (μmol kg$^{-1}$ y$^{-1}$) due to "dead-

35  zone" eddies in the SOMZ on density layers:

36

$$aOUR = nO_2' \frac{\pi r_{Eddy}^2 N_{SOMZ}^2}{A_{SOMZ} N_{Eddy}^2}$$

37

38  where $r_{Eddy}$ is the mean radius of the eddies.

39

6

Biogeosciences

Discussions

EGU

Open Access

## 3. Results

### 3.1 Low oxygen eddy observation from in-situ data

Several oxygen measurements with anomalously low oxygen concentrations for the ETNA region (below 40 $\mu$mol kg$^{-1}$ at shallow depth) could be identified from Argo floats, ship surveys, glider missions and from the CVOO mooring (Fig. 4). In total, 27 independent eddies with oxygen values <40 $\mu$mol kg$^{-1}$ in the upper 200 m were sampled with 173 profiles from 25 different platforms (Tab. 1). Almost all of the observed anomalous low oxygen values could be associated with mesoscale structures at the sea surface (CEs or ACMEs) from satellite data.

In-situ measurements for meridional velocity, temperature and oxygen of the CVOO mooring during the westward passage of one CE and one ACME with low oxygen concentrations are chosen to show examples of the vertical structure of the two different eddy types based on temporally high resolution data (Fig. 5). From October 2006 to December 2006 (Fig. 5a), a 65 km diameter CE passed the CVOO mooring position on a westward trajectory. At its closest the eddy center was located 20 km north of the CVOO mooring. The meridional velocities show a strong cyclonic rotation (first southward, later northward) with velocity maxima between the surface and 50 m depth at the edges of the eddy. In the core of the CE, the water mass was colder and less saline (not shown) than the surrounding water, the mixed layer (ML) depth is reduced and the isopycnals are shifted upwards. The oxygen content of the eddy core was decreased with values around 60 $\mu$molkg$^{-1}$ at 115 m depth (or at the isopycnal surface 26.61 kg m$^{-3}$) compared to surrounding waters, which have a mean ($\pm$ 1 standard deviation) oxygen content of 113 ($\pm$38) $\mu$mol kg$^{-1}$ at around 150 m depth or 26.60 ($\pm$0.32) kg m$^{-3}$ during the mooring period between 2006 to 2014.

From January 2007 to March 2007 (Fig. 5b), an ACME passed the CVOO mooring position. The core of the westward eddy passed 13 km to the north of the mooring. The velocity field shows strong subsurface anticyclonic rotation at the depths of the core between 80-100 m depth. In contrast to other typical anticyclonic eddies, the water mass in the eddy core of the ACME is colder and less saline (not shown) than the surrounding waters. The isopycnals above the core are elevated resulting in shallower MLs both resembling a cyclone. Beneath the core, the isopycnals are strongly depressed as in a "normal" anticyclone. Thus, dynamically this resembles a mode water anticyclone, an eddy type, which is e.g. well-known from the Mediterranean outflow regime (Bower et al., 1995; Richardson et al., 1989). In contrast to the historical known mode water anticyclones, the eddy core is shallower (just beneath the ML) and therefore the oxygen concentration is reduced. The oxygen content in the eddy's core recorded from the CVOO mooring is strongly decreased with values around 19 $\mu$mol kg$^{-1}$ at 123 m depth (or 26.50 kg m$^{-3}$) compared to the surrounding waters (113 ($\pm$38) $\mu$mol kg$^{-1}$). Within the entire time series, the CVOO mooring recorded the passage of several ACMEs with even lower oxygen concentrations (for more information see Karstensen et al. (2015) or Table 1).

### 3.2 Combining in-situ and satellite data for "dead-zone" eddy detection in the ETNA

Combining the location and time of in-situ detection of low oxygen eddies with the corresponding SLA satellite data reveals a clear link to the surface manifestation of mesoscale structures, CE and ACMEs likewise (Fig. 4). Composite surface signatures for SLA, SST and Chl from all identified anomalous low oxygen eddies from the in-situ data are shown in Figure 6. The composites for ACMEs are based on 17 independent eddies and on 922 surface maps. The detected ACMEs are characterized by an elevation of SLA, which is associated with an anticyclonic rotation at the sea surface. The magnitude of the SLA displacement is moderate compared to normal

1    anticyclones and CEs (Schütte et al., 2015). More distinct differences to normal anticyclones are the cold-water

2    anomaly and the elevated Chl concentrations in the eddy center of the ACMEs. Normal anticyclones are

3    associated with elevated SST and reduced Chl concentrations. Through a combination of the different satellite

4    products (SLA, SST, SSS) it is possible to determine "dead-zone" eddies from satellite data alone (further details

5    in Schütte et al. (2015)).

6    The composite mean surface signature for "dead-zone" CEs is based on 10 independent eddies and on 755

7    surface maps. The CEs are characterized by a negative SLA and SST anomaly. The observed negative SST

8    anomaly of the "dead-zone" CEs is twice as large (core value CE: -0.12 ±0.2 °C; core value ACME: -0.06 ±0.2

9    °C) as the corresponding anomaly of the ACMEs. The Chl concentration in the eddy center is also higher for

10   CEs compared to ACMEs (core value CE: 0.35 ±0.22 log mg m$^{-3}$; core value ACME: 0.21 ±0.17 log mg m$^{-3}$).

11   Note, that we only considered the measured low oxygen ACMEs and CEs from Table 1 to derive the composites.

12

13   Using the eddy-dependent surface signatures in SLA, SST and Chl the "dead-zone" eddies could be tracked and

14   an eddy trajectory could be derived (e.g. Fig. 4). All detected eddies were propagating westward into the open

15   ocean. North of 12°N, most of the eddies set off near the coast, whereas south of 12°N the eddies seem to be

16   generated in the open ocean. Detected CEs have a tendency to deflect poleward on their way into the open ocean

17   (Chelton et al., 2011), whereas ACMEs seem to have no meridional deflection. However, during their westward

18   propagation the oxygen concentration within the "dead-zone" eddy cores decreases with time. Using the

19   propagation time and an initial coastal oxygen profile (Fig. 3b) a mean apparent oxygen utilization rate per day

20   could be derived for all sampled eddies (Fig. 7). On average the oxygen concentration in the core of an isolated

21   CE (ACME) decreases by about 0.10 (0.19) ± 0.12 (0.08) µmol kg$^{-1}$ d$^{-1}$.

22

23   **3.4 Mean oxygen anomalies from "dead-zone" eddies in the ETNA**

24   In Figure 8 we compare the mean oxygen anomalies based purely on observations with those based on the

25   extended profile database including observed and reconstructed oxygen values (see section 2.4). It shows the

26   mean oxygen anomalies against the surrounding water for CE (Fig. 8a) and ACME (Fig. 8b) versus depth and

27   normalized radial distance. On the left side of each panel the anomaly is based on the in-situ and reconstructed

28   oxygen values (736 oxygen profiles; 575 in CEs; 161 in ACMEs), whereas on the right side the anomaly is based

29   only on the in-situ oxygen measurements (504 oxygen profiles; 395 in CEs; 109 in ACMEs). The distinct mean

30   negative oxygen anomalies for CEs and ACMEs indicate the low oxygen concentrations in the core of both eddy

31   types compared to the surrounding water. The strongest oxygen anomalies are located in the upper water

32   column, just beneath the ML. CEs feature maximum negative anomalies of around -100 µmol kg$^{-1}$ at around 70

33   m depth in the eddy core, with a slightly more pronounced oxygen anomaly on the left part including the

34   reconstructed values compared to the right part based only on observed oxygen concentrations (Fig. 8a). This is

35   contrary for the ACME with stronger oxygen anomalies on the right part than on the left (Fig. 8b). Both methods

36   deliver maximum negative anomalies of around -120 µmol kg$^{-1}$ at around 100 m depth in the ACME core. At

37   that depth, the diameter of the mean oxygen anomaly is about 100 km for ACMEs and 70 km for CEs. Beneath

38   150 m depth, magnitude and diameter of the oxygen anomalies decrease rapidly for both eddy types. Figure 8c is

39   based on both, the in-situ and reconstructed oxygen values, and shows the horizontal mean oxygen anomaly

40   profile of each eddy type against depth obtained by horizontally averaging the oxygen anomalies shown in Fig.

41   8a,b. The maximum anomalies are -100 µmol kg$^{-1}$ at around 90 m for ACMEs and -55 µmol kg$^{-1}$ at around 70 m

8

Biogeosciences
Discussions

Open Access

EGU

1   for cyclones. Both eddy types have the highest oxygen variance directly beneath the ML (in the eddy core) or

2   slightly above the eddy core. The oxygen anomaly (and associated variance) decreases rapidly with depth

3   beneath the eddy core and is smaller than around -10 ± 10 µmol kg$^{-1}$ beneath 350 m for both eddy types.

4

5   **4. Discussion**

6   The minimum oxygen concentrations for ETNA between the surface and 200 m depth (Fig. 1) from the MIMOC

7   climatology (Schmidtko et al., 2013) illustrates that oxygen values below 50 µmol kg$^{-1}$ are not a common feature

8   of the large scale oxygen field in the ETNA. However, oxygen concentrations below the canonical value of 40

9   µmol kg$^{-1}$ (Stramma et al., 2008) are found in oxygen profiles taken from various observing platforms (ships,

10  moorings, floats) and could nearly entirely be co-located with mesoscale features. In the current analysis we

11  could identify 27 independent low oxygen eddies (10 CEs and 17 ACMEs) from our database. Eddies are

12  defined as coherent structures with a lifetime of several weeks to more than a year (Chelton et al., 2007).

13  Although the ETNA is expected to have a low activity of long-lived eddies (Chaigneau et al., 2009; Chelton et

14  al., 2011), we could identify 234 CEs and 18 ACMEs per year in the ETNA with a radius > 45 km and a tracking

15  time of more than 3 weeks. For eddy detection we used an algorithm based on the combination of the Okubo-

16  Weiß method and a modified version of the geometric approach from Nencioli et al. (2010) with an adjusted

17  tracking for the ETNA (for more information see Schütte et al. (2015)). Tracking ACMEs in SLA data was

18  rather difficult due to the small signal to noise ratio (not the case for the CEs), which led to a failure of the

19  automatic tracking algorithms in most cases. However, we used other satellite data in parallel (Fig. 6). As

20  discussed in Schütte et al. (2015) in case of coincidence of low SST and low sea surface salinity (not shown

21  here) as well as intense near surface phytoplankton blooms (Karstensen et al. 2015) we expected a high

22  likelihood that a low oxygen eddy was present. Note, all tracks of ACMEs and CEs shown in Figure 4 were

23  visually verified. The weak surface signature of ACMEs suggests that their frequency of occurrence might be

24  underestimated (e.g. in Schütte et al. (2015) but also in other studies). Moreover, we identified a few occurrences

25  of ACMEs based on shipboard ADCP as well as hydrographic measurements (e.g. during the research cruises of

26  Ron Brown 2009 and Meteor 119) that did not have a significant SLA signature.

27  Anticyclonic rotating eddies with a low oxygen core are only observed for modewater type anticyclones (i.e.

28  ACMEs), but not for "normal" anticyclonic eddies. We could show here that the ACMEs and CEs with a low

29  oxygen core tend to have also anomalous water mass properties (cold and fresh). In summary, the heat, salt, and

30  oxygen anomalies of ACMEs in the ETNA are fundamentally different (cold/fresh) from normal anticyclones

31  (warm/salty) (Schütte et al. 2015). Consequently a further distinction into the two types of anticyclonic eddies in

32  global (Chelton et al., 2011; Zhang et al., 2013) as well as regional eddy assessments is necessary.

33  It has been shown that the low-oxygen eddies in the ETNA could be separated into two different regimes, north

34  and south of 12°N (Fig. 4). The eddies north of 12°N are generally generated along the coast and in particular

35  close to the headlands along the coast. Schütte et al. (2015) suggested that these eddies are generated from

36  instabilities of the northward directed alongshore boundary current. However, the detailed formation processes

37  need to be further investigated. The formation of the eddies south of 12°N needs to be further investigated as

38  well, because their generation, dynamics and water mass anomalies are different from the ACMEs in the north.

39  The southern eddies do transport low-oxygen anomalies, but do not originate from a coastal boundary upwelling

40  system. Following the trajectories it seems that the ACMEs are generated in the open ocean between 5°N and

41  7°N. The generation mechanism could be related to the presence of strong tropical instabilities in that region

9

Biogeosciences

Discussions

Open Access

EGU

1   (Menkes et al., 2002; von Schuckmann et al., 2008).

2   As the "northern" and "southern" eddies have different generation mechanisms and locations as well as different

3   characteristics they need to be discussed separately. The core of the eddies generated north of 12°N is

4   characterized by less saline and cold SACW (Schütte et al., 2015) and thereby forms a strong hydrographic

5   anomaly against the background field. On the contrary, the core of the eddies generated south of 12°N does not

6   show any significant hydrographic anomalies. However, both eddy regimes feature eddies which generate during

7   their westward propagation locally open ocean upwelling systems with high productivity at the surface and

8   enhanced respiration beneath the ML (Karstensen et al., 2016). In combination with the eddy dynamics and its

9   associated isolation of the CE (ACME) core, the oxygen content is decreasing on average by about 0.10 (0.19) ±

10  0.12 (0.08) µmol kg$^{-1}$ d$^{-1}$ in the ETNA. The apparent oxygen utilization rate (aOUR) is based on 504 oxygen

11  measurements in CEs and ACMEs. It is in the range of recently published aOUR estimates for CEs (Karstensen

12  et al., 2015) and ACMEs (Fiedler et al., 2016) based on single measurements in "dead-zone" eddies. An

13  important point regarding the method to derive the aOURs is the initial coastal oxygen concentration, which is

14  highly variable in coastal upwelling regions (Thomsen et al., 2015). However, all observed CEs or ACMEs

15  contain a negative oxygen anomaly, partly because they transport water with initial low oxygen concentrations

16  from the coast into the open ocean and additionally because the oxygen consumption in the eddies is more

17  intense then in the surrounding waters (Karstensen et al. 2015a, Fiedler et al. 2015). Due to the smaller Coriolis

18  parameter closer to the equator the southern eddies should be more short-lived compared to eddies north of 12°N

19  (Chelton et al., 2011). This would suggest that, to achieve similarly strong negative oxygen anomalies, the

20  oxygen consumption in the eddies south of 12°N must be even stronger than in the ACMEs further north.

21  Pronounced productivity patterns in tropical instability waves and vortices have been reported in the past

22  (Menkes et al., 2002), but were not connected to low oxygen eddies before.

23

24  The mean oxygen profiles from the coast and inside of all CEs and ACMEs (Fig. 3b) indicate no pronounced

25  oxygen difference beneath 250 m depth. The largest anomalies have been observed in the eddy cores at around

26  100 m depth (Fig. 8). As a result of the dynamic structure, the core water mass anomalies of the ACMEs are

27  more pronounced than the one of the CE (Karstensen et al. 2016) and consequently the oxygen anomalies are

28  stronger. This is supported by the differences in the oxygen anomaly based on the measured plus reconstructed

29  and the measured oxygen values. The reconstruction of oxygen values assumes a complete isolation of the eddy

30  core. The left side of Figure 8, which includes the reconstructed oxygen values, features a larger oxygen

31  anomaly than the right side based on measured oxygen values only. Consequently the CEs seem to be not

32  completely isolated and the evolving oxygen anomaly is affected by low lateral mixing. On the contrary, the

33  oxygen anomaly of ACMEs is smaller for the reconstruction than for the measured oxygen values. It seems that

34  the ACMEs are more effectively isolated resulting in enhanced apparent consumption in the ACME core. One

35  should mention, however, that one possible error source of the reconstructed oxygen values could be the

36  assumption of a linear decrease of oxygen with time.

37

38  In the following, an estimate of the contribution of the negative oxygen anomalies of "dead-zone" eddies to the

39  oxygen distribution of the SOMZ is presented. The SOMZ is located west of the boundary current coastal

40  region, south of the subtropical gyre region and north of the zonal equatorial current bands. It covers the

41  unventilated eastern boundary shadow zone and thereby is the region of the most pronounced shallow oxygen

10

Biogeosciences
Discussions

Open Access

EGU

1    minimum (see Fig. 1a). The satellite-based eddy tracking reveals that on average 14 (2) CEs (ACMEs) each year

2    are propagate from the upwelling system near the coast into the SOMZ and dissipate here. By deriving the

3    oxygen anomaly on density surfaces an oxygen loss profile due to "dead-zone" eddies in the SOMZ is derived

4    (Fig. 9). Note that due to the lower oxygen values within the eddies compared to the surrounding waters in the

5    SOMZ, the release of negative oxygen anomalies to the surrounding waters is equivalent to a local (eddy

6    volume) enhancement of the oxygen utilization by -7.35 (-2.41) $\mu$mol kg$^{-1}$ yr$^{-1}$ for CEs (ACMEs) for the depth

7    range of the shallow oxygen minimum in the SOMZ, i.e. 50 to 150 m depth.

8    An equivalent view is, by investigating a simple mix ratio of higher with lower oxygen waters in a box model

9    approach of the SOMZ. When averaging the oxygen concentrations of the eddies in the considered depth range,

10    i.e. 50 to 150 m depth, a mean oxygen concentration of 73 (66) $\mu$mol kg$^{-1}$ for CEs (ACMEs) is derived. The

11    background field oxygen concentration (118 $\mu$mol kg$^{-1}$, averaged over the same depth range between 50 and 150

12    m depth derived from the MIMOC climatology Schmidtko et al. (2013)) includes the effect of low oxygen

13    eddies. Considering the respective oxygen concentrations and volumes of the SOMZ and the eddies (multiplied

14    by their frequency of occurrence per year), we estimate the theoretical background oxygen concentration for the

15    SOMZ without eddies to 125 $\mu$mol kg$^{-1}$. Naturally due to the dispersion of negative oxygen anomalies, the

16    oxygen concentrations in the SOMZ without eddies must be higher than the observed values. Attributing the

17    difference of these values (oxygen concentration respiration without eddies (125 $\mu$molkg$^{-1}$) and observed values

18    with eddies (118 $\mu$molkg$^{-1}$) solely decreased due to the dispersion of eddies, we find that around 6% of the

19    observed oxygen concentrations in our box model can be associated to the dispersion of eddies. Consequently,

20    the oxygen consumption in the region is a mixture of the large-scale metabolism in the open ocean (Karstensen

21    et al. 2008) and the enhanced metabolism in low oxygen eddies (Karstensen et al. 2016, Fiedler et al. 2015). This

22    estimates should be considered as a lower limit due to the problems in detecting and tracking ACMEs (weak

23    SLA anomaly) and the assumption of zero lateral ventilation within the eddies. The real amount of "dead-zone"

24    eddies dissipate in the SOMZ is probably higher as only eddies which could be followed with tracking

25    algorithms directly from the coast into the transition zone and have a greater radius than 45 km and a lifetime

26    more than 21 days are considered.

27    This additional respiration term can be important in numerical simulations, where up to now only the large scale

28    consumption is taken into account. These results question the assumption that the oxygen consumption is

29    determined by the metabolism of the large-scale community alone. The observations presented here suggest

30    instead that hot spots of locally enhanced consumption may possibly need to be considered in the future.

31

## 5. Conclusion

33    In this study, we investigated the vertical structure of oxygen depleted eddies in the ETNA based on satellite (a

34    combination of SLA and SST) and in-situ oxygen and hydrography data (ship data, mooring data, profiling

35    floats, underwater glider). We frequently detected oxygen concentrations below the canonical value of 40 $\mu$mol

36    kg$^{-1}$ within the ETNA that are associated with CEs and ACMEs. Lowest oxygen concentration in these eddies

37    was observed at shallow depth between 50 to 150 m. Both eddy types are characterized by a positive Chl

38    anomaly, and therefore the enhanced productivity and subsequent respiration of the organic material is

39    responsible for creating the low oxygen core during the westward propagation of these eddies from their

40    formation region along the West African coast into the open ocean. Our assessment reveals that 234 CEs (18

Biogeosciences

Discussions

EGU

Open Access

1     ACMEs) are generated each year (mostly on the eastern side) in the ETNA and can be tracked longer than 3

2     weeks, which here are considered as coherent eddies. On average the oxygen concentration in the core of such an

3     isolated CE (ACME) decreases by about 0.10 (0.19) ± 0.12 (0.08) µmol kg$^{-1}$ d$^{-1}$. Beside the eddies originating in

4     formation regions along the West African coast, we observe low oxygen eddies (primarily ACMEs) relatively

5     close to the equator, south of 12°N. These eddies may be generated from flow instability processes occurring

6     during the formation of tropical instability waves.

7     However, both types of eddies (north of 12°N and south of 12°N) contain their minimum oxygen concentration

8     in the depth range where a shallow oxygen minimum is found in ETNA. The additional consumption within

9     these low oxygen eddies represents a substantial part of the total consumption in the open ETNA and might be

10    partly responsible for the formation of the shallow oxygen minimum.

11

31

12

Biogeosciences

Discussions

Open Access

EGU

1    **References**

2

3    Bower, A. S., Armi, L., and Ambar, I.: Direct evidence of meddy formation off the southwestern coast of
4    Portugal, Deep Sea Research Part I: Oceanographic Research Papers, 42, 1621-1630, 1995.

5    Brandt, P., Bange, H. W., Banyte, D., Dengler, M., Didwischus, S. H., Fischer, T., Greatbatch, R. J., Hahn, J.,
6    Kanzow, T., Karstensen, J., Körtzinger, A., Krahmann, G., Schmidtko, S., Stramma, L., Tanhua, T., and
7    Visbeck, M.: On the role of circulation and mixing in the ventilation of oxygen minimum zones with a focus on
8    the eastern tropical North Atlantic, Biogeosciences, 12, 489-512, 2015.

9    Chaigneau, A., Eldin, G., and Dewitte, B.: Eddy activity in the four major upwelling systems from satellite
10   altimetry (1992–2007), Progress in Oceanography, 83, 117-123, 2009.

11   Chavez, F. P. and Messié, M.: A comparison of Eastern Boundary Upwelling Ecosystems, Progress in
12   Oceanography, 83, 80-96, 2009.

13   Chelton, D. B., Schlax, M. G., and Samelson, R. M.: Global observations of nonlinear mesoscale eddies,
14   Progress in Oceanography, 91, 167-216, 2011.

15   Chelton, D. B., Schlax, M. G., Samelson, R. M., and de Szoeke, R. A.: Global observations of large oceanic
16   eddies, Geophysical Research Letters, 34, L15606, doi:10.1029/2007GL030812, 2007.

17   Fiedler, B., Grundle, D., Schütte, F., Karstensen, J., Löscher, C. R., Hauss, H., Wagner, H., Loginova, A., Kiko,
18   R., Silva, P., and Körtzinger, A.: Oxygen Utilization and Downward Carbon Flux in an Oxygen-Depleted Eddy
19   in the Eastern Tropical North Atlantic, Biogeosciences Discuss., 2016, 1-35, 2016.

20   Fischer, G., Karstensen, J., Romero, O., Baumann, K. H., Donner, B., Hefter, J., Mollenhauer, G., Iversen, M.,
21   Fiedler, B., Monteiro, I., and Körtzinger, A.: Bathypelagic particle flux signatures from a suboxic eddy in the
22   oligotrophic tropical North Atlantic: production, sedimentation and preservation, Biogeosciences Discuss., 12,
23   18253-18313, 2015.

24   Hahn, J., Brandt, P., Greatbatch, R. J., Krahmann, G., and Körtzinger, A.: Oxygen variance and meridional
25   oxygen supply in the Tropical North East Atlantic oxygen minimum zone, Clim Dyn, doi: 10.1007/s00382-014-
26   2065-0, 2014. 1-26, 2014.

27   Hauss, H., Christiansen, S., Schütte, F., Kiko, R., Edvam Lima, M., Rodrigues, E., Karstensen, J., Löscher, C.
28   R., Körtzinger, A., and Fiedler, B.: Dead zone or oasis in the open ocean? Zooplankton distribution and
29   migration in low-oxygen modewater eddies, Biogeosciences Discuss., 12, 18315-18344, 2015.

30   J. Karstensen, F. Schütte, A. Pietri, G. Krahmann, B. Fiedler, C. Löscher, D. Grundle, H. Hauss, A. Körtzinger,
31   P. Testor, N. Vieira, and M. Visbeck: Isolation, mixing and nitrate budget of an oxygen depleted anticyclonic
32   modewater eddy, Biogeosciences Discuss., (this special issue), in prep., 2016

33

34   Karstensen, J., Fiedler, B., Schütte, F., Brandt, P., Körtzinger, A., Fischer, G., Zantopp, R., Hahn, J., Visbeck,
35   M., and Wallace, D.: Open ocean dead zones in the tropical North Atlantic Ocean, Biogeosciences, 12, 2597-
36   2605, 2015.

37

38   Karstensen, J., Stramma, L., and Visbeck, M.: Oxygen minimum zones in the eastern tropical Atlantic and
39   Pacific oceans, Progress in Oceanography, 77, 331-350, 2008.

40   Lachkar, Z. and Gruber, N.: A comparative study of biological production in eastern boundary upwelling
41   systems using an artificial neural network, Biogeosciences, 9, 293-308, 2012.

42   Löscher, C. R., Fischer, M. A., Neulinger, S. C., Fiedler, B., Philippi, M., Schütte, F., Singh, A., Hauss, H.,
43   Karstensen, J., Körtzinger, A., Künzel, S., and Schmitz, R. A.: Hidden biosphere in an oxygen-deficient Atlantic

13

Biogeosciences
Discussions

Open Access

EGU

1    open-ocean eddy: future implications of ocean deoxygenation on primary production in the eastern tropical
2    North Atlantic, Biogeosciences, 12, 7467-7482, 2015.

3    Luyten, J. R., Pedlosky, J., and Stommel, H.: The ventilated thermocline, Journal of Physical Oceanography, 13,
4    292-309, 1983.

5    Menkes, C. E., Kennan, S. C., Flament, P., Dandonneau, Y., Masson, S., Biessy, B., Marchal, E., Eldin, G.,
6    Grelet, J., and Montel, Y.: A whirling ecosystem in the equatorial Atlantic, Geophysical Research Letters, 29,
7    48-41-48-44, 2002.

8    Messié, M., Ledesma, J., Kolber, D. D., Michisaki, R. P., Foley, D. G., and Chavez, F. P.: Potential new
9    production estimates in four eastern boundary upwelling ecosystems, Progress in Oceanography, 83, 151-158,
10    2009.

11    Nencioli, F., Dong, C., Dickey, T., Washburn, L., and McWilliams, J. C.: A Vector Geometry–Based Eddy
12    Detection Algorithm and Its Application to a High-Resolution Numerical Model Product and High-Frequency
13    Radar Surface Velocities in the Southern California Bight, J Atmos Ocean Tech, 27, 564-579, 2010.

14    Pastor, M. V., Pelegrí, J. L., Hernández-Guerra, A., Font, J., Salat, J., and Emelianov, M.: Water and nutrient
15    fluxes off Northwest Africa, Continental Shelf Research, 28, 915-936, 2008.

16    Richardson, P. L., Price, J. F., Walsh, D., Armi, L., and Schröder, M.: Tracking Three Meddies with SOFAR
17    Floats, Journal of Physical Oceanography, 19, 371-383, 1989.

18    Schmidtko, S., Johnson, G. C., and Lyman, J. M.: MIMOC: A global monthly isopycnal upper-ocean
19    climatology with mixed layers, Journal of Geophysical Research: Oceans, 118, 1658-1672, 2013.

20    Schütte, F., Brandt, P., and Karstensen, J.: Occurrence and characteristics of mesoscale eddies in the tropical
21    northeast Atlantic Ocean, Ocean Sci. Discuss., 12, 3043-3097, 2015.

22    Stramma, L., Brandt, P., Schafstall, J., Schott, F., Fischer, J., and Körtzinger, A.: Oxygen minimum zone in the
23    North Atlantic south and east of the Cape Verde Islands, J Geophys Res-Oceans, 113, doi:
24    10.1029/2007JC004369, 2008.

25    Thomsen, S., Kanzow, T., Krahmann, G., Greatbatch, R. J., Dengler, M., and Lavik, G.: The formation of a
26    subsurface anticyclonic eddy in the Peru-Chile Undercurrent and its impact on the near-coastal salinity, oxygen
27    and nutrient distributions, Journal of Geophysical Research: Oceans, 2015. doi: 10.1002/2015JC010878, 2015.

28    von Schuckmann, K., Brandt, P., and Eden, C.: Generation of tropical instability waves in the Atlantic Ocean, J
29    Geophys Res-Oceans, 113, doi: 10.1029/2007JC004712, 2008.

30    Wyrtki, K.: The oxygen minima in relation to ocean circulation, Deep-Sea Res, 9, 11-23, 1962.

31    Zhang, Z., Zhang, Y., Wang, W., and Huang, R. X.: Universal structure of mesoscale eddies in the ocean,
32    Geophysical Research Letters, 40, 3677-3681, 2013.
33

14

Biogeosciences
Discussions

Open Access

EGU

1
2  **Tables**
3
4  **Table 1:** All available oxygen measurements below 40µmol kg$^{-1}$ in the ETNA. The * indicates recent
5  observations which are not included in Fig. 4 due to not existent delayed time satellite products.

| | Time | min O$_2$ between 0-200 m | Associated eddy type |
|---|---|---|---|
| **11 Ship-Cruises:** (81 profiles) | | | |
| Meteor 68/3 | Summer 2006 | 17 | CE |
| L'Atalante GEOMAR 3 | Winter 2008 | 25 | ACME |
| Meteor 80/2 | Winter 2009 | 32 | ACME |
| Meteor 83/1 | Winter 2010 | 20 | ACME |
| Meteor 96 | Spring 2013 | 38 | ACME |
| Meteor 97 | Summer 2013 | 28 | ACME |
| Islandia | Spring 2014 | 10 | ACME |
| Meteor 105 | Spring 2014 | 4 | ACME |
| Meteor 116 | Spring 2015 | 17 | ACME* |
| Meteor 119 | Autumn 2015 | 30 | ACME* |
| Maria S. Merian 49 | Winter 2015 | 35 | CE* |
| **9 Argo floats:** (24 profiles) | | | |
| 6900632 | Autumn 2008 | 14 | CE |
| 1900652 | Winter 2008 | 26 | ACME |
| 1900650 | Summer 2009 | 27 | ACME |
| 1901360 | Autumn 2014 | 34 | CE |
| 1901361 | Autumn 2014 | 21 | CE |
| 1901362 | Autumn 2014 | 26 | CE |
| 1901363 | Autumn 2014 | 37 | CE |
| 1901364 | Autumn 2014 | 24 | ACME |
| 1901365 | Autumn 2014 | 24 | ACME |
| **4 Gliders:** (32 profiles) | | | |
| IFM 11 | Spring 2010 | 19 | ACME |
| IFM 05 | Summer 2013 | 9 | CE |
| IFM 12 | Winter 2014 | 1 | ACME |
| IFM 13 | Spring 2014 | 1 | ACME |
| **9 CVOO events:** (36 profiles) | | | |
| Optode at 127 m depth | Winter 2007 | 15 | ACME |
| Optode at 79 m depth | Autumn 2008 | 38 | CE |
| Optode at 54 m depth | Winter 2010 | 2 | ACME |

15

| Optode at 53 m depth | Winter 2012 | 17 | ACME |
|---|---|---|---|
| Optode at 53 m depth | Spring 2012 | 30 | CE |
| Optode at 45 m depth | Summer 2013 | 29 | ACME |
| Optode at 45 m depth | Winter 2013 | 9 | CE |
| Optode at 43 m depth | Winter 2015 | 2 | ACME* |
| Optode at 43 m depth | Summer 2015 | 6 | ACME* |
| **∑ 173 profiles** | | | **∑ 27 different eddies** |

1

1  **Figures**
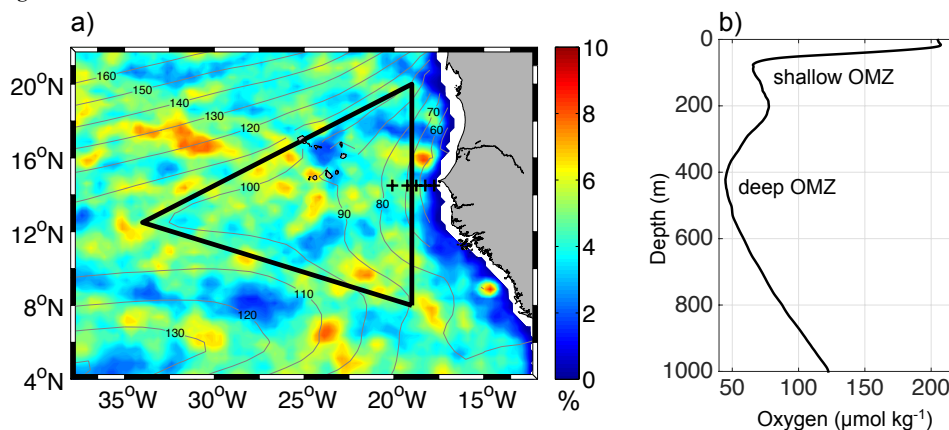


2
3
4  **Figure 1: a)** Map of the ETNA including contour lines of the oxygen minimum of the upper 200m (in µmol kg⁻

5  ¹) as obtained from the MIMOC climatology (Schmidtko et al., 2013). The color indicates the percentage of

6  "dead-zone" eddy coverage per year. The black triangle defines the SOMZ. The black crosses indicate the

7  position of the CTD stations of the research cruise M97, which are used to represent the vertical oxygen profile

8  shown on the right. **b)** mean vertical oxygen profile showing the shallow oxygen minimum centered around 80

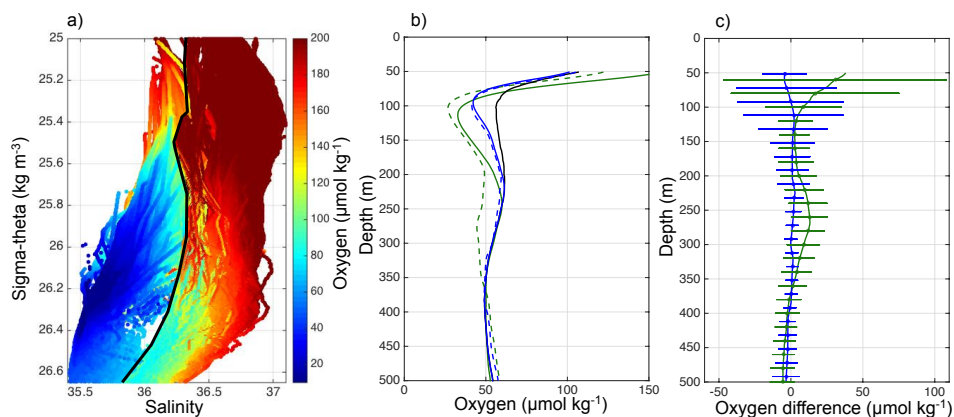9  m depths and the deep oxygen minimum centered at 450 m depth.

10
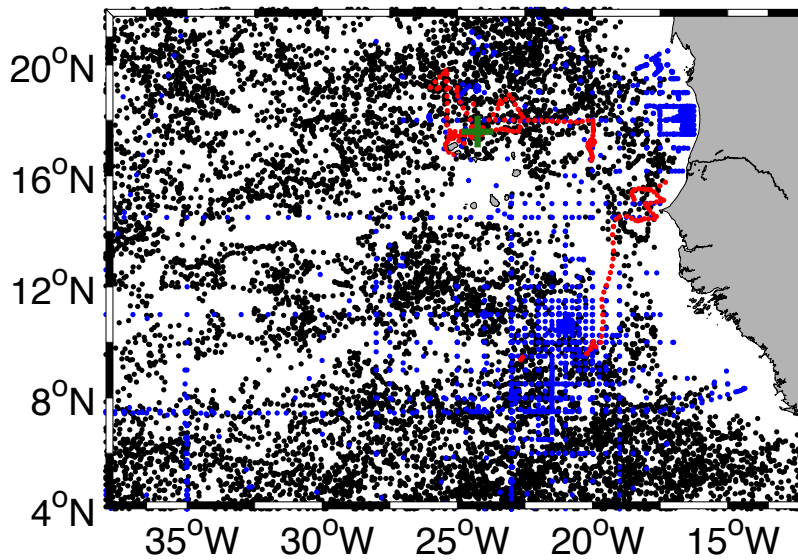
**Figure 2:** Map of ETNA containing all available profiles between 1998 and 2014. The green cross marks the CVOO position, blue dots mark shipboard CTD stations, red dots mark the locations of glider profiles and black dots locations of Argo float profiles.

18

1



2

3 **Figure 3: a)** Salinity-$\sigma_\theta$ diagram with color indicating the oxygen concentrations. The black line separates the

4 173 profiles with minimum oxygen concentration of <40 µmol kg$^{-1}$ (left side / more SACW characteristics) from

5 profiles of the surrounding water (right side / more NACW characteristics), taken from the same devices shortly

6 before and after the encounter with a low-oxygen eddy. **b)** Mean oxygen concentration versus depth of the

7 coastal region (east of 18°W, solid black line), of all CEs (solid blue line) and all ACMEs (solid green line) with

8 available oxygen measurements. The dashed line represents the reconstructed mean oxygen concentration for the

9 same CEs (blue) and ACMEs (green). **c)** Difference between the reconstructed and measured oxygen

10 concentrations in CEs (blue) and ACMEs (green) with associated standard deviation (horizontal lines).

11

19
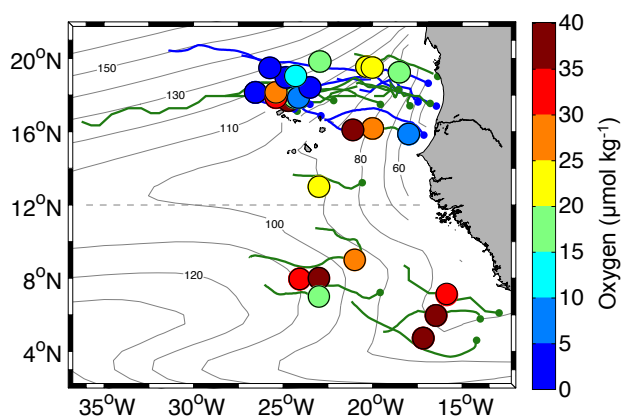
**Figure 4:** Minimum oxygen concentration (contour lines, µmol kg$^{-1}$) in the tropical Northeast Atlantic Ocean between the surface and 200 m depth as obtained from the MIMOC climatology (Schmidtko et al., 2013). Superimposed colored dots are all low oxygen measurements (below 40 µmol kg$^{-1}$ in the upper 200 m) which could be associated with eddy-like structures. The size of the dots represents a typical size of the mesoscale eddies. The associated trajectories of the eddies are shown in green for ACMEs and in blue for cyclones. The oxygen concentrations are from the combined dataset of shipboard, mooring, glider and Argo float measurements.

**Biogeosciences**
Discussions

Open Access

EGU
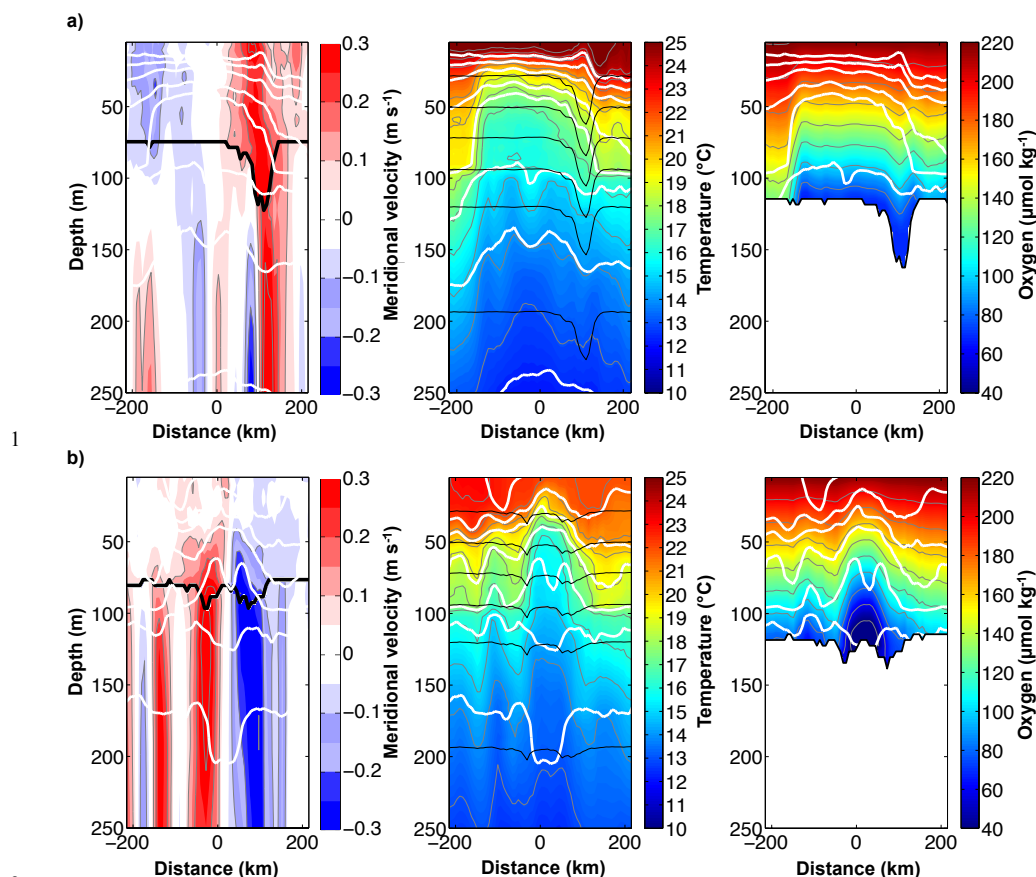


**Figure 5:** Meridional velocity, temperature and oxygen of an exemplary **a)** CE and **b)** ACME at the CVOO mooring. Both eddies passed the CVOO on a westward trajectory with the eddy center north of the mooring position (CE 20 km, ACME 13 km). The CE passed the CVOO from October to December 2006 and the ACME between January and March 2007. The thick black lines in the velocity plots indicate the position of an upward looking ADCP. Below that depth calculated geostrophic velocity is shown. The white lines represent density surfaces inside the eddies and the thin grey lines isolines of temperature and oxygen, respectively. Thin black lines in the temperature and oxygen plot mark the vertical position of the measuring devices. For the oxygen plot saturation at the surface is assumed and data is linearly interpolated between the measuring device and surface.

21

1
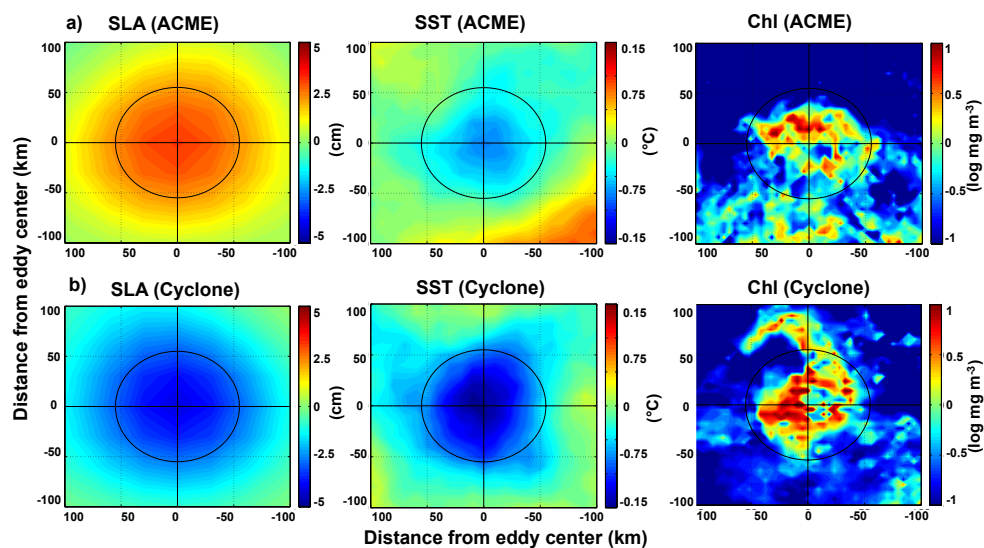


**Figure 6:** Composites of surface signature for SLA, SST and Chl from all detected "dead-zone" eddies: **a)** ACMEs and **b)** cyclones. The solid black cross marks the eddy center and the solid black circle the average radius. Due to significant cloud cover the number of Chl data are much less when compared the SLA and SST data, thus there is more lateral structure.

7

22

1
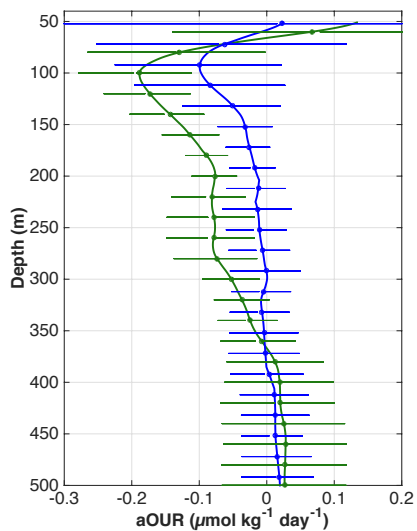


2

3      **Figure 7:** Depth profiles of a mean apparent oxygen utilization rate (aOUR, µmol kg$^{-1}$ d$^{-1}$) within CEs (blue) and

4      ACMEs (green) with associated standard deviation (horizontal lines).

23
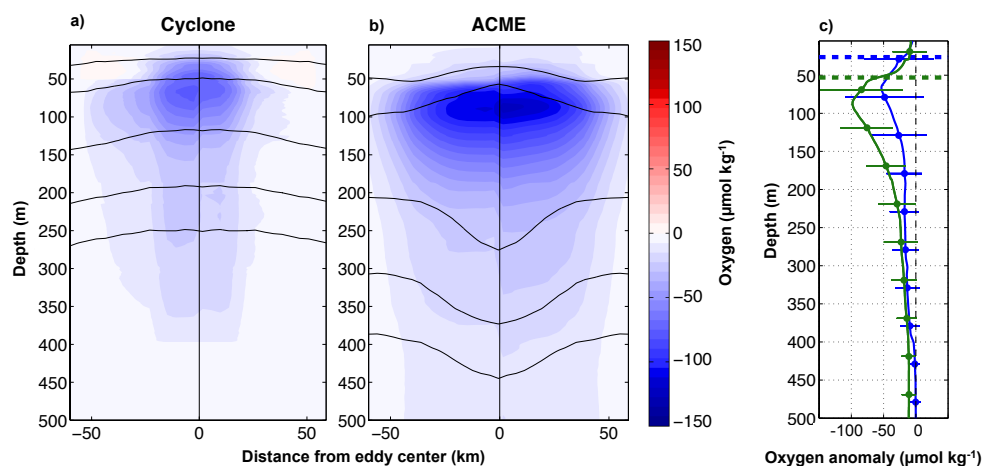
**Figure 8:** Vertical structure of oxygen from the composite **a)** CE and **b)** ACME in the ETNA presented as a half section across the eddies. The left side of each panel (-60 to 0 km) is based on reconstructed and measured oxygen profiles whereas the right side (0 to 60 km) is based on measured oxygen profiles only. The grey lines represents the density surfaces inside the eddies. **c)** Mean profiles of the oxygen anomalies based on measured profiles only, green colors are associated to ACMEs and blue to CEs. The thick dashed line indicates the mean ML within the different eddy types. The horizontal lines indicate the standard deviation at that point. The grey vertical dashed line represents zero oxygen.
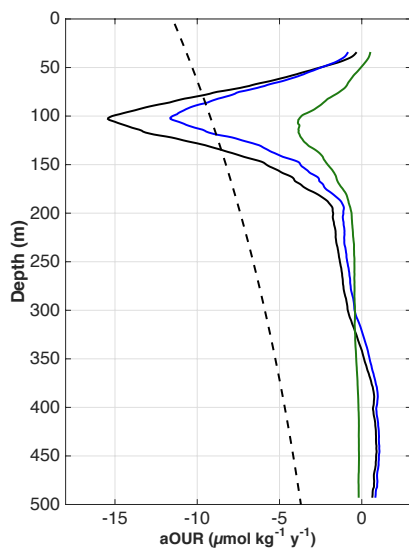
**Figure 9:** Depth profile of apparent oxygen utilization rate (aOUR, μmol kg$^{-1}$ y$^{-1}$) for the Atlantic as published from Karstensen et al. (2008) (dashed black line), the oxygen consumption profile due to "dead-zone" eddies in the SOMZ (solid black line) and the separation into CEs (blue) and ACMEs (green).

25

# 5 Upwelling and isolation in oxygen-depleted anticyclonic modewater eddies and implications for nitrate cycling

In order to explain the apparent paradox that the eddies are highly isolated but in parallel should support intense upwelling a high-resolution glider surveys through an oxygen-depleted ACME is examined. The glider track based on the data collected with the ëddy hunt älert system. A rich physical and biogeochemical co-variability could be revealed. The eddies are natural laboratories generating open ocean biogeochemical extremes. It could be shown that mesoscale ( 50 km) dynamics of the eddy is interacting with near inertial waves to drive submesoscale ( 1 km) upward nutrient flux at the eddy periphery. The eddy nitrate deficit is explained by local nitrate recycling from sinking of particles.

The manuscript is published in Biogeosciences Discussions (unreviewed publication) and is under review for Biogeosciences. The candidates contribution to this manuscript is as follows:

The Author conducted the data sampling. He identified a proper eddy via a satellite based monitoring system and deployed the gliders for eddy observations. He was responsible for the glider piloting and, onboard R/V Meteor (expedition M105), for the detection of the eddy and the shipboard ADCP measurements. The Author contributed to the manuscript in identifying the eddy location, trajectory and eddy periphery (all satellite based tasks). He produced figure 1 of the manuscript and contributed with ideas, discussion and comments to the manuscript.

**Biogeosciences**
Discussions

# Upwelling and isolation in oxygen-depleted anticyclonic modewater eddies and implications for nitrate cycling

Johannes Karstensen[1], Florian Schütte[1], Alice Pietri[2], Gerd Krahmann[1], Björn Fiedler[1], Damian Grundle[1], Helena Hauss[1], Arne Körtzinger[1,3], Carolin R. Löscher[1], Pierre Testor[2], Nuno Viera[4], Martin Visbeck[1,3]

[1]GEOMAR, Helmholtz Zentrum für Ozeanforschung Kiel, Düsternbrooker Weg 20, 24105 Kiel, Germany
[2]LOCEAN, UMPC; Paris, France
[3]Kiel University, Kiel Germany
[4]Instituto Nacional de Desenvolvimento das Pescas (INDP), Cova de Inglesa, Mindelo, São Vicente, Cabo Verde

*Correspondence to*: Johannes Karstensen (jkarstensen@geomar.de)

**Abstract.** The physical (temperature, salinity, velocity) and biogeochemical (oxygen, nitrate) structure of an oxygen depleted coherent, baroclinic, anticyclonic mode-water eddy (ACME) is investigated using high-resolution autonomous glider and ship data. A distinct core with a diameter of about 70 km is found in the eddy, extending from about 60 to 200 m depth and. The core is occupied by fresh and cold water with low oxygen and high nitrate concentrations, and bordered by local maxima in buoyancy frequency. Velocity and property gradient sections show vertical layering at the flanks and underneath the eddy characteristic for vertical propagation (to several hundred-meters depth) of near inertial internal waves (NIW) and confirmed by direct current measurements. A narrow region exists at the outer edge of the eddy where NIW can propagate downward. NIW phase speed and mean flow are of similar magnitude and critical layer formation is expected to occur. An asymmetry in the NIW pattern is seen that possible relates to the large-scale Ekman transport interacting with ACME dynamics. NIW/mean flow induced mixing occurs close to the euphotic zone/mixed layer and upward nutrient flux is expected and supported by the observations. Combing high resolution nitrate ($NO_3^-$) data with the apparent oxygen utilization (AOU) reveals $AOU:NO_3^-$ ratios of 16 which are much higher than in the surrounding waters (8.1). A maximum $NO_3^-$ deficit of 4 to 6 µmol kg$^{-1}$ is estimated for the low oxygen core. Denitrification would be a possible explanation. This study provides evidence that the recycling of $NO_3^-$, extracted from the eddy core and replenished into the core via the particle export, may quantitatively be more important. In this case, the particulate phase is of keys importance in decoupling the nitrogen from the oxygen cycling.

## Introduction

Eddies are associated with a wide spectrum of dynamical processes from the mesoscale (order of several 10 to 100 km) to the submesoscale (order of 10 meters to less than 1 km). The interaction of these processes creates transport patterns in and around eddies that provoke intense biogeochemical and biological feedback (Levy et al. 2012, Chelton et al. 2011a). At the ocean surface, the eddy rotation generates a sea level anomaly (SLA) pattern that allow for their remote detection (Chelton et al. 2011a).

1

But also in other surface parameters, such as seas surface temperature (SST) or chlorophyll-a fluoresence, eddies show anomalies that allow deriving their statistics (Chelton et al. 2011b; Gaube et al. 2015). Utilizing satellite data large/global scale analysis of eddy-generated anomalies has been conducted (Chaigneau et al. 2009, Chelton et al. 2011a, Gaube et al. 2015). More recently the vertical

5    structure of mesoscale eddies have been studied on regional (Chaigneau et al. 2011) and global scale (Zhang et al. 2013) combining eddy surface detection with concurrent, but opportunistic, in-situ profile data (e.g. Argo floats). These studies differentiate, based on the SLA being either positive or negative, cyclonically rotating and anti-cyclonically rotating eddies.

However, when vertical stratification is considered, a third group of mesoscale eddies emerges that

10    combine the downward displacement of isopycnals towards the eddy centre, as observed in "normal" anticyclonic eddies (AE), with the upward displacement of isopycnals, characterizing cyclonic eddies (CE). Such "hybrid eddies" are called anticyclonic mode-water eddies (ACME) or intra-thermocline eddies (McWilliams 1985, D'Asaro 1988, Kostianoy and Belkin 1989, Thomas 2008), because the depth interval between upward and downward displaced isopycnals creates a volume of rather

15    homogenous properties, sometimes called "mode" water. A recent study (Schütte et al. 2015) investigated the occurrence of these three different types of mesoscale eddies (CE, AE, and ACME) in the eastern tropical North Atlantic, combining in-situ profile data with satellite SLA and SST data. The authors found that ACME in the tropical eastern North Atlantic are characterized by a cold SST anomaly (in contrast to AEs that show a warm SST anomaly), which allowed a statistical assessment of

20    ACME in the tropical eastern North Atlantic based on satellite data alonse. Schütte et al. (2015) estimated that about 9% of all eddies (20% of all anticyclones) in the eastern tropical North Atlantic are ACME.

More than a decade ago a dedicated observational program was carried out to survey eddies in western North Atlantic (Sargasso Sea) in order to better understand the physical-biogeochemical interactions.

25    The surveys revealed that ACME showed particularly intense deep chlorophyll-a layers that aligned with a maximum concentrations of diatoms and maximum productivity (McGillicuddy et al. 2007). The high productivity was linked to a conceptual model that explains the intense vertical fluxes of nutrients within ACME with an Ekman divergence generated from the horizontal gradient in wind stress across an ACME (McGuillicuddy et al. 2007; going back to a work from Dewar and Flierl, 1987). The concept

30    itself was questioned (Mahadevan et al. 2008) and high-resolution ocean model simulations, comparing runs with or without eddy-wind interaction, reproduced only a marginal impact on ocean productivity (but a strong impact on physics; Eden and Dietze 2009). However, from a tracer release experiment within an ACME the magnitude of the vertical flux was found to be of the magnitude as expected from simple eddy-wind induced Ekman pumping estimates (order of meters per day; Ledwell et al. 2008).

2

A measure for the importance of local rotational effect relative to the Earth rotation is given by the Rossby number defined as $Ro = \frac{\zeta}{f}$, and where $\zeta = \frac{\partial V}{\partial x} - \frac{\partial U}{\partial y}$ is the vertical vorticity ($U, V$ are zonal and meridional velocity) and $f$ the planetary vorticity. Planetary flows have small $Ro$ say up to ~0.2, while local rotational effects gain importance with $Ro$ approaching 1. Mesoscale eddies often have $Ro$ close to

5    1 indicating that, for example, the geostrophic approximation does not hold locally. Anticyclonic rotating eddies (AE and ACME) have negative relative vorticity ($\zeta < 0$) and modify $f$ into an effective planetary vorticity ($f_{eff} = f + \frac{\zeta}{2}$) (Kunze 1985, Lee and Niller 1998). This local reduction in $f$ has for example implications for the propagation of internal waves that occur at frequencies in the range of the local buoyancy frequency (N) and $f$. For AEs, the local reduction of $f$ leads to a trapping of internal

10    waves of near inertial frequencies (NIW) and downward energy propagation inside of AEs (Kunze 1985, Gregg et al. 1986, Lee and Niller 1998, Koszalka et al. 2010, Joyce et al. 2013, Alford et al. 2016). Depending on the vertical distribution of N the downward NIW propagation can generate an amplification of the wave energy and eventually part of that energy is dissipated by critical layer absorption which in turn results in intense vertical mixing (Kunze 1985, Kunze et al. 1995, Whitt and

15    Thomas 2013).

The anticyclonic rotation of ACME also reduces $f$ but, in contrast to AE, a local N maximum at their upper boundary characterizes the ACME. This N maximum creates a "cap" and complicates NIW vertical propagation. Lee and Niller (1998) considered an ACME stratification in a model study on near inertial internal wave propagation, mimicking the stratification of a "California subsurface warm core

20    eddy", and found the accumulation of energy below the eddy. A recent study (Sheen et al. 2015) reported on hydrography, dissipation measurements, and current observations across an ACME observed at 2000 m depth in the Antarctic Circumpolar Current. The study found enhanced diapycnal mixing at the periphery of this particular ACME. Applying a ray tracing method to a stability profile from outside and from inside of the eddy Sheen et al. showed that, depending on their propagation

25    direction relative to the background shear, the modelled internal waves either encounter a critical layer above and below the eddy or are reflected at the eddy core.

A number of studies analysed NIW interaction with Mediterranean Outflow lenses in the North Atlantic ("Meddies", Armi and Zenk 1984), which are deep ACME (mode below 1000m). Krahmann et al. (2008) reported observations of enhanced NIW energy at the rim of a Meddie. For Meddies signatures

30    of layering at the eddy periphery have often been observed and related to the interaction of NIW with the baroclinic shear of the rotating lens, ultimately driving dissipation (Hua et al. 2013). The dissipation is often associated with Kelvin-Helmholtz instabilities (e.g. Kunze et al. 1995) but other mixing processes, such as double-diffusion may play a role too. In particular layering, produced by internal wave shear and strain, has been also reported to enhance double diffusive fluxes (St Laurent and

<div align="center">3</div>

**Biogeosciences**

Open Access

**Discussions**

EGU

Schmitt 1999), at least in regions that are already characterized by salt finger-favourable stratification (Kunze 1995).

Levy et al. (2012) summarized the submesoscale upwelling at fronts in general, not specifically for mesoscale eddies, and the impact on oceanic productivity. Vertical property flux of nutrients into the
5   euphotic zone plays a key role in the productivity scenarios and can be either by advection or by mixing. Regardless of the mechanism for vertical transport, mesoscale eddies have been found to be "retention regions" (d'Ovidio et al. 2013) and the upwelling of properties into the mixed layer, either inside or at the periphery of mesoscale eddies, is trapped in the eddy where it can be utilized efficiently.

Recently, ACME with very low oxygen concentrations in their cores where observed in the tropical
10  eastern North Atlantic (Karstensen et al. 2015). The generation of the low oxygen concentrations was linked to high productivity in the euphotic zone of the eddy and the subsequent remineralisation of the sinking organic matter, a process that requires a vertical fluxes of nutrients to supply the productivity in the euphotic zone. However, the eddy core were found to be highly isolated against surrounding waters and weak transport and mixing activity in and around the core was expected. As such it is surprising
15  that the isolated core can exist in parallel to the enhanced vertical flux, and that suggested that the processes responsible for the separation must act on small spatial scales. In this paper we further investigate the transport processes associated with a low oxygen ACME making use of high-resolution underwater glider and ship data. This paper is part of a series of publications that report on different genomic, biological and biogeochemical aspects of low oxygen ACME in the eastern tropical North
20  Atlantic (Löscher et al. 2015, Hauss et al. 2016, Fiedler et al. 2016, Schütte et al. 2016).


## 2 Data and Methods

Targeted eddy surveys are logistically challenging. Eddy locations can be identified using real-time satellite SLA data. To further differentiate a positive SLA (indicative for anticyclonic rotation) into either an AE or an ACME the SST anomaly across the eddy was inspected, because ACME in the
25  eastern tropical North Atlantic show a cold SST anomaly (Schütte et al. 2015, Schütte et al. 2016). For further evidence, but purely opportunistic, Argo profile data were inspected to detect anomalously low temperature/salinity signatures, indicative of low oxygen ACME in the region (Karstensen et al. 2015, Schütte et al 2016). In late December 2013 a candidate eddy was identified through this mechanisms and in late January 2014 a pre-survey was initiated, making use of autonomous gliders. After
30  confirmation that the candidate eddy was indeed a low oxygen ACME, two ship surveys (ISL, M105; Fiedler et al. 2016) and further glider surveys followed.

**BiogeosciencesOpen Access**
**Discussions**
**EGU**

## 2.1 Glider survey

Data from the glider IFM13 (1st deployment) and Glider IFM12 (2nd deployment) were used in this study (Fig. 1). IFM12 surveyed temperature, salinity, and oxygen to a depth of 500 m while IFM13 surveyed the same properties down to 700 m. Both glider measured chlorophyll-a fluorescence and

5  turbidity to 200 m depth. In addition to the standard sensors IFM13 was also equipped with a nitrate sensor that sampled to 700 m depth. IFM13 surveyed one full eddy section from April 3-7, 2014 (Fig. 1). For IFM12 we combined data from February 3-5 and from February 7-10, 2014 because, due to technical problems, data were not recorded in between these periods. All glider data was internally recorded as a time series along the flight path, while for the analysis the data was interpolated onto a

10 regular pressure grid of 1 dbar resolution. For the purposes of this study we consider the originally slanted profiles as vertical profiles.

## 2.2 Glider Sensor Calibrations

Both gliders were equipped with a pumped CTD and no evidence for further time lag correction of the conductivity sensor was found. Oxygen was recorded with AADI Aanderaa optodes (model 3830). The

15 optodes were calibrated in reference to SeaBird SBE43 sensors mounted on a regular ship-based CTD, which in turn were calibrated using Winkler titration of water samples (see Hahn et al. 2014). The calibration process also removes a large part of the effects of the slow optode response time via a reverse exponential filter (time constants were 21 and 23 seconds for IFM12 and IFM13, respectively). As there remained some spurious difference between down and up profiles we averaged up- and

20 downcast profiles to further minimize the slow sensor response problem in high gradient regions, particular the mixed layer base.

The nitrate measurements on IFM13 were collected using a Satlantic Deep SUNA sensor. The SUNA emits light pulses and measures spectra in UV range of the electromagnetic spectrum. It derives the nitrate concentration from the concentration-dependent absorption over a 1 cm long path through the

25 sampled seawater. During the descents of the glider the sensor was programmed to collect bursts of 5 measurements every 20 seconds or about every 4 m in the upper 200 m and every 100 seconds or about every 20 m below 200 m. The sensor had been factory calibrated 8 months prior to the deployment. The spectral measurements of the SUNA were post-processed using Satlantic's SUNACom software, which implements a temperature and salinity dependent correction to the absorption (Sakamoto et al., 2009).

30 The SUNA sensors' light source is subject to aging which results in an offset nitrate concentration (Johnson et al., 2013).

To determine the resulting offset, nitrate concentrations measured on bottle samples by the standard wet-chemical method were compared against the SUNA-based concentrations. The glider recorded profiles close to the CVOO mooring observatory (see Fiedler et al. 2016) at the beginning and end of

5

the mission. These we compared to the mean concentrations of ship samples taken in the vicinity of the CVOO location (Fiedler et al. 2016). In addition we compared glider measurements within the ACME to nitrate samples from two surveys performed during the eddy experiment (see Löscher et al. 2015, Fiedler et al. 2016). The comparison showed on average no offset ($0.0 \pm 0.2$ µmol kg$^{-1}$). However, near

5   the surface the bottle measurements indicated nitrate concentrations below 0.2 µmol kg$^{-1}$ at CVOO, while the SUNA delivered values of about 1.8 µmol kg$^{-1}$ possibly related to technical problems near the surface. We thus estimate the accuracy of the measurements to be better than 2.5 µmol kg$^{-1}$ with a precision of each value of about 0.5 µmol kg$^{-1}$.

All temperature and salinity data is reported in reference to TEOS-10 (IOC et al. 2010) and as such we

10   report absolute salinity (SA) and conservative temperature ($\Theta$). Calculations of relevant properties (e.g. buoyancy frequency, spiciness, oxygen saturation) were done using the TEOS-10 MATLAB toolbox (McDougall and Barker, 2011). We came across one problem related to the TEOS-10 thermodynamic framework when applied to nonlinear, coherent vortices. Because the vortices transfer properties nearly unaltered over large distances the application of a regional (observing location) correction for the

15   determination of the absolute salinity (McDougall et al. 2012) seems questionable. In the case of the surveyed eddy the impact was tested by applying the ion composition correction from 17°W (eddy origin) and compared that with the correction at the observational position, more than 700 km to the west, and found a salinity difference of little less than 0.001 g kg$^{-1}$.

**2.3 Ship survey**

20   In between the two glider surveys, a ship survey of the respective eddy was conducted on the 18th and 19th March 2014 (Fig. 1) with R/V METEOR (expedition M105), about 6 weeks after IFM12 and 3 weeks before IFM13. We make use of the water currents data recorded with a vessel mounted 75kHz Teledyne RDI ADCP device. The data was recorded in 8 m depth cells and standard processing routines where applied to remove the ship speed and correcting the transducer alignment in the ship's hull. The

25   final data was averaged in 15 min intervals. Only data recorded during steaming (defined as ship speed larger than 6 kn) is used for evaluating the currents structure of the eddy. It should be mentioned that the inner core of the eddy shows a gap in velocity records, which is caused by very low backscatter particle distribution (size about 1 to 2 cm) (see Hauss et al. 2016 for a more detailed analysis of the backscatter signal including net zooplankton catches).

30   In order to provide a frame to compare ship currents and glider section data, we interpolated data from 8 deep (>600 m) CTD stations performed during the eddy survey, and estimated oxygen and density distributions across the eddy section. More information about other data acquired during M105 in the eddy is given elsewhere (Löscher et al. 2015, Hauss et al. 2016, Fiedler et al. 2016).

6

**BiogeosciencesOpen Access**
Discussions
EGU

## 3 Results and Discussion

### 3.1 Vertical Eddy Structure

In order to compare the vertical structure of the eddy from the three different surveys, all sections were referenced to "kilometre distance from the eddy core" as the spatial coordinate, while the "centre" was

5 selected based on visual inspection. Comparing the oxygen concentrations from the three surveys reveals a core of low oxygen in the centre of the eddy (Fig. 2). The core extends over a depth range from about 60 to 200 m depth in all three surveys and its upper and lower boundaries are aligned with the curvature of isopycnals. Considering the whole section across the eddy it can be seen that towards the centre of the eddy the isopycnals show an upward bending in an upper layer (typically associated

10 with cyclonic rotating eddies) and a downward bending below (associated with anticyclonic rotating eddies) which is characteristic for ACME.

During the first survey (IFM12), lowest oxygen concentrations of about 8 $\mu$mol kg$^{-1}$ were observed in two vertically separated cores at about 80 m and 120 m depth, while in between the cores oxygen concentrations increased to about 15 $\mu$mol kg$^{-1}$. About 6 weeks later, during METEOR M105, lowest

15 concentrations of about 5 $\mu$mol kg$^{-1}$ were observed, centred at about 100 m depth and without a clear double minimum anymore. During the last survey (IFM13), another three weeks later, the minimum concentrations were < 3 $\mu$mol kg$^{-1}$ and now showed a single minimum at 120 m. It is unknown how much of the intensification of the minimum (by about 5 $\mu$mol kg$^{-1}$ in 2 months) is attributed to sampling the core during the individual surveys at different distances from the core. The broadening and

20 deepening however, seems to be a real signal. Underneath the eddy core, and best seen in the 40 $\mu$mol kg$^{-1}$ oxygen contour below 350 m, a slight increase in oxygen over time is found probably related to lateral exchange and the general increase in oxygen towards the west (ventilated gyre region).

The horizontal and vertical extent of the low oxygen core in the two glider surveys is rather similar (Fig. 2), perhaps a little larger during the second survey. The gridded oxygen contour from the ship

25 survey, based on eight stations, suggest a narrower core. However, these differences in the core characteristic may also be related to the survey having been made a few kilometres further away from (or closer to) the eddy centre. The similarity in the vertical structure suggests that the general eddy structure and the observed phenomena are stable across the three surveys, as expected for a coherent eddy (McWilliams 1985). A composite of the outermost ("last") closed geostrophic contour of the eddy

30 (Fig. 1, right), analysed from a selected set of SLA data (see Schütte et al. 2016 for details), revealed a diameter of about 60 km, which is in accordance with the dimensions of the vertical structures observed from the glider and the ship (Fig. 2 and 3).

Defining the low oxygen core by oxygen concentrations below the canonical value of 40 $\mu$mol kg$^{-1}$, we find that the core is composed of a fresh (and cold; not shown) water mass (Fig. 3a) that matches the

**BiogeosciencES** Open Access
Discussions EGU

characteristics of South Atlantic Central Water (SACW; Fiedler et al. 2016), which is typical for the low oxygen eddies in the eastern tropical North Atlantic (Karstensen et al. 2015, Schütte et al. 2015, 2016). These properties indicate that the ACME was formed in the coastal area off Mauritania (see Fiedler et al. 2016, Fig. 1, left) and that the eddy core did not experience significant exchange with the

5   surrounding waters. The core water mass characteristic is well expressed in the spiciness (McDougall and Krzysik 2015) section that shows the contrasting impact of $\Theta$ and $S_A$ on isopycnals (Fig. 3b). The core is well separated in spiciness from the surrounding waters, while the core itself shows only weak vertical structure in spiciness and a nearly horizontal orientation of isopycnals.

The low oxygen core of the ACME is well separated from the surrounding water through a maximum in
10   the squared buoyancy frequency ($N^2$; Fig. 3c) and as such in stability. The most stable conditions are found along the upper boundary of the core ($N^2 > 10 \cdot 10^{-5}$ s$^{-2}$) aligned with the mixed layer base. Here, vertical gradients in $\Theta$ ($S_A$) of 5 K (0.7 gr kg$^{-1}$) over vertical distances of 15 m are observed. At the lower side of the ACME the stability maximum is less strong ($N^2$ about $3 \cdot 10^{-5}$ s$^{-2}$) but separating the eddy surrounding water well from the low $N^2$ of the core (the "mode"). The stability also shows, as seen
15   in $S_A$, slanted vertical bands of alternating stability patterns at the rim and below the eddy.

The pattern are also evident in the stability ratio $R_\rho = \frac{\alpha^\theta \Theta_z}{\beta^\theta (S_A)_z}$, (here shown as a Turner angle; Tu; McDougall and Barker 2011) (Fig. 3d). The $R_\rho$ is the ratio of the vertical contribution from $\Theta$, weighted by the thermal expansion coefficient ($\alpha^\Theta$), over that from $S_A$, weighted by the haline contraction coefficient ($\beta^\Theta$), to the static stability (Fig. 3d). For convenience $R_\rho$ is converted to Tu
20   using the four-quadrant arctangent. For Tu between -45 to -90° the stratification is susceptibility to salt finger type double diffusion, while Tu 45° to 90° indicate susceptibility for diffusive convection. Regions were most likely double diffusion occurs are found for Tu close to ±90°. In the core of the eddy (Fig. 3d) the Tu indicate that diffusive convection is possible (Tu values close to +45°), however, no gradients exists and no fluxes are expected here. In contrast, below the core in the alternating and
25   vertically slanted Tu patterns, values within ±45° to ±90° can be seen. The structures do not align with the tilting of the isopycnals but cross isopycnals. Moreover, salinity (and temperature) gradients are seen in these depth ranges as well (see Fig. 3a) and salt finger fluxes is possible. A Tu between −75° to −85° at 120 m, 160 m, 210 m depth (salt finger susceptible) and Tu between 80° and 89° at 210 m, 320 m, 410 m depth (diffusive convection susceptible).

30   The ADCP zonal (Fig. 4a) and meridional (Fig. 4b) currents show a baroclinic, anticyclonic rotating flow, with a maximum swirl velocity of about 0.45 m s$^{-1}$ at about 100 m depth. The maximum rotation speed (approximately represented by the zonal section) decreases nearly linear to about 380 m depth where 0.1 m s$^{-1}$ is reached. Alternating currents with about 80 to 100 m wavelength can be seen close to the eddy edges and more clearly seen after subtracting 120 m boxcar filtered profiles (Fig. 4 c). The

8

**Biogeosciences**
Discussions
Open Access

EGU

local (at 19°N) inertial period is 36.7 h while the ADCP section was surveyed in 14 h (including station time) and only a moderate aliasing effects is expected in the sections. In contrast, the glider took more than 5 days (4 inertial periods) to complete the section (Fig. 3) and a mixture of time/space variability is mapped.

5   Considering the translation speed of the eddy of 3 to 5 km day^{-1} (see Fiedler et al. 2016) the nonlinearity parameter $\alpha$, relating maximum swirl velocity to the translation speed, is much larger than 1 (about 6.5 to 11 in the depth level of the low oxygen core) and indicates a high coherence of the eddy. At the depth of the maximum swirl velocity, and considering the eddy radius of 30 km, a full rotation would take about 5 days but for the deeper levels more.

10  **3.2 Eddy core isolation and vertical fluxes**

The concept proposed for the formation of the low oxygen zone is based on an isolation of the eddy core, in combination with high productivity and subsequent respiration of sinking organic material – in analogy to the formation of dead-zones in coastal and limnic systems (Karstensen et al. 2015). The water mass observed in the ACME defines a strong anomaly against the surrounding waters and is very

15  similar to water masses at the eastern boundary, where the ACME was formed (Fiedler et al. 2016). The constancy of hydrographic properties over a period of about 7 month have been shown for this ACME (Fiedler et al. 2016) and suggests that no significant exchange between eddy core and surrounding water through either lateral or diapycnal processes occurred.

The high nonlinearity parameter for the eddy ($\alpha \gg 1$) indicates its coherence and explains why the

20  eddy was so remarkably stable when comparing observations of the eddy 2 month apart (Fig. 2). However, the high $\alpha$ does not explain the isolation of the core against mixing. Mixing in the thermocline is closely related to breaking of internal waves (Gregg et al. 1986, Gregg 1989), maybe with local enhancement by double diffusive mixing in cases where vertical gradients are intense (St Laurent and Schmitt 1999). To determine the possible interaction of the low oxygen eddy with the

25  internal wave field we first calculate the relative vorticity $\zeta$ of the eddy (Fig. 5a) and then investigated the impact on the local $f$. The anticyclonic (negative) $\zeta$ in the core of the low oxygen eddy is about $-0.8 \cdot f$ ($Ro = -0.8$) and changes sign at the boundary of the core, where large $Ro$ remain (Ro ~0.4) suggesting that eddy rotational effect are important. The $f_{eff}$ in the ACME (Fig. 5b) is lowered to values of 0.6 in the core (Kunze et al 1995), while underneath the core, and below the lower $N^2$

30  maximum, still values of 0.8 are found. Such low $f_{eff}$ force NIW to propagate downward also called "inertial chimney" (Lee and Niller 1998). In contrast to a typical AE stratification (Kunze 1985, Kunze et al. 1995, Joyce et al. 2013) the low oxygen ACME has an intense $N^2$ maximum ($10^{-4}$ s$^{-2}$) defining its upper boundary and that also aligns with the mixed layer base (Fig. 3c). Model studies (Lee and Niiler 1998) and ray tracing analysis (Sheen et al. 2015) show for ACME that most of the NIW energy

9

accumulates below the eddy. As a consequence, mixing inside the core is low and is well separated from mixing outside the core. This separation of mixing regimes we interpret as why the low oxygen eddy core has been so constant in its water mass properties.

Having now the isolation explained as a consequence of eddy rotation and stratification and their joint

5  impact on the propagation of internal waves, it is tempting to investigate whether the vertical flux of nutrients into the euphotic layer of the eddy may also fit to this concept. The productivity associated with the ACME requires intense episodic or prolonged moderate upward fluxes of nutrients into the euphotic zone. From global assessments of productivity in mesoscale eddies based on satellite data (Chelton et al. 2011b; Gaube et al. 2015) the upwelling is identified in the centre of the eddies. Note,

10  that these studies do not explicitly consider ACME. Schütte et al. (2016) showed that low oxygen ACME do have productivity maxima (indicated by enhanced ocean color based Chlorophyll-a estimated) at the rim of the eddies, not at the centre. This may suggest that the vertical flux is also concentrated to the rim. Inspecting the glider section data (Fig. 3) does not show indications for upwelling in the centre, isopycnals in the core are flat and the core has only a weak (and vertical)

15  stratification. The mixed layer base is characterized by the very stable stratification and large gradients (e.g. 0.3 K m$^{-1}$ in temperature). The ship's thermosalinograph temperature data (Fig. 3a upper) show the eddy to be colder than the surroundings but also indicate that a local maximum in temperature is observed in the centre of the eddy, while local minima (0.2 K difference) at ±15 km distance from the centre. Considering the first glider oxygen section (IFM12, Fig. 2a), the upper of the two separate

20  minima is found very close to the depth of the mixed layer base and indicate that any exchange across the mixed layer by mixing processes must be very small.

Following up on the NIW discussion, we now consider the region outside the core and in the vicinity of the eddy. It is a reasonable assumption that a large fraction of the NIW energy originates from wind stress fluctuations (D'Asaro 1985). The NIW propagation in the upper layer of the eddy (above the

25  core) is primarily along the intense N contours/mixed layer base (Fig. 3c) and towards the eddy rim (shown in Sheen et al. 2015). At the eddy rim, but outside of the maximum N contour, the NIW can propagate downward (see Fig. 4 b,d) because $f_{eff} < 1$ (Fig. 5b). In this zone we observed the impact of the vertical propagation in the vertical shear profile directly via the modulation of the maximum swirl velocity (approximately Fig. 3a, at ~ −32 km distance).

30  In order to extract the velocity signal related to the NIW ($U'$), we subtracted the filtered (120 m boxcar filter) velocity profile data ($U_0$) from the observed profiles ($U$; Fig. 5c):

$$U = U_0 + U'$$

Magnitude and angle between the zonal and meridional NIW components of $U'$ show a vertically stacked pattern within the $f_{eff}$ region, suggesting the trapping of the NIW underneath the eddy (Lee

and Niiler 1998). The phase angle and its cyclonic rotation with depth indicate a downward propagation of the waves (Joyce et al. 2013). Another region where rotation and a maximum in amplitude is seen is the outer rim of the eddy in the region where $f_{eff}$ approaches 1, in the depth range between 50 and 120 m ($\sim$ −30 km). The NIWs have an amplitude of more than 0.1 m s$^{-1}$ and a vertical scale of about

5  70 to 90 m (Fig. 4d), similar to observations at mid latitude fronts (Kunze and Sanford 1984). The inertial radius for a wave with amplitude of 0. 1 m s$^{-1}$ is about 2 km. The NIW wave pattern underneath the eddy core aligns well with the pattern observed in the glider sections (Fig 2 and 3).

A Richardson gradient number $Ri_g = N^2/((\frac{\partial u}{\partial z})^2 + (\frac{\partial v}{\partial z})^2)$ cannot directly be estimated along the sections because no concurrent velocity and stratification section data exists. Considering single profile

10  data the shear in velocity is about 0.1 m s$^{-1}$ over 50 to 70 m depth (Fig. 3d) equals a variance of $0.2 - 0.4 \cdot 10^{-5}$ s$^{-2}$ that is implied along the wave propagation path. Outside of the mixed layer base N$^2$ maximum, a corresponding $Ri_g < 10$ can be expected to occur (see Fig. 2c), a value that may indicate generation of instabilities (Joyce et al. 2013).

Only vertical propagation of internal waves does not generate mixing, but the waves have to either

15  break (Kelvin-Helmholtz instabilities) or produce enough shear to generate critical layer absorption. When considering the maximum velocities (0.1m s$^{-1}$) associated with the NIW they account for about 25% of maximum swirl velocity. However, a region close to, but outside of, the maximum swirl velocity (about $\sim$ −32 km, 50 to 120m depth) is identified where $f_{eff} < 1$ and the NIW velocity ($U'$) is of similar magnitude as the flow ($U$) and thus susceptible for critical layer formation. Here the mean

20  flow could gain energy from the NIW but also vertical mixing. It has been shown that trapping of NIW inside an AE (Gulf Stream warm core ring, Joyce et al. 2013) generated most instabilities and mixing close to surface and where most horizontal shear in the baroclinic current is found. In case of the ACME discussed here, this is close to the mixed layer base and at 90 m depth (Fig. 4a) and potentially opening a pathway for properties from below into the mixed layer (and vice versa). Some evidence for

25  such a flux can be seen in the nitrate section (Fig. 6 b) that show a local maximum maybe associated with an upward filament at about 100 m depth/distance of about −32 km.

An asymmetry in the dynamical structure is seen for example in the $f_{eff}$ section (Fig. 5b). All sections run from south (most negative distance) to north and it is the southern part that is more coherent and energetic and this is also the flank were the NIW signal is strongest. It is possible that the interaction of

30  the eddy with the north-easterly trade winds play a role here because the eddy frontal flow is in the direction of the wind. Thomas (2005) showed the generation of a vertical flux at the mixed layer base that entrains water from underneath.

Below the eddy the S$_A$ gradients (Fig. 3a) do align well with the wave crests and that may indicate the impact of intense strain, and an thus a periodic intensification of S$_A$ gradients which in turn could

enhance the susceptibility to double diffusive mixing in regions where susceptibility of double diffusion is already indicated by the Tu distribution (Fig. 3d).

### 3.3 A nutrient budget for the eddy

In order to interpret the low oxygen concentrations in terms of biogeochemical processes, we calculated

5 the apparent oxygen utilization (AOU, Fig. 6a), which is defined as the difference between measured oxygen concentration and the oxygen concentration of a water parcel of the given $\theta$ and $S_A$ that is in equilibrium with air (Garcia and Gordon, 1992; 1993). AOU is an approximation for the total oxygen removal since a water parcel left the surface ocean. The low oxygen concentrations in the core of the eddy are equivalent to an AOU of about 240 µmol kg$^{-1}$ (Fig 6a). Along with high AOU we also find

10 very high $NO_3^-$ concentrations with a maximum of about 30 µmol kg$^{-1}$ (Fig 6b). The corresponding $AOU:NO_3^-$ ratio outside the core is 8.1 and thus close to the classical 8.625 Redfield ratio (138/16; Redfield et al. 1938). However, in the core an $AOU: NO_3^-$ ratio of >16 is found. This high ratio indicates that less $NO_3^-$ is released during respiration (AOU increase) than expected for a process following a Refieldian stoichiometry. By considering a linear fit to outside the core (Fig. 6c) the

15 respective $NO_3^-$ deficit can be estimated to up to 4-6 µmol kg$^{-1}$ for the highest AOU ($NO_3^-$) observations. By integrating $NO_3^-$ and $NO_3^-$-deficit over the core of the low oxygen eddy (defined here as the volume occupied by water with oxygen concentrations < 40 µmol kg$^{-1}$) we obtain a average $AOU: NO_3^-$ ratio of about 20:1.

One way to interpret this deficit is by $NO_3^-$ loss through denitrification processes. Loescher et al. (2015)

20 and Grundle et al. (in revision) both found evidence for the onset of denitrification in the core of the ACME discussed here. Oxygen concentrations in the core are very low (about 3 µmol kg$^{-1}$) and denitrification is possible. Evidence for denitrification in the core of the ACME was, however, demonstrated as being important for $N_2O$ cycling at the nanomolar range (Grundle et al. in revision), and not necessarily for overall $NO_3^-$ losses which are measured in the micromolar range. Estimates of

25 N* from the ACME show that even in the core of the ACME $NO_3^-$ losses were not detectable at the micromolar range (Fig. 6d). Thus, while denitrification may have played a minor role in causing the higher than expected $AOU:NO_3^-$ ratio which we have calculated, it is unlikely that it contributed largely to the loss of 5% of all $NO_3^-$ from the eddy as estimated based on the observed $AOU:NO_3^-$ ratios.

Alternatively, but perhaps not exclusively, the $NO_3^-$ recycling within the ACME could be the reason for

30 the $NO_3^-$ deficit. A high $AOU: NO_3^-$ ratio could be explained through a decoupling of $NO_3^-$ and oxygen recycling pathways in the eddy. In this scenario $NO_3^-$ molecules are used more than one time for the remineralization/respiration process and therefore the AOU increase without a balanced $NO_3^-$ remineralization. Such a decoupling can be conceptualized as follows (Fig. 7): consider an upward flux of dissolved $NO_3^-$ and oxygen in a given ratio with an amount of water that originates from the low

12

oxygen core. The upward flux partitions when reaching the mixed layer, one part disperses in the open waters outside of the eddy, the other part is keep in the eddy by retention (D'Ovidio et al. 2013). The upwelled $NO_3^-$ is utilized by autotrophs for primary production and thereby incorporated into particles (PON) while the corresponding oxygen production is ventilated to the atmosphere. The PON sinks out

5    of the mixed layer/euphotic zone and into the core of the eddy were remineralization of organic matter releases quickly some of the same $NO_3^-$ back into the core. In contrast, the upwelling of oxygen-deficient waters will drive an oxygen flux from the atmosphere into the ocean in order to reach chemical equilibrium. But because the stoichiometric equivalent of oxygen is lost to the atmosphere and therefore not transported back into the core by gravitational settling of particles, as is the case for nitrate

10   (via PON), the respiration associated with the remineralization of the recycled nitrate will results in a net increase in AOU. A potential problem with this concept is that the $NO_3^-$/oxygen from the eddy core is primarily outward, so it must be more an erosion rather then a flux, because a flux would also transport from outside into the core and thus slowly altering the core properties (which is not observed). It could be an erosion process that maintains an stability maximum along with the exchange and maybe

15   related to interleaving (Beal 2007). Further work is needed to understand this process in full.


## 4 Summary and Conclusion

Here we present a first analysis of high-resolution multidisciplinary glider and ship survey data of a low oxygen anticyclonic mode-water eddy (ACME) in the eastern tropical North Atlantic. The eddy has a diameter of about 70 to 80 km and maximum swirl velocity of 0.4 m s$^{-1}$ (at about 90 m depth) and can

20   be considered typical for the region (Schütte et al. 2015, 2015; Karstensen et al. 2015). The eddy originated from the Mauritanian upwelling region (Schütte et al. 2016; Fiedler et al. 2016) and had a distinct, anomalously fresh (and cold), water mass in its core that was located immediately below the mixed layer base (about 70 to 80 m) and a depth of 200 to 250 m. The core showed minimum oxygen concentrations of 8 μmol kg$^{-1}$ during the first glider survey (February 2014) and 3 μmol kg$^{-1}$ during the

25   second glider survey, 9 weeks later. Enhanced productivity was estimated for the eddy (Fiedler et al. 2016), implying a vertical flux of nutrient rich waters to the euphotic zone/mixed layer. A concept for the isolation of the core but enhanced vertical flux of nutrients in parallel was derived (Fig. 7). The velocity observations indicate that the eddy had a very distinct impact on the propagation of near inertial internal waves as expected (Kunze 1985, Kunze et al. 1995, Sheen et al. 2015). The

30   combination of a negative vorticity anomaly of an anticyclonic rotating eddy and a maximum in stratification that encloses the ACME's low oxygen core on the one side traps the NIW to the eddy vicinity but also prevent NIW to enter the core. A velocity shear variance maximum is found below the eddy that is interpreted as an NIW energy maximum, as seen from model simulations of NIW propagation around ACME (Lee and Niiler 1998). Outside the low oxygen core, at the upper bound of

35   the stability maximum, we expect enhanced mixing to occur, as shown for ACME in the deep ocean

13

Biogeosciences

Open Access

Discussions

EGU

(Sheen et al. 2015). Moreover, for AE it has been reported that in the depth range were the NIW interact with the maximum baroclinic flow (in our case at about 90 m) enhanced mixing can occur (Joyce et al. 2013) possibly by critical layer formation. Our analysis suffers from not having concurrent hydrography and currents data, and limited options for estimating balances (e.g. Richardson numbers) exists.

5   However, if we transfer the findings by Joyce et al. (2013) to our eddy the enhanced mixing would be at the mixed layer base, but outside the eddy. An asymmetry in the dynamical structure of the eddy is observed (not so much in hydrography though) with a more intense front in the southern part of the section and which is directly under the impact of the Ekman flow generated by the Norteast Trade winds. A NIW induced mixing would create an upward flux of nutrients, also supported by the $NO_3^-$

10  distribution. Once $NO_3^-$ is in the mixed layer the eddy retention (D'Ovidio et al. 2013) will trap a fraction of the upwelling waters. The $AOU:NO_3^-$ ratio of the eddy core is altered high (16) when compared with the classical Redfield ratio (8.625) or the background ratio (8.1). We estimated the $NO_3^-$ deficit for the eddy which is about 1:20 when referenced to the total $NO_3^-$ content. Denitrification is one possible process but the significant nitrate loss of the core seems unrealistic. What is more likely is a

15  local recycling of N but not oxygen and connected to the transfer of upwelled $NO_3^-$ from the core via sinking of PON. The isolation of the eddy core in combination with high productivity is a prerequisite for the formation of the low oxygen core and as such analogue to the formation of a "dead-zones", known to occur in coastal and limnic systems (Karstensen et al. 2015). The isolated core is the rare case of an isolated volume of water in the open ocean and which allow to study fundamental biogeochemical

20  cycling processes in the absence of significant physical transport processes. A number of surprising biogeochemical cycling processes and ecosystem responses have been reported from the studies on eastern tropical North Atlantic low-oxygen eddies (Löscher et al. 2015, Hauss et al. 2016, Fiedler et al. 2016; Fischer et al. 2016, Grundle et al. in revision, Schütte et al. 2016). The NIW concept for the vertical flux outside the core but likewise the isolation of the ACME core that we presented here is

25  based on internal wave processes that are not routinely resolved by numerical models. A strategy for parameterizing of these processes is however required considering the estimate by Schütte et al. (2016) who showed that the enhanced respiration in low oxygen eddies contribute about 20% to net respiration that creates the shallow oxygen minimum of the eastern tropical Atlantic.

**Acknowledgment**

14

**Biogeosciences**
Discussions

5

**References**

Alford, M.H., J.A. MacKinnon, H.L. Simmons, J.D. Nash, Near-Inertial Internal Gravity Waves in the Ocean, Annual Review of Marine Science 8, 95-123, 2016

Armi, L., and W. Zenk, Large lenses of highly saline Mediterranean water. J. Phys. Oceanogr., 14,
10      1560–1576, doi:10.1175/1520-0485(1984)014,1560:LLOHSM.2.0.CO;2., 1984

Beal, L.M., Is Interleaving in the Agulhas Current Driven by Near-Inertial Velocity Perturbations?. J. Phys. Oceanogr., 37, 932–945. doi: http://dx.doi.org/10.1175/JPO3040.1, 2007.

Booker, J.R. and Francis P. Bretherton, The critical layer for internal gravity waves in a shear flow. Journal of Fluid Mechanics, 27, pp 513-539 doi:10.1017/S0022112067000515, 1967.

15  Chaigneau, A., Eldin, G. and Dewitte, B.: Eddy activity in the four major upwelling systems from satellite        altimetry        (1992–2007),        Prog.        Oceanogr.,        83(1-4),        117–123, doi:10.1016/j.pocean.2009.07.012, 2009

Chaigneau, A., Le Texier, M., Eldin, G., Grados, C., and Pizarro, O.: Vertical structure of mesoscale eddies in the eastern South Pacific Ocean: A composite analysis from altimetry and Argo profiling
20      floats, Journal of Geophysical Research: Oceans, 116, C11025, 2011.

Chelton, D. B., Schlax, M. G. and Samelson, R. M.: Global observations of nonlinear mesoscale eddies, Prog. Oceanogr., 91(2), 167–216, doi:10.1016/j.pocean.2011.01.002, 2011a

Chelton, D., P. Gaube, M. Schlax, J. Early, and R. Samelson, The influence of nonlinear mesoscale eddies on near-surface oceanic chlorophyll. Science, 334, 328–332, doi:10.1126/ science.1208897,
25      2011b

Dewar, W.K. and G. R. Flierl, Some Effects of the Wind on Rings. J. Phys. Oceanogr., 17, 1653–1667. doi: http://dx.doi.org/10.1175/1520-0485, 1987.

D'Asaro, E., The energy flux from the wind to near-inertial motions in the mixed layer, J. Phys. Oceanogr., 15, 943–959, 1985.

30  D'Asaro, E.A., Generation of submesoscale vorticies: a new mechanism. J. Geophys. Res. 93, 6685–6693, 1988.

D'Ovidio F., De Monte S., Della Penna A., Cotté C. and Guinet C., Ecological implications of oceanic eddy retention in the open ocean: a Lagrangian approach. J. Phys. A: Math. Theor. 46: 254023 (doi:10.1088/1751-8113/46/25/254023), 2013.

15

Eden, C., and H. Dietze, Effects of mesoscale eddy/wind interactions on biological new production and eddy kinetic energy, J. Geophys. Res., 114, C05023, doi:10.1029/2008JC005129., 2009.

Fiedler, B., Grundle, D., Schütte, F., Karstensen, J., Löscher, C. R., Hauss, H., Wagner, H., Loginova, A., Kiko, R., Silva, P., and Körtzinger, A.: Oxygen Utilization and Downward Carbon Flux in an Oxygen-Depleted Eddy in the Eastern Tropical North Atlantic, Biogeosciences Discuss., doi:10.5194/bg-2016-23, in review, 2016.

Fischer, G., Karstensen, J., Romero, O., Baumann, K.-H., Donner, B., Hefter, J., Mollenhauer, G., Iversen, M., Fiedler, B., Monteiro, I. and Körtzinger, A.: Bathypelagic particle flux signatures from a suboxic eddy in the oligotrophic tropical North Atlantic: production, sedimentation and preservation, Biogeosciences Discuss., 12(21), 18253–18313, doi:10.5194/bgd-12-18253-2015, 2015.

Garcia, H.E., and L.I. Gordon, Oxygen solubility in seawater: Better fitting equations. Limnology and Oceanography, 37, 1307-1312, 1992.

Garcia, H.E., and L.I. Gordon, Erratum: Oxygen solubility in seawater: better fitting equations. Limnology and Oceanography, 38, 656, 1993.

Gaube, P., D.B. Chelton, R. M. Samelson, M.G. Schlax, and L.W. O'Neill, Satellite Observations of Mesoscale Eddy-Induced Ekman Pumping. J. Phys. Oceanogr., 45, 104–132. doi: http://dx.doi.org/10.1175/JPO-D-14-0032.1, 2015.

Gregg, M.C., E.A. D'Asaro, T.J. Shay, and N. Larson, Observations of Persistent Mixing and Near-Inertial Internal Waves. J. Phys. Oceanogr., 16, 856–885. doi: http://dx.doi.org/10.1175/1520-0485(1986)016<0856:OOPMAN>2.0.CO;2, 1986.

Gregg, M. C., Scaling turbulent dissipation in the thermocline, J. Geophys. Res., 94(C7), 9686–9698, doi:10.1029/JC094iC07p09686, 1989.

Hahn, J., Brandt, P., Greatbatch, R., Krahmann, G., and Körtzinger, A., Oxygen variance and meridional oxygen supply in the Tropical North East Atlantic oxygen minimum zone, Climate Dynamics, 43, 2999–3024, 2014.

Hauss, H., Christiansen, S., Schütte, F., Kiko, R., Edvam Lima, M., Rodrigues, E., Karstensen, J., Löscher, C. R., Körtzinger, A. and Fiedler, B.: Dead zone or oasis in the open ocean? Zooplankton distribution and migration in low-oxygen modewater eddies, Biogeosciences Discuss., 12(21), 18315–18344, doi:10.5194/bgd-12-18315-2015, 2016.

Hua, B. L., C. Menesguen, S. L. Gentil, R. Schopp, B. Marsset, and H. Aiki, Layering and turbulence surrounding an anticyclonic oceanic vortex: in situ observations and quasi-geostrophic numerical simulations, J. Fluid Mech., 731, 418-442, 2013.

IOC, SCOR and IAPSO, The international thermodynamic equation of seawater − 2010: Calculation and use of thermodynamic properties. Intergovernmental Oceanographic Commission, Manuals and Guides No. 56, UNESCO (English), 196 pp., 2010.

**Biogeosciences**  Open Access
Discussions  EGU

Johnson, K. S., L. J. Coletti, H, W. Jannasch, C.M. Sakamoto, D. Swift, S. C. Riser, Long-term nitrate measurements in the ocean using the In Situ Ultraviolet Spectrophotometer: sensor integration into the Apex profiling float. Journal of Atmospheric and Oceanic Technology, 30, 1854-1866, 2013.

Joyce, T. M., J. M. Toole, P. Klein, and L. N. Thomas, A near-inertial mode observed within a Gulf
5    Stream warm-core ring, J. Geophys. Res. Oceans, 118, 1797–1806, doi:10.1002/jgrc.20141, 2013.

Karstensen, J., Fiedler, B., Schütte, F., Brandt, P., Körtzinger, A., Fischer, G., Zantopp, R., Hahn, J., Visbeck, M., and Wallace, D.: Open ocean dead zones in the tropical North Atlantic Ocean, Biogeosciences, 12, 2597-2605, 2015.

Kostianoy, A., Belkin, I., A survey of observations on intrathermocline eddies in the world ocean. In
10    Mesoscale/Synoptic Coherent Structures in Geophysical Turbulence, Nihoul, J., Jamart, B. (eds.) Vol. 50, 821–841 (Elsevier, New York). 1989.

Koszalka, I. M., Ceballos, L. and Bracco, A., Vertical mixing and coherent anticyclones in the ocean: the role of stratification Nonlinear Processes in Geophysics, 17 (1). pp. 37-47. DOI 10.5194/npg-17-37-2010, 2010.

15  Krahmann, G., P. Brandt, D. Klaeschen, and T. Reston, Mid-depth internal wave energy off the Iberian Peninsula estimated from seismic reflection data, J. Geophys. Res., 113, C12016, doi:10.1029/2007JC004678, 2008.

Kunze, E., Near-inertial wave propagation in geostrophic shear, J. Phys. Oceanogr., 15, 544–565, 1985.

Kunze, E., R. W. Schmidt, and J. M. Toole, The energy balance in a warm core ring's near-inertial
20    critical layer. J. Phys. Ocean- ogr., 25, 942–957, 1995.

Ledwell J.R., D.J. McGillicuddy Jr., L.A. Anderson, Nutrient flux into an intense deep chlorophyll layer in a mode-water eddy, Deep-Sea Research, 55, 1139–1160, 2008.

Lee, D., and P. Niiler, The inertial chimney: The near-inertial energy drainage from the ocean surface to the deep layer. J. Geophys. Res., 103 (C4), 7579–7591, 1998.

25  Lévy, M., Ferrari, R., Franks, P. J. S., Martin, A. P., and Rivière, P.: Bringing physics to life at the submesoscale, Geophys. Res. Lett., 39, L14602, doi:10.1029/2012GL052756, 2012.

Löscher, C. R., Fischer, M. A., Neulinger, S. C., Fiedler, B., Philippi, M., Schütte, F., Singh, A., Hauss, H., Karstensen, J., Körtzinger, A., Künzel, S. and Schmitz, R. A.: Hidden biosphere in an oxygen-deficient Atlantic open ocean eddy: future implications of ocean deoxygenation on primary
30    production in the eastern tropical North Atlantic, Biogeosciences, 12, 7467-7482, doi:10.5194/bg-12-7467-2015, 2015.

Mahadevan, A., Thomas, L. N., Tandon, A., Comment on Eddy/Wind Interactions Stimulate Extraordinary Mid-Ocean Plankton Blooms. Science 320, 448, 2008.

McDougall, T.J. and P.M. Barker, Getting started with TEOS-10 and the Gibbs Seawater (GSW)
35    Oceanographic Toolbox, 28 pp., SCOR/IAPSO WG127, ISBN 978-0-646-55621-5, 2011.

McDougall, T.J., and O.A. Krzysik, Spiciness. Journal of Marine Research, 73, 141-152, 2015.

17

**Biogeosciences** Discussions

McDougall, T. J., Jackett, D. R., Millero, F. J., Pawlowicz, R., and Barker, P. M.: A global algorithm for estimating Absolute Salinity, Ocean Sci., 8, 1123-1134, doi:10.5194/os-8-1123-2012, 2012.

McGillicuddy, D. J., Anderson, L. A., Bates, N. R., Bibby, T., Buesseler, K. O., Carlson, C. A., Davis, C. S., Ewart, C., Falkowski, P. G., Goldthwait, S. A., Hansell, D. A., Jenkins, W. J., Johnson, R., Kosnyrev, V. K., Ledwell, J. R., Li, Q. P., Siegel, D. A. and Steinberg, D. K.: Eddy/Wind Interactions Stimulate Extraordinary Mid-Ocean Plankton Blooms, Science, 316 (5827), 1021–1026, doi:10.1126/science.1136256, 2007.

McWilliams, J.C., Submesoscale, coherent vortices in the ocean, Rev. Geophys., 23(2), 165–182, doi:10.1029/RG023i002p00165. 1985.

Redfield, A. C., Ketchum, B. H. and Richards, F. A.: The influence of organisms on the composition of seawater, in The Sea. Interscience, edited by M. N. Hill, pp. 26–77, 1963.

Sakamoto, C.M., Johnson, K.S. and Coletti, L.J., An improved algorithm for the computation of nitrate concentrations in seawater using an in situ ultraviolet spectrophotometer. Limnol. Oceanogr. Methods 7, 132-143, 2009.

Schütte, F., Karstensen, J., Krahmann, G., Hauss, H., Fiedler, B., Brandt, P., Visbeck, M., and Körtzinger, A.: Characterization of "dead-zone" eddies in the tropical Northeast Atlantic Ocean, Biogeosciences Discuss. , doi:10.5194/bg-2016-33, in review , 2016.

Schütte, F., Brandt, P. and Karstensen, J.: Occurrence and characteristics of mesoscale eddies in the tropical northeast Atlantic Ocean, Ocean Sci. Discuss., 12(6), 3043–3097, doi:10.5194/osd-12-3043-2015, 2015.

Sheen, K. L., J. A. Brearley, A. C. Naveira Garabato, D. A. Smeed, L. St Laurent, M. P. Meredith, A. M. Thurnherr, and S. N. Waterman, Modification of turbulent dissipation rates by a deep Southern Ocean eddy, Geophys. Res. Lett., 42, 3450–3457, doi:10.1002/2015GL063216, 2015.

St. Laurent, L., and R.W. Schmitt, 1999: The Contribution of Salt Fingers to Vertical Mixing in the North Atlantic Tracer Release Experiment. J. Phys. Oceanogr., 29, 1404–1424. doi: http://dx.doi.org/10.1175/1520-0485(1999)029<1404:TCOSFT>2.0.CO;2, 1999

Thomas, L. N., 2005: Destruction of potential vorticity by winds. J. Phys. Oceanogr., 35, 2457– 2466.

Thomas, L. N., Formation of intrathermocline eddies at ocean fronts by wind-driven destruction of potential vorticity, Dynam. Atmos. Oceans, 45, 252-273, 2008.

Whitt, D. B., and L. N. Thomas, Near-inertial waves in strongly baroclinic currents, Journal Physical Oceanography, doi:10.1175/JPO-D-12-0132.1, 2013

Zhang, Z., Zhang, Y., Wang, W., and Huang, R. X.: Universal structure of mesoscale eddies in the ocean, Geophysical Research Letters, 40, 3677-3681, 2013.

Biogeosciences

Discussions

Open Access

EGU
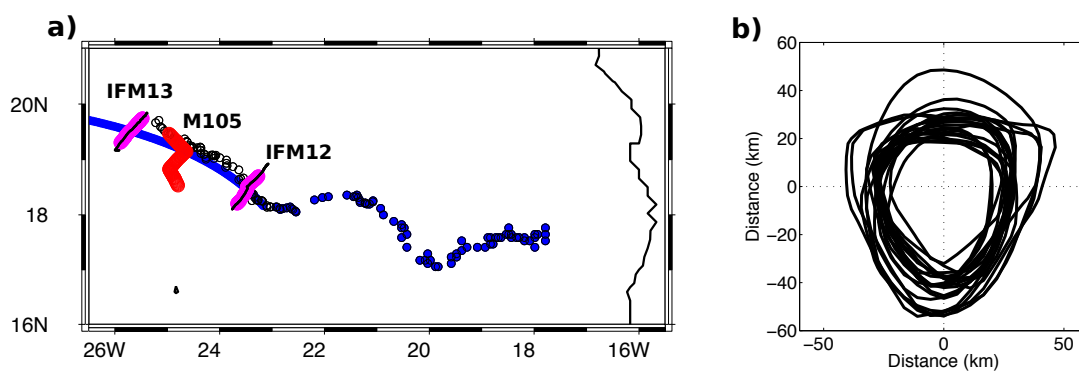
**Figures**



5  **Figure 1 (a) Location of the two glider surveys (black dots and magenta dots; IFM12, IFM13) and the ship survey (red dots; M105) in geographical context with our best estimate of the eddy centre trajectory from sea level anomaly data (see e.g. Fiedler et al. 2016). The smoothed trajectory west of about 23°W is derived from visible inspection, elsewhere it is based on an automatic tracking algorithms (see Schütte et al. 2015, 2016). (b) The eddy diameter from sea level anomaly data during the IMF12 survey projected on the eddy centre.**
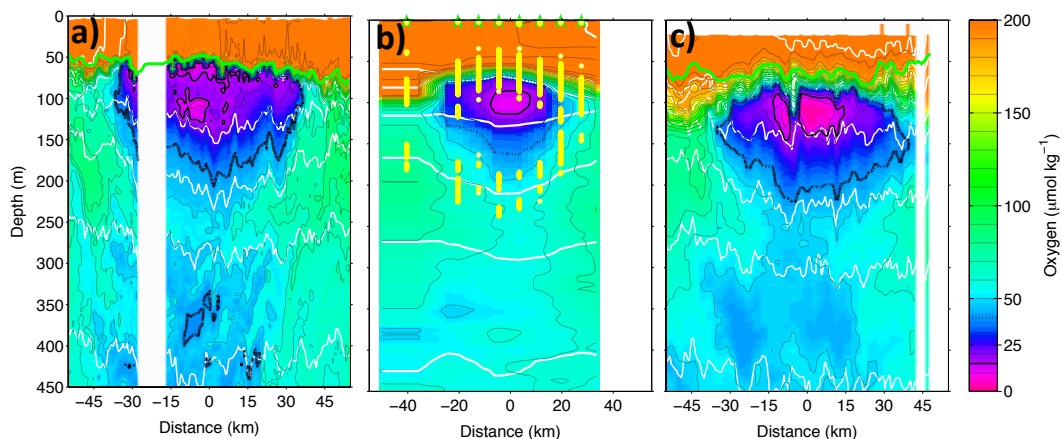
10

Figure 2: Oxygen distribution from the three surveys (locations of the surveys see Fig. 1) over a similar distance (-55 to 55 km relative to a subjectively selected eddy centre) a) IFM12, b) M105, and c) IFM13. The 15 µmol kg$^{-1}$ (40 µmol kg$^{-1}$) oxygen contour is indicated as bold (stippled) line, selected density anomaly contours are shown as white lines (Δσ = 0.2 kg m$^{-3}$). The green line indicates the mixed layer depth. The oxygen contour in b) was gridded based on the 8 stations (locations indicated by green stars) and mapped to a linear section in latitude, longitude. The yellow dots indicate positions of local stability maxima.

20

Biogeosciences
Discussions

Open Access

EGU
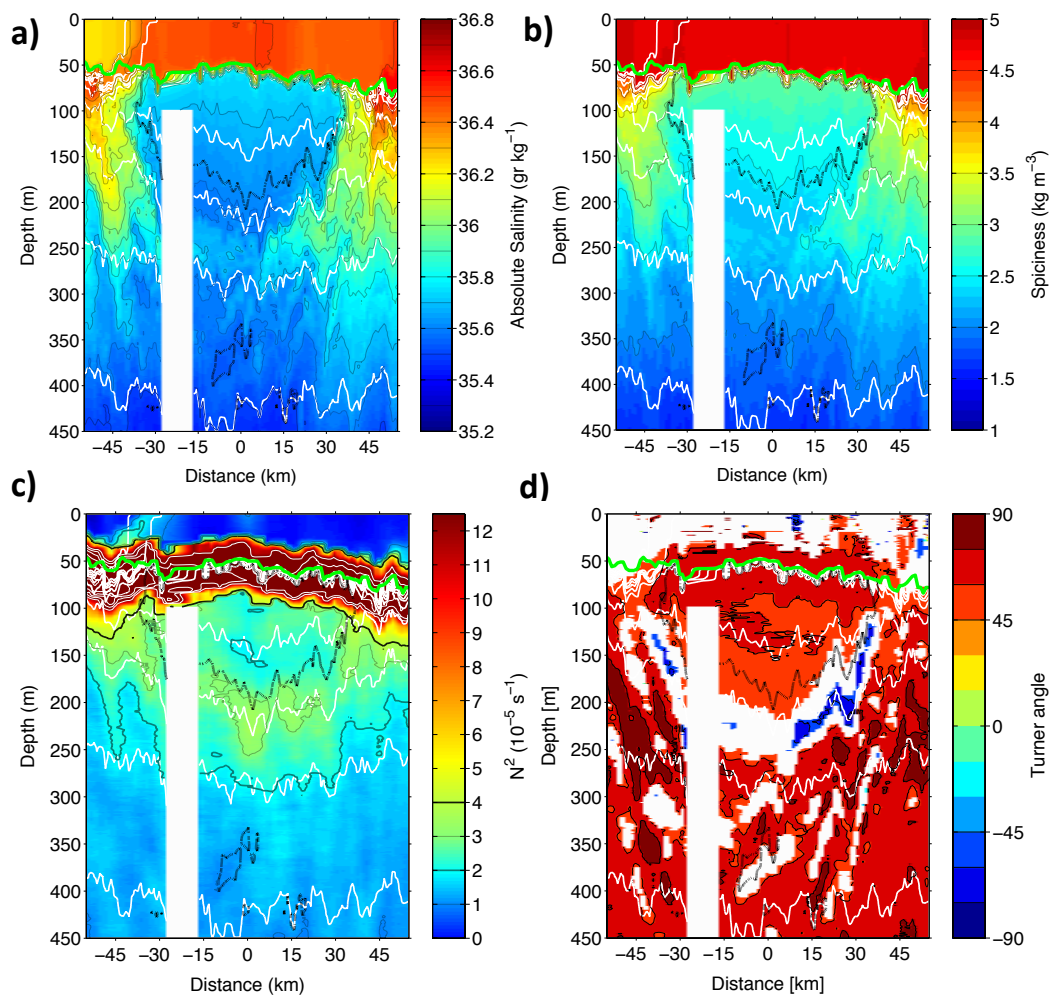


Figure 3: a) $S_A$, b) spiciness, c) buoyancy frequency/stability ($N^2$), d) Turner angle (only segment |45| to |90| is shown). All section are from IFM12. The thick black broken line indicates the 40 µmol kg$^{-1}$ oxygen concentration (see Fig. 2). Colour coding and selected contours see individual colour bar. Selected density anomaly contours are shown as white lines ($\Delta\sigma$ = 0.2 kg m$^{-3}$). The green line indicates the mixed layer depth.
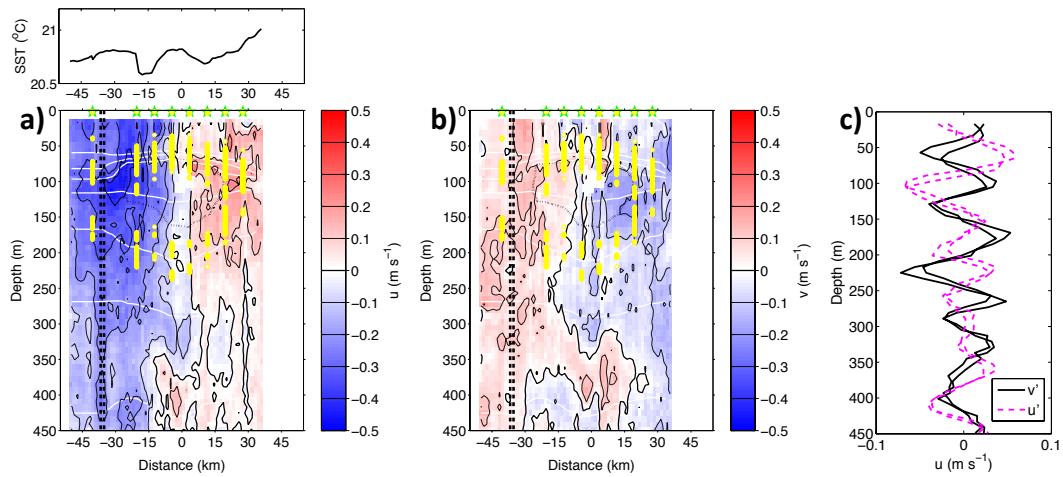
**Figure 4: a) Zonal velocity section (with thermosalinograph temperature on top), b) Meridional velocity section, c) Profiles (24 m box car filtered) of residual velocity after subtracting a 120m box car profile from observed (8 m bin) ADCP profile data (for location see vertical broken lines in a & b). In a & b the 40 µmol kg$^{-1}$ oxygen concentration (see Fig. 2) as well as selected density anomaly contours (a, c, Δσ=0.2 kg m$^{-3}$) are shown, derived from gridded CTD profile data (station marked by green stars). In a, b the yellow dots indicate the N$^2$ maximum from the CTD profiles.**

22

Biogeosciences

Discussions

Open Access

EGU
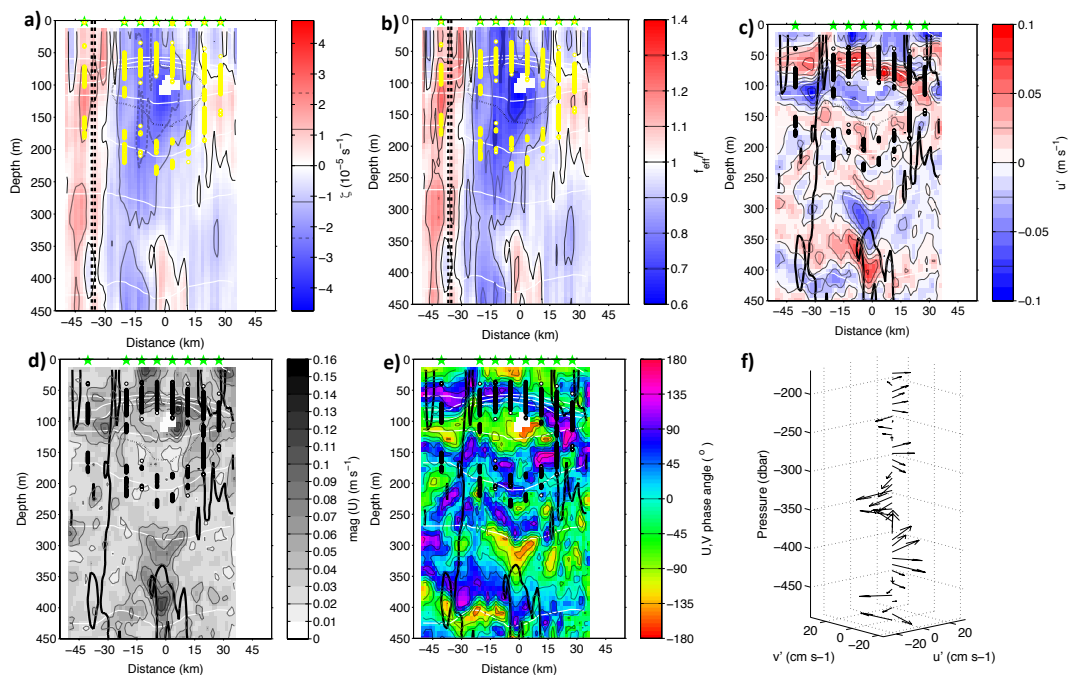


**Figure 5: From M105 survey: a) Vertical vorticity (colourscale covers the range +- *f*), b) effective planetary vorticity *f_eff*, c) zonal U' component (see also Fig. 4c for example profiles) d) magnitude of U' e) phase angle between u' and v' components, f) Phase angle at 0 km distance and only underneath the low oxygen core of the ACME. Vertical broken line in a), b) at about -32km distance indicate position of profiles Fig. 4c. For colour and line coding see individual colour bar. The yellow (black) dots in a, b (c, d, e) indicate the $N^2$ maximum from the CTD profiles. The white contours indicate selected isopycnals, black contour in c), d), e) is the $f_{eff}$=1 contour (See Fig. 5b).**
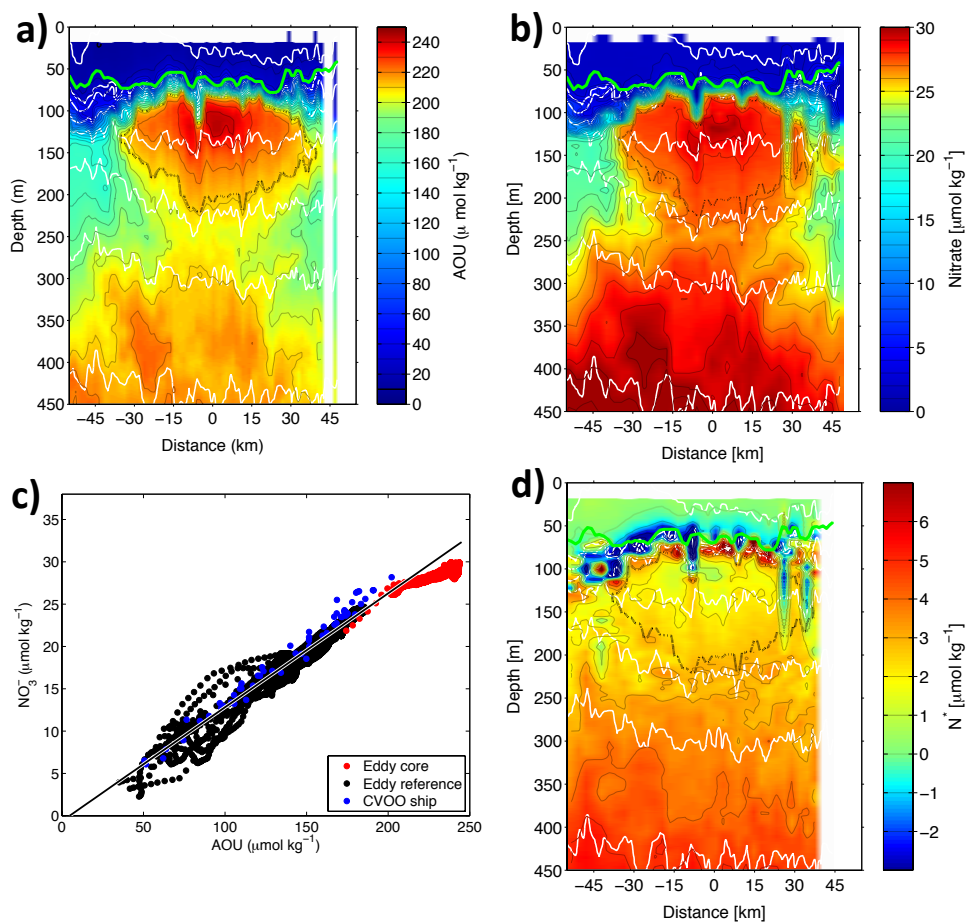
**Figure 6: a)** AOU and **b)** NO$_3^-$ from IFM13 glider survey. **c)** AOU versus NO$_3^-$ for the depth range 90 to 250m depth: (red dots) IFM13 glider survey in the low oxygen core, (black dots) IFM13 glider survey close to CVOO, (blue dots) CVOO ship data (see Fielder et al. 2016). The black line is the linear fit to all data (slope 8.1) and used to estimate an NO$_3^-$ deficit in the low oxygen core.
5   **d)** N* estimated from NO$_3^-$, AOU/(8.625), note, negative values close to mixed layer are related to different sensor response time of oxygen optode and SUNA and not further discussed.
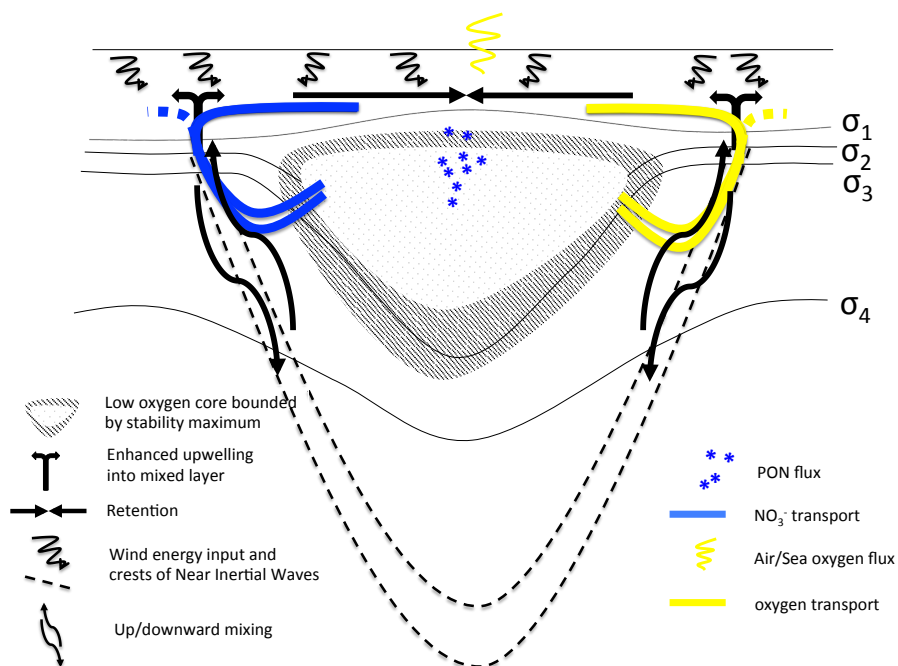
**Figure 7: Conceptual view of the physical and biogeochemical processes responsible for creating a low oxygen ACME. The recycling of Nitrate is decoupled from the oxygen cycling through the particulate matter phase (PON). The transport at the flanks and isolation of the eddy core are linked to the vertical stability ($N^2$) and the downward energy propagation of near inertial internal waves, which in turn drive enhanced mixing and thus vertical flux (upwelling and downwelling) of nutrient rich/oxygen low waters at boundaries of the eddy. The retention process ensures that part of the upwelled waters are trapped in the euphotic zone of the eddy and used for productivity. The separation (left/right) of oxygen (yellow) and $NO_3^-$ (blue) fluxes is for clarity reasons.**

_

# 6 Summary

In this thesis the characteristics of mesoscale eddies and their impacts on heat, salt and oxygen budgets of the ETNA region are examined. A combination of multiple ocean observing platforms (moorings, Argo floats, satellites, ships, gliders) is used to assess the general mesoscale activity. From various satellite data sets mean eddy surface patterns are constructed, in combination with vertical in-situ measurements mean vertical eddy anomalies of various properties relative to the background waters are calculated. The analysis reveals that an eddy-type depended connection between SLA and SST signatures of eddies in the ETNA exist, enabling the detection and examination of a third eddy type, a so-called ACME, from space. Based on this an eddy alert system was set up to identify and track ACMEs for detailed surveys. In early 2014 a multidisciplinary survey was performed. It included high-resolution glider surveys that resolve processes on the submesoscale ($100\ m$ to $10\ km$), enabling the investigation of vertical transport processes within and/or around the eddy.

## 6.1 Progress on scientific key questions

In the following the scientific key questions for this thesis raised in the introduction (Chapter 1.5) will be answered based on the results presented above.

**1) What are the characteristics of eddies generated in the ETNA region?**
(Chapter 2 and Chapter 3)

In the eastern boundary upwelling system of the North Atlantic (12-22°N and 15-26°W) about $146 \pm 4$ eddies per year with a minimum lifetime of 7 days are identified (52% cyclones, 39% anticyclones, 9% ACMEs). Corresponding SLA, SST and SSS signatures of these eddies are identified and two types of anticyclonic rotating eddies (identified by elevated SLA) could be distinguished. Using profile data from Argo floats, ships, and moorings, the two anticyclonic types of eddies are classified as "classical anticyclones" with a warm, saline surface (about 80% of all anticyclones) and as "anticyclonic modewater eddies (ACMEs)" with a cold and fresh surface (about 20% of all anticyclones). Cyclones are associated with a depression of SLA and a cold and fresh surface. All types of eddies have similar radii of $56 \pm 12\ km$ and most of them originate at the West African coast, where they seem to be generated at three distinct coastal headland regions (Cap-Vert, Saint-Louis (Senegal) and Cap-Timris (Mauretania)). Most of the eddies are generated in boreal summer, whereas cyclones form preferably in early summer while anticyclones and ACMEs are mostly generated in late summer. Thereby, elevated eddy generation and phases of strongest boundary current velocities, triggered by the seasonality of the wind

forcing, seem to be linked. It is assumed that the eddy generation is driven by flow separation of the eastern boundary currents at the headlands of the West African coast. As a consequence of the earth's rotation ($\beta$-effect), the eddies then propagate westward from their generation region, with a mean speed of about $3 \pm 2.15$ *km* per day. In the latitudinal band between 12°N and 22°N it takes on average 8 to 9 months for an eddy to propagate from the coast to the ventilated gyre regime north of the CVFZ. During their propagation they follow distinct corridors with a small meridional deflection dependent on the eddy type (anticyclones equatorwards, cyclones poleward, ACMEs no deflection). The mean "lifetime" of eddies, defined as the time they can be continuously observed, is about 30 days - however, some can be tracked for more than one year. Anticyclonic eddies tend to dominate the amount of eddies with longer life times, whereas for shorter lifetimes the relative occurrence of anticyclonic and cyclonic eddies is balanced.

**2) What is the mean vertical structure of the different eddy types in the ETNA region?** (Chapter 3 and Chapter 4)

Cyclones, anticyclones, and ACMEs are characterized by different structures in isopycnal surfaces. Anticyclones carry warm and saline water anomalies, whereas cyclones and ACMEs host colder and less saline water in their cores. This results in a positive density anomaly associated with cyclones (elevation of isopycnals throughout their vertical extent) and a negative density anomaly associated with anticyclones (deepening of isopycnals throughout their vertical extent). ACMEs however, show a positive density anomaly in the upper 100 *m* (elevation of isopycnals) and a negative density anomaly below down to about 350 *m* (deepening of isopycnals). Hence, the mode water in the core of the ACMEs is only weakly stratified. For all types of eddies, the maximum temperature anomaly is located below the mixed layer, at a depth of about 50 *m*, whereas the maximum salinity anomaly is located slightly below that depth. Cyclones (anticyclones) transport a temperature/salinity anomaly ($\pm$ standard deviation) of -2.42 $\pm$ 1.23 °C/-0.34 $\pm$ 0.25 (1.88 $\pm$ 1.37°C/0.25 $\pm$ 0.2), whereas ACMEs transport temperature/salinity anomalies, which are a factor of about 2 higher, of -4 $\pm$ 2.2 °C/0.72 $\pm$0.38. For all eddy types temperature, salinity, and density anomalies reach down to about 300-350 *m* depths. All of the detected eddies are nonlinear, meaning the maximum circumpolar geostrophic surface velocity is higher than the translation speed of the eddy. This implies that fluid is "trapped" within the eddy (coastal water of their generation region mostly composed of SACW) and the exchange with surrounding waters (mostly NACW) is reduced. The different eddy types have a different potential in trapping SACW. Cyclones contain on average 16% (core value 35%) more SACW than the surrounding water and ACMEs trap even 21% (core value 60%). In contrast, anticyclones even contain on average 4% (core value 10%) more NACW than the surrounding water. This implies a negative heat and salt anomaly along isopycnals layers inside cyclones and ACMEs and a small positive heat and salt anomaly along isopycnals layers inside anticyclones.

Furthermore, the ACME and cyclone cores could be associated with the formation of intense oxygen depleted areas. The strongest oxygen anomalies are located in the upper water column, just beneath the mixed layer. Cyclones feature on average maximum negative oxygen anomalies

of around -100 $\mu mol kg^{-1}$ compared to the surrounding water at around 70 $m$ depth and ACMEs around -120 $\mu mol kg^{-1}$ at around 100 $m$ depth in the eddy core. At these depths, the horizontal extent of the mean oxygen anomaly is about 100 $km$ for ACMEs and 70 $km$ for cyclones. Beneath 150 $m$ depth, magnitude and extent of the oxygen anomalies decrease rapidly for both eddy types.

**3) What is the impact of eddies on heat, salt and oxygen distributions in the ETNA region?** (Chapter 3 and Chapter 4)

All identified eddies serve as transport agents exporting water from the coast westwards (due to the beta-effect) into the open ocean. Using inferred temperature and salinity anomalies mentioned above, the associated heat (salt) transports for the different eddy types can be calculated. They amount to -4.6 x $10^11$ $W$ (-23.15 x $10^3$ $kgs^{-1}$) for cyclones, 3.5 x $10^11$ $W$ (12.9 x $10^3$ $kgs^{-1}$) for anticyclones, and -4.9 x $10^11$ $W$ (-29.9 x $10^3$ $kgs^{-1}$) for ACMEs. Interestingly, heat and salt anomalies carried by cyclones and classical anticyclones roughly balance each other, causing only little effect on the regional budget. However, AMCEs transport very large anomalies and therefore - despite their lower frequency of occurrence  are associated with the strongest fluxes. However, out of a total of 21 eddies formed each year along the eastern boundary, 5 dissipate in a band of about 250 $km$ width near the coast and about 16 propagate into the open ocean, which results in an annual eddy net heat (salt) transport of about 50 x $10^11$ $W$ (-150 x $10^3$ $kgs^{-1}$). The eddy transport of colder coastal waters towards the offshore ocean, where warmer waters prevail, can be associated with a cooling of the ocean and can explain about 10% of the net surface heat flux in that region. Considering the total tracer transport of the eddies along isopycnals (spiciness), the negative heat and salt anomaly within cyclones and ACMEs results in a mean volume transport of 2.07 $Sv$ of SACW from the boundary current region. About 0.36 $Sv$ of this SACW transport reaches the subtropical gyre region northwest of the Cape Verde Islands. Hence, the SACW transport due to eddies would renew the SACW part of the transition zone (a defined region, see chapter 3), located between the eastern boundary region and the subtropical gyre region within about 2.5 years, assuming a layer thickness of 350 $m$. This thesis also examines low oxygen concentrations within cyclone and AMCE cores and their potential contribution to the pronounced shallow oxygen minimum environment centered at around 80 $m$ and located within the shadow zone in the ETNA bounded by the subtropical gyre to the North and the equatorial region to the South. The analysis shows that low oxygen eddies occur more frequently than expected, are found even in the proximity of the equator (8°N), and are responsible for an additional oxygen utilization of -7.35 (-2.41) $\mu mol kg^{-1} yr^{-1}$ for cyclones (ACMEs) within the depth range of the shallow oxygen minimum. From budget calculations it can be shown that the dispersion of the low oxygen mode after decay of the eddies can explain up to 6% of the oxygen consumption in the upper northeast Atlantic.

Note, that all these calculations of transport and corresponding impact follow conservative assumptions, as the contribution of non-satellite-detectable, short-lived, non-coherent and small-scale eddies is not included.

**4) How do biogeochemical "extreme" environments develop within eddies in the ETNA region?** (Chapter 2, Chapter 4 and Chapter 5)

During the lifetime of an eddy the highly isolated water body generates a natural mesocosm environment in the open ocean. Within these mesoscosms, a biosphere can exist that greatly differs from the biosphere present in the surrounding area. Preferentially, these modified environments can be associated to either cyclones or ACMEs. Within both types of eddies, the shallow isopycnal surfaces (located at about 70-100 $m$ depth) rise, favoring biological productivity near the surface. In addition, an enhanced vertical transport of water mass properties (e.g. nutrients) at the periphery of the eddies is observed, which might be associated with the propagation of near-inertial waves (NIWs). Both processes enable the existence of specific ecosystems responsible for e.g. primary production, degradation processes or nitrogen loss far away from the coast in the usually oligotrophic open ocean. This has direct implications for the oxygen utilization and/or the nitrogen cycle within the eddy.

Indeed almost all observations of low oxygen concentrations below the canonical value of 40 $\mu mol kg^{-1}$ in the ETNA are co-located with mesoscale eddies (either cyclones or ACMEs). Negative oxygen anomalies are most pronounced right beneath the mixed layer and can be attributed both to high productivity in the surface waters (documented by positive chlorophyll anomalies estimated from satellite observations) and the subsequent respiration of organic material as well as to the dynamically induced isolation of the mesoscale structures with respect to lateral oxygen resupply (high nonlinearity parameter within the observed eddies). Hence, in contrast to the heat or salt transport, the observed oxygen minimum within the eddies is not only due to the transport of waters with low oxygen, but further enhanced by the internal dynamics. Within the cyclones (ACMEs) the effect is accumulated with time and the oxygen decreases on average by the apparent oxygen utilization ($AOU$) of 0.10 (0.19) $\pm$ 0.12 (0.08) $\mu mol kg^{-1} d^{-1}$, which results in hypoxic and even suboxic ($< 1$ $\mu mol kg^{-1}$) conditions in the eddy cores. These "dead zones" present specific threats to the ecosystem, such as the interruption of the diurnal migration of zooplankters.

In addition, it can be shown that the ACME cores are attributed with high nitrate concentrations. The combination of these high nitrate ($NO_3$) concentrations with the $AOU$ reveals $AOU : NO_3$ ratios of 16, which are much higher compared to the surrounding waters. A maximum $NO_3$ deficit of 4 to 6 $\mu mol kg^{-1}$ is estimated for the low oxygen core. A possible explanation would be that denitrification processes are taking place. However, within this thesis evidence is provided that the recycling of $NO_3$ may quantitatively be more important. $NO_3$ is extracted from the eddy core and replenished into the core via the sinking of particles. Following that theory, the particulate phase would be of key importance in decoupling the nitrogen from the oxygen cycling.

**5) Which processes drive vertical exchange in an isolated eddy?**
(Chapter 2, Chapter 4 and Chapter 5)

To establish biogeochemical extreme environments, as mentioned above, eddies need to be highly isolated but should support an intense upward nutrient flux at the same time. The contradiction is investigated by a high-resolution glider survey through an oxygen-depleted ACME. It reveals that the mesoscale ($\sim$50 $km$) dynamics of an eddy are interacting with NIWs to drive a submesoscale ($\sim$1 $km$) upward flux of nutrients at the eddy periphery. This is contrary to the view that vertical transport is concentrated in the center of the eddy as proposed by [e.g. *McGillicuddy et al.*, 2007]. However, vertical movements bring nutrients into the euphotic zone and drive the primary productivity (phytoplankton bloom). During the case study a distinct eddy core with a diameter of about 70 $km$ extending from about 60 to 200 $m$ depth could be identified. The core was bordered by local maxima in buoyancy frequency. In addition, indications for vertical propagation (extending to several hundred-meters depth) of NIWs at the flanks and underneath the eddy were found in property gradient sections (vertical layering). This could later be confirmed by direct current measurements from a shipboard ADCP crossing the same eddy. A narrow region exists at the outer edge of the eddy, where NIWs can propagate downward. Furthermore, the phase speed of the NIWs and the speed of the mean flow are of similar magnitude. Therefore, critical layer formation is expected and mixing is likely to occur close to the euphotic zone/mixed layer. These processes describe a mechanism that support an upward nutrient flux towards the euphotic zone and the coexistence with a highly isolated eddy core, which is expected and supported by the observations.

## 6.2 Integration of the results into the current level of knowledge

Comprehensive information on eddy dynamics was gained for the EBUSs of the Pacific Ocean [e.g. *Chaigneau and Pizarro*, 2005; *Chaigneau et al.*, 2008, 2011; *Liang et al.*, 2012; *Chang et al.*, 2012; *Kurian et al.*, 2011]. However, for the EBUSs of the northeastern Atlantic Ocean regional eddy studies have been rare. Here the general characteristics of the mesoscale eddy field in the ETNA region such as frequency of occurrence, eddy surface signatures or seasonality in eddy generation and lifetime have been undocumented so far. Overall, the study reveals that eddies in the EBUSs of the Atlantic and Pacific show similar eddy statistics, but differ in the distribution of eddy generation and eddy frequency/polarity, which indicates different forcing mechanisms at play.
Within this thesis it is shown that ACMEs, also known as "submesoscale coherent vortices (SCV)" described of *McWilliams* [1985], are detectable from space in the ETNA region. Recent model studies have shown that ACMEs represent a non-negligible part of the eddy field, particularly in EBUSs [*Combes et al.*, 2015; *Nagai et al.*, 2015]. That could be verified in this thesis by the first statistical assessment of the occurrence, characteristics and impact of ACMEs in the ETNA region based on observational data. The distinction of anticyclonic rotating eddies into ACMEs and "normal anticyclones" seems to be mandatory for future eddy studies

as these two eddy types strongly differ in their efficiency to transport water mass anomalies. Moreover, the biogeochemical responses in ACMEs have been found to be very distinct from normal anticyclones and a sufficient representation of both types of anticyclones in coupled physical-biogeochemical models may be crucial for a realistic simulation of eastern boundary upwelling systems [*Löscher et al.*, 2015; *Hauss et al.*, 2016; *Fiedler et al.*, 2016; *Nagai et al.*, 2015]. Particularly, since within this thesis the discovery of extremely low oxygen concentrations associated to ACME and cyclone cores in the ETNA is documented. The pelagic zones of the ETNA's OMZ are traditionally considered to be "hypoxic", with minimal oxygen concentrations of marginally below 40 $\mu mol kg^{-1}$ [*Stramma et al.*, 2009; *Karstensen et al.*, 2008; *Brandt et al.*, 2015]. However, during these studies eddy cores with oxygen values in the range of severe hypoxia ($< 20 \mu mol kg^{-1}$) and even anoxia ($\sim 1 \mu mol kg^{-1}$) conditions have been found in a surprisingly high number. The enhanced respiration in the eddy cores is associated to elevated primary production in the surface layer of the eddy. The results of this thesis are questioning the assumption that oxygen consumption is determined by the metabolism of the large-scale community alone. Instead, the observations presented here suggest instead that hot spots of locally enhanced consumption may possibly need to be considered in the future, particularly regarding the formation of the shallow OMZ [*Brandt et al.*, 2015; *Karstensen et al.*, 2008].

Enhanced primary productivity in oligotrophic regions such as the eastern tropical North Atlantic requires process at place, which exposes nutrients to the euphotic zone. Different processes, associated with mesoscale eddies, have been identified to be relevant: The first concepts considered the shoaling of isopycnal surfaces during the propagation of eddies/Rossby waves [*Falkowski et al.*, 1991; *McGillicuddy et al.*, 1998], and Ekman pumping due to interactions of the overlying wind field with the eddy currents [*Dewar and Flierl*, 1987; *McGillicuddy et al.*, 2007] and SST anomalies [*Chelton et al.*, 2004; *Gaube et al.*, 2014a], resulting in upwelling and downwelling in the cores of the eddies. But modeling studies [*Lévy et al.*, 2012] and recent observational studies [*Martin and Richards*, 2001; *Brannigan et al.*, 2015; *Omand et al.*, 2015] highlighting the point that submesoscale instabilities within or at the periphery of the eddies are responsible for vertical nutrient flux. Based on high-resolution glider and ship sections submesoscale processes at the eddy periphery could be examined in more detail in this thesis. The observations show evidence that another possible mechanisms for vertical transport at the eddy periphery is caused by vertical mixing driven by the interactions of NIWs with the eddy rotation.

## 6.3 Related results obtained in co-authored publications

Eddies show strong coupling of physical and biogeochemical processes, which enabled the author to participate in several interdisciplinary studies [*Zindler et al.*, 2014; *Löscher et al.*, 2015; *Hauss et al.*, 2016; *Fiedler et al.*, 2016]. In particular, the establishment of an eddy alert system in the ETNA region and the expertise of the author in satellite based ACME detection allowed the implementation of a multi-platform survey of an ACME north of the Cabo Verde Islands, which compromised the usage of three gliders and two ships. The interdisciplinary analysis reveals that the oxygen utilization and downward carbon export inside of the ACME exceeds known

values for this ocean region [*Fiedler et al.*, 2016]. While denitrification is usually absent in the open tropical Atlantic, the presence of nirS gene transcripts (the key functional marker for denitrification) in the ACME indicates a potential for nitrogen loss processes in the oxygen depleted eddy core. However, as indicated by close-to-Redfield N:P stoichiometry in the same ACME [*Löscher et al.*, 2015] and by the results of this thesis (chapter 5), there appears to be no large-scale net loss of bioavailable nitrogen. Furthermore, the intense oxygen minimum in the eddy cores has profound impacts on sensible metazoan communities and marine life [*Hauss et al.*, 2016]. For example, the compression of the habitable volume in the mixed layer above the eddy core (strong increase in integrated zooplankton abundance) increases the abundance of higher trophic levels (such as small pelagic forage fish and their predators), which benefit from the dense prey field. Nonetheless, the relative magnitude of nutrient upwelling/primary productivity, nitrogen fixation and denitrification may strongly vary among eddies of different ages, initial water mass composition as well as external forcing (in particular wind stress and dust/iron input).

## 6.4 Outlook

Since the advent of satellite remote sensing a lot of studies have investigated the mesoscale eddy field based on altimetry, which led to a good understanding and overview over the global eddy activity at the surface. Yet, there are still prospects for improvements of the altimeter data in particular regarding spatial resolution. The upcoming surface water and ocean topography (SWOT) mission (launch in 2020) will have a resolution of 10 to 70 m (`https://swot.jpl.nasa.gov/mission`) and will drastically enhance the understanding of small-scale eddy variability. Also other satellite products as for example the Soil Moisture and Ocean Salinity (SMOS) measurements needs further improvements [e.g. *Oliva et al.*, 2012; *Boutin et al.*, 2014; *Schlundt et al.*, 2014; *Kolodziejczyk et al.*, 2016]. However, most studies about mesoscale activity only differentiate between eddies of anticyclonic rotation (associated with high SLA) and cyclonic rotation (associated with low SLA). The present thesis highlights the effects of a special class of eddies (ACME), which most likely are also relevant to other regions where the presence of subsurface anticyclonic eddies is frequent. A method is developed, that can identify ACMEs from satellite data by distinguishing between three types of eddies from space. For the future a better understanding of the observed vertical structure of the different eddy types is needed to calculate correct tracer budgets, improve ocean model validation and eddy parameterizations. The latter are deficiencies among the increasing number of ocean models. Locally, the vertical structure of thermohaline characteristics of eddies has been investigated, but there still is a lack of regional or even global studies. Naturally, such studies are challenged by the limited vertical in-situ data base. However, the increasing observational datasets and the combination of different observational platforms (satellite with all available vertical profiles) will allow detailed studies of the vertical structure of eddies in the future. Hence, a logical follow-up on this thesis, which focused on the eddy activity in the ETNA and particularly on the eddies generated near the coast, would be a study comparing the vertical structure of all eddies in the four

different EBUSs and/or the vertical structure of eddies in the world oceans. In addition, further investigation of the mechanisms responsible for the formation of anticyclones, cyclones and especially of ACMEs is required  particularly in EBUSs, where the mesoscale eddies connect the coastal zone with the open ocean and partly control the productivity. In order to fulfill this task high-resolution model studies as well as denser observations of the eastern boundary current system and the submesoscale coastal filaments are needed. Furthermore, the analysis shows the occurrence and generation of ACMEs far offshore in the vicinity of the equator (5-8°N), which is rather astonishing and at the moment hard to explain.

At the moment only little is known about the frequency of occurrence of biogeochemical extreme environments. How relevant are these biogeochemical extreme environments for the budgets of the global ocean? What is their impact on marine life? Can these extreme environments be considered oases for adapted marine life? A detailed understanding of all contributing processes is required solely as isolated eddies may act as natural mesocosms, which - in light of future deoxygenation - might serve as a "crystal sphere" to observe the differential response of marine life to global change. Associated to that it is necessary to enhance the understanding of submesoscale processes and the associated vertical transports of tracer and biogeochemical properties around or within mesoscale eddies. Another focus should be set on estimating interannual variations of eddy transport, which could be caused by variability in the eddy activity, large-scale circulation or, in upwelling regions, of the upwelling itself. Another essential point is the exact mechanism of the decay of an eddy. Will the eddy spread its anomalies on isopycnal layers or due to strong mixing rather diapycnally?

During this thesis the complexity of processes, feedbacks and impacts related to mesoscale eddies became apparent. To further enhance our understanding in this field, strong interdisciplinary efforts will be required.

# 6.5 Own Publications

1. Zindler, C., Marandino, C. A., Bange, H. W., **Schütte, F.**, and Saltzman, E. S.: Nutrient availability determines dimethyl sulfide and isoprene distribution in the eastern Atlantic Ocean, **Geophysical Research Letters**, 41, doi:10.1002/2014GL059547, 2014

2. Karstensen, J., Fiedler, B., **Schütte, F.**, Brandt, P., Körtzinger, A., Fischer, G., Zantopp, R., Hahn, J., Visbeck, M., and Wallace, D.: Open ocean dead zones in the tropical North Atlantic Ocean, **Biogeoscience** 12, 2597-2605, doi: 10.5194/bg-12-2597-2015, 2015

3. Löscher, C. R., Fischer, M. A., Neulinger, S. C., Fiedler, B., Philippi, M., **Schütte, F.**, Singh, A., Hauss, H., Karstensen, J., Körtzinger, A., Knzel, S., and Schmitz, R. A.: Hidden biosphere in an oxygen-deficient Atlantic open-ocean eddy: future implications of ocean deoxygenation on primary production in the eastern tropical North Atlantic, **Biogeosciences**, 12, 7467-7482, doi: 10.5194/bg-12-7467-2015, 2015

4. Hauss, H., Christiansen, S., **Schütte, F.**, Kiko, R., Edvam Lima, M., Rodrigues, E., Karstensen, J., Löscher, C. R., Körtzinger, A., and Fiedler, B.: Dead zone or oasis in the open ocean? Zooplankton distribution and migration in low-oxygen modewater eddies, **Biogeosciences**, 13, 1977-1989, doi: 10.5194/bg-13-1977-2016, 2016

5. **Schütte, F.**, Brandt, P., and Karstensen, J.: Occurrence and characteristics of mesoscale eddies in the tropical northeastern Atlantic Ocean, **Ocean Science**, 12, 663-685, doi: 10.5194/os-12-663-2016, 2016

6. Fielder, B., Grundle, D., **Schütte, F.**, Karstensen, J., Löscher, C. R., Hauss, H., Wagner, H., Loginova, A., Kiko, R., Silva, P., and Körtzinger, A.: Oxygen Utilization and Downward Carbon Flux in an Oxygen-Depleted Eddy in the Eastern Tropical North Atlantic, **Biogeoscience Discuss.**, doi: 10.5194/bg-2016-23, 2016

7. **Schütte, F.**, Karstensen, J., Krahmann, G., Hauss, H., Fiedler, B., Brandt, P., Visbeck, M., and Körtzinger, A.: Characterization of dead-zone eddies in the tropical Northeast Atlantic Ocean, **Biogeoscience Discuss.**, doi: 10.5194/bg-2016-33, 2016

8. Karstensen, J., **Schütte, F.**, Pietri, A., Krahmann, G., Fiedler, B., Grundle, D., Hauss, H., Körtzinger, A., Lscher, C.R., Testor, P., Vieira, N., and Visbeck, M.: Upwelling and isolation in oxygen-depleted anticyclonic modewater eddies and implications for nitrate cycling, **Biogeoscience Discuss.**, doi: 10.5194/bg-2016-34, 2016

# References

Alford, M. H., A. Y. Shcherbina, and M. C. Gregg, Observations of near-inertial internal gravity waves radiating from a frontal jet, *Journal of Physical Oceanography*, *43*(6), 1225–1239, 2013.

Alford, M. H., J. A. MacKinnon, H. L. Simmons, and J. D. Nash, Near-inertial internal gravity waves in the ocean, *Annual Review of Marine Science, Vol 8*, *8*, 95–123, 2016.

Arbic, B. K., et al., Estimates of bottom flows and bottom boundary layer dissipation of the oceanic general circulation from global high-resolution models, *Journal of Geophysical Research-Oceans*, *114*, 2009.

Arbic, B. K., and G. R. Flierl, Baroclinically unstable geostrophic turbulence in the limits of strong and weak bottom ekman friction: Application to midocean eddies, *Journal of Physical Oceanography*, *34*(10), 2257–2273, 2004.

Armi, L., and W. Zenk, Large lenses of highly saline mediterranean water, *Journal of Physical Oceanography*, *14*(10), 1560–1576, 1984.

Baird, M. E., I. M. Suthers, D. A. Griffin, B. Hollings, C. Pattiaratchi, J. D. Everett, M. Roughan, K. Oubelkheir, and M. Doblin, The effect of surface flooding on the physicalbiogeochemical dynamics of a warm-core eddy off southeast australia, *Deep Sea Research Part II: Topical Studies in Oceanography*, *58*(5), 592–605, 2011.

Bakun, A., Global climate change and intensification of coastal ocean upwelling, *Science*, *247*(4939), 198–201, 1990.

Bakun, A., and C. S. Nelson, The seasonal cycle of wind-stress curl in subtropical eastern boundary current regions, *Journal of Physical Oceanography*, *21*(12), 1815–1834, 1991.

Bakun, A., and S. J. Weeks, Adverse feedback sequences in exploited marine systems: are deliberate interruptive actions warranted?, *Fish and Fisheries*, *7*(4), 316–333, 2006.

Barton, E. D., The poleward undercurrent on the eastern boundary of the subtropical north atlantic, in *Poleward Flows Along Eastern Ocean Boundaries*, edited by S. J. Neshyba, C. N. K. Mooers, R. L. Smith, and R. T. Barber, vol. 34 of *Coastal and Estuarine Studies*, book section 8, pp. 82–95, Springer New York, 1989.

Biastoch, A., C. W. Böning, F. U. Schwarzkopf, and J. R. E. Lutjeharms, Increase in agulhas leakage due to poleward shift of southern hemisphere westerlies, *Nature*, *462*(7272), 495–498, 2009.

Boutin, J., N. Martin, G. Reverdin, S. Morisset, X. Yin, L. Centurioni, and N. Reul, Sea surface salinity under rain cells: Smos satellite and in situ drifters observations, *Journal of Geophysical Research: Oceans*, *119*(8), 5533–5545, 2014.

Bower, A. S., L. Armi, and I. Ambar, Direct evidence of meddy formation off the southwestern coast of portugal, *Deep Sea Research Part I: Oceanographic Research Papers*, *42*(9), 1621–1630, 1995.

Brachet, S., P. Y. Le Traon, and C. Le Provost, Mesoscale variability from a high-resolution model and from altimeter data in the north atlantic ocean, *Journal of Geophysical Research: Oceans*, *109*(C12), n/a–n/a, 2004.

Brandt, P., et al., On the role of circulation and mixing in the ventilation of oxygen minimum zones with a focus on the eastern tropical north atlantic, *Biogeosciences*, *12*(2), 489–512, 2015.

Brannigan, L., D. P. Marshall, A. Naveira-Garabato, and A. J. G. Nurser, The seasonal cycle of submesoscale flows, *Ocean Modelling*, *92*, 69–84, 2015.

Brink, K. H., and T. J. Cowles, The coastal transition zone program, *Journal of Geophysical Research: Oceans*, *96*(C8), 14637–14647, 1991.

Brüggemann, N., and C. Eden, Evaluating different parameterizations for mixed layer eddy fluxes induced by baroclinic instability, *Journal of Physical Oceanography*, *44*(9), 2524–2546, 2014.

Bucklin, A., Population genetic responses of the planktonic copepod metridia pacifica to a coastal eddy in the california current, *Journal of Geophysical Research: Oceans*, *96*(C8), 14799–14808, 1991.

Bucklin, A., P. H. Wiebe, S. B. Smolenack, N. J. Copley, and M. E. Clarke, Integrated biochemical, molecular genetic, and bioacoustical analysis of mesoscale variability of the euphausiid nematoscelis difficilis in the california current, *Deep Sea Research Part I: Oceanographic Research Papers*, *49*(3), 437–462, 2002.

Calil, P. H. R., K. J. Richards, Y. L. Jia, and R. R. Bidigare, Eddy activity in the lee of the hawaiian islands, *Deep-Sea Research Part Ii-Topical Studies in Oceanography*, *55*(10-13), 1179–1194, 2008.

Capet, X., J. C. Mcwilliams, M. J. Mokemaker, and A. F. Shchepetkin, Mesoscale to submesoscale transition in the California current system. Part I: Flow structure, eddy flux, and observational tests, *Journal of Physical Oceanography*, *38*(1), 29–43, 2008a.

Capet, X., J. C. Mcwilliams, M. J. Molemaker, and A. F. Shchepetkin, Mesoscale to submesoscale transition in the California current system. Part II: Frontal processes, *Journal of Physical Oceanography*, *38*(1), 44–64, 2008b.

## References

Capet, X., J. C. McWilliams, M. J. Molemaker, and A. F. Shchepetkin, Mesoscale to submesoscale transition in the California current system. Part III: Energy balance and flux, *Journal of Physical Oceanography*, *38*(10), 2256–2269, 2008c.

Carr, S. D., X. J. Capet, J. C. McWilliams, J. Pennington, and F. P. Chavez, The influence of diel vertical migration on zooplankton transport and recruitment in an upwelling region: estimates from a coupled behavioral-physical model, *Fisheries Oceanography*, *17*(1), 1–15, 2008.

Chaigneau, A., and O. Pizarro, Eddy characteristics in the eastern south pacific, *Journal of Geophysical Research: Oceans*, *110*(C6), C06005, 2005.

Chaigneau, A., A. Gizolme, and C. Grados, Mesoscale eddies off peru in altimeter records: Identification algorithms and eddy spatio-temporal patterns, *Progress in Oceanography*, *79*(24), 106–119, 2008.

Chaigneau, A., G. Eldin, and B. Dewitte, Eddy activity in the four major upwelling systems from satellite altimetry (19922007), *Progress in Oceanography*, *83*(14), 117–123, 2009.

Chaigneau, A., M. Le Texier, G. Eldin, C. Grados, and O. Pizarro, Vertical structure of mesoscale eddies in the eastern south pacific ocean: A composite analysis from altimetry and argo profiling floats, *Journal of Geophysical Research: Oceans*, *116*(C11), C11025, 2011.

Challenor, P. G., P. Cipollini, and D. Cromwell, Use of the 3d radon transform to examine the properties of oceanic rossby waves, *Journal of Atmospheric and Oceanic Technology*, *18*(9), 1558–1566, 2001.

Chang, C.-H., S.-P. Xie, N. Schneider, B. Qiu, J. Small, W. Zhuang, B. Taguchi, H. Sasaki, and X. Lin, East pacific ocean eddies and their relationship to subseasonal variability in central american wind jets, *Journal of Geophysical Research: Oceans*, *117*(C10), C10001, 2012.

Charney, J. G., Geostrophic turbulence, *Journal of the Atmospheric Sciences*, *28*(6), 1087–&, 1971.

Chavez, F. P., and M. Messié, A comparison of eastern boundary upwelling ecosystems, *Progress in Oceanography*, *83*(14), 80–96, 2009.

Chelton, D. B., and M. G. Schlax, Global observations of oceanic rossby waves, *Science*, *272*(5259), 234–238, 1996.

Chelton, D. B., R. A. deSzoeke, M. G. Schlax, K. El Naggar, and N. Siwertz, Geographical variability of the first baroclinic rossby radius of deformation, *Journal of Physical Oceanography*, *28*(3), 433–460, 1998.

Chelton, D. B., M. G. Schlax, J. M. Lyman, and G. C. Johnson, Equatorially trapped rossby waves in the presence of meridionally sheared baroclinic flow in the pacific ocean, *Progress in Oceanography*, *56*(2), 323–380, 2003.

Chelton, D. B., M. G. Schlax, M. H. Freilich, and R. F. Milliff, Satellite measurements reveal persistent small-scale features in ocean winds, *Science*, *303*(5660), 978–983, 2004.

Chelton, D. B., M. G. Schlax, R. M. Samelson, and R. A. de Szoeke, Global observations of large oceanic eddies, *Geophysical Research Letters*, *34*(15), 2007.

Chelton, D. B., P. Gaube, M. G. Schlax, J. J. Early, and R. M. Samelson, The influence of nonlinear mesoscale eddies on near-surface oceanic chlorophyll, *Science*, *334*(6054), 328–332, 2011a.

Chelton, D. B., M. G. Schlax, and R. M. Samelson, Global observations of nonlinear mesoscale eddies, *Progress in Oceanography*, *91*(2), 167–216, 2011b.

Colas, F., J. C. McWilliams, X. Capet, and J. Kurian, Heat balance and eddies in the peru-chile current system, *Climate Dynamics*, *39*(1-2), 509–529, 2012.

Combes, V., S. Hormazabal, and E. Di Lorenzo, Interannual variability of the subsurface eddy field in the southeast pacific, *Journal of Geophysical Research-Oceans*, *120*(7), 4907–4924, 2015.

Correa-Ramirez, M. A., S. Hormazabal, and G. Yuras, Mesoscale eddies and high chlorophyll concentrations off central chile (29 degrees-39 degrees s), *Geophysical Research Letters*, *34*(12), 2007.

Cullen, *Down to the Sea for Science: 75 Years of Ocean Research, Education, and Exploration at the Woods Hole Oceanographic Institution.*, Woods Hole Oceanographic Inst., 2005.

Cushman-Roisin, B., B. Tang, and E. P. Chassignet, Westward motion of mesoscale eddies, *Journal of Physical Oceanography*, *20*(5), 758–768, 1990.

D'Asaro, E. A., Generation of submesoscale vortices - a new mechanism, *Journal of Geophysical Research-Oceans*, *93*(C6), 6685–6693, 1988.

Delworth, T. L., et al., Simulated climate and climate change in the gfdl cm2.5 high-resolution coupled climate model, *Journal of Climate*, *25*(8), 2755–2781, 2012.

Dewar, W. K., On too fast baroclinic planetary waves in the general circulation, *Journal of Physical Oceanography*, *28*(9), 1739–1758, 1998.

Dewar, W. K., and G. R. Flierl, Some effects of the wind on rings, *Journal of Physical Oceanography*, *17*(10), 1653–1667, 1987.

Duhaut, T. H. A., and D. N. Straub, Wind stress dependence on ocean surface velocity: Implications for mechanical energy input to ocean circulation, *Journal of Physical Oceanography*, *36*(2), 202–211, 2006.

Eady, E. T., Long waves and cyclone waves, *Tellus*, *1*(3), 33–52, 1949.

*References*

Early, J. J., R. M. Samelson, and D. B. Chelton, The evolution and propagation of quasigeostrophic ocean eddies, *Journal of Physical Oceanography*, *41*(8), 1535–1555, 2011.

Faghmous, J. H., I. Frenger, Y. Yao, R. Warmka, A. Lindell, and V. Kumar, A daily global mesoscale ocean eddy dataset from satellite altimetry, *Scientific Data*, *2*, 150028, 2015.

Falkowski, P. G., D. Ziemann, Z. Kolber, and P. K. Bienfang, Role of eddy pumping in enhancing primary production in the ocean, *Nature*, *352*(6330), 55–58, 1991.

Fang, F. X., and R. Morrow, Evolution, movement and decay of warm-core leeuwin current eddies, *Deep-Sea Research Part Ii-Topical Studies in Oceanography*, *50*(12-13), 2245–2261, 2003.

Ferrari, R., and C. Wunsch, Ocean circulation kinetic energy: Reservoirs, sources, and sinks, *Annual Review of Fluid Mechanics*, *41*, 253–282, 2009.

Fiedler, B., et al., Oxygen utilization and downward carbon flux in an oxygen-depleted eddy in the eastern tropical north atlantic, *Biogeosciences Discuss.*, *2016*, 1–35, 2016.

Fischer, G., et al., Bathypelagic particle flux signatures from a suboxic eddy in the oligotrophic tropical north atlantic: production, sedimentation and preservation, *Biogeosciences*, *13*(11), 3203–3223, 2016.

Flierl, G., and D. J. McGillicuddy, Mesoscale and submesoscale physical-biological interactions, *The sea*, *12*, 113–185, 2002.

Flierl, G. R., Particle motions in large-amplitude wave fields, *Geophysical & Astrophysical Fluid Dynamics*, *18*(1-2), 39–74, 1981.

Fox-Kemper, B., R. Ferrari, and R. Hallberg, Parameterization of mixed layer eddies. part i: Theory and diagnosis, *Journal of Physical Oceanography*, *38*(6), 1145–1165, 2008.

Frenger, I., N. Gruber, R. Knutti, and M. Munnich, Imprint of southern ocean eddies on winds, clouds and rainfall, *Nature Geosci*, *6*(8), 608–612, 2013.

Fu, L. L., Pattern and velocity of propagation of the global ocean eddy variability, *Journal of Geophysical Research-Oceans*, *114*, 2009.

Fuglister, F. C., *Cyclonic Gulf stream rings formed by the Gulf Stream 1965-66.*, vol. Vol. 1 of *Studies in Physical Oceanography*, Grodon and Breach, New York, 1972.

Gaube, P., D. B. Chelton, R. M. Samelson, M. G. Schlax, and L. W. O'Neill, Satellite observations of mesoscale eddy-induced ekman pumping, *Journal of Physical Oceanography*, *45*(1), 104–132, 2014a.

Gaube, P., D. J. McGillicuddy, D. B. Chelton, M. J. Behrenfeld, and P. G. Strutton, Regional variations in the influence of mesoscale eddies on near-surface chlorophyll, *Journal of Geophysical Research: Oceans*, *119*(12), 8195–8220, 2014b.

Gill, A. E., and A. J. Clarke, Wind-induced upwelling, coastal currents and sea-level changes, *Deep-Sea Research*, *21*(5), 325–345, 1974.

Glessmer, M. S., C. Eden, and A. Oschlies, Contribution of oxygen minimum zone waters to the coastal upwelling off mauritania, *Progress in Oceanography*, *83*(14), 143–150, 2009.

Gregg, M. C., E. A. Dasaro, T. J. Shay, and N. Larson, Observations of persistent mixing and near-inertial internal waves, *Journal of Physical Oceanography*, *16*(5), 856–885, 1986.

Gruber, N., Z. Lachkar, H. Frenzel, P. Marchesiello, M. Munnich, J. C. McWilliams, T. Nagai, and G.-K. Plattner, Eddy-induced reduction of biological production in eastern boundary upwelling systems, *Nature Geosci*, *4*(11), 787–792, 2011.

Gula, J., M. J. Molemaker, and J. C. McWilliams, Topographic vorticity generation, submesoscale instability and vortex street formation in the gulf stream, *Geophysical Research Letters*, *42*(10), 4054–4062, 2015.

Hauss, H., et al., Dead zone or oasis in the open ocean? zooplankton distribution and migration in low-oxygen modewater eddies, *Biogeosciences*, *13*(6), 1977–1989, 2016.

Hughes, C. W., and C. Wilson, Wind work on the geostrophic ocean circulation: An observational study of the effect of small scales in the wind stress, *Journal of Geophysical Research-Oceans*, *113*(C2), 2008.

Hughes, C. W., M. S. Jones, and S. Carnochan, Use of transient features to identify eastward currents in the southern ocean, *Journal of Geophysical Research-Oceans*, *103*(C2), 2929–2943, 1998.

Iselin, C. O., and F. C. Fuglister, Some recent developments in the study of the gulf stream, *Journal of Marine Research*, *7*(3), 317–329, 1948.

Isern-Fontanet, J., E. Garcia-Ladona, and J. Font, Identification of marine eddies from altimetric maps, *Journal of Atmospheric and Oceanic Technology*, *20*(5), 772–778, 2003.

Isoguchi, O., and H. Kawamura, Eddies advected by time-dependent sverdrup circulation in the western boundary of the subarctic north pacific, *Geophysical Research Letters*, *30*(15), 2003.

Jayne, S. R., and J. Marotzke, The oceanic eddy heat transport, *Journal of Physical Oceanography*, *32*(12), 3328–3345, 2002.

Johnson, G. C., and K. E. McTaggart, Equatorial pacific 13 degrees c water eddies in the eastern subtropical south pacific ocean, *Journal of Physical Oceanography*, *40*(1), 226–236, 2010.

Joyce, T. M., J. M. Toole, P. Klein, and L. N. Thomas, A near-inertial mode observed within a gulf stream warm-core ring, *Journal of Geophysical Research-Oceans*, *118*(4), 1797–1806, 2013.

*References*

Karstensen, J., L. Stramma, and M. Visbeck, Oxygen minimum zones in the eastern tropical atlantic and pacific oceans, *Progress in Oceanography*, *77*(4), 331–350, 2008.

Killworth, P. D., D. B. Chelton, and R. A. DeSzoeke, The speed of observed and theoretical long extratropical planetary waves, *Journal of Physical Oceanography*, *27*(9), 1946–1966, 1997.

Kolmogorov, A. N., The local structure of turbulence in incompressible viscous fluid for very large reynolds numbers, *Proceedings: Mathematical and Physical Sciences*, *434*(1890), 9–13, 1941.

Kolodziejczyk, N., J. Boutin, J.-L. Vergely, S. Marchand, N. Martin, and G. Reverdin, Mitigation of systematic errors in smos sea surface salinity, *Remote Sensing of Environment*, *180*, 164–177, 2016.

Kostianoy, A. G., and I. M. Belkin, A survey of observations on emtrathermocline eddies in the world ocean, in *Elsevier Oceanography Series*, edited by J. C. J. Nihoul, and B. M. Jamart, vol. Volume 50, pp. 821–841, Elsevier, 1989.

Koszalka, I., L. Ceballos, and A. Bracco, Vertical mixing and coherent anticyclones in the ocean: the role of stratification, *Nonlinear Processes in Geophysics*, *17*(1), 37–47, 2010.

Kunze, E., Near-inertial wave-propagation in geostrophic shear, *Journal of Physical Oceanography*, *15*(5), 544–565, 1985.

Kurian, J., F. Colas, X. Capet, J. C. McWilliams, and D. B. Chelton, Eddy properties in the california current system, *Journal of Geophysical Research: Oceans (19782012)*, *116*(C8), 2011.

LaCasce, J. H., and J. Pedlosky, The instability of rossby basin modes and the oceanic eddy field, *Journal of Physical Oceanography*, *34*(9), 2027–2041, 2004.

Lachkar, Z., and N. Gruber, What controls biological production in coastal upwelling systems? insights from a comparative modeling study, *Biogeosciences*, *8*(10), 2961–2976, 2011.

Lachkar, Z., and N. Gruber, A comparative study of biological production in eastern boundary upwelling systems using an artificial neural network, *Biogeosciences*, *9*(1), 293–308, 2012.

Lázaro, C., M. J. Fernandes, A. M. P. Santos, and P. Oliveira, Seasonal and interannual variability of surface circulation in the cape verde region from 8 years of merged t/p and ers-2 altimeter data, *Remote Sensing of Environment*, *98*(1), 45–62, 2005.

Le Traon, P.-Y., Contribution of satellite altimetry to the observation of oceanic mesoscale variability, *Oceanologica Acta*, *15*(5), 441–457, 1992.

LeBlond, P., and L. Mysak, *Waves in the Ocean*, Elsevier Scientific Publishing, New York, USA, 1978.

Lee, D. K., and P. P. Niiler, The inertial chimney: The near-inertial energy drainage from the ocean surface to the deep layer, *Journal of Geophysical Research-Oceans*, *103*(C4), 7579–7591, 1998.

Levy, M., P. Klein, and A. M. Treguier, Impact of sub-mesoscale physics on production and subduction of phytoplankton in an oligotrophic regime, *Journal of Marine Research*, *59*(4), 535–565, 2001.

Levy, M., R. Ferrari, P. J. S. Franks, A. P. Martin, and P. Riviere, Bringing physics to life at the submesoscale, *Geophysical Research Letters*, *39*, 2012.

Lévy, M., D. Iovino, L. Resplandy, P. Klein, G. Madec, A. M. Trguier, S. Masson, and K. Ta-kahashi, Large-scale impacts of submesoscale dynamics on phytoplankton: Local and remote effects, *Ocean Modelling*, *43?44*, 77–93, 2012.

Liang, J.-H., J. C. McWilliams, J. Kurian, F. Colas, P. Wang, and Y. Uchiyama, Mesoscale variability in the northeastern tropical pacific: Forcing mechanisms and eddy properties, *Journal of Geophysical Research: Oceans*, *117*(C7), C07003, 2012.

Lilly, J. M., P. B. Rhines, F. Schott, K. Lavender, J. Lazier, U. Send, and E. D'Asaro, Observations of the labrador sea eddy field, *Progress in Oceanography*, *59*(1), 75–176, 2003.

Logerwell, E. A., and P. E. Smith, Mesoscale eddies and survival of late stage pacific sardine (sardinops sagax) larvae, *Fisheries Oceanography*, *10*(1), 13–25, 2001.

Löscher, C. R., et al., Hidden biosphere in an oxygen-deficient atlantic open-ocean eddy: future implications of ocean deoxygenation on primary production in the eastern tropical north atlantic, *Biogeosciences*, *12*(24), 7467–7482, 2015.

Lukas, R., and F. Santiago-Mandujano, Extreme water mass anomaly observed in the hawaii ocean time-series, *Geophysical Research Letters*, *28*(15), 2931–2934, 2001.

Luyten, J. R., J. Pedlosky, and H. Stommel, The ventilated thermocline, *Journal of Physical Oceanography*, *13*(2), 292–309, 1983.

Ma, X., P. Chang, R. Saravanan, R. Montuoro, J.-S. Hsieh, D. Wu, X. Lin, L. Wu, and Z. Jing, Distant influence of kuroshio eddies on north pacific weather patterns?, *Scientific Reports*, *5*, 17785, 2015.

Ma, Z., X.and Jing, et al., Western boundary currents regulated by interaction between ocean eddies and the atmosphere, *Nature*, 2016, accepted.

Mahadevan, A., Ocean science eddy effects on biogeochemistry, *Nature*, *506*(7487), 168–169, 2014.

Mahadevan, A., L. N. Thomas, and A. Tandon, Comment on 'eddy/wind interactions stimulate extraordinary mid-ocean plankton blooms', *Science*, *320*(5875), 2008.

## References

Marchesiello, P., J. C. McWilliams, and A. Shchepetkin, Equilibrium structure and dynamics of the california current system, *Journal of Physical Oceanography*, *33*(4), 753–783, 2003.

Marshall, D., Subduction of water masses in an eddying ocean, *Journal of Marine Research*, *55*(2), 201–222, 1997.

Marshall, D. P., and A. C. N. Garabato, A conjecture on the role of bottom-enhanced diapycnal mixing in the parameterization of geostrophic eddies, *Journal of Physical Oceanography*, *38*(7), 1607–1613, 2008.

Martin, A. P., and K. J. Richards, Mechanisms for vertical nutrient transport within a north atlantic mesoscale eddy, *Deep-Sea Research Part Ii-Topical Studies in Oceanography*, *48*(4-5), 757–773, 2001.

McGillicuddy, D. J., et al., Eddy/wind interactions stimulate extraordinary mid-ocean plankton blooms, *Science*, *316*(5827), 1021–1026, 2007.

McGillicuddy, D. J., A. R. Robinson, D. A. Siegel, H. W. Jannasch, R. Johnson, T. Dickeys, J. McNeil, A. F. Michaels, and A. H. Knap, Influence of mesoscale eddies on new production in the sargasso sea, *Nature*, *394*(6690), 263–266, 1998.

McWilliams, J. C., Submesoscale, coherent vortices in the ocean, *Reviews of Geophysics*, *23*(2), 165–182, 1985.

McWilliams, J. C., and G. R. Flierl, Evolution of isolated, non-linear vortices, *Journal of Physical Oceanography*, *9*(6), 1155–1182, 1979.

McWilliams, J. C., and M. J. Molemaker, Baroclinic frontal arrest: A sequel to unstable frontogenesis, *Journal of Physical Oceanography*, *41*(3), 601–619, 2011.

Messié, M., J. Ledesma, D. D. Kolber, R. P. Michisaki, D. G. Foley, and F. P. Chavez, Potential new production estimates in four eastern boundary upwelling ecosystems, *Progress in Oceanography*, *83*(1-4), 151–158, 2009.

Mittelstaedt, E., The ocean boundary along the northwest african coast - circulation and oceanographic properties at the sea-surface, *Progress in Oceanography*, *26*(4), 307–355, 1991.

Molemaker, M. J., J. C. McWilliams, and X. Capet, Balanced and unbalanced routes to dissipation in an equilibrated eady flow, *Journal of Fluid Mechanics*, *654*, 35–63, 2010.

Molemaker, M. J., J. C. McWilliams, and W. K. Dewar, Submesoscale instability and generation of mesoscale anticyclones near a separation of the california undercurrent, *Journal of Physical Oceanography*, *45*(3), 613–629, 2015.

Morrow, R., and P. Y. Le Traon, Recent advances in observing mesoscale ocean dynamics with satellite altimetry, *Advances in Space Research*, *50*(8), 1062–1076, 2012.

Morrow, R., F. Birol, D. Griffin, and J. Sudre, Divergent pathways of cyclonic and anti-cyclonic ocean eddies, *Geophysical Research Letters*, *31*(24), 2004.

Nagai, T., N. Gruber, H. Frenzel, Z. Lachkar, J. C. McWilliams, and G. K. Plattner, Dominant role of eddies and filaments in the offshore transport of carbon and nutrients in the california current system, *Journal of Geophysical Research-Oceans*, *120*(8), 5318–5341, 2015.

Nencioli, F., C. Dong, T. Dickey, L. Washburn, and J. C. McWilliams, A vector geometry based eddy detection algorithm and its application to a high-resolution numerical model product and high-frequency radar surface velocities in the southern california bight, *Journal of Atmospheric and Oceanic Technology*, *27*(3), 564–579, 2010.

Niiler, P. P., N. A. Maximenko, G. G. Panteleev, T. Yamagata, and D. B. Olson, Near-surface dynamical structure of the kuroshio extension, *Journal of Geophysical Research-Oceans*, *108*(C6), 2003.

Nikurashin, M., and R. Ferrari, Radiation and dissipation of internal waves generated by geostrophic motions impinging on small-scale topography: Application to the southern ocean, *Journal of Physical Oceanography*, *40*(9), 2025–2042, 2010.

Nikurashin, M., G. K. Vallis, and A. Adcroft, Routes to energy dissipation for geostrophic flows in the southern ocean, *Nature Geoscience*, *6*(1), 48–51, 2013.

Nof, D., T. Pichevin, and J. Sprintall, teddies" and the origin of the leeuwin current, *Journal of Physical Oceanography*, *32*(9), 2571–2588, 2002.

Olbers, D., J. Willebrand, and C. Eden, *Ocean Dynamics*, Springer Verlag Berlin, Berlin, 2012.

Oliva, R., E. Daganzo, Y. H. Kerr, S. Mecklenburg, S. Nieto, P. Richaume, and C. Gruhier, Smos radio frequency interference scenario: Status and actions taken to improve the rfi environment in the 1400-1427-mhz passive band, *IEEE Transactions on Geoscience and Remote Sensing*, *50*(5), 1427–1439, 2012.

Oliver, K. I. C., T. Eldevik, D. P. Stevens, and A. J. Watson, A greenland sea perspective on the dynamics of postconvective eddies, *Journal of Physical Oceanography*, *38*(12), 2755–2771, 2008.

Omand, M. M., E. A. D'Asaro, C. M. Lee, M. J. Perry, N. Briggs, I. Cetinic, and A. Mahadevan, Eddy-driven subduction exports particulate organic carbon from the spring bloom, *Science*, *348*(6231), 222–225, 2015.

Oschlies, A., Nao-induced long-term changes in nutrient supply to the surface waters of the north atlantic, *Geophysical Research Letters*, *28*(9), 1751–1754, 2001.

Oschlies, A., Can eddies make ocean deserts bloom?, *Global Biogeochemical Cycles*, *16*(4), 2002.

## References

ONeill, L. W., D. B. Chelton, and S. K. Esbensen, The effects of sst-induced surface wind speed and direction gradients on midlatitude surface vorticity and divergence, *Journal of Climate*, *23*(2), 255–281, 2010.

Pantoja, D., S. Marinone, A. Pars-Sierra, and F. Gmez-Valdivia, Numerical modeling of seasonal and mesoscale hydrography and circulation in the mexican central pacific modelacin numrica de la hidrografa y circulacin estacional y de mesoescala en el pacfico central mexicano, *Ciencias Marinas*, *38*(2), 363–379, 2012.

Pares-Sierra, A., W. B. White, and C. K. Tai, Wind-driven coastal generation of annual mesoscale eddy activity in the california current, *Journal of Physical Oceanography*, *23*(6), 1110–1121, 1993.

Pauly, D., and V. Christensen, Primary production required to sustain global fisheries, *Nature*, *374*(6519), 255–257, 1995.

Peña Izquierdo, J., J. L. Pelegrí, M. V. Pastor, P. Castellanos, M. Emelianov, M. Gasser, J. Salvador, and E. Vázquez-Domínguez, The continental slope current system between cape verde and the canary islands, *Scientia Marina*, *76*(S1), 65–78, 2012.

Peña Izquierdo, J., E. van Sebille, J. L. Pelegrí, J. Sprintall, E. Mason, P. J. Llanillo, and F. Machín, Water mass pathways to the north atlantic oxygen minimum zone, *Journal of Geophysical Research: Oceans*, 2015.

Pegliasco, C., A. Chaigneau, and R. Morrow, Main eddy vertical structures observed in the four major eastern boundary upwelling systems, *Journal of Geophysical Research: Oceans*, *120*(9), 6008–6033, 2015.

Qiu, B., R. B. Scott, and S. Chen, Length scales of eddy generation and nonlinear evolution of the seasonally modulated south pacific subtropical countercurrent, *Journal of Physical Oceanography*, *38*(7), 1515–1528, 2008.

Qiu, B., S. Chen, and H. Sasaki, Generation of the north equatorial undercurrent jets by triad baroclinic rossby wave interactions, *Journal of Physical Oceanography*, *43*(12), 2682–2698, 2013.

Richardson, P. L., J. F. Price, D. Walsh, L. Armi, and M. Schrder, Tracking three meddies with sofar floats, *Journal of Physical Oceanography*, *19*(3), 371–383, 1989.

Riser, S. C., W. B. Owens, H. T. Rossby, and C. C. Ebbesmeyer, The structure, dynamics, and origin of a small-scale lens of water in the western north-atlantic thermocline, *Journal of Physical Oceanography*, *16*(3), 572–590, 1986.

Robinson, A. R., and W. G. Leslie, Estimation and prediction of oceanic eddy fields, *Progress in Oceanography*, *14*, 485–510, 1985.

Roemmich, D., and J. Gilson, Eddy transport of heat and thermocline waters in the north pacific: A key to interannual/decadal climate variability?, *Journal of Physical Oceanography*, *31*(3), 675–687, 2001.

Rossby, T., C. Flagg, P. Ortner, and C. Hu, A tale of two eddies: Diagnosing coherent eddies through acoustic remote sensing, *Journal of Geophysical Research-Oceans*, *116*, 2011.

Rubio, A., B. Blanke, S. Speich, N. Grima, and C. Roy, Mesoscale eddy activity in the southern benguela upwelling system from satellite altimetry and model data, *Progress in Oceanography*, *83*(14), 288–295, 2009.

Sangrà, P., et al., The canary eddy corridor: A major pathway for long-lived eddies in the subtropical north atlantic, *Deep Sea Research Part I: Oceanographic Research Papers*, *56*(12), 2100–2114, 2009.

Schafstall, J., M. Dengler, P. Brandt, and H. Bange, Tidal-induced mixing and diapycnal nutrient fluxes in the mauritanian upwelling region, *Journal of Geophysical Research-Oceans*, *115*, 2010.

Schlundt, M., P. Brandt, M. Dengler, R. Hummels, T. Fischer, K. Bumke, G. Krahmann, and J. Karstensen, Mixed layer heat and salinity budgets during the onset of the 2011 atlantic cold tongue, *Journal of Geophysical Research: Oceans*, *119*(11), 7882–7910, 2014.

Schmidtko, S., G. C. Johnson, and J. M. Lyman, Mimoc: A global monthly isopycnal upper-ocean climatology with mixed layers, *Journal of Geophysical Research: Oceans*, *118*(4), 1658–1672, 2013.

Scott, R. B., and F. M. Wang, Direct evidence of an oceanic inverse kinetic energy cascade from satellite altimetry, *Journal of Physical Oceanography*, *35*(9), 1650–1666, 2005.

Seki, M. P., R. Lumpkin, and P. Flament, Hawaii cyclonic eddies and blue marlin catches: The case study of the 1995 hawaiian international billfish tournament, *Journal of Oceanography*, *58*(5), 739–745, 2002.

Sen, A., R. B. Scott, and B. K. Arbic, Global energy dissipation rate of deep-ocean low-frequency flows by quadratic bottom boundary layer drag: Computations from current-meter data, *Geophysical Research Letters*, *35*(9), 2008.

Shapiro, G. I., and S. L. Meschanov, Distribution and spreading of red-sea water and salt lens formation in the northwest indian-ocean, *Deep-Sea Research Part a-Oceanographic Research Papers*, *38*(1), 21–34, 1991.

Siegel, D. A., D. J. McGillicuddy, and E. A. Fields, Mesoscale eddies, satellite altimetry, and new production in the sargasso sea, *Journal of Geophysical Research-Oceans*, *104*(C6), 13359–13379, 1999.

*References*

Siegel, D. A., D. B. Court, D. W. Menzies, P. Peterson, S. Maritorena, and N. B. Nelson, Satellite and in situ observations of the bio-optical signatures of two mesoscale eddies in the sargasso sea, *Deep Sea Research Part II: Topical Studies in Oceanography*, *55*(1013), 1218–1230, 2008.

Siegel, D. A., P. Peterson, D. J. McGillicuddy, S. Maritorena, and N. B. Nelson, Bio-optical footprints created by mesoscale eddies in the sargasso sea, *Geophysical Research Letters*, *38*, 2011.

Smith, K. S., Eddy amplitudes in baroclinic turbulence driven by nonzonal mean flow: Shear dispersion of potential vorticity, *Journal of Physical Oceanography*, *37*(4), 1037–1050, 2007.

Souza, J. M. A. C. d., C. De Boyer Montegut, and P.-Y. Le Traon, Comparison between three implementations of automatic identification algorithms for the quantification and characterization of mesoscale eddies in the south atlantic ocean, *Ocean Science*, *7*(3), 317–334, 2011.

Spear, L. B., L. T. Ballance, and D. G. Ainley, Response of seabirds to thermal boundaries in the tropical pacific: the thermocline versus the equatorial front, *Marine Ecology Progress Series*, *219*, 275–289, 2001.

Stammer, D., Global characteristics of ocean variability estimated from regional topex/poseidon altimeter measurements, *Journal of Physical Oceanography*, *27*(8), 1743–1769, 1997.

Stammer, D., and C. Wunsch, Temporal changes in eddy energy of the oceans, *Deep Sea Research Part II: Topical Studies in Oceanography*, *46*(1), 77–108, 1999.

Stramma, L., M. Visbeck, P. Brandt, T. Tanhua, and D. Wallace, Deoxygenation in the oxygen minimum zone of the eastern tropical north atlantic, *Geophysical Research Letters*, *36*, 2009.

Stramma, L., H. W. Bange, R. Czeschel, A. Lorenzo, and M. Frank, On the role of mesoscale eddies for the biological productivity and biogeochemistry in the eastern tropical pacific ocean off peru, *Biogeosciences*, *10*(11), 7293–7306, 2013.

Strub, P. T., F. A. Shillington, C. James, and S. J. Weeks, Satellite comparison of the seasonal circulation in the benguela and california current systems, *South African Journal of Marine Science*, *19*(1), 99–112, 1998.

Swart, N. C., I. J. Ansorge, and J. R. E. Lutjeharms, Detailed characterization of a cold antarctic eddy, *Journal of Geophysical Research: Oceans*, *113*(C1), n/a–n/a, 2008.

Szoeke, R. A. d., and D. B. Chelton, The modification of long planetary waves by homogeneous potential vorticity layers, *Journal of Physical Oceanography*, *29*(3), 500–511, 1999.

Tailleux, R., and J. C. McWilliams, The effect of bottom pressure decoupling on the speed of extratropical, baroclinic rossby waves, *Journal of Physical Oceanography*, *31*(6), 1461–1476, 2001.

Taupier-Letage, I., I. Puillat, C. Millot, and P. Raimbault, Biological response to mesoscale eddies in the algerian basin, *Journal of Geophysical Research: Oceans*, *108*(C8), 2003.

The Ring Group, Gulf stream cold-core rings: their physics, chemistry, and biology, *Science*, *212*(4499), 1091, 1981.

Thomas, L. N., Formation of intrathermocline eddies at ocean fronts by wind-driven destruction of potential vorticity, *Dynamics of Atmospheres and Oceans*, *45*(3-4), 252–273, 2008.

Thomsen, S., C. Eden, and L. Czeschel, Stability analysis of the labrador current, *Journal of Physical Oceanography*, *44*(2), 445–463, 2014.

Thomsen, S., T. Kanzow, G. Krahmann, R. J. Greatbatch, M. Dengler, and G. Lavik, The formation of a subsurface anticyclonic eddy in the peru-chile undercurrent and its impact on the near-coastal salinity, oxygen, and nutrient distributions, *Journal of Geophysical Research: Oceans*, *121*(1), 476–501, 2016.

Tomczak, J. M., An investigation into the occurrence and development of cold water patches in the upwelling region off NW Africa, in *"Meteor" Forschungsergebnisse*, vol. 13, pp. 1–42, 1973.

Tomczak, M., D. G. B. Large, and N. Nancarrow, Identification of diapycnal mixing through optimum multiparameter analysis .1. test of feasibility and sensitivity, *Journal of Geophysical Research-Oceans*, *99*(C12), 25267–25274, 1994.

Turi, G., Z. Lachkar, and N. Gruber, Spatiotemporal variability and drivers of pco(2) and air-sea co2 fluxes in the california current system: an eddy-resolving modeling study, *Biogeosciences*, *11*(3), 671–690, 2014.

Van Aken, H., G. Van Heijst, and L. Maas, Observations of fronts in the north sea, *Journal of Marine Research*, *45*(3), 579–600, 1987.

Villas Bôas, A. B., O. T. Sato, A. Chaigneau, and G. P. Castelão, The signature of mesoscale eddies on the air-sea turbulent heat fluxes in the south atlantic ocean, *Geophysical Research Letters*, p. 2015GL063105, 2015.

Vollmer, L., and C. Eden, A global map of meso-scale eddy diffusivities based on linear stability analysis, *Ocean Modelling*, *72*, 198–209, 2013.

von Storch, J. S., C. Eden, I. Fast, H. Haak, D. Hernandez-Deckers, E. Maier-Reimer, J. Marotzke, and D. Stammer, An estimate of the lorenz energy cycle for the world ocean based on the 1/10 degrees storm/ncep simulation, *Journal of Physical Oceanography*, *42*(12), 2185–2205, 2012.

Williams, P. D., P. L. Read, and T. W. N. Haine, Spontaneous generation and impact of inertia-gravity waves in a stratified, two-layer shear flow, *Geophysical Research Letters*, *30*(24), 2003.

Williams, P. D., T. W. N. Haine, and P. L. Read, Inertia-gravity waves emitted from balanced flow: Observations, properties, and consequences, *Journal of the Atmospheric Sciences*, *65*(11), 3543–3556, 2008.

## References

Williams, R. G., and M. J. Follows, *Ocean dynamics and the carbon cycle: Principles and mechanisms*, Cambridge University Press, 2011.

Wu, Q. L., Region-shrinking: A hybrid segmentation technique for isolating continuous features, the case of oceanic eddy detection, *Remote Sensing of Environment*, *153*, 90–98, 2014.

Wyrtki, K., The oxygen minima in relation to ocean circulation, *Deep-Sea Research*, *9*(1), 11–23, 1962.

Xu, L. X., S. P. Xie, J. L. McClean, Q. Y. Liu, and H. Sasaki, Mesoscale eddy effects on the subduction of north pacific mode waters, *Journal of Geophysical Research-Oceans*, *119*(8), 4867–4886, 2014.

Yen, P. P. W., W. J. Sydeman, S. J. Bograd, and K. D. Hyrenbach, Spring-time distributions of migratory marine birds in the southern california current: Oceanic eddy associations and coastal habitat hotspots over 17 years, *Deep-Sea Research Part Ii-Topical Studies in Oceanography*, *53*(3-4), 399–418, 2006.

Zamudio, L., H. E. Hurlburt, E. J. Metzger, and C. E. Tilburg, Tropical waveinduced oceanic eddies at cabo corrientes and the mara islands, mexico, *Journal of Geophysical Research: Oceans (19782012)*, *112*(C5), 2007.

Zamudio, L., E. J. Metzger, and P. Hogan, Modeling the seasonal and interannual variability of the northern gulf of california salinity, *Journal of Geophysical Research-Oceans*, *116*, 2011.

Zenk, W., B. Klein, and M. Schroder, Cape verde frontal zone, *Deep Sea Research Part A. Oceanographic Research Papers*, *38, Supplement 1*(0), S505–S530, 1991.

Zhai, X. M., H. L. Johnson, and D. P. Marshall, Significant sink of ocean-eddy energy near western boundaries, *Nature Geoscience*, *3*(9), 608–612, 2010.

Zhang, Z., Y. Zhang, W. Wang, and R. X. Huang, Universal structure of mesoscale eddies in the ocean, *Geophysical Research Letters*, *40*(14), 3677–3681, 2013.

Zhang, Z., W. Wang, and B. Qiu, Oceanic mass transport by mesoscale eddies, *Science*, *345*(6194), 322–324, 2014.

Zhang, Z. W., J. W. Tian, B. Qiu, W. Zhao, P. Chang, D. X. Wu, and X. Q. Wan, Observed 3d structure, generation, and dissipation of oceanic mesoscale eddies in the south china sea, *Scientific Reports*, *6*, 2016.

Zhurbas, V., T. Stipa, P. Malkki, V. Paka, N. Golenko, I. Hense, and V. Sklyarov, Generation of subsurface cyclonic eddies in the southeast baltic sea: Observations and numerical experiments, *Journal of Geophysical Research-Oceans*, *109*(C5), 2004.

Zindler, C., C. A. Marandino, H. W. Bange, F. Schtte, and E. S. Saltzman, Nutrient availability determines dimethyl sulfide and isoprene distribution in the eastern atlantic ocean, *Geophysical Research Letters*, *41*(9), 2014GL059547, 2014.

# 7 Acknowlegdements

# Erklärung

Hiermit erkläre ich an Eides Statt, dass ich die vorliegende Dissertation - abgesehen von der Beratung durch meinen Betreuer Prof. Dr. Peter Brandt - selbstständig und ohne fremde Hilfe angefertigt, keine anderen als die angegebenen Quellen und Hilfsmittel benutzt und die den benutzten Quellen wörtlich oder inhaltlich entnommenen Stellen als solche kenntlich gemacht habe. Diese Arbeit hat in gleicher oder ähnlicher Form noch keiner Prüfungsbehörde vorgelegen. Sie ist unter Einhaltung der Regeln guter wissenschaftlicher Praxis der Deutschen Forschungsgemeinschaft entstanden.

Kiel, 2016

_____

(Florian Schütte)